JUSTUS-LIEBIG-
UNIVERSITÄT
GIESSEN

NADPH-producing Enzymes from the Pentose Phosphate Pathway of *Plasmodium* and *Leishmania* as Targets for New Anti-infective Agents

CUMULATIVE DISSERTATION

A thesis submitted in fulfilment of the German degree

doctor rerum naturalium

– Dr. rer. nat. –

To the Faculty of Biology & Chemistry, FB 08

of Justus Liebig University, Giessen, Germany

by

Isabell Berneburg

Giessen, June 2023

The work reported in this thesis was carried out at the Interdisciplinary Research Center, Chair of Biochemistry and Molecular Biology, Justus Liebig University, Giessen, Germany. The thesis was supervised by Prof. Dr. med. Katja Becker and Prof. Dr. rer. nat. Peter Friedhoff.

The thesis defense examination committee was composed of:

Prof. Dr. med. Katja Becker
Chair of Biochemistry and Molecular Biology
Institute for Nutritional Sciences
Justus Liebig University Giessen
Interdisciplinary Research Center (IFZ)
Heinrich-Buff-Ring 26-32, 35392 Giessen

Prof. Dr. rer. nat. Peter Friedhoff
Institute for Biochemistry
Justus Liebig University Giessen
Heinrich-Buff-Ring 17, 35392 Giessen

Prof. Dr. med. Eveline Baumgart-Vogt
Chair of Medical Cell Biology
Institute for Anatomy und Cell Biology
Justus Liebig University Giessen
Aulweg 123, 35385 Giessen

Prof. Dr. rer. nat. Ritva Tikkanen
Institute for Biochemistry
Justus Liebig University Giessen
Friedrichstraße 24, 35392 Giessen

Declaration / Eidesstattliche Erklärung

I declare that I have completed this dissertation single-handedly without the unauthorized help of a second party and only with the assistance acknowledged therein. I have appropriately acknowledged and cited all text passages that are derived verbatim from or are based on the content of published work of others, and all information relating to verbal communications. I consent to the use of an anti-plagiarism software to check my thesis. I have abided by the principles of good scientific conduct laid down in the charter of the Justus Liebig University Giessen „Satzung der Justus-Liebig-Universität Gießen zur Sicherung guter wissenschaftlicher Praxis“ in carrying out the investigations described in the dissertation.

Ich erkläre: Ich habe die vorgelegte Dissertation selbstständig und ohne unerlaubte fremde Hilfe und nur mit den Hilfen angefertigt, die ich in der Dissertation angegeben habe. Alle Textstellen, die wörtlich oder sinngemäß aus veröffentlichten Schriften entnommen sind, und alle Angaben, die auf mündlichen Auskünften beruhen, sind als solche kenntlich gemacht. Ich stimme einer evtl. Überprüfung meiner Dissertation durch eine Antiplagiat-Software zu. Bei den von mir durchgeführten und in der Dissertation erwähnten Untersuchungen habe ich die Grundsätze guter wissenschaftlicher Praxis, wie sie in der „Satzung der Justus-Liebig-Universität Gießen zur Sicherung guter wissenschaftlicher Praxis“ niedergelegt sind, eingehalten.

Giessen, June 2023

_____

Isabell Berneburg

Table of contents

List of Publications

This thesis is based on the following peer-reviewed publications:

1. **Berneburg I***, Peddibhotla S*, Heimsch KC, Haeussler K, Maloney P, Gosalia P, Preuss J, Rahbari M, Skorokhod O, Valente E, Ulliers D, Simula LF, Buchholz K, Hedrick MP, Hershberger P, Chung TDY, Jackson MR, Schwarzer E, Rahlfs S, Bode L, Becker K, Pinkerton AB. An optimized dihydrodibenzothiazepine lead compound (SBI-0797750) as a potent and selective inhibitor of *Plasmodium falciparum* and *P. vivax* glucose 6-phosphate dehydrogenase 6-Phosphogluconolactonase. ***Antimicrob Agents Chemother*** 66**,** e0210921 (2022); https://doi.org/10.1128/aac.02109-21.

2. **Berneburg I**, Rahlfs S, Becker K & Fritz-Wolf K. Crystal structure of *Leishmania donovani* glucose 6-phosphate dehydrogenase reveals a unique N-terminal domain. ***Communic Biol*** 5, 1353 (2022); https://doi.org/10.1038/s42003-022-04307-7.

3. **Berneburg I,** Stumpf M, Velten A-S, Rahlfs S, Przyborski J, Becker K, Fritz-Wolf K. Structure of *Leishmania donovani* 6-phosphogluconate dehydrogenase and inhibition by phosphine gold(I) complexes: A potential approach to leishmaniasis treatment. ***Int J Mol Sci*** 24 (2023); https://doi.org/10.3390/ijms24108615.

* These authors contributed equally to this work.

Further publications related to this thesis:

1. Haeussler K, **Berneburg I**, Jortzik E, Hahn J, Rahbari M, Schulz N, Preuss J, Zapol'skii VA, Bode L, Pinkerton AB, Kaufmann DE, Rahlfs S, Becker K. Glucose 6-phosphate dehydrogenase 6-phosphogluconolactonase: characterization of the *Plasmodium vivax* enzyme and inhibitor studies. ***Malar J*** 18, 22 (2019); https://doi.org/10.1186/s12936-019-2651-z.

2. Blum L, Gul S, Ulshöfer T, Henke M, Krieg R, **Berneburg I**, Thomas D, Trautmann S, Kurz J, Geyer J, Geisslinger G, Becker K, Parnham MJ, Schiffmann S. In-vitro safety and off-target profile of the anti-parasitic arylmethylaminosteroid 1o. ***Sci Rep*** 10, 7534 (2020); https://doi.org/10.1038/s41598-020-64382-w.

3. Blum L, Ulshöfer T, Henke M, Krieg R, **Berneburg I**, Geisslinger G, Becker K, Parnham MJ, Schiffmann S. The immunomodulatory potential of the arylmethylaminosteroid sc1o. ***J Mol Med*** **(Berl)** 99, 261–272 (2021); https://doi.org/10.1007/s00109-020-02024-4.

4. Zapol'skii VA, **Berneburg I**, Bilitewski U, Dillenberger M, Becker K, Jungwirth S, Shekhar A, Krueger B, Kaufmann DE. Chemistry of polyhalogenated nitrobutadienes, 17:

Efficient synthesis of persubstituted chloroquinolinyl-1H-pyrazoles and evaluation of their antimalarial, anti-SARS-CoV-2, antibacterial, and cytotoxic activities. ***Beilstein J Org Chem*** 18, 524–532 (2022); https://doi.org/10.3762/bjoc.18.54.

5. Wagner MP, Formaglio P, Gorgette O, Dziekan JM, Huon C, **Berneburg I**, Rahlfs S, Barale J-C, Feinstein SI, Fisher AB, Ménard D, Bozdech Z, Amino R, Touqui L, Chitnis CE. Human peroxiredoxin 6 is essential for malaria parasites and provides a host-based drug target. ***Cell Rep*** 39, 110923 (2022); https://doi.org/10.1016/j.celrep.2022.110923.

---

6. **Berneburg I**, Shamsara J, Schmelzle S, Bogola K, Rahlfs S, van Zandbergen G, Kolb P. Identification and characterization of novel *Leishmania* G6PD inhibitors. *In preparation.*

7. **Berneburg I**, Chiu C, Nguyen Z, Wright K, Rahlfs S, Grevelding C, Haeberlein S, Auld D. High-throughput screening of small molecules reveals novel *Schistosoma* G6PD inhibitors. *In preparation.*

8. **Berneburg I**, Shamsara J, Rahlfs S, Schaefer J, van Zandbergen G, Diederich W, Kolb P. Fragment screening of a DNA-encoded library reveals novel inhibitors against *Leishmania donovani* G6PD. *In preparation.*

Contributions to Conferences

1. 11th Annual Conference of the International Giessen Graduate School for the Life Sciences, Giessen, Germany, September 19th–20th 2018, ***poster***.
2. 1st Retreat of the LOEWE Center DRUID (Novel Drug Targets against Poverty-Related and Neglected Tropical Infectious Diseases), Rauischholzhausen, Germany, November 26th–27th, 2018, ***talk***.
3. 2nd Spring Symposium LOEWE Center DRUID, Marburg, Germany, February 18th–19th 2019, *talk*.
4. Joint meeting of the 20th Anniversary Drug Design & Development Seminar (DDDS) of the German Society for Parasitology (DGP) & the LOEWE Center DRUID, Giessen, Germany, March 26th–29th, 2019, ***talk***.
5. 15th Annual BioMalPar conference on the "Biology and Pathology of the Malaria Parasite" Heidelberg, Germany, May 28th – 30th 2019, ***poster***.
6. 12th Annual Conference of the International Giessen Graduate School for the Life Sciences, Giessen, Germany, September 4th – 5th 2019, ***poster***.
7. 2nd Retreat of the LOEWE Center DRUID, Rauischholzhausen, Germany, November 25th–26th, 2019, ***poster + elevator pitch***.
8. 3rd Spring Symposium LOEWE Center DRUID, Frankfurt am Main, Germany, February 3rd–4th, 2020, ***talk***.
9. Molecular approaches to malaria 2020, Lorne, Victoria, Australia, February 23rd–27th, 2020, ***poster***.
10. 1st digital Conference of the International Giessen Graduate School for the Life Sciences, Giessen, Germany, September 29th–30th 2020, ***talk + chairperson***.
11. 3rd Retreat of the LOEWE Center DRUID, online, October 26th–28th, 2020, ***talk***.
12. 4th Spring Symposium LOEWE Center DRUID, online, February 22nd–24th, 2021, ***talk***.
13. 29th Annual Meeting of the German Society for Parasitology (DGP), online, March 15th–17th, 2021, ***talk***.
14. 4th Retreat of the LOEWE Center DRUID, online, November 18th–19th, 2020, ***talk***.
15. 5th Spring Symposium LOEWE Center DRUID, online, February 14th–15th, 2022, ***talk***.
16. 22nd Drug Design & Development Seminar (DDDS) of the German Society for Parasitology (DGP), Munich, Germany, July 12th–15th, 2022, ***talk***.
17. 5th Retreat of the LOEWE Center DRUID, Rauischholzhausen, Germany, September 12th–13th, 2022, ***poster + elevator pitch***.
18. 6th Spring Symposium LOEWE Center DRUID, Marburg, Germany, February 27th–28th, 2023, ***poster + elevator pitch***.

Abstract

Malaria and the so-called neglected tropical diseases (NTDs) such as leishmaniasis, Chagas disease, and schistosomiasis remain a major public health problem that disproportionately affects the most vulnerable populations in low-income countries. These diseases cause a substantial burden on affected communities, resulting in around 800,000 deaths per year, and millions more suffering from long-term disabilities, and socioeconomic consequences. Current chemotherapeutic agents to treat malaria and NTDs, face challenges related to safety, efficacy, and drug resistance. As a result, there is an urgent need for novel anti-infective drugs with new mechanisms of action.

A promising approach is targeting the major enzymes glucose 6-phosphate dehydrogenase (G6PD) and 6-phosphogluconate dehydrogenase (6PGD) of the pentose phosphate pathway (PPP) that produce NADPH, the primary electron source for antioxidant defense in intracellular parasites. Previous studies have demonstrated the potential of these enzymes as drug targets in *Plasmodium falciparum* (*Pf*). A high-throughput screening against *Pf*G6PD, also called GluPho, identified two promising compounds, ML276 and ML304, from the National Institutes of Health collection. Further optimization of ML304 resulted in SBI-0797750 as the most promising candidate in terms of potency and efficacy.

One aim of this work was to further characterize the mode of inhibition (MOI) and action of SBI-0797750. Dose-response studies revealed an approximately 25-fold more potent compound with low nanomolar activity against recombinant *Pf*GluPho, *Plasmodium (P.) vivax* G6PD, and asexual blood stage parasites. SBI-0797750 is highly selective over the human counterpart and, like ML304, competes with G6P for its binding site. The mode of action is related to a disruption of the cytosolic glutathione-dependent redox potential, as well as the cytosolic and mitochondrial H_2O_2 homeostasis of *P. falciparum* blood stages. In addition, the studies have shown that SBI-0797750 does not affect the integrity of erythrocytes from either G6PD-normal or G6PD-deficient patients, whose erythrocytes are also highly dependent on NADPH production by their own G6PD.

Based on the results from *Plasmodium*, this work aimed to transfer the concept to G6PDs and 6PGDs from NTD-causing pathogens, such as *Leishmania* and *Schistosoma*. To this end, the respective enzymes were first recombinantly produced and their oligomerization behavior and kinetic properties were determined. The next step was to determine their three-dimensional structure and identify novel inhibitors.

In this work, the first three-dimensional crystal structure of *Leishmania donovani* G6PD (*Ld*G6PD), both native and complexed with one or both substrates, was solved. In contrast to previous kinetoplastid G6PD structures, the unique N-terminal domain is fully visible. The N-domain is not essential for enzyme activity, but this study indicates that it is involved in tetramerization, albeit quite different to the previously observed tetramer of *Trypansoma*

cruzi G6PD, which lacks the N-terminal domain. Structural and kinetic studies of the substrate binding mode further indicated G6P-dependent domain motions involving the N-domains.

This work also led to the solution of the first crystal structure of *Leishmania* donovani 6PGD (*Ld*6PGD). Most interestingly, a previously unknown conformation of NADPH was observed in the respective structure. In addition, auranofin, and most likely gold(I)-containing compounds in general, were identified as an interesting class of compounds against *Leishmania* 6PGDs. Although previous studies have shown that auranofin, which was used over decades against rheumatoid arthritis, is also highly effective against parasites, trypanothione reductase and its orthologues were previously thought to be the sole target of auranofin. Interestingly, *Leishmania* and *Plasmodium* 6PGD were also inhibited in the low micromolar range, while the human 6PGD remained fully active. MOI studies revealed that the gold(I) moiety of auranofin is responsible for the observed inhibition, competing with 6-phosphogluconate for its binding site, followed by a rapid irreversible inhibition.

The findings of this thesis contribute to the understanding of parasitic G6PDs and 6PGDs and their potential as drug targets. The novel structural and biochemical insights into *Kinetoplastida* G6PDs and 6PGDs, exhibiting major differences to the human enzymes, will provide an excellent basis for further structure-based inhibitor studies and increase the prospects of developing selective G6PD / 6PGD inhibitors.

Zusammenfassung

Malaria und die sog. vernachlässigten Tropenkrankheiten (*neglected tropical diseases*, NTDs) wie Leishmaniose, die Chagas-Krankheit und Bilharziose stellen nach wie vor eine große Bürde für die öffentliche Gesundheit dar. Am stärksten gefährdet sind dabei Bevölkerungsgruppen in Ländern mit sehr niedrigem Einkommen. Diese Krankheiten sind eine gravierende Belastung für die betroffenen Gemeinschaften und führen jährlich zu ca. 800.000 Todesfällen. Bei Millionen weiterer Menschen führen sie zu langfristigen körperlichen Behinderungen und den damit verbundenen negativen sozioökonomischen Folgen. Da die derzeitigen medikamentösen Behandlungsstrategien gegen Malaria und NTDs zudem vor großen Herausforderungen in Bezug auf Sicherheit, Wirksamkeit und Arzneimittelresistenz stehen, besteht aktuell ein dringender Bedarf an neuartigen Antiinfektiva mit neuen Wirkmechanismen.

Spezielle Enzyme des Pentosephosphatweges (PPP) (Glucose-6-Phosphat-Dehydrogenase (G6PD) und 6-Phosphogluconat-Dehydrogenase (6PGD)) stellen ein vielversprechendes Wirkstoffziel dar, da sie NADPH als primäre Elektronenquelle für die antioxidative Abwehr in intrazellulären Parasiten produzieren. Bereits in früheren Studien an *Plasmodium falciparum* (*Pf*) konnte gezeigt werden, dass diese Enzyme ein großes Potential als zukünftige Wirkstoffziele aufweisen. Durch den Einsatz eines Hochdurchsatz-Screening gegen *Pf*G6PD, auch GluPho genannt, konnten bereits zwei vielversprechende antiplasmodiale Verbindungen, ML276 und ML304, aus der Sammlung des „National Institutes of Health“ identifiziert werden. Die weitere Optimierung von ML304 ergab die Verbindung SBI-0797750 als den am vielversprechendsten Kandidaten in Bezug auf Potenz und Wirksamkeit.

Ein Ziel dieser Arbeit war es, den Hemm-Mechanismus und die Wirkungsweise von SBI-0797750 weiter zu charakterisieren. Die durchgeführten Dosis-Wirkungs-Studien ergaben dabei einen etwa 25-fach wirksameren Inhibitor mit niedriger nanomolarer Aktivität gegen rekombinante *Pf*GluPho, *Plasmodium* (*P.*) *vivax* G6PD und gegen asexuelle Parasiten im Blutstadium. SBI-0797750 zeigte sich hochselektiv gegenüber dem menschlichen Enzym und konkurriert, wie ML304, mit G6P um dessen Bindungsstelle. Die Wirkungsweise von SBI-0797750 steht im Zusammenhang mit einer Störung des cytosolischen Glutathion-abhängigen Redoxpotentials sowie der cytosolischen und mitochondrialen H_2O_2-Homöostase von *P. falciparum*-Blutstadien. Darüber hinaus konnte gezeigt werden, dass SBI-0797750 die Integrität von Erythrozyten sowohl von G6PD-normalen als auch von G6PD-defizienten Patienten nicht beeinträchtigt, obwohl deren Erythrozyten ebenfalls in hohem Maße von der NADPH-Produktion durch ihre eigene G6PD abhängig sind.

Ausgehend von den Ergebnissen aus *Plasmodium* sollte das Konzept anschließend auf G6PDs und 6PGDs aus Pathogenen wie *Leishmania* und *Schistosoma* (NTDs) übertragen werden. Dazu wurden die entsprechenden Enzyme zunächst rekombinant hergestellt und sowohl ihr Oligomerisierungsverhalten als auch ihre kinetischen Eigenschaften bestimmt. In einem

nächsten Schritt sollte die dreidimensionale Struktur der Enzyme entschlüsselt und neue Inhibitoren identifiziert werden.

Im Rahmen dieser Arbeit, konnte die erste dreidimensionale Kristallstruktur von *Leishmania donovani* G6PD (*Ld*G6PD) gelöst werden, sowohl in nativer Form als auch im Komplex mit einem oder beiden Substraten. Im Gegensatz zu früheren kinetoplastiden G6PD-Strukturen ist die einzigartige N-terminale Domäne vollständig sichtbar. Die N-Domäne ist zwar nicht essentiell für die Enzymaktivität, aber diese Studie deutet darauf hin, dass sie an der Tetramerisierung beteiligt ist, allerdings mit großem Unterschied zum zuvor beobachteten Tetramer der *Trypansoma cruzi* G6PD ohne N-terminale Domäne. Strukturelle und kinetische Untersuchungen des Substratbindemechanismus wiesen außerdem auf eine G6P-abhängige Domänenbewegung hin, an denen die N-Domänen ebenfalls beteiligt sind.

Die vorliegende Arbeit führte ebenfalls zur Lösung der ersten Kristallstruktur von *Leishmania donovani* 6PGD (*Ld*6PGD). Besonders interessant ist hierbei, dass in der vorliegenden Struktur eine bisher unbekannte Konformation von NADPH zu sehen ist. Darüber hinaus wurden Auranofin und potentiell Gold(I)-haltige Verbindungen im Allgemeinen als eine interessante Klasse von Inhibitoren gegen *Leishmania* 6PGDs identifiziert. Obwohl frühere Studien gezeigt haben, dass Auranofin, das jahrzehntelang gegen rheumatoide Arthritis eingesetzt wurde, auch antiparasitäre Eigenschaften besitzt, wurde bisher angenommen, dass die Trypanothionreduktase und ihre Orthologe die einzigen Ziele dieser Verbindung sind. Interessanterweise wurden jedoch auch *Leishmania* und *Plasmodium* 6PGD im niedrigen mikromolaren Bereich gehemmt, wobei die humane 6PGD ihre volle Aktivität behielt. Die durchgeführten Studien zum Hemm-Mechanismus ergaben, dass die im Auranofin enthaltene Gold(I)-Einheit für die beobachtete Hemmung verantwortlich ist, indem diese mit 6-Phosphogluconat um dessen Bindungsstelle konkurriert, gefolgt von einer schnellen irreversiblen Hemmung.

Die Ergebnisse dieser Arbeit tragen zum Verständnis der parasitären G6PDs und 6PGDs bei und verdeutlichen ihr Potenzial als Wirkstoffziele. Die neuen strukturellen und biochemischen Erkenntnisse über die G6PDs und 6PGDs von *Kinetoplastida*, die sich erheblich von den menschlichen Enzymen unterscheiden, bilden eine hervorragende Grundlage für weitere strukturbasierte Hemmstoffstudien und erhöhen die Chancen auf die Entwicklung selektiver G6PD / 6PGD-Inhibitoren.

List of Figures and Tables

List of Abbreviations

6PG	6-phosphogluconate
6PGD	6-phosphogluconate dehydrogenase
6PGL	6-phosphogluconolactonase
ACT	Artemisinin-based combination therapies
ADME/T	Absorption, distribution, metabolism, excretion, toxicity
AMB-D	Amphotericin B deoxycholate
ART	Artemisinin
AT	Adenine + thymine
CL	Cutaneous leishmaniasis
CNSHA	Non-spherocytic hemolytic anemia
CQ	Chloroquine
DHEA	Dehydroepiandrosterone
DNA	Desoxyribonucleic acid
EA	Epiandrosterone
EC_{50}	Median effective concentration
FDA	Food and Drug Administration
G6P	Glucose 6-phosphate
G6PD	Glucose 6-phosphate dehydrogenase
GluPho	Glucose 6-phosphate dehydrogenase 6-phospho gluconolactonase
GR	Glutathione reductase
Grx	Glutaredoxins
GSH	Glutathione
GSSG	Glutathione disulfide
GST	Glutathione S-transferase
HIV	Human immunodeficiency virus
HK	Hexokinase
Hs	*Homo sapiens*
IC_{50}	Median inhibitory concentration
L.	*Leishmania*
LAmB	Lipid formulations of amphotericin B
LOPAC	Library of Pharmacologically Active Compounds
MCL	Mucocutaneous leishmaniasis
MLSMR	Molecular Libraries Small Molecule Repository
MOA	Mode of action
$NADP^+$	Nicotinamide adenine dinucleotide phosphate (oxidized from)
NADPH	Nicotinamide adenine dinucleotide phosphate (reduced from)
NIH	National Institutes of Health
NO	Nitric oxide
NTDs	Neglected tropical diseases
P.	*Plasmodium*

PAMPA	Parallel artificial membrane permeability
Pf	*Plasmodium falciparum*
*Pf*EMP1	*Plasmodium falciparum* erythrocyte membrane protein 1
PGI	Phosphoglucose isomerase
PKDL	Post-kala-azar dermal leishmaniasis
Plrx	Plasmoredoxin
PMNs	Polymorphonuclear neutrophil granulocytes
PPP	Pentose phosphate pathway
PQ	Primaquine
Prx	Peroxiredoxins
Pv	*Plasmodium vivax*
R5P	Ribose 5-phosphate
RBCs	Red blood cells
RNAi	RNA interference
RNS	Reactive nitrogen species
ROS	Reactive oxygen species
RPI	Ribose 5-phosphate isomerase
Ru5P	Ribulose 5-phosphate
RuPE	Ribulose 5-phosphate epimerase
SAR	Structure activity relationship
Sb^{3+}	Trivalent antimonials
Sb^{5+}	Pentavalent antimonials
SOD	Superoxide dismutase
SP	Sulfadoxine-pyrimethamine
Ssp.	Subspecies
T.	*Trypanosoma*
TKL	Transketolase
TAL	Transaldolase
TrxR	Thioredoxin reductase
TR	Trypanothione reductase
$Trx(SH)_2$	Reduced thioredoxin
$TrxS_2$	Oxidized thioredoxin
$T(SH)_2$	Reduced trypanothione
TS_2	Oxidized trypanothione
Txn	Tryparedoxin
TxnP	Tryparedoxin peroxidases
VL	Visceral leishmaniasis
WHO	World Health Organization
X5P	Xylulose 5-phosphate

1. INTRODUCTION

Malaria and neglected tropical diseases (NTDs), a diverse group of 20 diseases, including Chagas disease, leishmaniasis, schistosomiasis, dengue and trachoma among others, remain a major public health problem. Mainly prevalent in tropical and subtropical areas, they disproportionately affect the most vulnerable populations in low-income countries[1]. Despite their global impact, NTDs in particular have received limited attention and resources compared to the so-called "big three" – malaria, human immunodeficiency virus (HIV) and tuberculosis[1,2]. According to the latest estimates from the Global Burden of Disease Study, together malaria and NTDs caused 747,000 deaths in 2019[3], and millions more are suffering from long-term disabilities. This results in a devastating human, social, and economic burden in affected areas[1].

1.1. Malaria

Malaria is a vector-borne infectious disease that has been a major global health problem of humans through history and is a leading cause of death and disease in many tropical and subtropical countries[4,5]. Compared to the beginning of the millennium, significant progress has been made in the fight against malaria, with a global decrease in incidence and mortality of approximately 30% due to the increased use of insecticide-treated bed nets, indoor residual spraying, and slightly improved access to appropriate diagnosis and treatment. However, the high level of global involvement makes it still to one of the most important infectious diseases. In 2021, malaria was endemic in 84 countries, with an estimated 247 million cases and 619,000 deaths worldwide. Over the two peak years of the COVID-19 pandemic (2020–2021), COVID-19-related disruption to essential malaria services led to about 13 million more malaria cases and 63,000 more malaria deaths compared to the years before. The World Health Organization (WHO) African Region continues to carry a disproportionately high share of the global malaria burden, with 95% of all malaria cases and 92% of all malaria associated deaths. Children under the age of five are particularly vulnerable and account for about 80% of all malaria deaths in the Region[5].

The protozoan parasite *Plasmodium*, belonging to the group of *Apicomplexa*, is transmitted to humans by the bite of the female *Anopheles* mosquito[6,7]. *Plasmodium (P.) vivax*, *P. ovale*, *P. malariae, P. knowlesi* and *P. falciparum* are the five human-pathogenic species of *Plasmodium* and cause different types of malaria with different pathogenesis (*malaria tertiana*, *malaria quartana*, and *malaria tropica*). Most cases of malaria are caused by *P. falciparum* and *P. vivax*. Malaria and the associated symptoms are typically divided into uncomplicated and severe malaria. Symptoms of uncomplicated malaria are very unspecific and can include fever, chills, fatigue, body-aches, headaches, cough and diarrhea[8]. *P. falciparum,* mainly found in sub-Saharan Africa, causes the most severe form of malaria, *malaria tropica*, and is responsible for almost all malaria-related deaths[5,8]. Most common manifestations of severe malaria are cerebral malaria, acute lung injury that can progress to acute respiratory distress syndrome,

acute kidney injury and acidosis. Severe anemia, without major organ dysfunction, is a common presentation in children[8].

P. vivax, the causative agent of *malaria tertiana*, is responsible for 2% of all malaria cases but is the dominant parasite in most countries outside sub-Saharan Africa[5]. Compared to *P. falciparum*, *P. vivax* was considered a relatively benign parasite due to its mild course of infection and low incidence of deaths. However, recent studies reported that rates of severe disease and death due to *falciparum* or *vivax* malaria are comparable[4,9]. *P. vivax* parasites form liver stages (hypnozoites) and are responsible for a significant number of relapse infections that can occur months or even years after infection, particularly affecting the development of infants[4,8,9].

1.1.1. Life Cycle of *Plasmodium*

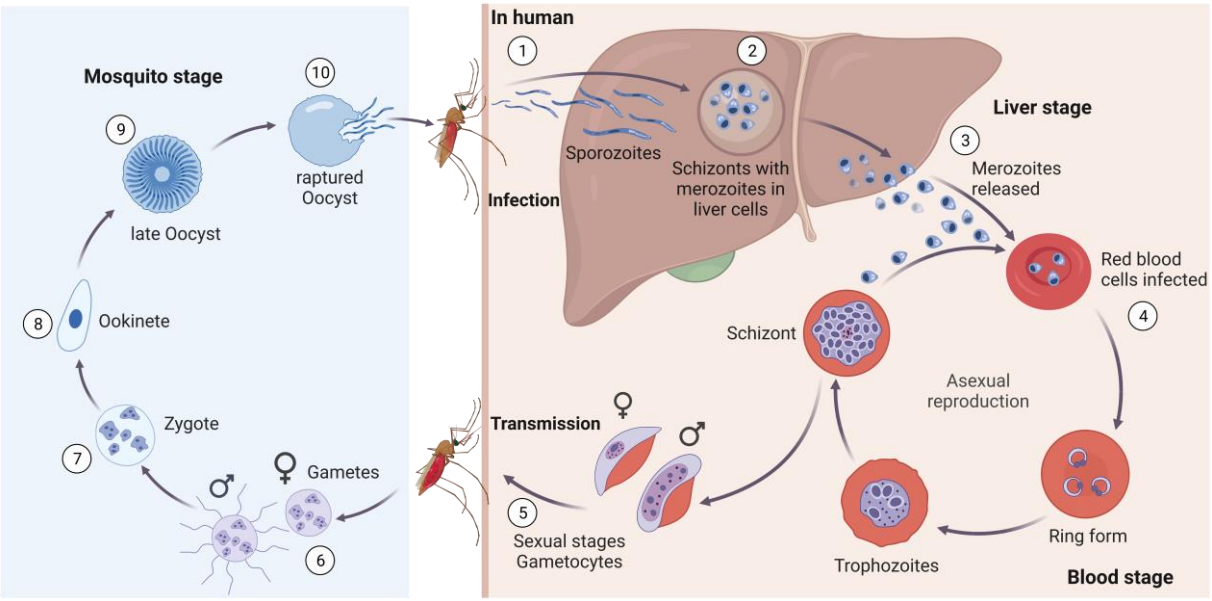

Figure 1. Life cycle of *Plasmodium falciparum* in the human host and the *Anopheles* mosquito.
The *Plasmodium* life cycle consists of three stages: The liver stage and the blood stage in the human host and the mosquito stage in *Anopheles*. Further details are described in the text below. Modified according to CDC[10] and White *et al*.[7], created with BioRender.

The complex life cycle of all human pathogenic *Plasmodium* subspecies (ssp.), depicted in **Figure 1**, is very similar and can be divided into a sexual phase within the *Anopheles* mosquito, and an asexual phase, within the human host[4]. The infective stages, the sporozoites, are first transmitted to the human host through the bite of an infected female *Anopheles* mosquito ①. The sporozoites then mature into schizonts ② during the exoerythrocytic liver stage, which typically lasts for 1–2 weeks, and release merozoites when they burst into the bloodstream ③[8,10]. In the case of *P. vivax*, hypnozoites, the dormant stage of the parasite, can persist in the liver and cause relapses by entering the bloodstream weeks or years later[7]. Once the merozoites have invaded red blood cells (RBCs) ④, the parasite undergoes serial cycles of asexual replication in the erythrocyte (blood stage), during which the merozoites develop into a ring form and later into trophozoites and mature schizonts. After schizont

rupture, more merozoites are released into the bloodstream, which can then infect more RBCs. The intraerythrocytic cycle takes approximately 48 h for *P. falciparum* and *P. vivax*, while it takes 72 h for *P. knowlesi* or *P. malariae*. This asexual intraerythrocytic cycle, in particular the rupture of the erythrocytes at the end of each stage, causes the typical fever attacks and other malaria symptoms, which first appear when the parasitemia exceeds 100 parasites per µL of blood. A subpopulation of intraerythrocytic parasites produces female and male gametocytes, the sexual stages of the parasite ⑤, which transmit malaria to the mosquito via a blood meal. Inside the mosquito midgut, gametocytes form exflagellated male and female gametes ⑥, which fuse to form zygotes ⑦. The zygotes are then transformed into mobile ookinetes ⑧ that pass through the gut wall and develop into oocysts ⑨. When the oocysts rupture ⑩, sporozoites are released and migrate to the salivary glands of the mosquito, ready to be transmitted to the human host with the next mosquito bite[7,8,10].

P. falciparum virulence is primarily based on its ability to evade the human immune system by modifying infected RBCs. Key players in this process are proteins of the *P. falciparum* erythrocyte membrane protein (*Pf*EMP1) family. These adhesive proteins are expressed by the parasite and exported to the surface of infected RBCs, where they mediate the adhesion of infected RBCs to the vascular endothelium[4,11]. This allows the parasite to avoid clearance by the spleen and causes endothelial cell injury as well as microvascular obstruction[8]. These polymorphic proteins are encoded by a multi-copy gene family known as *var*. As the immune system produces antibodies against the currently expressed *Pf*EMP1, a subset of parasites switch expression to antigen distinct isoforms of *Pf*EMP1, allowing them to evade immune destruction and reestablish infection[4,11].

1.1.2. Treatment of Malaria

Current malaria control strategies rely on preventive measures, such as vector control with long-lasting insecticide-treated bed nets, chemoprophylaxis in pregnant women and young children, and case management, consisting of early diagnosis and artemisinin-based combination therapies[12,13]. With these measures two billion malaria cases and 11.7 million malaria deaths were averted in the period from 2000–2021[5]. Chemotherapy is currently the only accessible strategy to treat and control malaria infection[14]. To prevent a severe progression of the disease, the primary goal of malaria treatment is a rapid and complete clearance of the malaria parasite from the patient's bloodstream. Effective treatment reduces transmission of the parasite to other individuals and also prevents the emergence and spread of antimalarial drug resistance[15,16], which is the major reason for the high mortality rates caused by malaria[17]. Due to the emergence of resistant parasites to several effective antimalarial drugs, the WHO recommends an artemisinin-based combination therapy (ACT) for uncomplicated malaria[14,15]. ACT combines an artemisinin derivative that rapidly reduces parasitemia with a partner drug that removes residual parasites over a longer period. The leading ACTs recommended by the WHO are artemether-lumefantrine, artesunate-amodiaquine, artesunate-mefloquine, dihydroartemisinin-piperaquine, artesunate +

sulfadoxine-pyrimethamine and artesunate-pyronaridine[15]. Some of these currently used antimalarials are briefly described in the following section.

Artemisinin and derivatives

Artemisinin (ART) is a sesquiterpene lactone compound originally derived from the sweet wormwood plant *Artemisia annua*. Derivatives of ART used as antimalarials are dihydroartemisinin, artesunate and artemether, which have improved bioavailability and efficacy. The exact mechanism of action (MOA) of ART is not yet fully understood. Drug activation is thought to involve iron-catalyzed reductive cleavage of the endoperoxide bond of the drug, generating free radicals that react with susceptible groups in parasite proteins as well as with unsaturated membrane lipids and heme itself[18]. Among others, ART has also been shown to inhibit phosphoinositide 3-kinase, whose activity plays also a role in hemoglobin endocytosis to the digestive vacuole of the parasite[19,20]. ART is exceptionally fast-acting against intraerythrocytic blood stage parasites, and already effective against very early asexual ring stage parasites[18].

4-aminoquinolines

This group of antimalarials includes chloroquine (CQ) and amodiaquine. CQ accumulation in the parasite's digestive vacuole prevents the formation of hemozoin crystals, which are necessary for the parasite to digest hemoglobin and detoxify heme[21,22]. CQ has been used to treat severe malaria for nearly eight decades and was also the most successful single drug for malaria treatment and prophylaxis[14,21]. CQ is a safe and affordable drug but resistant malaria strains to CQ have developed very early and spread over almost the entire malaria regions where *P. falciparum* is endemic[12,21]. However, CQ is still used for uncomplicated malaria caused by *P. vivax*, *P. ovale* or *P. malariae*[7,8].

Arylaminoalcohols

Arylaminoalcohols include antimalarials such as quinine, mefloquine and lumefantrine. Similar to 4-aminoquinolines, this class of compounds may also partially interfere with hemozoin formation and detoxification of hemoglobin degradation by-products. However, the MOA is not fully understood[21,22]. Quinine was the first successful antimalarial drug and already used in the 17th century. Although resistant strains have already developed and quinine has many serious side effects, it is still one of the most important drugs for uncomplicated malaria and also important for severe malaria as intravenous applications are available[12,21]. Mefloquine is widely used to treat multidrug-resistant *P. falciparum* malaria and as prophylaxis in travellers, but it is also associated with neuropsychiatric side effects[14,21].

8-aminoquinoline

Primaquine (PQ) is currently the only antimalarial of this compound class and different from other antimalarials as it is active against liver and sexual stages, but also dormant hypnozoites, which are responsible for relapses caused by *P. vivax* and *P. ovale*[14,21]. PQ is metabolized to

5-hydroxyprimaquine, which generates reactive oxygen species (ROS) in erythrocytes leading to cytoskeletal and membrane lipid peroxidation and hemolysis. In addition, the rapid glutathione (GSH) depletion in erythrocytes as a consequence of ROS production can cause severe hemolysis in individuals with glucose 6-phosphate dehydrogenase (G6PD) deficiency and is therefore contraindicated (see 1.3.5). Therefore, in countries with a high incidence of G6PD deficiency, testing for G6PD deficiency is recommended prior to treatment with PQ[7,14,21,23].

Vaccines

The development of malaria vaccines has taken a lot of time, effort and money. The RTS,S/AS01 vaccine is the first and currently the only malaria vaccine that is recommended for use by the WHO[15] and based on the circumsporozoite protein on the surface of pre-erythrocytic *P. falciparum* stages[7]. Since October 2021, WHO recommends broad use of the RTS,S/AS01 vaccine among children living in regions with moderate to high *P. falciparum* malaria transmission. Although the vaccine is non-inferior to seasonal malaria chemoprevention, and should be used in combination, the vaccine has been shown to significantly reduce malaria, and deadly severe malaria, among young children[5,15]. Vaccine efficacy and cases averted were highest in the site with the lowest malaria transmission, reaching up to 75% during 48 months of follow-up[24].

Two more vaccine candidates are currently approaching late-stage clinical evaluation. The R21/Matrix-M vaccine targeting also the circumsporozoite protein[15,25], and the attenuated whole sporozoites vaccine *Pf*SPZ[15]. New technologies such as DNA- and mRNA-based vaccines and the ongoing development of adjuvants and delivery platforms are being explored for use in malaria vaccines[15,24].

In summary, effective preventive measures and drugs are currently available to treat and eliminate *P. falciparum* and *P. vivax*. However, current chemotherapeutic agents for malaria, including ACTs, face challenges related to safety, efficacy, and the emergence of drug-resistant parasites due to the complex life cycle and mutation rate of the malaria parasite, which can appear more quickly under the influence of drugs. As a result, there is an urgent need for novel, cost-effective, non-toxic and efficacious antimalarial drugs with low propensity to develop drug resistance and new mechanisms of action[8,12,14,15,21].

1.2. Leishmaniasis

The vector-borne infectious disease leishmaniasis is classified by the WHO as one of the 20 poverty-related NTDs. Leishmaniasis is caused by the protozoan parasite of the genus *Leishmania*, belonging to the *Trypanosomatidae* family, and transmitted through the bite of female sandflies of the genus *Phlebotomus* in Old World leishmaniasis or *Lutzomyia* in the Americas (New World). Only a small fraction of those infected with *Leishmania* will develop the disease, which is why the term leishmaniasis refers to the condition of becoming sick due to a *Leishmania* infection, rather than being generally infected with *Leishmania* parasites.

Depending on the species and the caused symptoms, the WHO classifies three main clinical forms of leishmaniasis: cutaneous, mucocutaneous, and visceral leishmaniasis, also known as kala-azar or black fever[26,27].

Visceral leishmaniasis (VL) is the most severe form of the disease. Typical symptoms of VL include irregular episodes of fever, splenomegaly, hepatomegaly, weight loss and anemia (**Figure 2A**)[26]. Due to secondary bacterial infection or severe anemia the disease is in over 95% of cases fatal within two years if left untreated[26,27]. An estimated 50,000 to 90,000 new cases of VL occur annually, most of them in Brazil, East Africa and India, although only 25–45% are reported to the WHO. As a sequel of VL, 5–10% of the patients develop post-kala-azar dermal leishmaniasis (PKDL). PKDL is usually characterized by asymptomatic macular, papular or nodular rash on face, upper arms and other parts of the body (**Figure 2B**)[26]. The underlying mechanism is not completely known, but an altered immune response due to treatment or self-healing is presumed. Since diagnosis is difficult in the field, it is often made clinically[28].

Figure 2. Symptoms of different leishmaniasis forms. **A**. A child with hepatosplenomegaly caused by visceral leishmaniasis (VL). **B**. A child with erythematous maculopapular rash caused by post-kala-azar dermal leishmaniasis (PKDL), which can occur after recovered VL. **C**. Skin lesions of a male patient infected with cutaneous leishmaniasis (CL). **D**. A male patient with severe oronasal lesions caused by mucocutaneous leishmaniasis (MCL). The images were taken from Burza *et al.*[27] and the Pan American Health Organization[29].

Cutaneous leishmaniasis (CL) is the most common form of the disease. It causes skin lesions, mainly ulcers, on exposed parts of the body (**Figure 2C**). Although most of the lesions will self-heal within the first two years, the disease leaves life-long disfiguring scars, serious disability and / or stigma[26,27]. An estimated 600,000 to one million new cases occur worldwide annually, 95% of the disease in America, the Mediterranean Basin, the Middle East and Central Asia[26].

Mucocutaneous leishmaniasis (MCL) is a severe form of CL and leads to partial or total destruction of mucous membranes of the nose, mouth and throat (**Figure 2D**)[26]. Due to the late stage destruction of the oronasopharyngeal mucosa and cartilage, leading occasionally to aspiration pneumonia, MCL is potentially life-threatening[27]. More than 90% of the MCL cases occur in Bolivia, Brazil, Ethiopia and Peru[26].

The different clinical manifestations of a *Leishmania* infection depend on the type of the infecting species and the host's immune response. More than 20 *Leishmania* species are infectious to humans, some seem to be more adapted to target the skin and others to invade visceral organs. VL is typically caused by *Leishmania (L.) donovani* and *L. infantum*, whereas the latter can also cause CL. *L. major, L. tropica, L. aethiopica, L. mexicana, L. braziliensis*, *and L. guyanensis* are typical strains causing CL, with the latter two having the potential to develop MCL[27,30].

1.2.1. Life Cycle of *Leishmania*

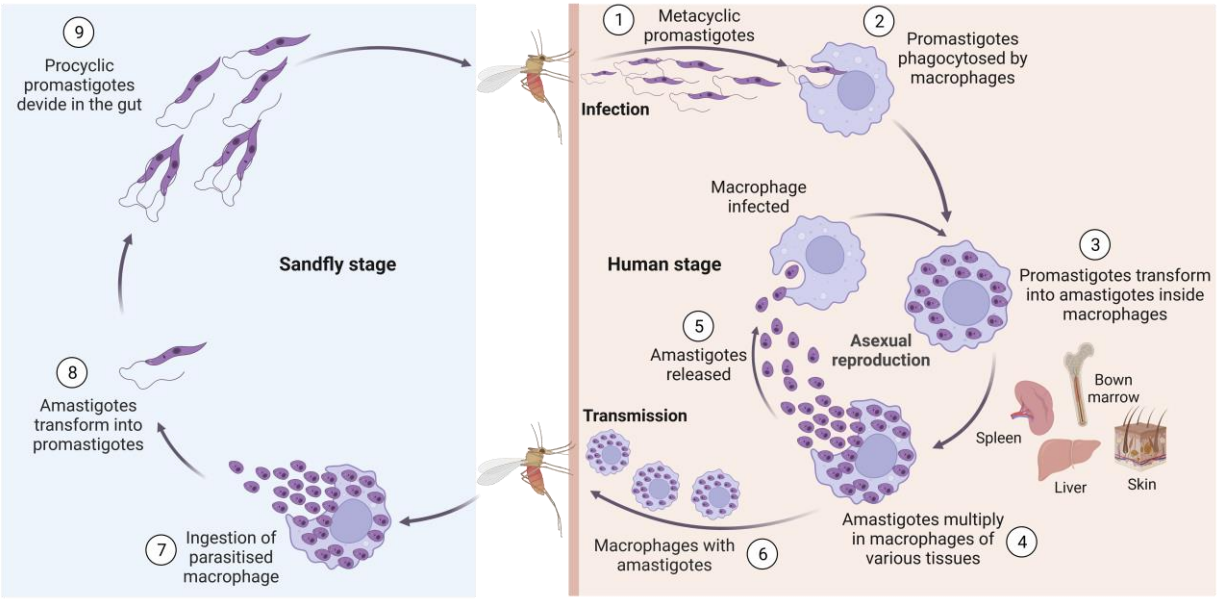

Figure 3. Life cycle of the *Leishmania* parasite in the human host and in the sandfly.
The *Leishmania* life cycle consists of two stages with a flagellated promastigote form in the sandfly and a nonflagellated amastigote form in the human host. Further details are described in the text below. Modified according to CDC[31] and Burza *et al.*[27], created with BioRender.

The life cycle of human pathogenic *Leishmania* ssp. is diphasic and can be divided into the flagellated promastigote form in the sandfly vector and the nonflagellated amastigote form in the human host (**Figure 3**). With the bite of a female sandfly, infectious metacyclic promastigotes are injected into the human host ① and quickly phagocytosed by several cell types of the host, such as macrophages and other mononuclear phagocytic cells ②[31–33]. The metacyclic promastigotes are then transformed into intracellular nonflagellated amastigotes ③, which undergo replication by simple division in a parasitophorous vacuole in the host cell ④ (asexual reproduction)[32]. After cell rupture local phagocytes are reinfected with amastigotes ⑤[34]. Depending on the host and parasite factors, the parasite infects phagocytes at the site of cutaneous infection (CL) or in organs rich in macrophages like secondary lymphoid organs, bone marrow and liver (VL)[32,35]. The transmission cycle is completed when infected phagocytes are taken up by another sandfly with a blood meal ⑥+⑦, either with an active skin lesion in CL or MCL or with parasitemia in VL. Amastigotes then convert into procyclic promastigotes ⑧ in the sandfly midgut and reproduce to high numbers in 4–14 days ⑨[32,34]. After migrating to the salivary glands of the

sandfly they transform into non-dividing metacyclic promastigotes, ready to be injected into a new host with the next blood meal[34]. *Leishmania* parasites possess unique and complex virulence mechanisms to evade the host immune system and are able to persist within the host cells to establish long-term chronic infection[32,35]. Pathogenesis and macrophage-*Leishmania* interactions vary significantly depending on the infecting *Leishmania* species[36]. After promastigotes are injected into the human host, polymorphonuclear neutrophil granulocytes (PMNs) are rapidly recruited to the site of infection under the guidance of chemokines[37]. The parasites survive inside the PMNs by inhibiting the phagosome acidification, but do not transform into amastigotes or proliferate[32,38]. Recruited by the PMNs, the second wave of macrophages enters the site of infection two to three days later. Like a "Trojan Horse" the PMNs help to transfer the promastigotes safely inside macrophages by forming apoptotic bodies[34]. Macrophages are the final host cells of *Leishmania*, in which the parasites begin to differentiate into amastigotes and multiply. It is during this phase that the first symptoms appear in the host[37].

1.2.2. Treatment of Leishmaniasis

Despite many attempts, an effective human vaccine to combat leishmaniasis does not yet exist[39]. Therefore, current leishmaniasis control strategies rely upon case management, vector control and drug treatment.

The first line treatment for visceral and cutaneous leishmaniasis are pentavalent antimonials (Sb^{5+}), with sodium stibogluconate and meglumine antimoniate as compounds of this family. For antileishmanial activity these prodrugs need to be reduced to trivalent antimonials (Sb^{3+}), which can occur either in the host cell or directly in the parasite[40,41]. For this purpose, thiols like GSH from host macrophages or the equivalent trypanothione from *Leishmania* parasites may serve as possible reducing agents[40,42]. Although the MOA of these antimonials is not yet fully understood, an Sb^{3+}-induced GSH and trypanothione efflux in promastigotes and amastigotes, as well as the trypanothione reductase as potential target of Sb^{3+}, suggest an involvement of the parasite's redox system[41,43,44].

In addition, amphotericin B deoxycholate (AmB-D) is used for leishmaniasis treatment. It targets ergosterol on the surface membranes of *Leishmania* parasites, leading to increased permeability and thus disruption of the parasite membrane[45,46]. Its intravenous administration, high toxicity, and adverse effects are major disadvantages. Liposomal formulations (LAmB) reduced these side effects, but high costs and the need of medical supervision make the use of these drugs still impractical[41,46]. However, LAmB has a high efficiency with a cure rate of >95%, which is why it is also considered as a first line drug for VL[47–49].

The only registered oral drug for leishmaniasis treatment is miltefosine. Several MOA have been identified. Miltefosine inhibits phosphatidylcholine synthesis[50], but also cytochrome C oxidase, disrupting the overall mitochondrial function[51]. Other studies showed that miltefosine is able to activate the Ca^{2+} channels in the parasite's plasma membrane, inducing

an alkalinisation of the *Leishmania* acidocalcisomes[52]. An induced apoptosis-like cell death is also discussed as MOA of miltefosine[53,54]. Despite its gastrointestinal toxicity and its teratogenicity, high efficiency and the ease of use, made miltefosine the first-choice treatment in many countries. However, commercialization and lack of control resulted in suboptimal use and subsequently drug resistance, which is why other antileishmanials like LAmB are still preferred[55,56].

In summary, there are only a few drugs available to treat leishmaniasis, which are mainly based on chemotherapeutic agents, often high in costs, toxic and with severe side effects. In addition, these drugs are highly divergent in terms of effectiveness across subspecies in different regions of the world, problematic in co-infected patients such as HIV/*Leishmania* and after decades of usage already emerged resistant strains[41,56,57]. Therefore, new drug targets and anti-infective agents with new MOA are urgently required.

1.3. The Pentose Phosphate Pathway

The pentose phosphate pathway (PPP) is a metabolic pathway that plays a central role in cellular metabolism. The PPP provides precursors for nucleotide and amino acid biosynthesis, reducing molecules for antioxidant defense and anabolism, and is important to maintain carbon homeostasis. As an alternative pathway to oxidize glucose, the PPP is tightly connected to glycolysis as the major consumer of glucose. The intermediate glucose 6-phosphate can either enter the PPP or continue through glycolysis[58,59].

1.3.1. Redox Metabolism in Protozoan Parasites

ROS and reactive nitrogen species (RNS) are reactive radical and non-radical derivatives of oxygen and nitrogen, respectively that are commonly generated within cells. The negative effects of these species on cellular functions are countered by antioxidant defense mechanisms. An imbalance between ROS/RNS production and antioxidant defense mechanisms induces oxidative stress, which is associated with oxidative damage to DNA, lipids and proteins[60,61].

For parasites, generation of oxidative stress is particularly critical, which is why antioxidant defense mechanisms of the parasites are considered promising anti-parasitic drug targets. The sources of ROS and RNS that act on the parasite during its life cycle are manifold. They originate from the host's immune response, but also from the parasite itself, for example through increased metabolism during reproduction and growth. Depending on the parasite and its stage in the life cycle, more ROS/RNS sources act on the parasite. *Plasmodium* parasites, for example, are exposed to increased oxidative stress during the intraerythrocytic blood stage (**Figure 1**) due to hemoglobin degradation[62]. The same is true for the intracellular stages of *Leishmania* parasites that live in mammalian macrophages (**Figure 3**), where oxidative stress is induced by enzymes such as nicotinamide adenine dinucleotide phosphate (NADPH) oxidase or nitric oxide (NO) synthase[63–65]. To counteract these extreme oxidative stress conditions, the parasites have a number of antioxidant defense mechanisms (**Figure 4**).

Like most other eukaryotic organisms, the antioxidative system of *Plasmodium* consists of superoxide dismutases (SODs) and the glutathione and thioredoxin systems[62,66–68], which are located in different subcellular compartments[69]. The glutathione system includes glutathione reductase (GR), glutathione (GSH), glutaredoxins (Grx) and glutaredoxin-like proteins, glutathione S-transferase (GST) and glyoxalases[62,67,68]. A lack of GR in *P. berghei* results in arrest of parasite development in the mosquito[70,71]. Disruption of enzymes of the glutathione system in *P. falciparum* has so far been unsuccessful, suggesting an essential role in parasite development[72].

The thioredoxin system consists of thioredoxin reductase (TrxR), thioredoxin (Trx) and thioredoxin-like proteins, peroxiredoxins (Prx) and plasmoredoxin (Plrx), which is unique for *Plasmodium*[62,66,68]. TrxR has been shown to be essential for the survival of intraerythrocytic *P. falciparum* parasites[73].

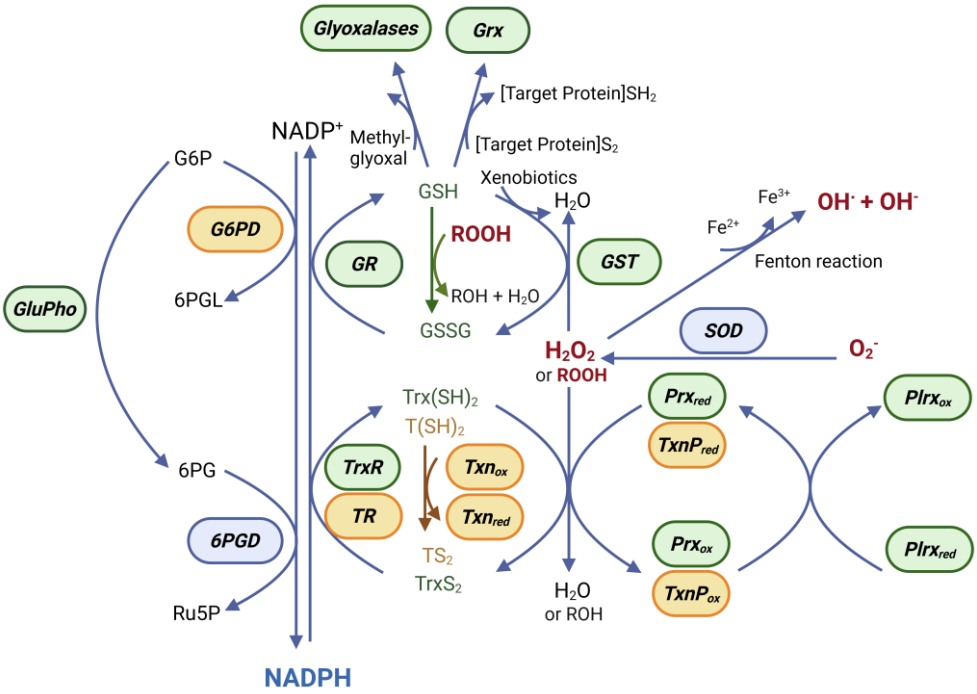

Figure 4. Antioxidant defense mechanisms of *Plasmodium* and *Leishmania* parasites.
Enzymes that are only present in *Plasmodium* are outlined in green, those that are only present in *Leishmania* are outlined in yellow and enzymes that are present in both species are outlined in blue. 6PG = 6-phosphogluconate, 6PGL= 6-phosphogluconolactone, 6PGD = 6-phosphogluconate dehydrogenase, G6P = glucose 6-phosphate, G6PD = glucose 6-phosphate dehydrogenase, GluPho = glucose 6-phosphate dehydrogenase 6-phosphogluconolactonase, GR = glutathione reductase, Grx = glutaredoxin, GSH = reduced glutathione, GST = glutathione S-transferase, GSSG = oxidized glutathione, Plrx = plasmoredoxin (reduced and oxidized), Prx = peroxiredoxin (reduced and oxidized), Ru5P = ribulose 5-phosphate, SOD = superoxide dismutase, TR = trypanothione reductase, TxnP = tryparedoxin peroxidases (reduced and oxidized), Txn = tryparedoxin (reduced and oxidized), TrxR = thioredoxin reductase, $Trx(SH)_2$ = reduced thioredoxin, $TrxS_2$ = oxidized thioredoxin, $T(SH)_2$ = reduced trypanothione, TS_2 = oxidized trypanothione. Modified according to Jortzik and Becker *et al.*[68], Krauth-Siegel *et al.*[74] and Irigoín *et al.*[75], created with BioRender.

In contrast to *Plasmodium* and their hosts, *Kinetoplastida* parasites lack GR and TrxR. Instead, they possess a trypanothione system, which is based on trypanothione ($T(SH)_2$), consisting of two GSH molecules covalently linked to spermidine, trypanothione reductase (TR),

tryparedoxin (Txn) and tryparedoxin peroxidases (TxnP)[74,75]. TR has been shown to be essential for *Trypanosoma* (*T.*) *brucei*[76] and *L. donovani*[77] viability. Unlike their hosts, both *Kinetoplastida*[74] and *Plasmodium*[68] parasites lack a catalase and selenocysteine-containing glutathione peroxidase.

These antioxidant defense systems of both *Plasmodium* and *Kinetoplastida* parasites highly depend on NADPH as their primary electron source (**Figure 4**)[68,74]. In most parasites the main source of NADPH is the PPP, which is why enzymes of this key metabolic pathway are considered promising drug targets for the control of protozoan parasites such as *Leishmania*, *Trypanosoma*[41,78,79] and *Plasmodium*[80,81].

1.3.2. Phases of the Pentose Phosphate Pathway

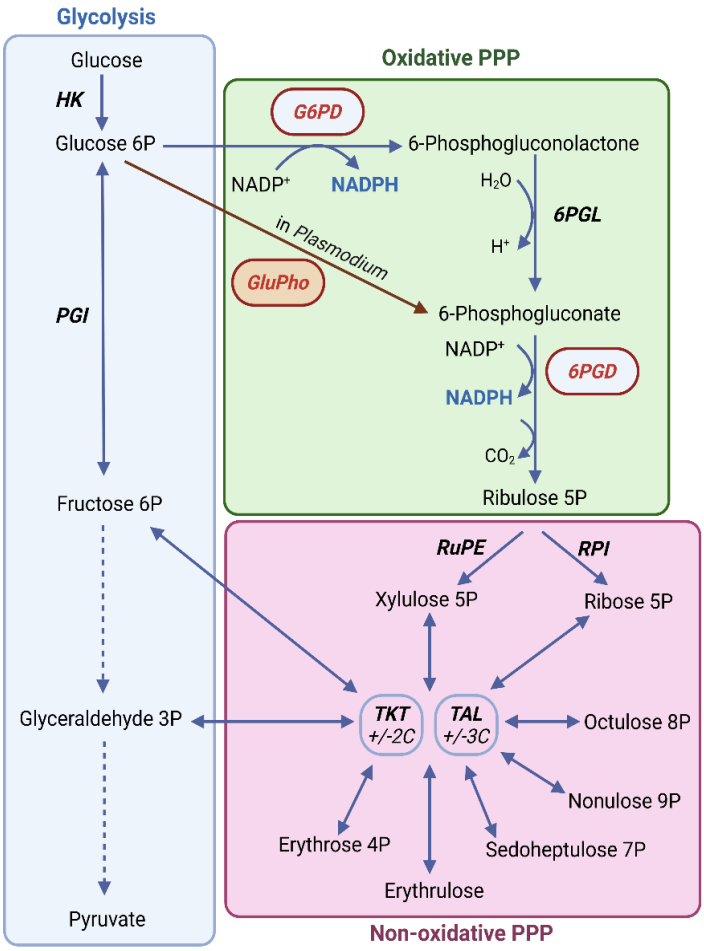

Figure 5. The pentose phosphate pathway. Glucose 6-phosphate can be metabolized by glycolysis or by the pentose phosphate pathway (PPP). The glycolytic pathway is shaded blue and the enzymes hexokinase (HK) and phosphoglucose isomerase (PGI) are shown. Other glycolytic reactions between fructose 6-phosphate, glyceraldehyde 3-phosphate and pyruvate are summarized and symbolized by dotted lines. The oxidative branch of PPP, shown in green, comprises the enzymes glucose 6-phosphate dehydrogenase (G6PD), 6-phosphogluconolactonase (6PGL) and 6-phosphogluconate dehydrogenase (6PGD). Instead of G6PD, glucose 6-phosphate dehydrogenase 6-phosphoglucono-lactonase (GluPho) is shown for *Plasmodium*. The non-oxidative branch, shown in red, comprises the enzymes ribulose 5-phosphate epimerase (RuPE), ribose 5-phosphate isomerase (RPI), transketolase (TKT) and transaldolase (TAL). TKT and TAL are able to shuffle two (+/- 2C) or three (+/- 3C) carbon units between a range of different intermediates. Phosphate is abbreviated as P. Modified according to Kovářová and Barrett *et al.*[82], created with BioRender.

The PPP is divided into two branches – the oxidative and non-oxidative PPP (**Figure 5**). The main function of the oxidative PPP is the production of NADPH. NADPH is an essential reducing agent for several cellular processes, such as antioxidant defense, fatty acid synthesis and other anabolic processes. In the unidirectional oxidative PPP, glucose 6-phosphate (G6P) from glycolysis is converted to ribulose 5-phosphate (Ru5P) by three irreversible enzymatic reactions that produce two molecules of NADPH per mole of consumed G6P. The first reaction is catalyzed by glucose 6-phosphate dehydrogenase (G6PD), which oxidizes G6P to 6-phosphoglucono-δ-lactone, resulting in one molecule of NADPH. The second reaction is

catalyzed by 6-phosphogluconolactonase (6PGL), which hydrolyses 6-phosphoglucono-δ-lactone to 6-phosphogluconate (6PG)[58,59]. In *Plasmodium* the first and the second enzyme of the PPP are bifunctionally fused to one enzyme, called glucose 6-phosphate dehydrogenase 6-phosphogluconolactonase (GluPho)[83].The final reaction of the oxidative PPP is catalyzed by 6-phosphogluconate dehydrogenase (6PGD), which decarboxylates 6PG to Ru5P, generating a second molecule NADPH and CO_2[58,59].

In the bidirectional non-oxidative phase, Ru5P from the oxidative branch is converted to a variety of three- to seven-carbon species that are used for nucleotide and amino acid synthesis and as glycolytic intermediates (**Figure 5**). Ru5P is either subsequently transformed into ribose 5-phosphate (R5P) by ribose 5-phosphate isomerase (RPI) or into xylulose 5-phosphate (X5P) by ribulose 5-phosphate epimerase (RuPE). Depending on the cellular need, these pentoses can be further converted to other intermediates, such as erythrose 4-phosphate and sedoheptulose 7-phosphate via the enzymes transketolase (TKL) and transaldolase (TAL)[58,59]. However, the cellular need of NADPH often exceeds that of R5P and X5P for nucleotide biosynthesis, which is why the interconversion reactions of TKL and TAL are also used to connect the non-oxidative PPP to glycolysis and with that to regulate the $NADPH/NADP^+$ ratio[58,78]: By catalyzing the transfer of two- and three-carbon units, TKL and TAL produce glyceraldehyde 3-phosphate and fructose 6-phosphate, which can then enter glycolysis and consequently via glucose 6-phosphate isomerase, which converts fructose 6-phosphate to G6P, enter again the PPP to produce more NADPH. As these reactions are reversible, the products of glycolysis can conversely enter the non-oxidative PPP when more precursors are needed for nucleotide or amino acid synthesis[58,59,78]. The interconversion reactions catalyzed by TKL and TAL are much more complex and are better considered as a sum of half-reactions, where both enzymes can use and combine multiple substrate and product pairs[82].

1.3.3. Localization in Protozoan Parasites

The protozoan parasites, *Leishmania* and *Plasmodium*, which were studied in this work, possess a complete PPP as described above. Like in *Plasmodium* and the human host, the PPP of most organisms is located in the cytosol[82,84]. However, there are some exceptions. The PPP can also be located between the cytosol and other organelles. This is true for the PPP of *Leishmania* and other trypanosomatid parasites. Although the cytosol is still the primary location of the PPP in trypanosomatids, the PPP as well as other enzymes of important metabolic pathways are also localized in peroxisome related and trypanosomatid specific glycosomes[82,85]. It is assumed that the compartmentalization of these crucial pathways in glycosomes enables a fast metabolic adaption to environmental changes and prevents accumulation of toxic metabolites[85–87].

1.3.4. Alternative Sources of NADPH

Membranes are considered impermeable for NADPH, which is why NADPH recycling and *de novo* biosynthesis are compartment-specific[59,88]. In most organisms, the PPP is the major contributor to the cytosolic NADPH pool. However, there are several other enzymes that can

generate NADPH, e.g., the cytosolic isoforms isocitrate dehydrogenase, glutamate dehydrogenase, methylenetetrahydrofolate dehydrogenase, aldehyde dehydrogenase and malate dehydrogenase[59,89–91].

Mammalian RBCs lack a nucleus or mitochondria, making the PPP the assumed primary source of NADPH[59,84,92]. *Plasmodium* parasites also seem to lack alternative cytosolic NADPH sources besides the PPP. While the role of mitochondrial isocitrate dehydrogenase is still unclear, cytosolic glutamate dehydrogenase has been shown to be dispensable for the parasite[93–95]. Additionally, NADPH-dependent malate dehydrogenase ("malic enzyme"), which significantly contributes to the NADPH pool in other organisms, seems to be absent in *Plasmodium*[96]. The absence of relevant alternative NADPH sources, combined with reliance of the host cells (erythrocytes) on the PPP as their primary NADPH source, emphasizes the crucial role of the PPP, specifically G6PD and 6PGD, in *Plasmodium* parasites[80].

Similar to *Plasmodium*, trypanosomatid parasites possess NADPH-producing enzymes, such as mitochondrial isocitrate dehydrogenase, glutamate dehydrogenase and methylenetetrahydrofolate dehydrogenase[97–100]. However, the contribution to the NADPH pool is thought to be negligible[82,101]. Unlike *Plasmodium*, trypanosomatid parasites possess a malic enzyme that uses malate to produce pyruvate and NADPH[102,103]. *T. brucei* and *T. cruzi* possess a cytosolic and mitochondrial malic enzyme. Recent studies suggest that this is also true for *Leishmania*[103,104]. The mitochondrial malic enzyme was found to be essential for precyclic *T. brucei* parasites, whereas the cytosolic enzyme is dispensable. Interestingly, simultaneous depletion of cytosolic malic enzyme and G6PD is lethal to the parasite, indicating a synergistic contribution of the PPP and malic enzyme to the NADPH pool[105].

1.3.5. Human G6PD Deficiency and Malaria

G6PD deficiency is the most common enzyme deficiency, affecting over 500 million people worldwide. The X-linked gene encoding for G6PD is highly polymorphic. Around 400 different G6PD variants have been identified so far, which correspond to 230 mutations[107]. These mutations cause quantitative and qualitative changes in the enzyme, resulting in varying enzyme activities, which is why the WHO has grouped the G6PD variant into classes[108,109].

Table 1. Proposed WHO classification of G6PD genetic variants in homozygous and hemizygous individuals.

Class	Median of G6PD activity	Hemolysis
Class A	<20%	Chronic (CNSHA)
Class B	<45%	Acute, triggered
Class C	60–150%	No hemolysis
Class U	Any	Uncertain clinical significance

CNSHA = chronic non-spherocytic hemolytic anemia. The table is adapted from the WHO[106].

The WHO Malaria Policy Advisory Group recently revised the current classes and recommended a classification of the G6PD variations based on the median residual enzyme activity expressed as a percentage of normal activity, which is shown in **Table 1**. There is a gap

between the proposed Classes B and C, as no variants have been identified in homozygous deficient females or hemizygous deficient males that have residual G6PD activity between 45% and 60%. New variants falling in this range should be included in class U until solid evidence is found that they induce acute hemolytic anemia (Class B) or do not pose a hemolytic risk (Class C)[106].

As RBCs do not possess a nucleus or organelles such as mitochondria, there are no alternative sources of NADPH other than the PPP (see 1.3.4). For the same reasons these cells do not need NADPH for the biosynthetic pathways discussed above (see 1.3.2), which is why the central role of G6PD in RBCs is to produce NADPH for antioxidant defense. In fact, RBCs in particular are constantly exposed to endogenous oxidative stress, because their central role in loading, carrying and unloading the hemoglobin-bound oxygen can generate superoxide radicals via the Fenton reaction (see **Figure 4**, chapter 1.3.1), making the supply of NADPH critical for RBCs[108,110]. For these reasons, it is clear why RBCs are more susceptible to the consequences of G6PD deficiency than other cells.

In normal RBCs, G6PD activity is only about 1% of its maximum due to the suppression of NADPH and ATP under physiological "steady state" conditions. Under oxidative stress, NADPH is consumed and G6PD is highly activated. In contrast, in G6PD-deficient RBCs, the $NADPH/NADP^+$ ratio is low, so the enzyme activity is already at its maximum under physiological conditions (depending on the variant) and cannot be up-regulated under oxidative stress, or only to a small extent[84]. The problem is exacerbated by the fact that mature RBCs can no longer carry out protein synthesis, so G6PD activity continues to decline as the cells age[111]. For this reason, most people with G6PD deficiency remain asymptomatic throughout their lives, unless they are exposed to oxidative stress. Possible oxidative stressors include the consumption of fava beans, infections (e.g. hepatitis, cytomegalovirus, COVID-19) and various drugs such as some antimalarials or antibiotics[92,107,109]. The lack of NADPH and consequently of GSH in G6PD-deficient RBCs exposed to oxidative stress, results in oxidized disulfide and sulfoxide groups on hemoglobin, leading to the precipitation of denatured hemoglobin as Heinz bodies and the formation of hemichromes. Together with ROS, this irreversibly damages the RBC membrane, leading to erythrocyte hemolysis, which can occur both intracellularly, resulting in hemoglobinuria, and extracellularly, with an increase in bilirubin. Less damaged RBCs are degraded by macrophages[112]. Besides acute hemolysis and non-spherocytic hemolytic anemia (CNSHA), other symptoms may include neonatal jaundice, fatigue and back pain[92,107,112].

The prevalence of G6PD deficiency correlates with the geographical distribution of malaria. It is therefore not surprising that G6PD deficiency has been shown to protect against malaria infection, or at least against a severe course of the disease. The degree of protection depends on many factors, including the G6PD variant, the gene carrier and the parasite strain[92,107,113–117]. The underlying mechanism of malaria protection is still not fully understood. Most likely a difference in host immune response is involved, where G6PD-deficient RBCs infected with *Plasmodium* are phagocytosed more intensively than normal infected cells[118]. In the early

intraerythrocytic ring stage, parasite G6PD activity is very low compared to host G6PD, probably leading to a lack of antioxidant protection and therefore to an increased phagocytosis with reduced parasitemia in G6PD-deficient RBCs. In the later trophozoite stage, the G6PD activity of the parasite exceeds that of the G6PD-deficient host, but it is thought that by this time the cell membrane of G6PD-deficient RBCs has already significantly changed so that they are also easily phagocytosed, independent of G6PD activity[118]. The hypothesized mechanism behind this phagocytosis potentially involves the recognition and binding of band 3 aggregates by naturally occurring antibodies. During parasite growth, hemoglobin is increasingly oxidized, resulting in the formation of hemichromes. The hemichromes in turn bind preferentially to the cytoplasmic domain of band 3, causing them to form clusters that are recognized by antibodies that trigger phagocytosis of infected RBCs[118]. In addition, proteomic studies revealed that specific host proteins are selectively oxidized in infected G6PD-deficient RBCs. These proteins are involved in the oxidative stress defense and response, as well as in the transport and assembly of exported parasite proteins in the erythrocyte cytoskeleton[119]. Courtin *et al.* observed a lower increase in immunoglobulin IgG3 levels against a group of *P. falciparum* merozoite surface proteins in infected G6PD-deficient carriers, possibly leading to a weaker stimulation of specific antibody responses compared to non-carriers. The protective mechanism may involve cell-mediated immune activity[120]. It is likely that many other factors are involved in the protective mechanism.

As mentioned above, some antimalarials such as PQ and analogues are known for their hemolytic risk in G6PD-deficient patients (see 1.1.2) [107,121–124]. Due to the increased prevalence of G6PD deficiency in malaria endemic areas, understanding the mechanisms behind this is critical to maintain RBC integrity in G6PD-deficient carriers when considering new targets and drugs[125]. As the first crucial step in hemolysis is a decrease in NADPH and consequently GSH[112], this becomes even more important when *Plasmodium* G6PD, the main supplier of NADPH, is used as a drug target against malaria (see **Publication I**[81]).

1.4. Glucose 6-Phoshate Dehydrogenase as a Drug Target in Protozoan Parasites

The $NADP^+$-dependent oxidoreductase G6PD is the first enzyme of the PPP and oxidizes G6P to 6-phosphoglucono-δ-lactone, while producing the first molecule of NADPH (see 1.3.2). As the first enzyme of the unidirectional oxidative PPP, it is also considered to be the key regulatory enzyme of the PPP, meaning that any factor that alters the activity, expression levels or localization of G6PD will also determine the activity and flux of the PPP [59,126].

1.4.1. Glucose 6-Phosphate Dehydrogenase 6-Phosphogluconolactonase of *Plasmodium*

The gene for G6PD from *P. falciparum* (*Pf*GluPho) is encoded on chromosome 14 and consists of 2,733 bp resulting in a product of 910 amino acids (UniProtKB acc. no Q8IKU0)[127]. In accordance with the generally high adenine + thymine (AT) content (80.6%) of the plasmodial genome[128], the AT content of *Pf*GluPho is 77.5%[127]. The presence of G6PD activity in

Plasmodium was first demonstrated in 1981 in cell extracts from *P. falciparum*-infected RBCs, which showed an additional band of G6PD activity on a polyacrylamide gel compared to uninfected RBCs[129]. Initial experiments on *Pf*GluPho demonstrated quickly that the plasmodial enzyme is different from the human G6PD (*Hs*G6PD). *Pf*GluPho, purified from infected RBCs, showed a higher affinity to its substrates and the enzyme was rather large compared to human and other G6PDs[127,130]. Unique to *Plasmodium* and some other *Apicomplexa* ssp.[131], *Pf*GluPho exists as a bifunctional enzyme – it combines the activities of the first two enzymes of the PPP that are isofunctional in most other species – explaining why the enzyme is much larger than G6PDs of other species. The C-terminal part of *Pf*GluPho (amino acids 311–910) is homologous to other G6PDs, whereas the N-terminal part of *Pf*GluPho (amino acids 1–310) encodes for 6PGL. This is why the enzyme is called glucose 6-phosphate dehydrogenase 6-phosphogluconolactonase (GluPho)[83,132]. The schematic structure of *Pf*GluPho compared to its human homologue is shown in **Figure 6**. The C-terminal G6PD domain of *Pf*GluPho comprises a unique insertion sequence that has been shown to be crucial for G6PD activity in *P. berghei*[133]. Interestingly, the activity of the enzyme was maintained when the *P. berghei* GluPho insertion was replaced by the *P. falciparum* GluPho insertion. However, this insertion varies in size and sequence between *Plasmodium* species. For example, the insertion in *P. berghei* GluPho, with 113 amino acids, is almost twice as large as in the homologous enzyme in *P. falciparum*, with 62 amino acids, which could explain the different consequences of its deletion[133]. However, the exact function of this insertion still needs to be clarified.

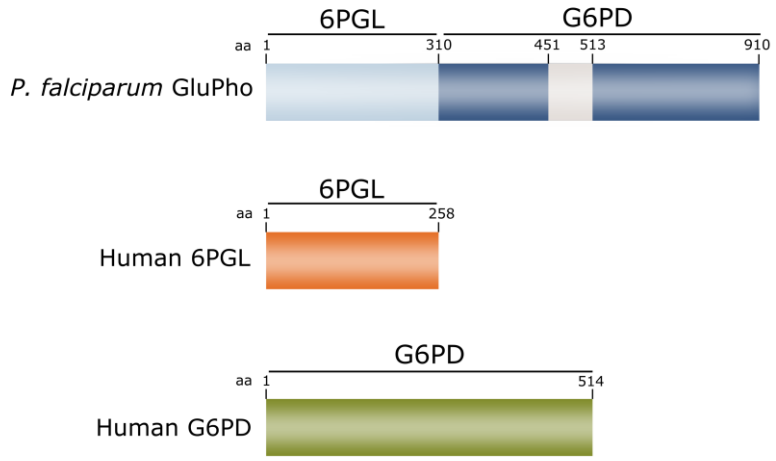

Figure 6. Scheme of bifunctional *P. falciparum* GluPho and the human counterparts 6PGL and G6PD.
In *P. falciparum*, the first two steps of the oxidative PPP are catalyzed by the bifunctional enzyme GluPho, which combines the G6PD and 6PGL reactions. In humans, this reaction is catalyzed by two separate enzymes, G6PD and 6PGL. The insertion (amino acids (aa) 451–513) in the G6PD part of *Pf*GluPho is specific for *Plasmodium*. Modified according to Preuss *et al.*[84].

The biochemical characterization of recombinant *Pf*GluPho by Jortzik *et al.* confirmed initial results from infected RBCs[83]. The enzyme is active as a tetramer (443 kDa) with a calculated molecular mass of 107 kDa per monomer. In contrast to the human enzyme, the tetramer formation is independent from substrates, product inhibitors, pH, or reducing agents. It was also confirmed that the affinity of *Pf*GluPho to its substrates G6P and $NADP^+$ is higher compared to most other G6PDs. It was further suggested, that *Pf*GluPho follows a rapid

equilibrium random Bi-Bi-substrate binding mode in which both substrates must bind before product formation can occur. In addition, a sequential order of substrate binding was determined for *Pf*GluPho, but without a leading substrate[83]. The GluPho homologue in *P. vivax* (*Pv*GluPho), to which *Pf*GluPho shares 71% sequence identity and 80% similarity, was also biochemically characterized[134]. However, only the C-terminal part, the G6PD activity (*Pv*G6PD), was studied, revealing different oligomerization and kinetics. The *Pv*G6PD oligomerized as a hexamer and the catalytic efficiency of the enzyme was lower compared to *Pf*GluPho, which is why it was suggested that *Pf*GluPho has advantages when competing with the human host G6PD for substrates. However, the catalytic efficiency of the isolated *Pf*G6PD enzyme was also lower, although not as low as for *Pv*G6PD, which might be explained by structural advantages of the full-length GluPho enzyme[83,134].

Target validation

The fact that human G6PD deficiency, the most common human enzyme deficiency worldwide, protects to a certain extent against malaria infection, highlights the importance of GluPho for *Plasmodium* parasites (see 1.3.5)[107].

Interestingly, infected erythrocytes exhibited a 78-fold higher activity of the oxidative PPP than uninfected erythrocytes, with *Plasmodium* parasites responsible for 82% of this activity[135]. This underscores the potential of *Plasmodium* GluPho as a drug target, and is further supported by the detailed biochemical characterization of the bifunctional enzyme[83,134]. The identified structural and mechanistic differences between *Plasmodium* GluPho and its human homologous enzyme increase the likelihood of selective inhibition of the plasmodial enzyme. To prove conclusively that *Pf*GluPho is essential for the parasites, genetic target validation is required. Initial attempts were made using RNA interference (RNAi)-mediated gene silencing of *Pf*GluPho, which resulted in arrested parasite growth at the trophozoite stage, increased gametocyte formation and enhanced TrxR transcription[136]. However, the significance of these result is not clear, as *Plasmodium* parasites seem to lack a RNAi machinery[137]. Allen *et al.*, performed a double crossover knockout approach in asexual blood stage parasites, which was lethal for the parasites[80]. As the authors showed that they were able to target the *Pf*GluPho locus, these findings either indicate that *Pf*GluPho is essential for blood stage parasites, or that loss of this enzyme is highly deleterious for the parasite[80]. The use of a rescue plasmid or an inducible knockout system, such as is currently used in combination with the CRISPR-Cas9 knockout system, would be required to provide definitive evidence[138,139].

It has been suggested that *Pf*GluPho is regulated in response to oxidative stress. However, the presence of H_2O_2 or pro-oxidant drugs such as artemisinin[140], chloroquine[141] and methylene blue[142] did not increase the expression levels of *Pf*GluPho, indicating that the enzyme is not upregulated in response to these pro-oxidative conditions[80]. Although it has been suggested that *Pf*GluPho activity may be redox-regulated via post-translational modifications[83], as has

been shown for glycolytic enzymes such as glyceraldehyde 3-phosphate dehydrogenase[143] or pyruvate kinase[144], there is currently no consistent data to support this hypothesis[134].

The polyphenol plant extract ellagic acid has already been used in traditional medicine in Africa to treat malaria (**Figure 7**)[145]. Ellagic acid inhibits *P. falciparum* parasites with a median effective concentration (EC_{50}) between 105 and 330 nM and acts synergistically with other antimalarial drugs, such as chloroquine, mefloquine and artesunate[145]. Among others, ellagic acid has been shown to target *Pf*GluPho with an median inhibitory concentration (IC_{50}) of 77 ± 24 nM[80], and the corresponding enzyme in *P. vivax* (*Pv*G6PD) with an IC_{50} of 32.5 ± 13.4 nM[134]. While it also inhibits enzymes of the GSH metabolism, such as GR, GST, and TrxR[146], ellagic acid is three orders of magnitude more potent against *Plasmodium* GluPho than against these redox enzymes[80,146]. Therefore, the observed GSH depletion in *Plasmodium* after treatment with ellagic acid is more likely associated with *Pf*GluPho inhibition, resulting in NADPH depletion and therefore less efficient GSSG reduction[80]. However, this inhibition is not selective for *Plasmodium* as *Hs*G6PD is inhibited in a similar range[80,134].

Based on a chemical compound screening and following structure activity relationship (SAR) studies, a set of novel *Plasmodium* GluPho inhibitors was synthesized and assessed by Haeussler *et al.*[134]. Two compounds of this series, vz1732 and vz0527 (**Figure 7**), exhibited nanomolar activity with IC_{50} values of 0.9 ± 0.2 µM against *Pf*GluPho and 0.2 µM for *Pv*G6PD, and 1.7 ± 0.3 µM for *Pf*GuPho and 0.2 ± 0.1 µM for *Pv*G6PD, respectively[134]. However, selectivity over the *Hs*G6PD is rather low, as vz1732 and vz0527 inhibit the *Hs*G6PD with IC_{50}s of 34.7 ± 21 µM and 8.3 ± 2.7 µM. Kinetic investigations of the most potent compound vz1732 indicated a non-competitive binding mechanism towards both G6P and $NADP^{+}$[134]. Whether these inhibitors are also active *in vitro* against the malaria parasite remains to be investigated.

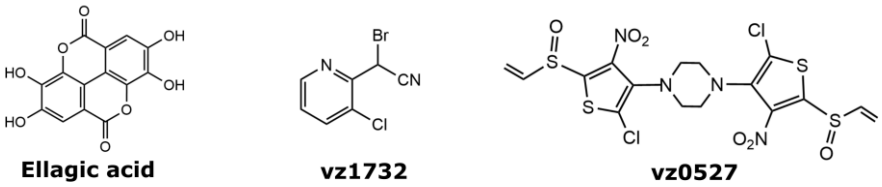

Figure 7. *Plasmodium* GluPho inhibitors.
Shown are the *Plasmodium* GluPho inhibitors ellagic acid from plant extract[80,134], and vz1732 and vz0527 newly synthesized by Dieter Kaufmann and Viktor Zapol'skii from Clausthal University of Technology[134].

Further attempts to find a selective *Pf*GluPho inhibitor were made by Preuss *et al.*, who screened approximately 400,000 compounds in a high-throughput format from various compound libraries including Library of Pharmacologically Active Compounds (LOPAC®1280), Spectrum, DIVERSet and the Molecular Libraries Small Molecule Repository (MLSMR) collection of the National Institutes of Health (NIH) against the recombinant *Pf*GluPho[147]. Two dibenzothiazepine-derived compounds from the NIH MLSMR collection, ML276 ((R,Z)-N-((1-ethylpyrrolidin-2-yl)methyl)-2-(2-fluorobenzylidene)-3-oxo-3,4-dihydro-2H-benzo[b][1,4]-thiazine-6-carboxamide)[148,149] and ML304 ((R)-N-((1-ethylpyrrolidin-2-yl)methyl)-4-methyl-11-oxo-10,11-dihydrodibenzo[b,f]-[1,4]thiazepine-8-car-boxamide)[150], were finally identified, inhibiting *Pf*GluPho with IC_{50} values of 0.89 µM and 0.19 µM, respectively. ML304 was also

found to inhibit *Pv*G6PD with an IC_{50} of 2.6 ± 0.8 µM[134]. ML276 and ML304 inhibit the plasmodial enzyme selectively over the human enzyme, as *Hs*G6PD was not inhibited up to a concentration of 80 µM (IC_{50} > 80 µM)[149,150]. On *P. falciparum* blood stage parasites, ML276 and ML304 showed EC_{50} values of 2.3 ± 0.2 µM and 0.5 µM for the chloroquine sensitive 3D7 strain, respectively[148]. Kinetic investigations revealed that both compounds act as competitive inhibitors against G6P and as a mixed type – indicated by parameters between a competitive and non-competitive inhibition – against $NADP^+$ [134,148]. Initial MOA studies with ML304 using redox probes indicated that its lethal effect on asexual *Plasmodium* parasites is linked to a disruption of the cytosolic glutathione-dependent redox potential[134].

Interestingly, ML304 has been shown to act synergistically to methylene blue in gametocytes, the sexual stage of *Plasmodium*. The MOA of methylene blue is linked to a NADPH depletion due to its redox-cycling activity. This NADPH depletion is most likely augmented by the concomitant inhibition of *Pf*GluPho-dependent NADPH production by ML304, explaining the observed synergy of methylene blue and ML304. Therefore, ML304 and methylene blue could also be used as a transmission blocking agent[151].

To further evaluate compound ML276 and ML304 as a potential antimalarial drug, both compounds were studied in a detailed *in vitro* pharmacology screen and revealed reasonable ADME/T (absorption, distribution, metabolism, excretion, toxicity) properties[148–150]. These include excellent solubility and no toxicity towards Fa2N-4 immortalized human hepatocyte cell lines in the tested range (LD_{50} > 50 µM). Consistent with their high solubility, the compounds exhibit high permeability in a standard parallel artificial membrane permeability assay (PAMPA) as well as when incubated with an artificial membrane that models the blood-brain barrier. ML276 and ML304 have a good plasma stability and were highly plasma protein bound which may contribute to its high plasma stability. Therefore the compounds would remain in the plasma and are hardly distributed to organs or tissues, increasing the exposure of the compound to the blood-borne malaria parasite[148–150]. To address the pharmacologic question of how long the compounds will remain circulating in plasma within the body, a microsomal stability assay was performed. ML276 exhibited moderate stability in human and modest stability in mouse liver homogenates[148,149]. Unfortunately, ML304 is almost completely metabolized in these cells within one hour[150].

To optimize the potency and ADME/T properties of ML276 and ML304, SAR studies were performed. The most promising candidate in terms of efficacy was SBI-0797750, a derivative of ML304. The medicinal chemistry optimization led to an approximately 25-fold more active compound SBI-0797750 with an IC_{50} of 6.7 ± 1.8 nM and 31.0 ± 3.1 nM against recombinant *Pf*GluPho and *Pv*G6PD, respectively and an EC_{50} of 22.5 ± 2.2 nM against asexual blood stage parasites. Optimization to SBI-0797750 did not change selectivity over the human enzyme or the mode of inhibition and action. In addition, SBI-0797750 was shown to have no effect on the integrity of RBCs from either G6PD-normal or G6PD-deficient individuals, whose erythrocytes are also highly dependent on NADPH production by their own G6PD. The detailed characterization of this lead compound is described in **Publication I**[81].

1.4.2. Glucose 6-Phosphate Dehydrogenase of *Leishmania*

As mentioned before, PPP enzymes in *Kinetoplastida* are mainly localized in the cytosol, but also in the glycosomes (see 1.3.3). Interestingly, G6PD has a higher glycosomal proportion than other PPP enzymes. For *Trypanosoma*, for example, 40–50% of the G6PD activity was measured in glycosomes[152,153].

The number of genes encoding for G6PD differs among trypanosomatids. While *T. brucei* and *Leishmania* have one copy of the G6PD gene per haploid genome[86,153], *T. cruzi* harbors five putative sequences, two of which are pseudogenes[154]. Trypanosomatid G6PDs share about 50% sequence identity on amino acid level with *Hs*G6PD[78]. Within the *Trypanosomatidae* family, sequence identity is higher. *T. cruzi* and T. *brucei* share 64% and 66% sequence identity with *Leishmania* parasites, respectively. Within the *Leishmania* family the sequence identity of G6PD is almost identical with >95%.

Compared to other G6PDs, trypanosomatid G6PDs have a unique N-terminal domain. This domain is extended by 37 amino acids in *T. brucei* and *T. cruzi* and by 40 amino acids in *Leishmania* parasites. The sequence of *Trypanosoma* G6PDs has two possible start codons, allowing the expression of the typical long form in *Kinetoplastida* with the 37 amino acid extension, or the expression of a short form corresponding to the length of most other G6PDs outside the *Kinetoplastida* family. Although it has been shown that *T. cruzi* predominantly expresses the long form in all four life-cycle stages, the physiological relevance of the expression of a long and a short form has not yet been elucidated. Since *Leishmania* parasites lack a second start codon in the G6PD sequence, they produce only the long form of the enzyme[154]. Structural comparison between the elongated N-termini of *Kinetoplastida* G6PDs reveals only 50% identity and 62% similarity between *T. cruzi* and *T. brucei*, and 24% identity and 44% similarity between *T. cruzi* and *L. donovani* G6PD. In contrast to *Leishmania* and most other G6PDs, *T. cruzi* G6PD was shown to be redox-regulated, as the activity was strongly affected by the addition of dithiothreitol and glutathione. This was observed only for the long form, but not for the short form of the enzyme. Based on kinetic studies and site-directed mutagenesis, it was suggested that two cysteines, C8 and C34, which are absent in *T. brucei* and *Leishmania* G6PDs, are responsible for this phenomenon by stabilizing intra-dimer disulfide bridges that modulate enzymatic activity[154,155]. However, truncation of the N-terminal extension of *Tc*G6PD did not affect the overall kinetic efficiency, indicating that the elongation is not essential for enzyme activity[155].

Among *Kinetoplastida* G6PDs, only *Tc*G6PD has been crystallized so far. Moreover, *Tc*G6PD has only been crystallized in a truncated form, and thus without the N-terminal extension[155,156]. To our knowledge, we were the first who crystallized wild-type *Ld*G6PD with the complete N-terminal domain (**Publication II**[157]). Solving this three-dimensional structure is an important contribution to understanding the so far enigmatic function of the elongated N-terminal domain. In accordance with previous studies, the N-terminal domain of *Ld*G6PD is not essential for enzyme activity, but our investigations indicate that the N-domain of *Ld*G6PD is involved in tetramerization, completely different to the previous observed tetramer of

*Tc*G6PD, which lacks the N-terminal domain. Structural and kinetic studies also indicated G6P-dependent domain motions involving the N-domains. These new structural and biochemical insights into a *Kinetoplastida* G6PD, which also shows major differences to other G6PDs, in particular *Hs*G6PD, will provide an excellent basis for further structure-based inhibitor studies and increase the chances of developing a selective *Ld*G6PD inhibitor.

Target validation

G6PD has been shown to be crucial for redox balance in kinetoplastids. The expression of *Tc*G6PD, for example, is regulated in a stage-specific and redox-dependent manner. While epimastigotes, which are naturally not exposed to oxidative stress, repressed G6PD expression and activity after peroxide treatment, expression levels of G6PD in metacyclic trypomastigotes, which are naturally exposed to ROS during cell invasion, were upregulated and the enzyme activity increased when the parasites were treated with peroxides. In addition, these parasites were more resistant to peroxides than epimastigotes[154]. The same was observed for *Leishmania* parasites, which increased G6PD expression levels not only during differentiation from promastigotes to amastigotes, but also under oxidative stress, which could not be explained by increased glucose uptake[65,158]. *Leishmania* parasites are able to shift the metabolic glucose flux from glycolysis towards the PPP as a mode of defense against redox stress. The redox homeostasis of *Leishmania* parasites highly depends on a balanced NADPH/$NADP^+$ ratio and therefore on the NADPH-producing enzymes of the PPP, which was also shown in *Leishmania* cell lines overexpressing episomal *Ld*G6PD. This cell line was less susceptible to oxidative stress, being able to maintain a balanced NADPH/$NADP^+$ ratio and thiol content compared to the wild-type[65]. The MOA of commonly used antileishmanials such as amphotericin B[159], sodium antimony gluconate[160] and miltefosine[161] is thought to be related to ROS-mediated killing of the parasites, and resistance to these drugs to an upregulation of the PPP. This was confirmed by *Leishmania* cell lines overexpressing *Ld*G6PD, making the parasites resistant to these drugs[65].

RNAi-mediated depletion of G6PD in *T. brucei* bloodstream cells caused a reduction in growth rate followed by culture death after 48 h, indicating that *Tb*G6PD is essential for the blood stage parasite and that alternative sources of NADPH produced by other enzymes than G6PD are not sufficient for the parasite to deal with oxidative stress[162].

Intermediates of human steroids, such as epiandrosterone (EA) and dehydropeiandrosterone (DHEA), are potent inhibitors of mammalian and *Trypanosoma* G6PDs[162,163]. By optimizing derivatives of EA and DHEA, the selectivity of the steroids for the pathogen over the host enzyme was even increased 28–130-fold[164]. The steroids killed both blood stage parasites and epimastigotes of *T. cruzi in vitro* and reduced parasite levels in infected mice, confirming the efficacy of these drugs against *Tc*G6PD[162,163]. Direct evidence that these steroids target *Trypanosoma* G6PDs was provided by Ortiz *et al.*, who showed that the specific G6PD activity in cell extracts of *T. cruzi* epimastigotes as well as the fluorescence signal for G6PD activity *in situ* decreased in a dose-dependent manner with respect to EA[164]. In addition, using redox

probes, Ortiz *et al.* detected a disruption of the thiol-redox homeostasis in *T. cruzi* bloodstream parasites after *Tc*G6PD inhibition by steroids, highlighting the key role of G6PD in NADPH homeostasis and the lack of complementary and efficient back-up systems in these parasites[164]. The molecular mechanism by which the steroids inhibit human and *Trypanosoma* G6PD is not yet known. Kinetic studies have shown that they inhibit the enzyme uncompetitively[162]. Further *in silico* studies on *Tc*G6PD suggest that the steroids may bind in a pocket below the G6P binding site and close to the dimerization domain[164]. In any case, the binding pocket must be significantly different from the *Leishmania* G6PD binding pocket, as the steroids neither inhibit *Leishmania* G6PD nor affect the parasite *in vitro*[162]. This shows that it is possible to selectively inhibit *Leishmania* G6PDs despite high sequence identity with other G6PDs. The high resolution structure and the biochemical insights of *Ld*G6PD from this work may contribute to this (**Publication II**).

1.5. 6-Phosphogluconate Dehydrogenase as a Drug Target in *Leishmania*

6-phosphogluconate dehydrogenase (6PGD) catalyzes the last step of the oxidative PPP by oxidizing and decarboxylating 6PG to Ru5P while one molecule NADPH is produced (see 1.3.2). Therefore, it contributes equally to the NADPH pool as G6PD[41,82].

Like the other two enzymes of the oxidative PPP, trypanosomatid 6PGDs are localized in the cytosol and the glycosomes (see 1.3.3), although the glycosomal fraction is much smaller at around 15%[152,165,166]. *Leishmania* 6PGDs have a high sequence identity with other *Kinetoplastida* 6PGDs. They share >90% within *Leishmania* ssp. and >70% with *Trypanosoma* ssp. With the human enzyme they share only about 35% sequence identity[167]. Although the active site residues are highly conserved among 6PGDs, making it challenging to find selective 6PGD inhibitors, there are still remarkable differences. The human 6PGDs and 6PGDs from other multicellular eukaryotes[168–170] have an elongated C-terminal domain of about 10–15 residues in contrast to prokaryotic and unicellular eukaryotic 6PGDs, such as from *Trypanosomatidae* or *Plasmodium*[167,171–173].

The 6PGD gene from *T. brucei* (*Tb*6PGD) was the first identified 6PGD from a trypanosomatid species[174]. To date, 6PGDs from *T. brucei*[175–177] , *T. cruzi*[178], *L. mexicana*[167] and *L. donovani*[179] have been biochemically characterized, but only *T. brucei* 6PGD has been crystallized with a resolution of 2.8 Å[172]. To our knowledge, we are the first who have successfully crystallized a *Leishmania* 6PGD (**Publication III**)[180]. All previously available *Leishmania* 6PGD structures are based on homology modelling and therefore computer-derived. Interestingly, our novel structure shows a previously unknown conformation of NADP(H). The 6PGD crystal structures available so far indicate that all 6PGDs are active as dimers[167–173,181]. Consistent with the conserved active sites described above, the kinetic properties of the characterized 6PGDs are also similar[167,173,175,178,182,183]. While kinetic studies on 6PGD clearly show a sequential binding mechanism, there is no consistent data on whether substrate binding and product release is random or ordered[170,173,175,184–186]. In addition, studies on 6PGDs from human, sheep, yeast and *T. brucei* suggest half-side reactivity for 6PGDs, associated with an asymmetric

conformation of the enzyme. Accordingly, in the presence of the substrate 6PG, the cosubstrate $NADP^+$ can only bind to one subunit of the 6PGD dimer during the formation of the ternary complex. In the absence of 6PG, $NADP^+$ can bind to both subunits. The fact that the 6PG binding site is formed by residues from both subunits and is thought to be significantly involved in the conversion of the open to the closed conformation of the enzyme, is seen as a possible explanation for the half-side reactivity of the enzyme[187–190].

Target validation

Although G6PD is the rate-limiting enzyme of the PPP, the activity of 6PGD has been shown to be equally crucial for the survival of trypanosomatid parasites. As already described in detail for *Leishmania* G6PD (see 1.4.2), oxidative stress has been shown to shift glucose flux from glycolysis to PPP[65,158]. In line with this, the expression levels of *Leishmania* 6PGD have also been shown to be upregulated under redox stress[65].

RNAi knockdown of *T. brucei* 6PGD was lethal for blood stage parasites[166]. It was initially thought that the toxic accumulation of the substrate 6PG alone is lethal to the parasite, because 6PG is an inhibitor of the glycolytic enzyme glucose 6-phosphate isomerase, resulting in inhibition of the glycolytic pathway via a positive feedback loop[41,166,191,192]. As neither fructose nor ribose addition prevented cell death of the parasite knockdown line, it was suggested that the loss of the oxidative branch, and therefore the loss of NADPH, is lethal to the parasite, rather than the toxic accumulation of 6PG[166].

Several attempts have been made to identify inhibitors against 6PGD from *Trypanosomatidae* – all are based on screenings or designs against *T. brucei* 6PGD. First inhibitors were identified using substrate-based approaches to inhibitor design and also included intermediate and transition state analogues. Among them several phosphorylated carbohydrates inhibited the enzyme in the micro- to submicromolar range[175,176,192–194]. The most potent inhibitor was 4-phospho-D-erythronohydroxamate with an inhibition constant K_i of 10 nM against recombinant *Tb*6PGD and a 250-fold selectivity over the sheep enzyme. The compound competitively inhibits the oxidation of 6PG and probably mimics the 1,2-enediol transition state of the 6PGD reaction. However, these compounds were either toxic or inactive *in vitro* against *T. brucei*, *T. cruzi*, *Leishmania* and *Plasmodium*, presumably because phosphorylation of the compounds prevents or reduces cellular permeation[176]. Further attempts to optimize the compounds by masking the charged phosphate moiety resulted in a series of arylphosphoramide derivatives[195,196]. The most promising candidate (derivative of 2,3-O-isopropylidene erythronocarboxamate) exhibited EC_{50} values of 8 nM against *T. brucei* parasites. Unfortunately, these compounds showed a very short half-life in mouse blood, probably due to the presence of esterases in the serum that unmask the prodrugs in the blood, making further optimization necessary[196]. A virtual fragment screening identified a new set of compounds, whose functional groups resemble the phosphate moiety of 6PG. Three of the scaffolds inhibited the recombinant *Tb*6PGD in the low micromolar range and appear to have promising physicochemical and pharmacological properties[197]. Though, how these

compounds perform *in vitro* and *in vivo* remains to be determined. In summary, there is currently no promising class of compounds that efficiently and selectively inhibit trypanosomatid 6PGDs and also have the potential to kill the parasite *in vitro* and *in vivo*. Similar approaches for *Leishmania* 6PGDs are lacking.

Within this study auranofin, and most likely gold(I)-containing compounds in general, were identified as an interesting class of compounds against *Leishmania* 6PGDs (**Publication III**)[180]. In contrast to previous approaches, gold(I)-containing compounds have been extensively studied in the past and the Food and Drug Administration (FDA) approved drug auranofin has been used for decades against rheumatoid arthritis[198–204]. Together with the three-dimensional crystal structure of *Ld*6PGD, this provides a valid basis for further structure-based studies on gold(I)-containing compounds against trypanosomatid parasites.

1.6. Objectives of this Study

As already mentioned, intracellular parasites highly depend on NADPH as the primary electron source for antioxidant defense, the main NADPH-producing enzymes G6PD and 6PGD of the PPP are considered promising antiparasitic drug targets[41,68,74,80,82]. There potential as drug targets was already proven in previous work on *Plasmodium falciparum* G6PD / GluPho and 6PGD[80,83,134,173]. Through a high-throughput screening of the NIH collection against *Pf*GluPho[147–150], followed by SAR studies and lead optimization, the highly potent and selective *Pf*GluPho inhibitor SBI-0797750 was identified.

The present study was conducted within the LOEWE Center DRUID (Novel Drug Targets against Poverty-Related and Neglected Tropical Infectious Diseases). Therefore, based on previous results from *Plasmodium* G6PD and 6PGD, the aim of this project was to address the following topics:

1. Characterization of *Pf*GluPho inhibitor SBI-0797750 in terms of mode of inhibition and action.
2. Transfer of the concept from *Plasmodium* to other G6PDs and 6PGDs from pathogens within the DRUID consortium, such as those from *Leishmania* and *Schistosoma*.
    a. Recombinant production, purification and characterization of the enzymes.
    b. Crystallization of the enzymes to solve the three-dimensional structures.
    c. Identification and characterization of potential inhibitors using structure-based drug design or high-throughput screening against the recombinant enzymes for which corresponding assays need to be established.

This cumulative work contains only published data on the *Leishmania* and *Plasmodium* species. The doctoral thesis was further enriched by a high-throughput screening and surface plasmon resonance (SPR) studies against recombinant G6PD and 6PGD from *Leishmania* and *Schistosoma*, carried out at the FastLAB of the Novartis Institutes for BioMedical Research (NIBR, Cambridge, USA). Using a structure-based drug design approach, carried out in collaboration with the lab from Peter Kolb (Philipps University Marburg) further inhibitors against *Ld*G6PD were identified and tested against the recombinant protein and the parasite. Another collaboration with the Novartis FastDEL team (Basel, Switzerland) led to the identification of additional *Ld*G6PD inhibitors, which will be investigated in more detail in the future.

2. REFERENCES

1. WHO. Ending the neglect to attain the sustainable development goals: a road map for neglected tropical diseases 2021–2030 (2020). Available at https://www.who.int/publications/i/item/9789240010352.
2. Hotez, P. J. The poverty-related neglected diseases: Why basic research matters. *PLoS Biol* 15, e2004186 (2017); https://doi.org/10.1371/journal.pbio.2004186.
3. Institute for Health Metrics and Evaluation. Neglected tropical diseases and malaria — Level 2 cause. Global burden of disease study 2019 (2020). Available at https://www.healthdata.org/results/gbd_summaries/2019/neglected-tropical-diseases-and-malaria-level-2-cause.
4. Cowman, A. F., Healer, J., Marapana, D. & Marsh, K. Malaria: Biology and disease. *Cell* 167, 610–624 (2016); https://doi.org/10.1016/j.cell.2016.07.055.
5. WHO. World malaria report 2022 (2022). Available at https://www.who.int/publications/i/item/9789240064898.
6. Kalanon, M. & McFadden, G. I. Malaria, *Plasmodium falciparum* and its apicoplast. *Biochem Soc Trans* 38, 775–782 (2010); https://doi.org/10.1042/BST0380775.
7. White, N. J. *et al.* Malaria. *Lancet* 383, 723–735 (2014); https://doi.org/10.1016/S0140-6736(13)60024-0.
8. Ashley, E. A., Pyae Phyo, A. & Woodrow, C. J. Malaria. *Lancet* 391, 1608–1621 (2018); https://doi.org/10.1016/S0140-6736(18)30324-6.
9. Naing, C., Whittaker, M. A., Nyunt Wai, V. & Mak, J. W. Is *Plasmodium vivax* malaria a severe malaria?: a systematic review and meta-analysis. *PLoS Negl Trop Dis* 8, e3071 (2014); https://doi.org/10.1371/journal.pntd.0003071.
10. Centers of Disease Control and Prevention. About malaria, biology, lifecycle (2020). Available at https://www.cdc.gov/malaria/about/biology/index.html.
11. Pasternak, N. D. & Dzikowski, R. *Pf*EMP1: an antigen that plays a key role in the pathogenicity and immune evasion of the malaria parasite *Plasmodium falciparum*. *Int J Biochem Cell Biol* 41, 1463–1466 (2009); https://doi.org/10.1016/j.biocel.2008.12.012.
12. Ashley, E. A. & Phyo, A. P. Drugs in development for malaria. *Drugs* 78, 861–879 (2018); https://doi.org/10.1007/s40265-018-0911-9.
13. Ashley, E. A. & Poespoprodjo, J. R. Treatment and prevention of malaria in children. *Lancet Child Adolesc Health* 4, 775–789 (2020); https://doi.org/10.1016/S2352-4642(20)30127-9.
14. Gujjari, L., Kalani, H., Pindiprolu, S. K., Arakareddy, B. P. & Yadagiri, G. Current challenges and nanotechnology-based pharmaceutical strategies for the treatment and control of malaria. *Parasite Epidemiol Control* 17, e00244 (2022); https://doi.org/10.1016/j.parepi.2022.e00244.
15. WHO. WHO guidelines for malaria (2023). Available at https://www.who.int/publications/i/item/guidelines-for-malaria.
16. White, N. J. Malaria parasite clearance. *Malar J* 16, 88 (2017); https://doi.org/10.1186/s12936-017-1731-1.
17. Alven, S. & Aderibigbe, B. Combination therapy strategies for the treatment of malaria. *Molecules* 24 (2019); https://doi.org/10.3390/molecules24193601.

18. Tilley, L., Straimer, J., Gnädig, N. F., Ralph, S. A. & Fidock, D. A. Artemisinin action and resistance in *Plasmodium falciparum*. *Trends Parasitol* 32, 682–696 (2016); https://doi.org/10.1016/j.pt.2016.05.010.

19. Vaid, A., Ranjan, R., Smythe, W. A., Hoppe, H. C. & Sharma, P. *Pf*PI3K, a phosphatidylinositol-3 kinase from *Plasmodium falciparum*, is exported to the host erythrocyte and is involved in hemoglobin trafficking. *Blood* 115, 2500–2507 (2010); https://doi.org/10.1182/blood-2009-08-238972.

20. Mbengue, A. *et al.* A molecular mechanism of artemisinin resistance in *Plasmodium falciparum* malaria. *Nature* 520, 683–687 (2015); https://doi.org/10.1038/nature14412.

21. Schlitzer, M. Antimalarial drugs - what is in use and what is in the pipeline. *Arch Pharm* 341, 149–163 (2008); https://doi.org/10.1002/ardp.200700184.

22. Wicht, K. J., Mok, S. & Fidock, D. A. Molecular mechanisms of drug resistance in *Plasmodium falciparum* malaria. *Annu Rev Microbiol* 74, 431–454 (2020); https://doi.org/10.1146/annurev-micro-020518-115546.

23. Kavishe, R. A., Koenderink, J. B. & Alifrangis, M. Oxidative stress in malaria and artemisinin combination therapy: Pros and cons. *FEBS J* 284, 2579–2591 (2017); https://doi.org/10.1111/febs.14097.

24. WHO. Malaria vaccines: preferred product characteristics and clinical development considerations (2022). Available at https://www.who.int/publications/i/item/9789240057463.

25. Datoo, M. S. *et al.* Efficacy of a low-dose candidate malaria vaccine, R21 in adjuvant Matrix-M, with seasonal administration to children in Burkina Faso: a randomised controlled trial. *Lancet* 397, 1809–1818 (2021); https://doi.org/10.1016/S0140-6736(21)00943-0.

26. WHO. Leishmaniasis (2022). Available at https://www.who.int/news-room/fact-sheets/detail/leishmaniasis.

27. Burza, S., Croft, S. L. & Boelaert, M. Leishmaniasis. *Lancet* 392, 951–970 (2018); https://doi.org/10.1016/S0140-6736(18)31204-2.

28. Zijlstra, E. E. Biomarkers in Post-kala-azar dermal leishmaniasis. *Front Cell Infect Microbiol* 9, 228 (2019); https://doi.org/10.3389/fcimb.2019.00228.

29. Pan American Health Organization. Manual of procedures for leishmaniases surveillance and control in the Americas (2019). Available at https://iris.paho.org/handle/10665.2/51838.

30. Pace, D. Leishmaniasis. *J Infect* 69 Suppl 1, S10-8 (2014); https://doi.org/10.1016/j.jinf.2014.07.016.

31. Centers of Disease Control and Prevention. Leishmaniasis biology (2020). Available at https://www.cdc.gov/parasites/leishmaniasis/biology.html.

32. Esch, K. J. & Petersen, C. A. Transmission and epidemiology of zoonotic protozoal diseases of companion animals. *Clin Microbiol Rev* 26, 58–85 (2013); https://doi.org/10.1128/CMR.00067-12.

33. Sheikh, S., Amir, Amaar. A., Amir, B. A., Amir, A. A. Leishmaniasis. In *Parasitology and Microbiology Research,* edited by G. Antonio Bastidas Pacheco & A. Ali Kamboh (IntechOpen2020).

34. Kaye, P. & Scott, P. Leishmaniasis: complexity at the host-pathogen interface. *Nat Rev Microbiol* 9, 604–615 (2011); https://doi.org/10.1038/nrmicro2608.

35. Gupta, A. K., Das, S., Kamran, M., Ejazi, S. A. & Ali, N. The pathogenicity and virulence of *Leishmania* - interplay of virulence factors with host defenses. *Virulence* 13, 903–935 (2022); https://doi.org/10.1080/21505594.2022.2074130.

36. Lambertz, U. *et al.* Secreted virulence factors and immune evasion in visceral leishmaniasis. *J Leukoc Biol* 91, 887–899 (2012); https://doi.org/10.1189/jlb.0611326.

37. Laskay, T., van Zandbergen, G. & Solbach, W. Neutrophil granulocytes-Trojan horses for *Leishmania major* and other intracellular microbes? *Trends Microbiol* 11, 210–214 (2003); https://doi.org/10.1016/s0966-842x(03)00075-1.

38. Laufs, H. *et al.* Intracellular survival of *Leishmania major* in neutrophil granulocytes after uptake in the absence of heat-labile serum factors. *Infect Immun* 70, 826–835 (2002); https://doi.org/10.1128/iai.70.2.826-835.2002.

39. Ikeogu, N. M. *et al. Leishmania i*mmunity: Advancing immunotherapy and vaccine development. *Microorganisms* 8 (2020); https://doi.org/10.3390/microorganisms8081201.

40. Frézard, F., Demicheli, C. & Ribeiro, R. R. Pentavalent antimonials: new perspectives for old drugs. *Molecules* 14, 2317–2336 (2009); https://doi.org/10.3390/molecules14072317.

41. Loureiro, I. *et al.* Potential drug targets in the pentose phosphate pathway of trypanosomatids. *Curr Med Chem* 25, 5239–5265 (2018); https://doi.org/10.2174/0929867325666171206094752.

42. Ferreira, C. d. S. *et al.* Thiol-induced reduction of antimony(V) into antimony(III): a comparative study with trypanothione, cysteinyl-glycine, cysteine and glutathione. *Biometals* 16, 441–446 (2003); https://doi.org/10.1023/a:1022823605068.

43. Wyllie, S., Cunningham, M. L. & Fairlamb, A. H. Dual action of antimonial drugs on thiol redox metabolism in the human pathogen *Leishmania donovani*. *J Biol Chem* 279, 39925–39932 (2004); https://doi.org/10.1074/jbc.M405635200.

44. Cunningham, M. L. & Fairlamb, A. H. Trypanothione reductase from *Leishmania donovani*. Purification, characterisation and inhibition by trivalent antimonials. *Eur J Biochem* 230, 460–468 (1995); https://doi.org/10.1111/j.1432-1033.1995.tb20583.x.

45. Kumar Saha, A., Mukherjee, T. & Bhaduri, A. Mechanism of action of amphotericin B on *Leishmania donovani* promastigotes. *Mol Biochem Parasitol* 19, 195–200 (1986); https://doi.org/10.1016/0166-6851(86)90001-0.

46. Bern, C. *et al.* Liposomal amphotericin B for the treatment of visceral leishmaniasis. *Clin Infect Dis* 43, 917–924 (2006); https://doi.org/10.1086/507530.

47. Rodrigo, C., Weeratunga, P., Fernando, S. D. & Rajapakse, S. Amphotericin B for treatment of visceral leishmaniasis: systematic review and meta-analysis of prospective comparative clinical studies including dose-ranging studies. *Clin Microbiol Infect* 24, 591–598 (2018); https://doi.org/10.1016/j.cmi.2017.11.008.

48. Sundar, S., Singh, A., Agrawal, N. & Chakravarty, J. Effectiveness of single-dose liposomal amphotericin B in visceral leishmaniasis in Bihar. *Am J Trop Med Hyg* 101, 795–798 (2019); https://doi.org/10.4269/ajtmh.19-0179.

49. Ekram, M. R. *et al.* Efficacy and safety of single-dose liposomal amphotericin B in patients with visceral leishmaniasis in Bangladesh: a real-life experience. *J Parasit Dis* 45, 903–911 (2021); https://doi.org/10.1007/s12639-021-01379-w.

50. Urbina, J. A. Mechanisms of action of lysophospholipid analogues against trypanosomatid parasites. *Trans R Soc Trop Med Hyg* 100 Suppl 1, S9-S16 (2006); https://doi.org/10.1016/j.trstmh.2006.03.010.

51. Luque-Ortega, J. R. & Rivas, L. Miltefosine (hexadecylphosphocholine) inhibits cytochrome c oxidase in *Leishmania donovani* promastigotes. *Antimicrob Agents Chemother* 51, 1327–1332 (2007); https://doi.org/10.1128/AAC.01415-06.

52. Pinto-Martinez, A. K., Rodriguez-Durán, J., Serrano-Martin, X., Hernandez-Rodriguez, V. & Benaim, G. Mechanism of action of miltefosine on *Leishmania donovani* involves the impairment of acidocalcisome function and the activation of the sphingosine-dependent plasma membrane Ca^{2+} channel. *Antimicrob Agents Chemother* 62 (2018); https://doi.org/10.1128/AAC.01614-17.

53. Paris, C., Loiseau, P. M., Bories, C. & Bréard, J. Miltefosine induces apoptosis-like death in *Leishmania donovani* promastigotes. *Antimicrob Agents Chemother* 48, 852–859 (2004); https://doi.org/10.1128/AAC.48.3.852-859.2004.

54. Marinho, F. d. A. *et al.* Miltefosine induces programmed cell death in *Leishmania amazonensis* promastigotes. *Mem Inst Oswaldo Cruz* 106, 507–509 (2011); https://doi.org/10.1590/S0074-02762011000400021.

55. Sundar, S. *et al.* Efficacy of miltefosine in the treatment of visceral leishmaniasis in India after a decade of use. *Clin Infect Dis* 55, 543–550 (2012); https://doi.org/10.1093/cid/cis474.

56. Chakravarty, J. & Sundar, S. Current and emerging medications for the treatment of leishmaniasis. *Expert Opin Pharmacother* 20, 1251–1265 (2019); https://doi.org/10.1080/14656566.2019.1609940.

57. Roatt, B. M. *et al.* Recent advances and new strategies on leishmaniasis treatment. *Appl Microbiol Biotechnol* 104, 8965–8977 (2020); https://doi.org/10.1007/s00253-020-10856-w.

58. Wamelink, M. M. C., Struys, E. A. & Jakobs, C. The biochemistry, metabolism and inherited defects of the pentose phosphate pathway: a review. *J Inherit Metab Dis* 31, 703–717 (2008); https://doi.org/10.1007/s10545-008-1015-6.

59. Stincone, A. *et al.* The return of metabolism: biochemistry and physiology of the pentose phosphate pathway. *Biol Rev Camb Philos Soc* 90, 927–963 (2015); https://doi.org/10.1111/brv.12140.

60. Liguori, I. *et al.* Oxidative stress, aging, and diseases. *Clin Interv Aging* 13, 757–772 (2018); https://doi.org/10.2147/CIA.S158513.

61. Vasquez, M., Zuniga, M. & Rodriguez, A. Oxidative stress and pathogenesis in malaria. *Front Cell Infect Microbiol* 11, 768182 (2021); https://doi.org/10.3389/fcimb.2021.768182.

62. Becker, K., Koncarevic, S. & Hunt, N. H. Oxidative stress and antioxidant defense in malarial parasites. In *Molecular approaches to malaria,* edited by I. W. Sherman (ASM Press, Washington, DC, USA, 2005), pp. 365–383.

63. Solbach, W. & Laskay, T. The host response to *Leishmania i*nfection. In *Advances in immunology,* edited by F. J. Dixon. 1st ed. (Elsevier textbooks, s.l., 1999), Vol. 74, pp. 275–317.

64. Moradin, N. & Descoteaux, A. *Leishmania* promastigotes: building a safe niche within macrophages. *Front Cell Infect Microbiol* 2, 121 (2012); https://doi.org/10.3389/fcimb.2012.00121.

65. Ghosh, A. K. *et al.* Metabolic reconfiguration of the central glucose metabolism: a crucial strategy of *Leishmania donovani* for its survival during oxidative stress. *FASEB J* 29, 2081–2098 (2015); https://doi.org/10.1096/fj.14-258624.

66. Rahlfs, S., Schirmer, R. H. & Becker, K. The thioredoxin system of *Plasmodium falciparum* and other parasites. *Cell Mol Life Sci* 59, 1024–1041 (2002); https://doi.org/10.1007/s00018-002-8484-9.

67. Becker, K., Rahlfs, S., Nickel, C. & Schirmer, R. H. Glutathione-functions and metabolism in the malarial parasite *Plasmodium falciparum*. *Biol Chem* 384, 551–566 (2003); https://doi.org/10.1515/BC.2003.063.

68. Jortzik, E. & Becker, K. Thioredoxin and glutathione systems in *Plasmodium falciparum*. *Int J Med Microbiol* 302, 187–194 (2012); https://doi.org/10.1016/j.ijmm.2012.07.007.

69. Kehr, S., Sturm, N., Rahlfs, S., Przyborski, J. M. & Becker, K. Compartmentation of redox metabolism in malaria parasites. *PLoS Pathog* 6, e1001242 (2010); https://doi.org/10.1371/journal.ppat.1001242.

70. Buchholz, K. *et al.* Molecular genetics evidence for the *in vivo* roles of the two major NADPH-dependent disulfide reductases in the malaria parasite. *J Biol Chem* 285, 37388–37395 (2010); https://doi.org/10.1074/jbc.M110.123323.

71. Pastrana-Mena, R. *et al.* Glutathione reductase-null malaria parasites have normal blood stage growth but arrest during development in the mosquito. *J Biol Chem* 285, 27045–27056 (2010); https://doi.org/10.1074/jbc.M110.122275.

72. Patzewitz, E.-M., Wong, E. H. & Müller, S. Dissecting the role of glutathione biosynthesis in *Plasmodium falciparum*. *Mol Microbiol* 83, 304–318 (2012); https://doi.org/10.1111/j.1365-2958.2011.07933.x.

73. Krnajski, Z., Gilberger, T.-W., Walter, R. D., Cowman, A. F. & Müller, S. Thioredoxin reductase is essential for the survival of *Plasmodium falciparum* erythrocytic stages. *J Biol Chem* 277, 25970–25975 (2002); https://doi.org/10.1074/jbc.M203539200.

74. Krauth-Siegel, R. L. & Comini, M. A. Redox control in trypanosomatids, parasitic protozoa with trypanothione-based thiol metabolism. *Biochim Biophys Acta* 1780, 1236–1248 (2008); https://doi.org/10.1016/j.bbagen.2008.03.006.

75. Irigoín, F. *et al.* Insights into the redox biology of *Trypanosoma cruzi*: Trypanothione metabolism and oxidant detoxification. *Free Radic Biol Med* 45, 733–742 (2008); https://doi.org/10.1016/j.freeradbiomed.2008.05.028.

76. Krieger, S. *et al.* Trypanosomes lacking trypanothione reductase are avirulent and show increased sensitivity to oxidative stress. *Mol Microbiol* 35, 542–552 (2000); https://doi.org/10.1046/j.1365-2958.2000.01721.x.

77. Tovar, J., Cunningham, M. L., Smith, A. C., Croft, S. L. & Fairlamb, A. H. Down-regulation of *Leishmania donovani* trypanothione reductase by heterologous expression of a trans-dominant mutant homologue: effect on parasite intracellular survival. *Proc Natl Acad Sci USA* 95, 5311–5316 (1998); https://doi.org/10.1073/pnas.95.9.5311.

78. Gupta, S., Igoillo-Esteve, M., Michels, P. A. M. & Cordeiro, A. T. Glucose-6-phosphate dehydrogenase of trypanosomatids: characterization, target validation, and drug discovery. *Mol Biol Int* 2011, 135701 (2011); https://doi.org/10.4061/2011/135701.

79. Comini, M. A., Ortíz, C. & Cazzulo, J. J. Drug targets in trypanosomal and leishmanial pentose phosphate pathway. In *Trypanosomatid diseases,* edited by T. Jäger, O. Koch & L. Flohé (Wiley-VCH Verlag GmbH & Co. KGaA, Weinheim, Germany, 2013), pp. 297–313.

80. Allen, S. M. *et al. Plasmodium falciparum* glucose-6-phosphate dehydrogenase 6-phosphogluconolactonase is a potential drug target. *FEBS J* 282, 3808–3823 (2015); https://doi.org/10.1111/febs.13380.

81. Berneburg, I. *et al.* An optimized dihydrodibenzothiazepine lead compound (SBI-0797750) as a potent and selective inhibitor of *Plasmodium falciparum* and *P. vivax* glucose 6-phosphate dehydrogenase 6-phosphogluconolactonase. *Antimicrob Agents Chemother* 66, e0210921 (2022); https://doi.org/10.1128/aac.02109-21.

82. Kovářová, J. & Barrett, M. P. The pentose phosphate pathway in parasitic trypanosomatids. *Trends Parasitol* 32, 622–634 (2016); https://doi.org/10.1016/j.pt.2016.04.010.

83. Jortzik, E. *et al.* Glucose-6-phosphate dehydrogenase-6-phosphogluconolactonase: a unique bifunctional enzyme from *Plasmodium falciparum*. *Biochem J* 436, 641–650 (2011); https://doi.org/10.1042/BJ20110170.

84. Preuss, J., Jortzik, E. & Becker, K. Glucose-6-phosphate metabolism in *Plasmodium falciparum*. *IUBMB Life* 64, 603–611 (2012); https://doi.org/10.1002/iub.1047.

85. Michels, P. A. M., Bringaud, F., Herman, M. & Hannaert, V. Metabolic functions of glycosomes in trypanosomatids. *Biochim Biophys Acta* 1763, 1463–1477 (2006); https://doi.org/10.1016/j.bbamcr.2006.08.019.

86. Hannaert, V., Bringaud, F., Opperdoes, F. R. & Michels, P. am. Evolution of energy metabolism and its compartmentation in *Kinetoplastida*. *Kinetoplastid. Biol. Dis.* 2, 11 (2003); https://doi.org/10.1186/1475-9292-2-11.

87. Haanstra, J. R. *et al.* Compartmentation prevents a lethal turbo-explosion of glycolysis in trypanosomes. *Proc Natl Acad Sci USA* 105, 17718–17723 (2008); https://doi.org/10.1073/pnas.0806664105.

88. Pollak, N., Niere, M. & Ziegler, M. NAD kinase levels control the NADPH concentration in human cells. *J Biol Chem* 282, 33562–33571 (2007); https://doi.org/10.1074/jbc.M704442200.

89. Lee, S. M. *et al.* Cytosolic $NADP^+$-dependent isocitrate dehydrogenase status modulates oxidative damage to cells. *Free Radic Biol Med* 32, 1185–1196 (2002); https://doi.org/10.1016/s0891-5849(02)00815-8.

90. Fan, J. *et al.* Quantitative flux analysis reveals folate-dependent NADPH production. *Nature* 510, 298–302 (2014); https://doi.org/10.1038/nature13236.

91. Scheibe, R. $NADP^+$-malate dehydrogenase in C3-plants: Regulation and role of a light-activated enzyme. *Physiol Plant* 71, 393–400 (1987); https://doi.org/10.1111/j.1399-3054.1987.tb04362.x.

92. Cappellini, M. D. & Fiorelli, G. Glucose-6-phosphate dehydrogenase deficiency. *Lancet* 371, 64–74 (2008); https://doi.org/10.1016/S0140-6736(08)60073-2.

93. Werner, C., Stubbs, M. T., Krauth-Siegel, R. L. & Klebe, G. The crystal structure of *Plasmodium falciparum* glutamate dehydrogenase, a putative target for novel antimalarial drugs. *J Mol Biol* 349, 597–607 (2005); https://doi.org/10.1016/j.jmb.2005.03.077.

94. Storm, J. *et al. Plasmodium falciparum* glutamate dehydrogenase a is dispensable and not a drug target during erythrocytic development. *Malar J* 10, 193 (2011); https://doi.org/10.1186/1475-2875-10-193.

95. Wrenger, C. & Müller, S. Isocitrate dehydrogenase of *Plasmodium falciparum*. *Eur J Biochem* 270, 1775–1783 (2003); https://doi.org/10.1046/j.1432-1033.2003.03536.x.

96. Chan, M. & Sim, T. S. Functional characterization of an alternative lactate dehydrogenase-like malate dehydrogenase in *Plasmodium falciparum*. *Parasitol Res* 92, 43–47 (2004); https://doi.org/10.1007/s00436-003-0996-1.

97. Walter, R. D. & Ebert, F. Evidence for NADH- and NADPH-linked glutamate dehydrogenases in *Trypanosoma cruzi* epimastigotes. *J Protozool* 26, 653–656 (1979); https://doi.org/10.1111/j.1550-7408.1979.tb04214.x.

98. Barderi, P. *et al.* The $NADP^+$-linked glutamate dehydrogenase from *Trypanosoma cruzi*: sequence, genomic organization and expression. *Biochem J* 330 (Pt 2), 951–958 (1998); https://doi.org/10.1042/bj3300951.

99. Leroux, A. E., Maugeri, D. A., Cazzulo, J. J. & Nowicki, C. Functional characterization of NADP-dependent isocitrate dehydrogenase isozymes from *Trypanosoma cruzi*. *Mol Biochem Parasitol* 177, 61–64 (2011); https://doi.org/10.1016/j.molbiopara.2011.01.010.

100. Vickers, T. J. & Beverley, S. M. Folate metabolic pathways in *Leishmania*. *Essays Biochem* 51, 63–80 (2011); https://doi.org/10.1042/bse0510063.

101. Cordeiro, A. T. NADPH producing enzymes as promising drug targets for Chagas disease. *Curr Med Chem* 26, 6564–6571 (2019); https://doi.org/10.2174/0929867325666181009152844.

102. Leroux, A. E., Maugeri, D. A., Opperdoes, F. R., Cazzulo, J. J. & Nowicki, C. Comparative studies on the biochemical properties of the malic enzymes from *Trypanosoma cruzi* and *Trypanosoma brucei*. *FEMS Microbiol Lett* 314, 25–33 (2011); https://doi.org/10.1111/j.1574-6968.2010.02142.x.

103. Giordana, L. *et al.* Molecular and functional characterization of two malic enzymes from *Leishmania* parasites. *Mol Biochem Parasitol* 219, 67–76 (2018); https://doi.org/10.1016/j.molbiopara.2017.11.001.

104. Mondal, D. K., Pal, D. S., Abbasi, M. & Datta, R. Functional partnership between carbonic anhydrase and malic enzyme in promoting gluconeogenesis in *Leishmania major*. *FEBS J* 288, 4129–4152 (2021); https://doi.org/10.1111/febs.15720.

105. Allmann, S. *et al.* Cytosolic NADPH homeostasis in glucose-starved procyclic *Trypanosoma brucei* relies on malic enzyme and the pentose phosphate pathway fed by gluconeogenic flux. *J Biol Chem* 288, 18494–18505 (2013); https://doi.org/10.1074/jbc.M113.462978.

106. WHO. Malaria Policy Advisory Group (MPAG) meeting (March 2022) (2022). Available at https://www.who.int/publications/i/item/9789240048430.

107. Luzzatto, L., Ally, M. & Notaro, R. Glucose-6-phosphate dehydrogenase deficiency. *Blood* 136, 1225–1240 (2020); https://doi.org/10.1182/blood.2019000944.

108. Luzzatto, L., Nannelli, C. & Notaro, R. Glucose-6-phosphate dehydrogenase deficiency. *Hematol Oncol Clin North Am* 30, 373–393 (2016); https://doi.org/10.1016/j.hoc.2015.11.006.

109. Devarashetty, S. P., Ponna, P. K., Devarakonda, V. & Ramadas, P. COVID-19 infection unmasking glucose-6-phosphate dehydrogenase deficiency. *QJM* 115, 771–772 (2022); https://doi.org/10.1093/qjmed/hcac184.

110. Müller, S. Redox and antioxidant systems of the malaria parasite *Plasmodium falciparum*. *Mol Microbiol* 53, 1291–1305 (2004); https://doi.org/10.1111/j.1365-2958.2004.04257.x.

111. Morelli, A., Benatti, U., Gaetani, G. F. & Flora, A. de. Biochemical mechanisms of glucose-6-phosphate dehydrogenase deficiency. *Proc Natl Acad Sci USA* 75, 1979–1983 (1978); https://doi.org/10.1073/pnas.75.4.1979.

112. Luzzatto, L. & Seneca, E. G6PD deficiency: a classic example of pharmacogenetics with on-going clinical implications. *Br J Haematol* 164, 469–480 (2014); https://doi.org/10.1111/bjh.12665.

113. Ruwende, C. *et al.* Natural selection of hemi- and heterozygotes for G6PD deficiency in Africa by resistance to severe malaria. *Nature* 376, 246–249 (1995); https://doi.org/10.1038/376246a0.

114. Guindo, A., Fairhurst, R. M., Doumbo, O. K., Wellems, T. E. & Diallo, D. A. X-linked G6PD deficiency protects hemizygous males but not heterozygous females against severe malaria. *PLoS Med* 4, e66 (2007); https://doi.org/10.1371/journal.pmed.0040066.

115. Mbanefo, E. C. *et al.* Association of glucose-6-phosphate dehydrogenase deficiency and malaria: a systematic review and meta-analysis. *Sci Rep* 7, 45963 (2017); https://doi.org/10.1038/srep45963.

116. Awab, G. R. *et al.* Protective effect of Mediterranean-type glucose-6-phosphate dehydrogenase deficiency against *Plasmodium vivax* malaria. *Elife* 10 (2021); https://doi.org/10.7554/eLife.62448.

117. Louicharoen, C. *et al.* Positively selected G6PD-Mahidol mutation reduces *Plasmodium vivax* density in Southeast Asians. *Science* 326, 1546–1549 (2009); https://doi.org/10.1126/science.1178849.

118. Cappadoro, M. *et al.* Early phagocytosis of glucose-6-phosphate dehydrogenase (G6PD)-deficient erythrocytes parasitized by *Plasmodium falciparum* may explain malaria protection in G6PD deficiency. *Blood* 92, 2527–2534 (1998).

119. Méndez, D., Linares, M., Diez, A., Puyet, A. & Bautista, J. M. Stress response and cytoskeletal proteins involved in erythrocyte membrane remodeling upon *Plasmodium falciparum* invasion are differentially carbonylated in G6PD A- deficiency. *Free Radic Biol Med* 50, 1305–1313 (2011); https://doi.org/10.1016/j.freeradbiomed.2011.02.024.

120. Courtin, D. *et al.* G6PD A-variant influences the antibody responses to *Plasmodium falciparum* MSP2. *Infect Genet Evol* 11, 1287–1292 (2011); https://doi.org/10.1016/j.meegid.2011.04.016.

121. Chu, C. S. *et al.* Haemolysis in G6PD heterozygous females treated with primaquine for *Plasmodium vivax m*alaria: A nested cohort in a trial of radical curative regimens. *PLoS Med* 14, e1002224 (2017); https://doi.org/10.1371/journal.pmed.1002224.

122. Chu, C. S., Bancone, G., Nosten, F., White, N. J. & Luzzatto, L. Primaquine-induced haemolysis in females heterozygous for G6PD deficiency. *Malar J* 17, 101 (2018); https://doi.org/10.1186/s12936-018-2248-y.

123. Commons, R. J., McCarthy, J. S. & Price, R. N. Tafenoquine for the radical cure and prevention of malaria: the importance of testing for G6PD deficiency. *Med J Aust* 212, 152-153.e1 (2020); https://doi.org/10.5694/mja2.50474.

124. Rueangweerayut, R. *et al.* Hemolytic potential of tafenoquine in female volunteers heterozygous for glucose-6-phosphate dehydrogenase (G6PD) deficiency (G6PD Mahidol variant) versus G6PD-normal volunteers. *Am J Trop Med Hyg* 97, 702–711 (2017); https://doi.org/10.4269/ajtmh.16-0779.

125. Pakparnich, P. *et al.* Combined effects of double mutations on catalytic activity and structural stability contribute to clinical manifestations of glucose-6-phosphate dehydrogenase deficiency. *Sci Rep* 11, 24307 (2021); https://doi.org/10.1038/s41598-021-03800-z.

126. García-Domínguez, E. *et al.* Glucose 6-P dehydrogenase-An antioxidant enzyme with regulatory functions in skeletal muscle during exercise. *Cells* 11 (2022); https://doi.org/10.3390/cells11193041.

127. O'Brien, E. *et al.* Cloning of the glucose 6-phosphate dehydrogenase gene from *Plasmodium falciparum*. *Mol Biochem Parasitol* 64, 313–326 (1994); https://doi.org/10.1016/0166-6851(94)00028-x.

128. Gardner, M. J. *et al.* Genome sequence of the human malaria parasite *Plasmodium falciparum*. *Nature* 419, 498–511 (2002); https://doi.org/10.1038/nature01097.

129. Hempelmann, E. & Wilson, R. J. Detection of glucose-6-phosphate dehydrogenase in malarial parasites. *Mol Biochem Parasitol* 2, 197–204 (1981); https://doi.org/10.1016/0166-6851(81)90100-6.

130. Kurdi-Haidar, B. & Luzzatto, L. Expression and characterization of glucose-6-phosphate dehydrogenase of *Plasmodium falciparum*. *Mol Biochem Parasitol* 41, 83–91 (1990); https://doi.org/10.1016/0166-6851(90)90099-8.

131. Stover, N. A., Dixon, T. A. & Cavalcanti, A. R. O. Multiple independent fusions of glucose-6-phosphate dehydrogenase with enzymes in the pentose phosphate pathway. *PLoS One* 6, e22269 (2011); https://doi.org/10.1371/journal.pone.0022269.

132. Clarke, J. L., Scopes, D. A., Sodeinde, O. & Mason, P. J. Glucose-6-phosphate dehydrogenase-6-phosphogluconolactonase. A novel bifunctional enzyme in malaria parasites. *Eur J Biochem* 268, 2013–2019 (2001); https://doi.org/10.1046/j.1432-1327.2001.02078.x.

133. Clarke, J. L., Sodeinde, O. & Mason, P. J. A unique insertion in *Plasmodium berghei* glucose-6-phosphate dehydrogenase-6-phosphogluconolactonase: evolutionary and functional studies. *Mol Biochem Parasitol* 127, 1–8 (2003); https://doi.org/10.1016/s0166-6851(02)00298-0.

134. Haeussler, K. *et al.* Glucose 6-phosphate dehydrogenase 6-phosphogluconolactonase: characterization of the *Plasmodium vivax* enzyme and inhibitor studies. *Malar J* 18, 22 (2019); https://doi.org/10.1186/s12936-019-2651-z.

135. Atamna, H., Pascarmona, G. & Ginsburg, H. Hexose-monophosphate shunt activity in intact *Plasmodium falciparum*-infected erythrocytes and in free parasites. *Mol Biochem Parasitol* 67, 79–89 (1994); https://doi.org/10.1016/0166-6851(94)90098-1.

136. Crooke, A., Diez, A., Mason, P. J. & Bautista, J. M. Transient silencing of *Plasmodium falciparum* bifunctional glucose-6-phosphate dehydrogenase- 6-phosphogluconolactonase. *FEBS J* 273, 1537–1546 (2006); https://doi.org/10.1111/j.1742-4658.2006.05174.x.

137. Baum, J. *et al.* Molecular genetics and comparative genomics reveal RNAi is not functional in malaria parasites. *Nucleic Acids Res* 37, 3788–3798 (2009); https://doi.org/10.1093/nar/gkp239.

138. Ghorbal, M. *et al.* Genome editing in the human malaria parasite *Plasmodium falciparum* using the CRISPR-Cas9 system. *Nat Biotechnol* 32, 819–821 (2014); https://doi.org/10.1038/nbt.2925.

139. Wagner, J. C., Platt, R. J., Goldfless, S. J., Zhang, F. & Niles, J. C. Efficient CRISPR-Cas9-mediated genome editing in *Plasmodium falciparum*. *Nat Methods* 11, 915–918 (2014); https://doi.org/10.1038/nmeth.3063.

140. Klonis, N. *et al.* Artemisinin activity against *Plasmodium falciparum* requires hemoglobin uptake and digestion. *Proc Natl Acad Sci USA* 108, 11405–11410 (2011); https://doi.org/10.1073/pnas.1104063108.

141. Radfar, A., Diez, A. & Bautista, J. M. Chloroquine mediates specific proteome oxidative damage across the erythrocytic cycle of resistant *Plasmodium falciparum*. *Free Radic Biol Med* 44, 2034–2042 (2008); https://doi.org/10.1016/j.freeradbiomed.2008.03.010.

142. Schirmer, R. H. *et al.* Methylene blue as an antimalarial agent. *Redox Rep* 8, 272–275 (2003); https://doi.org/10.1179/135100003225002899.

143. Wang, L. *et al.* Protein S-nitrosylation in *Plasmodium falciparum*. *Antioxid Redox Signal* 20, 2923–2935 (2014); https://doi.org/10.1089/ars.2013.5553.

144. Dillenberger, M., Rahlfs, S., Becker, K. & Fritz-Wolf, K. Prominent role of cysteine residues C49 and C343 in regulating *Plasmodium falciparum* pyruvate kinase activity. *Structure* 30, 1452-1461.e3 (2022); https://doi.org/10.1016/j.str.2022.08.001.

145. Soh, P. N. *et al. In vitro* and *in vivo* properties of ellagic acid in malaria treatment. *Antimicrob Agents Chemother* 53, 1100–1106 (2009); https://doi.org/10.1128/AAC.01175-08.

146. Sturm, N. *et al.* Compounds structurally related to ellagic acid show improved antiplasmodial activity. *Antimicrob Agents Chemother* 53, 622–630 (2009); https://doi.org/10.1128/AAC.00544-08.

147. Preuss, J. *et al.* High-throughput screening for small-molecule inhibitors of *Plasmodium falciparum* glucose-6-phosphate dehydrogenase 6-phosphogluconolactonase. *J Biomol Screen* 17, 738–751 (2012); https://doi.org/10.1177/1087057112442382.

148. Preuss, J. *et al.* Discovery of a *Plasmodium falciparum* glucose-6-phosphate dehydrogenase 6-phosphogluconolactonase inhibitor (R,Z)-N-((1-ethylpyrrolidin-2-yl)methyl)-2-(2-fluorobenzyl-idene)-3-oxo-3,4-dihydro-2H-benzob1,4thiazine-6-carboxamide (ML276) that reduces parasite growth *in vitro*. *J Med Chem* 55, 7262–7272 (2012); https://doi.org/10.1021/jm300833h.

149. Maloney, P. *et al. Probe Reports from the NIH Molecular Libraries Program. A selective inhibitor of Plasmodium falciparum glucose-6-phosphate dehydrogenase (PfG6PDH)* (Bethesda (MD), 2010).

150. Maloney, P. *et al. Probe Reports from the NIH Molecular Libraries Program. A 2nd selective inhibitor of Plasmodium falciparum glucose-6-phosphate dehydrogenase (PfG6PDH) - Probe 2* (Bethesda (MD), 2010).

151. Siciliano, G. *et al.* A high susceptibility to redox imbalance of the transmissible stages of *Plasmodium falciparum* revealed with a luciferase-based mature gametocyte assay. *Mol Microbiol* 104, 306–318 (2017); https://doi.org/10.1111/mmi.13626.

152. Heise, N. & Opperdoes, F. R. Purification, localisation and characterisation of glucose-6-phosphate dehydrogenase of *Trypanosoma brucei*. *Mol Biochem Parasitol* 99, 21–32 (1999); https://doi.org/10.1016/S0166-6851(98)00176-5.

153. Duffieux, F., van Roy, J., Michels, P. A. & Opperdoes, F. R. Molecular characterization of the first two enzymes of the pentose-phosphate pathway of *Trypanosoma brucei*. Glucose-6-phosphate dehydrogenase and 6-phosphogluconolactonase. *J Biol Chem* 275, 27559–27565 (2000); https://doi.org/10.1074/jbc.M004266200.

154. Igoillo-Esteve, M. & Cazzulo, J. J. The glucose-6-phosphate dehydrogenase from *Trypanosoma cruzi*: its role in the defense of the parasite against oxidative stress. *Mol Biochem Parasitol* 149, 170–181 (2006); https://doi.org/10.1016/j.molbiopara.2006.05.009.

155. Ortíz, C., Botti, H., Buschiazzo, A. & Comini, M. A. Glucose-6-phosphate dehydrogenase from the human pathogen *Trypanosoma cruzi e*volved unique structural features to support efficient product formation. *J Mol Biol* 431, 2143–2162 (2019); https://doi.org/10.1016/j.jmb.2019.03.023.

156. Mercaldi, G. F., Dawson, A., Hunter, W. N. & Cordeiro, A. T. The structure of a *Trypanosoma cruzi* glucose-6-phosphate dehydrogenase reveals differences from the mammalian enzyme. *FEBS Lett* 590, 2776–2786 (2016); https://doi.org/10.1002/1873-3468.12276.

157. Berneburg, I., Rahlfs, S., Becker, K. & Fritz-Wolf, K. Crystal structure of *Leishmania donovani* glucose 6-phosphate dehydrogenase reveals a unique N-terminal domain. *Commun Biol* 5, 1353 (2022); https://doi.org/10.1038/s42003-022-04307-7.

158. Sardar, A. H. *et al.* Proteome changes associated with *Leishmania donovani* promastigote adaptation to oxidative and nitrosative stresses. *J Proteomics* 81, 185–199 (2013); https://doi.org/10.1016/j.jprot.2013.01.011.

159. Purkait, B. *et al.* Mechanism of amphotericin B resistance in clinical isolates of *Leishmania donovani*. *Antimicrob Agents Chemother* 56, 1031–1041 (2012); https://doi.org/10.1128/AAC.00030-11.

160. Sudhandiran, G. & Shaha, C. Antimonial-induced increase in intracellular Ca^{2+} through non-selective cation channels in the host and the parasite is responsible for apoptosis of intracellular *Leishmania donovani* amastigotes. *J Biol Chem* 278, 25120–25132 (2003); https://doi.org/10.1074/jbc.M301975200.

161. Mishra, J. & Singh, S. Miltefosine resistance in *Leishmania donovani* involves suppression of oxidative stress-induced programmed cell death. *Exp Parasitol* 135, 397–406 (2013); https://doi.org/10.1016/j.exppara.2013.08.004.

162. Cordeiro, A. T., Thiemann, O. H. & Michels, P. A. M. Inhibition of *Trypanosoma brucei* glucose-6-phosphate dehydrogenase by human steroids and their effects on the viability of cultured parasites. *Bioorg Med Chem* 17, 2483–2489 (2009); https://doi.org/10.1016/j.bmc.2009.01.068.

163. Cordeiro, A. T. & Thiemann, O. H. 16-bromoepiandrosterone, an activator of the mammalian immune system, inhibits glucose 6-phosphate dehydrogenase from *Trypanosoma cruzi* and is toxic to these parasites grown in culture. *Bioorg Med Chem* 18, 4762–4768 (2010); https://doi.org/10.1016/j.bmc.2010.05.008.

164. Ortíz, C. *et al.* Glucose 6-phosphate dehydrogenase from trypanosomes: Selectivity for steroids and chemical validation in bloodstream *Trypanosoma brucei*. *Molecules* 26 (2021); https://doi.org/10.3390/molecules26020358.

165. Maugeri, D. A. & Cazzulo, J. J. The pentose phosphate pathway in *Trypanosoma cruzi*. *FEMS Microbiol Lett* 234, 117–123 (2004); https://doi.org/10.1016/j.femsle.2004.03.018.

166. Kerkhoven, E. J. *et al.* Handling uncertainty in dynamic models: the pentose phosphate pathway in *Trypanosoma brucei*. *PLoS Comput Biol* 9, e1003371 (2013); https://doi.org/10.1371/journal.pcbi.1003371.

167. González, D. *et al.* The 6-phosphogluconate dehydrogenase of *Leishmania mexicana*: gene characterization and protein structure prediction. *J Mol Microbiol Biotechnol* 19, 213–223 (2010); https://doi.org/10.1159/000320697.

168. Hitosugi, T. *et al.* Phosphoglycerate mutase 1 coordinates glycolysis and biosynthesis to promote tumor growth. *Cancer Cell* 22, 585–600 (2012); https://doi.org/10.1016/j.ccr.2012.09.020.

169. Adams, M. J., Ellis, G. H., Gover, S., Naylor, C. E. & Phillips, C. Crystallographic study of coenzyme, coenzyme analogue and substrate binding in 6-phosphogluconate dehydrogenase: implications for NADP specificity and the enzyme mechanism. *Structure* 2, 651–668 (1994); https://doi.org/10.1016/S0969-2126(00)00066-6.

170. He, W., Wang, Y., Liu, W. & Zhou, C.-Z. Crystal structure of *Saccharomyces cerevisiae* 6-phosphogluconate dehydrogenase Gnd1. *BMC Struct Biol* 7, 38 (2007); https://doi.org/10.1186/1472-6807-7-38.

171. Sundaramoorthy, R. *et al.* Crystal structures of a bacterial 6-phosphogluconate dehydrogenase reveal aspects of specificity, mechanism and mode of inhibition by analogues of high-energy reaction intermediates. *FEBS J* 274, 275–286 (2007); https://doi.org/10.1111/j.1742-4658.2006.05585.x.

172. Phillips, C., Dohnalek, J., Gover, S., Barrett, M. P. & Adams, M. J. A 2.8 A resolution structure of 6-phosphogluconate dehydrogenase from the protozoan parasite *Trypanosoma brucei*: comparison with the sheep enzyme accounts for differences in activity with coenzyme and substrate analogues. *J Mol Biol* 282, 667–681 (1998); https://doi.org/10.1006/jmbi.1998.2059.

173. Haeussler, K., Fritz-Wolf, K., Reichmann, M., Rahlfs, S. & Becker, K. Characterization of *Plasmodium falciparum* 6-phosphogluconate dehydrogenase as an antimalarial drug target. *J Mol Biol* 430, 4049–4067 (2018); https://doi.org/10.1016/j.jmb.2018.07.030.

174. Barrett, M. P. & Le Page, R. W. A 6-phosphogluconate dehydrogenase gene from *Trypanosoma brucei*. *Mol Biochem Parasitol* 57, 89–99 (1993); https://doi.org/10.1016/0166-6851(93)90247-u.

175. Hanau, S., Rippa, M., Bertelli, M., Dallocchio, F. & Barrett, M. P. 6-Phosphogluconate dehydrogenase from *Trypanosoma brucei*. Kinetic analysis and inhibition by trypanocidal drugs. *Eur J Biochem* 240, 592–599 (1996); https://doi.org/10.1111/j.1432-1033.1996.0592h.x.

176. Dardonville, C. *et al.* Selective inhibition of *Trypanosoma brucei* 6-phosphogluconate dehydrogenase by high-energy intermediate and transition-state analogues. *J Med Chem* 47, 3427–3437 (2004); https://doi.org/10.1021/jm031066i.

177. Hanau, S. *et al.* Evidence for dimer/tetramer equilibrium in *Trypanosoma brucei* 6-phosphogluconate dehydrogenase. *Biochim Biophys Acta* 1834, 2647–2652 (2013); https://doi.org/10.1016/j.bbapap.2013.09.018.

178. Esteve, M. I. & Cazzulo, J. J. The 6-phosphogluconate dehydrogenase from *Trypanosoma cruzi*: the absence of two inter-subunit salt bridges as a reason for enzyme instability. *Mol Biochem Parasitol* 133, 197–207 (2004); https://doi.org/10.1016/j.molbiopara.2003.10.007.

179. Jakkula, P., Narsimulu, B. & Qureshi, I. A. Biochemical and structural insights into 6-phosphogluconate dehydrogenase from *Leishmania donovani*. *Appl Microbiol Biotechnol* 105, 5471–5489 (2021); https://doi.org/10.1007/s00253-021-11434-4.

180. Berneburg, I. *et al.* Structure of *Leishmania donovani* 6-phosphogluconate dehydrogenase and inhibition by phosphine gold(I) complexes: A potential approach to leishmaniasis treatment. *Int J Mol Sci* 24 (2023); https://doi.org/10.3390/ijms24108615.

181. Pearse, B. M. & Rosemeyer, M. A. Human 6-phosphogluconate dehydrogenase. Purification of the erythrocyte enzyme and the influence of ions and NADPH on its activity. *Eur J Biochem* 42, 213–223 (1974); https://doi.org/10.1111/j.1432-1033.1974.tb03331.x.

182. Dyson, J. E., D'Orazio, R. E. & Hanson, W. H. Sheep liver 6-phosphogluconate dehydrogenase: isolation procedure and effect of pH, ionic strength, and metal ions on the kinetic parameters. *Arch Biochem Biophys* 154, 623–635 (1973); https://doi.org/10.1016/0003-9861(73)90017-9.

183. Morales-Luna, L. *et al.* Cloning, purification, and characterization of the 6-phosphogluconate dehydrogenase (6PGDH) from *Giardia lamblia*. *Mol Biochem Parasitol* 244, 111383 (2021); https://doi.org/10.1016/j.molbiopara.2021.111383.

184. Topham, C. M., Matthews, B. & Dalziel, K. Kinetic studies of 6-phosphogluconate dehydrogenase from sheep liver. *Eur J Biochem* 156, 555–567 (1986); https://doi.org/10.1111/j.1432-1033.1986.tb09615.x.

185. Price, N. E. & Cook, P. F. Kinetic and chemical mechanisms of the sheep liver 6-phosphogluconate dehydrogenase. *Arch Biochem Biophys* 336, 215–223 (1996); https://doi.org/10.1006/abbi.1996.0551.

186. Moritz, B., Striegel, K., Graaf, A. A. de & Sahm, H. Kinetic properties of the glucose-6-phosphate and 6-phosphogluconate dehydrogenases from *Corynebacterium glutamicum* and their application for predicting pentose phosphate pathway flux *in vivo*. *Eur J Biochem* 267, 3442–3452 (2000); https://doi.org/10.1046/j.1432-1327.2000.01354.x.

187. Rippa, M., Bellini, T., Signorini, M. & Dallocchio, F. The stabilization by a coenzyme analog of a conformational change induced by substrate in 6-phosphogluconate dehydrogenase. *Arch Biochem Biophys* 196, 619–623 (1979); https://doi.org/10.1016/0003-9861(79)90315-1.

188. Dallocchio, F., Matteuzzi, M. & Bellini, T. Half-site reactivity in 6-phosphogluconate dehydrogenase from human erythrocytes. *Biochem J* 227, 305–310 (1985); https://doi.org/10.1042/bj2270305.

189. Hanau, S., Dallocchio, F. & Rippa, M. Subunits asymmetry in the ternary complex of lamb liver 6-phosphogluconate dehydrogenase detected by a NADP analogue. *Biochim Biophys Acta* 1159, 262–266 (1992); https://doi.org/10.1016/0167-4838(92)90054-h.

190. Montin, K., Cervellati, C., Dallocchio, F. & Hanau, S. Thermodynamic characterization of substrate and inhibitor binding to *Trypanosoma brucei* 6-phosphogluconate dehydrogenase. *FEBS J* 274, 6426–6435 (2007); https://doi.org/10.1111/j.1742-4658.2007.06160.x.

191. Marchand, M. *et al.* Glucosephosphate isomerase from *Trypanosoma brucei*. Cloning and characterization of the gene and analysis of the enzyme. *Eur J Biochem* 184, 455–464 (1989); https://doi.org/10.1111/j.1432-1033.1989.tb15038.x.

192. Hanau, S. *et al.* 6-phosphogluconate dehydrogenase: a target for drugs in African trypanosomes. *Curr Med Chem* 11, 2639–2650 (2004); https://doi.org/10.2174/0929867043364441.

193. Pasti, C. *et al.* Sugar derivatives as new 6-phosphogluconate dehydrogenase inhibitors selective for the parasite *Trypanosoma brucei*. *Bioorg Med Chem* 11, 1207–1214 (2003); https://doi.org/10.1016/s0968-0896(02)00650-8.

194. Dardonville, C. *et al.* Synthesis and biological evaluation of substrate-based inhibitors of 6-phosphogluconate dehydrogenase as potential drugs against African trypanosomiasis. *Bioorg Med Chem* 11, 3205–3214 (2003); https://doi.org/10.1016/S0968-0896(03)00191-3.

195. Ruda, G. F. *et al.* Synthesis and biological evaluation of phosphate prodrugs of 4-phospho-D-erythronohydroxamic acid, an inhibitor of 6-phosphogluconate dehydrogenase. *ChemMedChem* 2, 1169–1180 (2007); https://doi.org/10.1002/cmdc.200700040.

196. Ruda, G. F. *et al.* Aryl phosphoramidates of 5-phospho erythronohydroxamic acid, a new class of potent trypanocidal compounds. *J Med Chem* 53, 6071–6078 (2010); https://doi.org/10.1021/jm1004754.

197. Ruda, G. F. *et al.* Virtual fragment screening for novel inhibitors of 6-phosphogluconate dehydrogenase. *Bioorg Med Chem* 18, 5056–5062 (2010); https://doi.org/10.1016/j.bmc.2010.05.077.

198. Finkelstein, A. E. *et al.* Auranofin. New oral gold compound for treatment of rheumatoid arthritis. *Ann Rheum Dis* 35, 251–257 (1976); https://doi.org/10.1136/ard.35.3.251.

199. Katz, W. A. *et al.* The efficacy and safety of auranofin compared to placebo in rheumatoid arthritis. *J Rheumatol Suppl* 8, 173–178 (1982).

200. Kuntz, A. N. *et al.* Thioredoxin glutathione reductase from *Schistosoma mansoni*: an essential parasite enzyme and a key drug target. *PLoS Med* 4, e206 (2007); https://doi.org/10.1371/journal.pmed.0040206.

201. Sharlow, E. R. *et al.* Auranofin is an apoptosis-simulating agent with *in vitro* and *in vivo* anti-leishmanial activity. *ACS Chem Biol* 9, 663–672 (2014); https://doi.org/10.1021/cb400800q.

202. Jortzik, E. *et al.* Antiglioma activity of GoPI-sugar, a novel gold(I)-phosphole inhibitor: chemical synthesis, mechanistic studies, and effectiveness *in vivo*. *Biochim Biophys Acta* 1844, 1415–1426 (2014); https://doi.org/10.1016/j.bbapap.2014.01.006.

203. Da Silva, M. T. A. *et al. In vivo* and *in vitro* auranofin activity against *Trypanosoma cruzi*: Possible new uses for an old drug. *Exp Parasitol* 166, 189–193 (2016); https://doi.org/10.1016/j.exppara.2015.05.012.

204. Feng, L. *et al.* Repurposing auranofin and evaluation of a new gold(I) compound for the search of treatment of human and cattle parasitic diseases: From Protozoa to Helminth Infections. *Molecules* 25 (2020); https://doi.org/10.3390/molecules25215075.

3. PUBLICATIONS

3.1. Publication I

An optimized dihydrodibenzothiazepine lead compound (SBI-0797750) as a potent and selective inhibitor of *Plasmodium falciparum* and *P. vivax* glucose 6-phosphate dehydrogenase 6-phosphogluconolactonase

Berneburg I*, Peddibhotla S*, Heimsch KC, Haeussler K, Maloney P, Gosalia P, Preuss J, Rahbari M, Skorokhod O, Valente E, Ulliers D, Simula LF, Buchholz K, Hedrick MP, Hershberger P, Chung TDY, Jackson MR, Schwarzer E, Rahlfs S, Bode L, Becker K, Pinkerton AB

Antimicrob Agents Chemother 66, e0210921

2022

https://doi.org/10.1128/aac.02109-21

* These authors contributed equally to this work.

AMERICAN SOCIETY FOR MICROBIOLOGY | Antimicrobial Agents and Chemotherapy®

EXPERIMENTAL THERAPEUTICS

An Optimized Dihydrodibenzothiazepine Lead Compound (SBI-0797750) as a Potent and Selective Inhibitor of *Plasmodium falciparum* and *P. vivax* Glucose 6-Phosphate Dehydrogenase 6-Phosphogluconolactonase

Isabell Berneburg,[a] Satyamaheshwar Peddibhotla,[b] Kim C. Heimsch,[a] Kristina Haeussler,[a,c] Patrick Maloney,[b] Palak Gosalia,[b] Janina Preuss,[a,c] Mahsa Rahbari,[a] Oleksii Skorokhod,[d] Elena Valente,[e] Daniela Ulliers,[e] Luigi Felice Simula,[f] Kathrin Buchholz,[a] Michael P. Hedrick,[b] Paul Hershberger,[b] Thomas D. Y. Chung,[b] Michael R. Jackson,[b] Evelin Schwarzer,[e] Stefan Rahlfs,[a] Lars Bode,[c] Katja Becker,[a] Anthony B. Pinkerton[b]

[a]Justus Liebig University Giessen, Biochemistry and Molecular Biology, Interdisciplinary Research Center, Giessen, Germany
[b]Conrad Prebys Center for Chemical Genomics, Sanford Burnham Prebys Medical Discovery Institute, La Jolla, California, USA
[c]University of California, San Diego, La Jolla, California, USA
[d]Department of Life Sciences and Systems Biology, University of Torino, Turin, Italy
[e]Department of Oncology, University of Torino, Turin, Italy
[f]Department of Clinical Chemistry, Ospedale Civile, Alghero, Italy

Isabell Berneburg and Satyamaheshwar Peddibhotla contributed equally to this article. Author order was determined by the corresponding author after negotiation.

ABSTRACT In *Plasmodium*, the first two and rate-limiting enzymes of the pentose phosphate pathway, glucose 6-phosphate dehydrogenase (G6PD) and the 6-phosphogluconolactonase, are bifunctionally fused to a unique enzyme named GluPho, differing structurally and mechanistically from the respective human orthologs. Consistent with the enzyme's essentiality for malaria parasite proliferation and propagation, human G6PD deficiency has immense impact on protection against severe malaria, making *Pf*GluPho an attractive antimalarial drug target. Herein we report on the optimized lead compound *N*-(((2R,4S)-1-cyclobutyl-4-hydroxypyrrolidin-2-yl)methyl)-6-fluoro-4-methyl-11-oxo-10,11-dihydrodibenzo[b,f][1,4]thiazepine-8-carboxamide (SBI-0797750), a potent and fully selective *Pf*GluPho inhibitor with robust nanomolar activity against recombinant *Pf*GluPho, *Pv*G6PD, and *P. falciparum* blood-stage parasites. Mode-of-action studies have confirmed that SBI-0797750 disturbs the cytosolic glutathione-dependent redox potential, as well as the cytosolic and mitochondrial H_2O_2 homeostasis of *P. falciparum* blood stages, at low nanomolar concentrations. Moreover, SBI-0797750 does not harm red blood cell (RBC) integrity and phagocytosis and thus does not promote anemia. SBI-0797750 is therefore a very promising antimalarial lead compound.

KEYWORDS G6PDH, inhibitors, malaria, *Plasmodium*, *Plasmodium falciparum*, *Plasmodium vivax*

Malaria is one of the world's most devastating infectious diseases, transmitted to the human host by female *Anopheles* mosquitoes. In 2019, an estimated 229 million cases of malaria resulting in 409,000 deaths occurred worldwide (1). *Plasmodium falciparum* is responsible for 90% of all malaria-related deaths and is therefore the most important *Plasmodium* species; however, infections with *Plasmodium vivax* can also manifest as severe malaria and thereby threaten the health and welfare of people in countries where the organism is endemic (2, 3). Currently, WHO recommends an artemisinin-based combination therapy (ACT) for treating uncomplicated falciparum malaria and chloroquine or an ACT to treat uncomplicated vivax malaria (4). However,

Address correspondence to Anthony B. Pinkerton, apinkerton@SBPdiscovery.org.

The authors declare no conflict of interest.

Received 31 October 2021
Returned for modification 29 November 2021
Accepted 26 January 2022
Published 10 March 2022

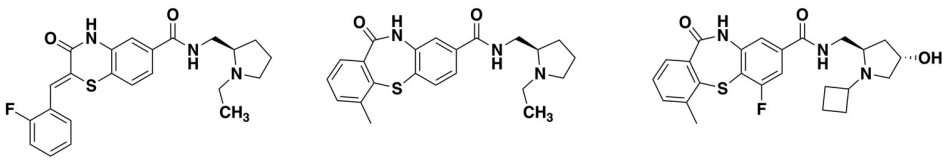

FIG 1 Previously described *Pf*GluPho inhibitors ML276 and ML304 and optimized lead compound SBI-0797750.

increasing resistance of both *P. falciparum* and *P. vivax* against these commonly used drugs is hampering the fight against the disease (4–6). Therefore, ambitious efforts to develop new antimalarial drugs are needed.

Naturally occurring evidence for a connection of the pentose phosphate pathway (PPP) and malaria is demonstrated by the fact that deficiency of the enzyme glucose 6-phosphate dehydrogenase in humans (*Homo sapiens* G6PD [*Hs*G6PD]) leads to partial resistance to the disease. The very similar distribution patterns of malaria and *Hs*G6PD deficiency further underscore this correlation (7, 8). Currently, around 400 million people are affected by G6PD deficiency, which can be caused by over 200 known mutations in the *Hs*G6PD-encoding gene (8). The mild and most common mutations result in reduced G6PD activity. It is assumed that their protective effect against malaria is the result of increased phagocytosis of parasitized G6PD-deficient erythrocytes (9–11).

Plasmodium parasites have a complex life cycle with changing environments in the *Anopheles* mosquito vector and the human host (12). During their life, *Plasmodium* parasites are continuously exposed to reactive oxygen species (ROS) and reactive nitrogen species (RNS) of different sources, mainly detoxified by the thioredoxin and glutathione systems. These systems are highly dependent on the supply of NADPH as a reducing equivalent (13), underscoring the importance of the oxidative PPP as the major source of NADPH for the parasites (14). A noticeable structural difference between the plasmodial and human PPP is that in *Plasmodium* the first two enzymes, G6PD and 6-phosphogluconolactonase, are fused to form a unique bifunctional enzyme named GluPho, which differs structurally and functionally from the human orthologs (15). Using double-crossover disruption, we were able to show that *Pf*GluPho is essential for the growth of asexual blood-stage parasites, validating this enzyme as an excellent target for the development of new, specific antimalarial drugs (16). To follow up on this hypothesis, we performed a high-throughput screen of 348,911 compounds in the NIH's Molecular Libraries Small Molecule Repository (MLSMR) collection (17) and identified two promising compounds with selective inhibition of *Pf*GluPho in the nanomolar range, ML276 (18) and ML304 (19). In this study, we now present the characterization of an optimized lead from the dibenzothiazepine-derived second probe ML304 (19), SBI-0797750 (Fig. 1), with low nanomolar activity against recombinant *Pf*GluPho, *Pv*G6PD, and *P. falciparum* blood-stage parasites and negligible effects on host red blood cell (RBC) integrity and phagocytosis.

RESULTS

SBI-0797750 inhibits *Pf*GluPho and *Pv*G6PD in a highly selective manner at low nanomolar concentrations. The 50% inhibitory concentration (IC_{50}) of SBI-0797750 was first determined using the diaphorase-coupled assay and confirmed with the orthogonal assay without diaphorase. We determined an IC_{50} of 6.7 $\pm$ 1.8 nM for *Pf*GluPho and of 31.0 $\pm$ 3.1 nM for *Pv*G6PD. The human homologue *Hs*G6PD was tested up to 99,000 nM with inhibition below 50% (20), indicating high selectivity of SBI-0797750 for the plasmodial enzymes (Table 1).

Mode-of-inhibition studies indicated that SBI-0797750 competes with G6P for the substrate binding site, which was evident by increasing K_m for G6P and constant V_{max} with increasing drug concentration (Fig. 2A and B). Similarly, the K_m for $NADP^+$

TABLE 1 Biochemical and cellular activities of ML304 and SBI-0797750[a]

	IC_{50} (nM) for biochemical/recombinant protein			EC_{50} (nM) for cellular/*in vitro P. falciparum*		
Compound	*Pf*GluPho	*Pv*G6PD	*Hs*G6PD	3D7, asexual	NF54-*attB*, asexual	NF54, sexual
ML304	190*	2,600 ± 800**	>79,000*	471 ± 40†**	1,700‡	ND
SBI-0797750	6.7 ± 1.8	31.0 ± 3.1	>99,000	22.5 ± 2.2,† 64.6 ± 9.6‡	83.8 ± 17.3‡	73.9 ± 22

[a]Values are means ± SD from at least three independent determinations with different batches. †, value determined with the ^{3}H incorporation assay; ‡, value determined with the SYBR green assay; *, value taken from reference 19; **, value taken from reference 26. ND, not determined.

increased with increasing compound concentrations, but V_{max} decreased (Fig. 2C and D), suggesting a mixed-type inhibition of SBI-0797750 against $NADP^+$.

To test for reversibility of *Pf*GluPho inhibition by SBI-0797750, the enzyme was first incubated with a high compound concentration (1.65 μM), following dilution below the IC_{50} (3.3 nM), and again incubated to allow compound dissociation. Activities were compared to controls containing either no SBI-0797750 (CTL, 0 nM; 100% activity) or 3.3 nM SBI-0797750 (CTL, 3.3 nM), which corresponds to the concentration after dilution. The diluted sample (postdilution, 3.3 nM) showed a residual activity of 79.2% ± 1.5%, almost identical to the control with 77.2% ± 1.6% (CTL, 3.3 nM). In contrast, incubation of the enzyme with 1.65 μM SBI-0797750 (predilution, 1.65 μM) revealed a residual activity of 2.4% ± 0.3%, proving complete inhibition of the enzyme before dilution. Since the small remaining activity could be due to the competition of SBI-0797750 with G6P at saturation (Fig. 2A and B), we performed the same experiment under K_m conditions, and indeed, enzyme activity was reduced to 0.3% ± 0.2%. Finally, the data clearly indicate a fully reversible inhibition of *Pf*GluPho by SBI-0797750 (Fig. 3).

Activity against *P. falciparum* 3D7 and NF54-*attB* asexual parasites and NF54 gametocytes in culture. Moreover, we tested the activity of SBI-0797750 against *P. falciparum* blood stages *in vitro* by using different assays, strains, and parasite stages (Table 1). For asexual stages of 3D7 strains, 50% effective concentrations (EC_{50}s) of 22.5 ± 2.2 nM were determined using the [^{3}H]hypoxanthine incorporation assay, and EC_{50}s of 64.6 ± 9.6 nM were obtained using the SYBR green assay. For the NF54-*attB*

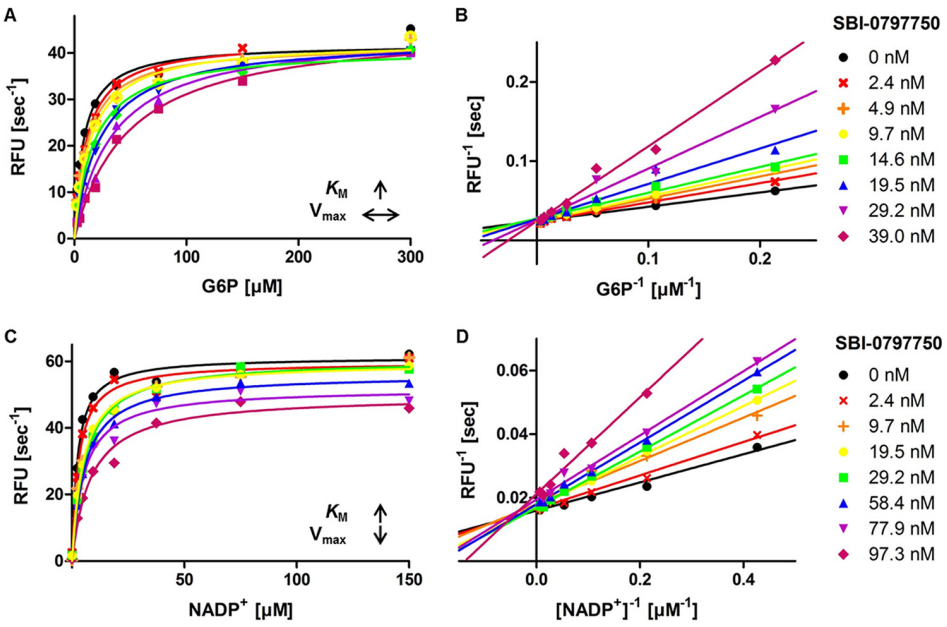

FIG 2 Mechanism of inhibition of SBI-0797750 against *Pf*GluPho. (A and B) Various compound concentrations were titrated against G6P. SBI-0797750 acts as a competitive inhibitor against *Pf*GluPho, since the K_m value for G6P increases with increasing compound concentrations, while V_{max} stays constant. (C and D) Titration of $NADP^+$ against different compound concentrations. The K_m value for $NADP^+$ increases, while V_{max} decreases, indicating a mixed-type inhibition. *Pf*GluPho activity is in relative fluorescence units per second (modified from reference 20).

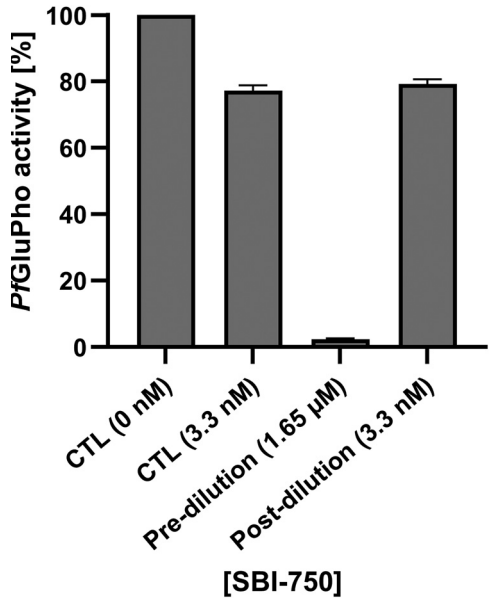

FIG 3 Reversibility of the *Pf*GluPho inhibition by SBI-0797750. Reversibility of *Pf*GluPho inhibition by SBI-0797750 (SBI-750) was determined by incubating the enzyme with a high compound concentration of 1.65 μM (predilution), followed by dilution to 3.3 nM (postdilution). The diluted sample had the same activity as a control containing the same final compound concentration (CTL, 3.3 nM), while the undiluted sample was completely inhibited. Treatment without SBI-750 was defined as 100% activity (CTL, 0 nM). Values are means and SD from three independent determinations, each including two measurements.

parasites, the SYBR green assay resulted in EC_{50}s of 83.8 $\pm$ 17.3 nM. In addition, initial experiments with *P. falciparum* NF54 gametocytes revealed comparable inhibitory effects with EC_{50}s of 73.9 nM $\pm$ 22 nM.

Effects on the glutathione redox state of NF54-*attB*$^{[hGrx1\text{-}roGFP2]}$ parasites. The oxidative effect of SBI-0797750 and ML304 on the glutathione redox system was determined using the cytosolic glutathione redox sensor hGrx1-roGFP2, stably integrated into NF54-*attB* parasites. Mid- and long-term exposures were carried out via confocal laser scanning microscopy (CLSM) as described in Materials and Methods. Control studies excluded a direct interaction of SBI-0797750, ML304, and the control drugs artesunate (ATS) and chloroquine (CQ) with the recombinant hGrx1-roGFP2 probe at the concentrations used in this study. Four-hour incubations with 1$\times$ EC_{50} SBI-0797750 and ML304 showed a highly significant increase in redox ratio (Fig. 4A) as well as in the degree of oxidation (OxD), which was 75.6% $\pm$ 1.6% for SBI-0797750 and 83.3% $\pm$ 2.8% for ML304. Thus, the improved drug SBI-07977504 disrupts the redox homeostasis to the same extent as ML304, even at lower concentrations. In contrast, the parasites could compensate for the oxidizing effect of 1$\times$ EC_{50} SBI-0797750 and ML304 after a long incubation period of 24 h (Fig. 4B), and no significant change in the redox ratio could be measured. For comparison, we tested antimalarials such as ATS and CQ on the redox sensors. However, in agreement with previous data (21), no effect was observed after 4 h or 24 h, even at concentrations of 100$\times$ and 10$\times$ EC_{50}, respectively (see Fig. S1 in the supplemental material).

Effects on H_2O_2 homeostasis in NF54-*attB*$^{[roGFP2\text{-}Orp1]}$ and NF54-*attB*$^{[Mito\text{-}roGFP2\text{-}Orp1]}$ parasites. To determine whether SBI-0797750 can directly affect H_2O_2 levels in the cytosol and mitochondrion of *P. falciparum* N54-*attB* parasites, mid- and long-term experiments were carried out using NF54-*attB*$^{[roGFP2\text{-}Orp1]}$ and NF54-*attB*$^{[Mito\text{-}roGFP2\text{-}Orp1]}$ parasites via CLSM (22). Control studies excluded a direct interaction of SBI-0797750 with the recombinant H_2O_2 probes. Studies using 4 h of incubation with approximately 1$\times$ EC_{50} ML304 and SBI-0797750 increased significantly the 405/488-nm fluorescence ratio (Fig. 5A). With a time delay, this increase could also be determined in the mitochondrion (Fig. 5B). In comparison, the control compound CQ increased the redox ratio

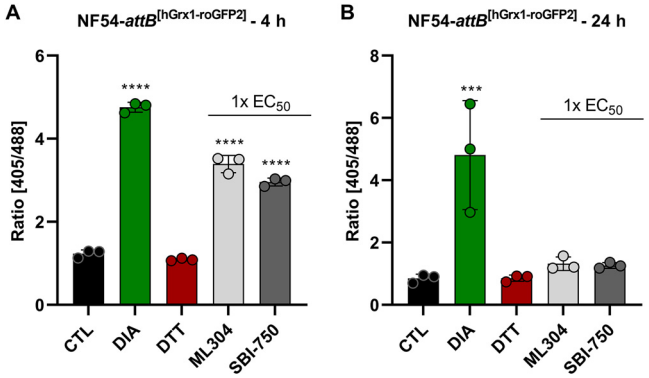

FIG 4 Mid- and long-term effects of ML304 and its derivative SBI-0797750 on the redox ratio of *P. falciparum* NF54-*attB*$^{[hGrx1\text{-}roGFP2]}$ parasites. In 4-h and 24-h experiments, *P. falciparum* NF54-*attB*$^{[hGrx1\text{-}roGFP2]}$ parasites were incubated with 1× EC_{50} ML304 and SBI-0797750 (SBI-750). Via CLSM, a significant increase of the 405/488-nm fluorescence ratio of the redox sensor could be observed in the 4-h-incubation experiment (A). In the 24-h-incubation experiment, neither ML304 nor SBI-0797750 significantly changed the redox ratio (B). Nontreated parasites served as controls. All experiments included fully oxidized (1 mM DIA) and fully reduced (10 mM DTT) parasites. CLSM data were obtained from 10 to 20 trophozoites for each experiment and each incubation time. Values are means and SD from three independent experiments. A one-way ANOVA with 95% confidence intervals with the Dunnett's multiple-comparison test was applied for statistical analysis of significance (***, $P < 0.001$; ****, $P < 0.0001$).

after 4 h (100× EC_{50}) in the cytosol (Fig. S2). However, in contrast to our previous publication (22), this did not reach significance, likely due to biological variations. No increase in redox ratio could be measured in the mitochondrion. Studies of 4 h and 24 h of incubation with the control compound ATS (100× and 10× EC_{50}) showed hardly any effect on the 405/488-nm fluorescence ratio in the cytosol and the mitochondrion (Fig. S2).

Absence of SBI-0797750 adverse effects on RBCs from G6PD-normal subjects and G6PD-deficient hemizygous males. Since a very good therapeutic index of SBI-0797750 (Table 1) is a promising prerequisite for therapeutic application, we analyzed potential adverse effects of the substance on the parasites' host cells, the RBCs, whose integrity depends on *Hs*G6PD activity. The lack of effect of SBI-0797750 was tested in RBCs from G6PD-normal and -deficient donors *ex vivo*.

First, the potential oxidative effect of the *Pf*GluPho inhibitor SBI-0797750 on RBCs was determined by measuring reduced glutathione (GSH). GSH levels of G6PD-normal RBCs did not change during 1 h and 24 h of incubation with any of the tested inhibitor

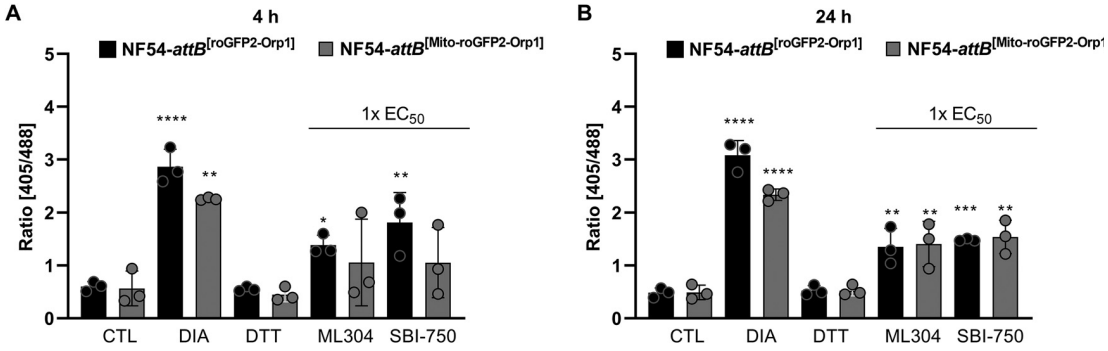

FIG 5 Mid- and long-term effects of ML304 and its derivative SBI-0797750 on the redox ratio of *P. falciparum* NF54-*attB*$^{[roGFP2\text{-}Orp1]}$ and NF54-*attB*$^{[Mito\text{-}roGFP2\text{-}Orp1]}$-transfected parasites. Four and 24 h of incubation of NF54-*attB*$^{[roGFP2\text{-}Orp1]}$ transfectants with 1× EC_{50} SBI-0797750 (SBI-750) and ML304 significantly increased the fluorescence ratio of the cytosolic sensor, as determined using CLSM. In NF54-*attB*$^{[Mito\text{-}roGFP2\text{-}Orp1]}$ transfectants, ML304 and SBI-0797750 increased the redox ratio after 4 h (A), both of which reached significance after 24 h of incubation (B). Nontreated parasites served as controls. All experiments included fully oxidized (1 mM DIA) and fully reduced (10 mM DTT) parasites. CLSM data comprised 10 to 20 trophozoites analyzed per experiment for each incubation. Values are means and SD (error bars) for three independent experiments. A one-way ANOVA with 95% confidence intervals with the Dunnett's multiple-comparison test was applied for statistical analysis of significance (*, $P < 0.05$; **, $P < 0.01$; ***, $P < 0.001$; ****, $P < 0.0001$).

concentrations up to 20 μM (4,000× IC_{50} against *Pf*GluPho) (Table 1; Fig. 6A). The same results were obtained for G6PD-deficient RBCs, with the exception of the highest inhibitor concentration (20 μM), which provoked a significant loss (−20%) of GSH (Fig. 6A) after 24 h inhibitor exposure. Under these conditions, GSH dropped to approximately 1 mM within G6PD-deficient RBCs (which is half the normal GSH level in G6PD-normal RBCs). In contrast, treating G6PD-deficient and G6PD-normal RBCs with the *Hs*G6PD inhibitor CB83 (23) for 24 h resulted in a significant GSH decrease at concentrations of 0.8 μM (2× IC_{50} against *Hs*G6PD) (23) and 4 μM (10× IC_{50}), respectively (Fig. 6B). G6PD-normal or -deficient RBCs pretreated with 2 μM (400× IC_{50}) of SBI-0797750 did not potentiate the 70% GSH drop induced by the oxidative stress of diamide and did not interfere with the GSH recovery rate after exposure (Fig. 6C). These findings confirm the lack of *Hs*G6PD inhibition by SBI-0797750 in intact RBCs at a biologically plausible concentration for parasite growth inhibition.

Furthermore, SBI-0797750 was shown to have no major effect on RBC phagocytosis. Oxidatively modified RBCs, vulnerable to phagocytosis, are recognized by spleen phagocytes and removed from circulation *in vivo*, leading to anemia (24, 25). To exclude adverse effects of the *Pf*GluPho inhibitor leading to oxidation-induced phagocytosis of RBCs, SBI-0797750 was tested in an *in vitro* phagocytosis assay. For this purpose, RBCs were treated with increasing concentrations of SBI-0797750 for 1 h and 24 h and subsequently exposed to human monocytic phagocytes.

Both parameters quantifying the phagocytosis of RBCs—the amount of phagocytes that phagocytosed (Fig. 7A, C, E, and G) and the mean number of RBCs taken up by a single phagocytosis-positive phagocyte (Fig. 7B, D, F, and H)—consistently show that the *Pf*GluPho inhibitor does not significantly increase the phagocytosis rate of RBCs in G6PD-normal RBCs (up to 20 μM; 4,000× IC_{50}) and G6PD-deficient RBCs (up to 2 μM; 400× IC_{50}) compared to nontreated controls. Only in G6PD-deficient RBCs treated with 20 μM SBI-0797750 was the basal phagocytosis rate (5%) increased (10 to 20%), but it remained low compared to that of the positive control (IgG anti-D-opsonized RBCs), where 30 to 40% phagocytosing THP-1 was detected (Fig. 7). The compound did not harm RBCs during short- or long-term incubations at either low or high hematocrit. These different incubation conditions were used to ensure cytosolic concentrations in RBCs, which might be plausible for an *in vivo* supplementation of the substance.

In contrast, 10 μM (25× IC_{50}) of the *Hs*G6PD inhibitor CB83 significantly increased phagocytosis in G6PD-deficient RBCs incubated at low hematocrit, allowing the substance to accumulate in the cytosol over time (Fig. 7). Here, the phagocytosis rate was similar to that of the positive phagocytosis control, IgG anti-D-opsonized RBCs. The highest concentration (125× IC_{50}; 50 μM) of CB83 resulted in significantly increased phagocytosis of G6PD-deficient RBCs, even at high hematocrit, and of G6PD-normal RBCs at low hematocrit.

Finally, a loss of RBC integrity was quantified via hemoglobin release from RBCs, which occurs when the membrane becomes damaged and leaky from the inhibitor, and was expressed as the hemolysis rate. After 24 h of incubation with biologically relevant concentrations of SBI-0797750 (up to 2 μM; 400× IC_{50}), the inhibitor did not induce significant hemolysis in either G6PD-normal or G6PD-deficient cells independent of hematocrit (Fig. 8). Only the highest concentration of the *Pf*GluPho inhibitor tested (20 μM; 4,000× IC_{50}) caused a moderate hemoglobin release. Thus, the basal hemolysis rates in G6PD-normal RBCs, with 2% and 40% hematocrit, were increased by 30% and 80%, respectively, after 1 h of incubation and by 80% and 40% after 24 h. Similarly, G6PD-deficient RBCs were not damaged by SBI-0797750, and only the highest concentration of 20 μM caused hemolysis after 1 h and 24 h of incubation (+80% and +100%, respectively, at 2% hematocrit and +60% and +65% at 40% hematocrit compared to untreated RBCs) (Fig. 8).

We also showed that the *Hs*G6PD inhibitor CB83 is safe for RBCs up to a concentration of 10 μM (25× IC_{50}) in G6PD-normal and -deficient cells, incubated at 2 or 40% hematocrit. However, inhibitor concentrations of 50 μM (125× IC_{50}) resulted in

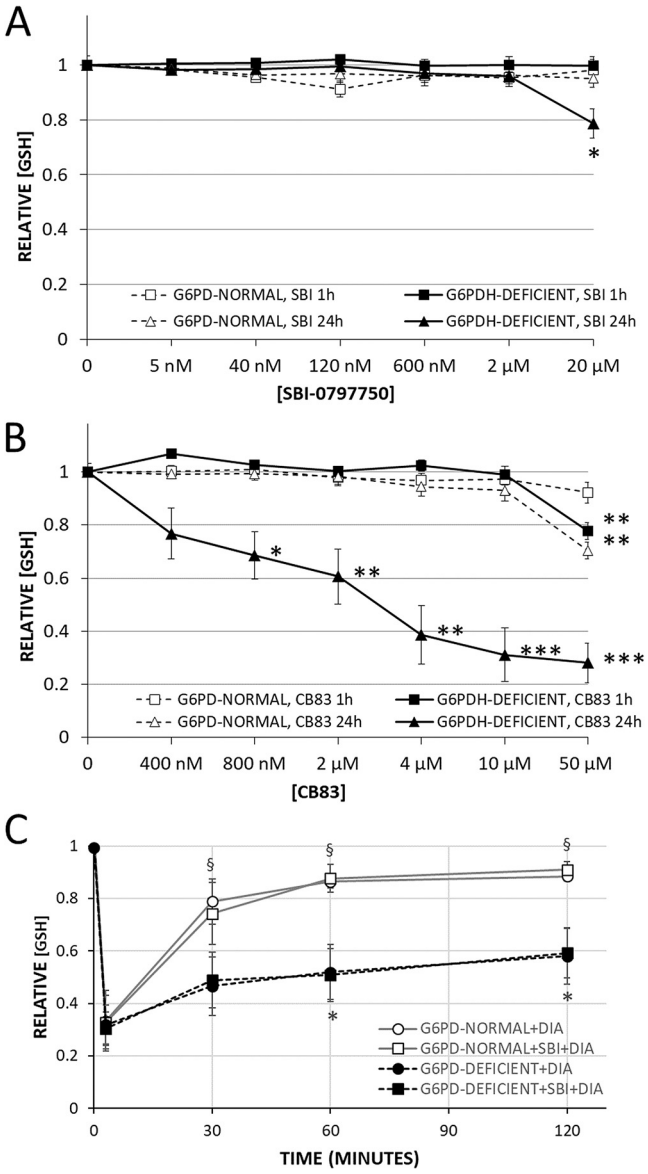

FIG 6 Effect of SBI-0797750 and CB83 on steady-state concentration and recovery of GSH after oxidative challenge in G6PD-normal and G6PD-deficient RBCs. G6PD-normal and -deficient RBCs were incubated with SBI-0797750 (A) or CB83 (B) at indicated concentrations or kept under the same conditions without inhibitor treatment (0 nM). GSH concentrations in RBCs were measured after 1 and 24 h of incubation as indicated. GSH concentrations were normalized by referring them to the hemolysis of respective untreated RBCs (0 nM). Mean GSH concentrations and SE in untreated RBCs (0 nM) were 2.86 $\pm$ 0.13 mM and 2.65 $\pm$ 0.13 mM for G6PD-normal RBCs (n = 5) and 1.89 $\pm$ 0.13 mM and 1.24 $\pm$ 0.23 mM for G6PD-deficient ones (n = 8) after 1 and 24 h of incubation, respectively. Normalized GSH concentrations in RBCs (relative [GSH]) of G6PD-normal (n = 5) and G6PD-deficient (n = 8) donors are shown as means and SE. Significant differences relative to untreated RBCs are indicated: *, $P < 0.05$; **, $P < 0.01$; ***, $P < 0.001$. (C) GSH was measured in RBCs after preincubation with or without 2 μM SBI-0797750, and G6PD-normal and -deficient RBCs were subsequently challenged with 0.5 and 1.0 mM DIA (final concentrations), respectively, at time zero. RBC suspensions were incubated for 3 min at 4°C and afterward at 37°C. GSH values of RBCs measured at 3, 30, 60, and 120 min after DIA supplementation were referred to the corresponding starting GSH value (t = 0) of the same RBC suspension measured immediately before DIA supplementation (relative [GSH]). Mean GSH concentrations and SE of G6PD-normal and -deficient RBCs at time zero were 2.71 $\pm$ 0.15 mM and 1.66 $\pm$ 0.15 mM, respectively, without SBI-0797750 and 2.82 $\pm$ 0.17 mM and 1.68 $\pm$ 0.14 mM, respectively, with SBI-0797750. Relative GSH concentrations in RBCs of G6PD-normal (n = 5) and G6PD-deficient (n = 8) donors are shown as means and SE. Significant differences relative to respective values at 3 min (*, $P < 0.05$) and differences between G6PD-normal and -deficient RBCs (§, $P < 0.05$) are indicated.

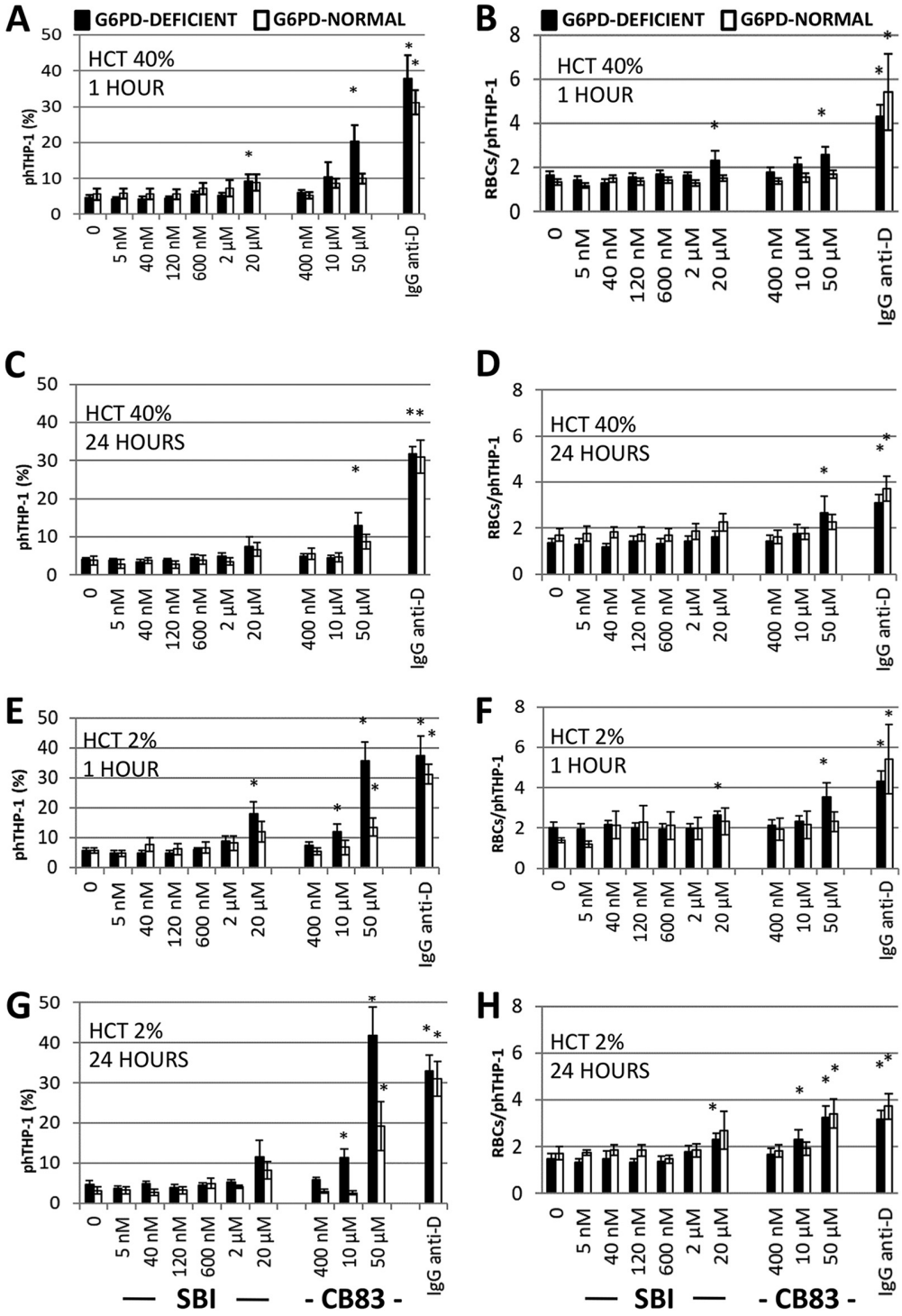

FIG 7 Effect of SBI-0797750 and CB83 on the phagocytosis of G6PD-normal and G6PD-deficient RBCs by human phagocytes. G6PD-normal and -deficient RBCs were incubated at a hematocrit of either 40% (A to D) or 2% (E to H) with SBI-0797750 (SBI) or CB83 at the indicated concentrations for 1 h and 24 h or kept under the same conditions without inhibitor treatment (0 nm). RBCs were fluorescence stained with carboxyfluorescein diacetate succinimidyl ester (CFDA-SE). Erythrophagocytosis by THP-1 phagocytes expressed as a proportion of phagocytosis-positive phagocytes (phTHP-1 [%]) and the number of RBCs phagocytosed per phagocyte (RBCs/phTHP-1) were assessed via FACS. IgG anti-D-opsonized RBCs were included as a positive phagocytosis control. For details, see Materials and Methods. Columns represent means and SE of RBC phagocytosis from G6PD-normal ($n = 5$) and G6PD-deficient ($n = 8$) donors. Significant differences compared to untreated RBCs are indicated: *, $P < 0.05$.

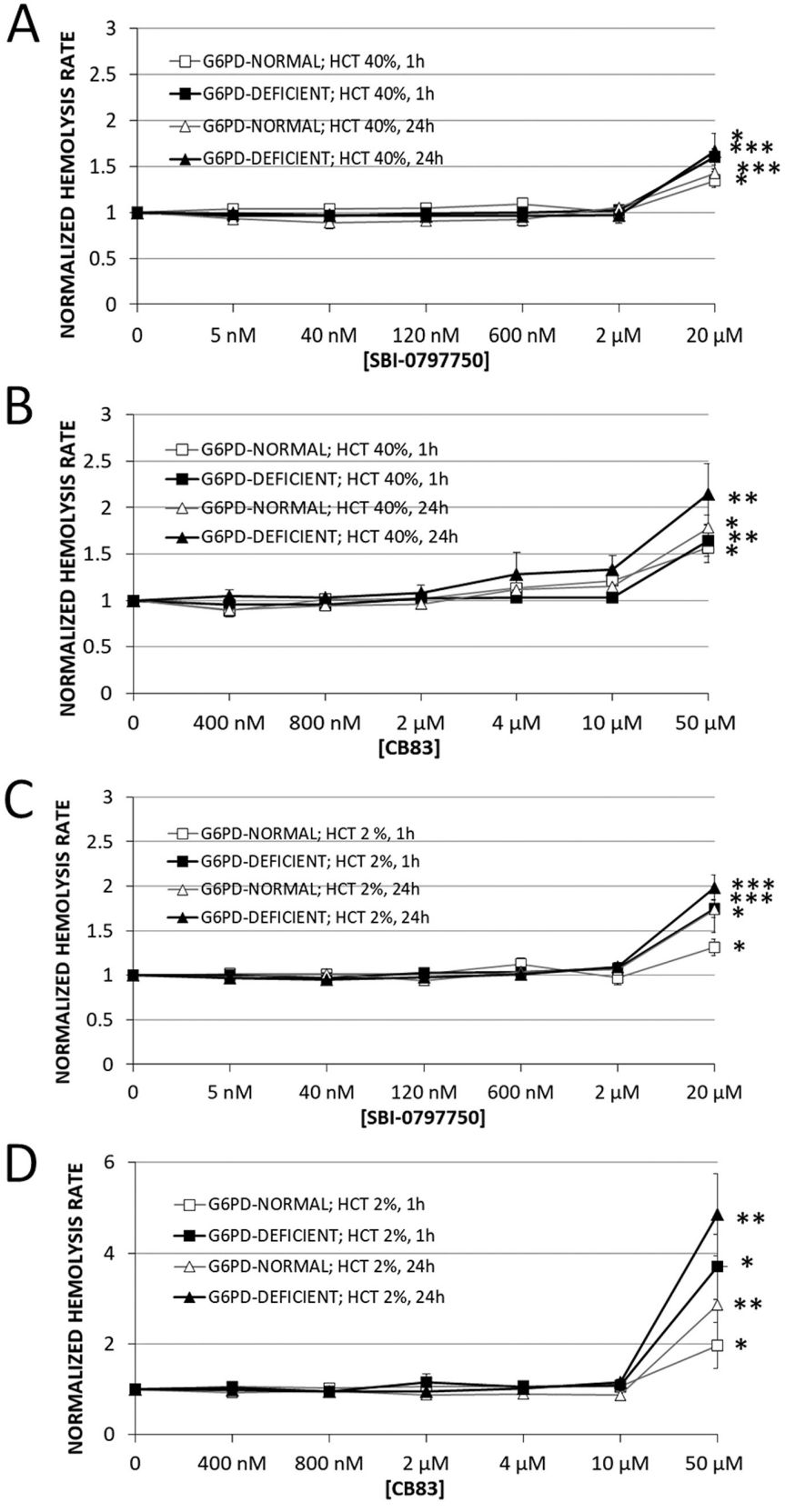

FIG 8 Effect of SBI-0797750 and CB83 on hemolysis in G6PD-normal and -deficient RBCs. G6PD-normal and -deficient RBCs were incubated at a hematocrit of either 40% (A and B) or 2% (C and D)

(Continued on next page)

significantly higher hemolysis rates than in all experiments with SBI-0797750. In G6PD-normal and -deficient RBCs with 2% hematocrit, 2.0- and 3.7-fold-higher values were measured after 1 h and 2.8- and 4.8-fold higher values after 24 h than in untreated RBCs. During RBC incubation at 40% hematocrit with CB83, we observed a dark-brownish discoloration of the RBC suspension (not shown) which is typical of methemoglobin (MetHb) formation. Hemoglobin aggregation and Heinz body formation at the membrane accompany MetHb formation, which might explain the lower hemoglobin release (hemolysis rate) at high hematocrit than at 2% hematocrit (Fig. 8).

DISCUSSION

Bifunctional plasmodial GluPho, including the enzymes G6PD and 6PGL of the oxidative PPP, is a promising target for developing new antimalarial drugs against *P. falciparum*, since the enzyme differs structurally and functionally from the human orthologs and is essential for blood-stage parasites (15, 16). The enzyme shares high sequence identity to its orthologs in other *Plasmodium* species such as *P. vivax* (*Pv*GluPho) (71.2% identity and 79.8% similarity at the amino acid level [26]), increasing the probability that potential drugs may also inhibit the G6PD of other *Plasmodium* species. Previously we identified two promising compounds, ML276 (18) and ML304 (19), which selectively inhibited *Pf*GluPho in the nanomolar range via a high-throughput screening of about 400,000 molecules (17). In this study, we present the optimization of the dibenzothiazepine-derived second probe, ML304, to a single-digit-nanomolar lead compound, SBI-0797750.

ML304 inhibits recombinant *Pf*GluPho with an IC_{50} of 190 nM (19) and *P. falciparum* 3D7 asexual blood stages with an EC_{50} of 471.3 $\pm$ 39.5 nM (26). Medicinal chemistry optimization around the ML304 scaffold led to SBI-0797750, which is approximately 25-fold more active against the recombinant enzyme (IC_{50} = 6.7 $\pm$ 1.8 nM) and *in vitro* (EC_{50} = 22.5 $\pm$ 2.2 nM). Consistent with previous results on ML304 (EC_{50} = 1.25 μM [27]), initial experiments with SBI-0797750 showed that it is also active against sexual *P. falciparum* gametocytes (EC_{50} = 73.9 $\pm$ 22 nM). These preliminary results suggest that SBI-0797750 could potentially also be used as a transmission-blocking agent and is currently being investigated in more detail.

Furthermore, the optimization did not change the nature of inhibition since we confirmed a competition with the substrate G6P and a mixed type of inhibition against $NADP^+$ (Fig. 2). In line with that, we could also show that the inhibitor is fully reversible on increasing the substrate to compound ratio (Fig. 3).

As shown for ML304 (20), SBI-0797750 also inhibits the corresponding enzyme of *P. vivax*—*Pv*G6PD—with an IC_{50} of 31.0 $\pm$ 3.1 nM which is comparable to the inhibitory activity on the *P. falciparum* enzyme. This value is about 2 orders of magnitude lower than ML304 (IC_{50} = 2.6 $\pm$ 0.8 μM [26]). Since the G6P and $NADP^+$ binding sites are highly conserved in *Plasmodium*, the higher IC_{50} of *Pv*G6PD compared to the full-length enzyme *Pf*GluPho might be explained by the structural disadvantage of the truncated enzyme, also showing higher K_m values (26). Consequently, higher substrate concentra-

FIG 8 Legend (Continued)
with SBI-0797750 (SBI) (A and C) or CB83 (B and D) at indicated concentrations or kept under the same conditions without inhibitor treatment (0 nM). The hemolysis rate was assessed in terms of hemoglobin release from RBCs and was measured in the supernatant after 1 h and 24 h of incubation. Supernatant hemoglobin was referred to total hemoglobin in the RBC suspension to obtain the hemolysis rate. These rates were normalized by referring any measured value to the hemolysis rate assessed in respective untreated RBCs (0 nM). Mean hemolysis rates and SE in untreated RBCs (0 nM) incubated at a hematocrit of 40% were 0.9% $\pm$ 0.09% and 1.47% $\pm$ 0.16% for G6PD-normal (n = 5) and 1.17% $\pm$ 0.23% and 1.56% $\pm$ 0.36% for G6PD-deficient RBCs (n = 8) after 1 h and 24 h of incubation, respectively (A and B). Mean hemolysis rates and SE in untreated RBCs (0 nM) incubated at a hematocrit of 2% were 1.95% $\pm$ 0.28% and 2.94% $\pm$ 0.48% for G6PD-normal (n = 5) and 2.40% $\pm$ 0.26% and 3.56% $\pm$ 0.59% for G6PD-deficient RBCs (n = 8) after 1 h and 24 h of incubation, respectively (C and D). Normalized hemolysis rates of RBCs are shown as means and SE of G6PD-normal (n = 5) and G6PD-deficient (n = 8) donors. Significant differences to untreated RBCs are indicated: *, $P < 0.05$; **, $P < 0.01$; ***, $P \leq 0.001$.

tions were used in the *Pv*G6PD inhibition studies, providing another possible explanation for the higher IC_{50} against *Pv*G6PD, as SBI-0797750 competes with the G6P binding pocket. Since the human enzyme was hardly inhibited up to a concentration of 99 μM, SBI-0797750 represents a highly selective and robust inhibitor of plasmodial GluPhos with *in vitro* activity comparable to those of FDA-approved antimalarials such as CQ and ATS (28).

Investigations of SBI-0797750 and ML304 with the cytosolically expressed glutathione redox sensor hGrx1-roGFP2 and with the cytosolically and mitochondrially expressed H_2O_2 biosensors roGFP2-Orp1 and Mito-roGFP2-Orp1, respectively, revealed that the mode of action of these drugs is likely linked to a disruption of glutathione and H_2O_2 homeostasis. The cytosolic probes demonstrated that oxidative effects were already occurring at 4 h of incubation with low nanomolar concentrations (1$\times$ EC_{50}) of SBI-0797750, comparable to ML304. These effects were even increased in the cytosolic roGFP2-Orp1 sensor after 24 h, at which time the oxidation of the mitochondrial probes reached significance as well. In contrast, the clinically used drug CQ only increased the 405/488-nm ratio of the cytosolic roGFP2-Orp1 sensor in the 4-h experiment (100$\times$ EC_{50}), but not significantly. The antimalarial ATS hardly affected the 405/488-nm ratio of all tested sensors and under all conditions. These results clearly indicate that the mode of action of ML304 and SBI-0797750 in *P. falciparum* blood stages is likely linked to GSH and H_2O_2 homeostasis, which perfectly fits the role of G6PD as a central and essential enzyme for redox balance.

Similarly to *Plasmodium* parasites, host RBCs are dependent on NADPH generation by its own G6PD. It was therefore important to demonstrate that SBI-0797750 did not harm RBCs from either G6PD-normal or G6PD-deficient individuals when the inhibitor was supplemented to cells *ex vivo*. Both mechanisms of RBC damage *in vivo*, hemolysis and phagocytosis, which result in anemia, were not increased by SBI-0797750 when added in a relevant concentration.

In conclusion, with the optimization of ML304 to SBI-0797750, we have developed a very potent and selective *Pf*GluPho and *Pv*G6PD inhibitor that gives robust inhibition in *P. falciparum* cellular assays. The excellent selectivity of SBI-0797750 over the human enzyme should result in a significant therapeutic window. Indeed, SBI-0797750 has great promise as a first-in-class therapeutic, and *in vivo* studies on humanized mouse models are under way to explore this utility. A cross-species effect of our G6PD inhibitor against a range of other parasites will be investigated to determine if this compound may have other applications.

MATERIALS AND METHODS

Drugs and chemicals. All chemicals used were of the highest available purity and were obtained from Roth (Karlsruhe, Germany), Sigma-Aldrich (Steinheim, Germany), or Merck (Darmstadt, Germany). RPMI 1640 medium was purchased from Gibco (Paisley, United Kingdom), chloroquine (CQ) and artesunate (ATS) from Sigma-Aldrich (Steinheim, Germany), methylene blue (MB) and artemisinin (ART) from Roth (Karlsruhe, Germany), and SYBR green I from Thermo Scientific (Schwerte, Germany). SBI-0797750 was prepared in a fashion similar to that described for ML304 (19). Stock solutions of SBI-0797750, MB, and ART were prepared in dimethyl sulfoxide (DMSO); CQ was dissolved in double-distilled water (ddH_2O).

Production and purification of recombinant *Pf*GluPho, *Pv*G6PD, and *Hs*G6PD. The recombinant enzymes used for kinetic characterization of SBI-0797750 were produced as described by Jortzik et al. (15). Since the recombinant production of full-length *Pv*GluPho remained challenging, we used the isolated *Pv*G6PD domain, representing the C-terminal part of the bifunctional enzyme (26), to characterize the inhibitory action of SBI-0797750.

Resazurin-/diaphorase-coupled assay. Dose-response curves of SBI-0797750 for *Pf*GluPho, *Pv*G6PD, and *Hs*G6PD were determined as described previously with slight modifications (18). Briefly, various volumes of compound in 100% DMSO (highest final compound concentration of 4 μM for *Pf*GluPho and *Pv*G6PD and 79 μM for *Hs*G6PD) were transferred to 1,536-well plates using an Echo 550 (Labcyte) acoustic dispenser. One volume of enzyme mix (final concentrations, 50 mM Tris [pH 7.5], 0.005% Tween 20, 1 mg mL^{-1} BSA, 0.075 μg mL^{-1} *Pf*GluPho/0.15 μg mL^{-1} *Pv*G6PD/0.15 μg mL^{-1} *Hs*G6PD) was added to all wells using the Multidrop Combi reagent dispenser (Thermo Fisher). To start the reaction, 1 volume substrate mix (final concentrations, 50 mM Tris [pH 7.5], 0.005% Tween 20, 1 mg mL^{-1} bovine serum albumin [BSA], 3.3 mM $MgCl_2$, 1 U mL^{-1} diaphorase, 25/60/140 μM resazurin, 20/30/125 μM G6P, 4/12/6 μM $NADP^+$ for *Pf*GluPho/*Pv*G6PD/*Hs*G6PD) was added to the wells. Substrate mix

without G6P served as a positive control (100% inhibition), and a mix without compound but with additional DMSO served as a negative control (100% activity). The plates were centrifuged at 1,500 rpm for 1 min and incubated in the dark for 2 h. Increasing fluorescence of resorufin was measured at an excitation wavelength of 530 nm and an emission wavelength of 580 nm (ex530/em580) using a ViewLux (PerkinElmer) plate reader. The reaction rate was calculated by dividing the relative fluorescence units (RFU) by time, and IC_{50} values were calculated using CBIS (Chemical and Biological Information Systems [www.cheminnovation.com]).

Orthogonal assay. In order to exclude compounds that interfere with resazurin or diaphorase, IC_{50}s were determined using the orthogonal enzyme assay without coupled resazurin and diaphorase. Plates were prepared as described above. For *Pf*GluPho and *Pv*G6PD, a 4 μM concentration of the highest compound concentration was used; for *Hs*G6PD, 99 μM was used. The enzyme mix contained 0.05 μg mL^{-1} *Pf*GluPho, 0.025 μg mL^{-1} *Pv*G6PD, and 0.0045 μg mL^{-1} *Hs*G6PD. The reaction was started by adding the substrate mix described above but without resazurin and diaphorase. After centrifuging the plates, NADPH production was monitored at ex350/em460 over 45 min with a PHERAstar multiwell plate reader. IC_{50}s were calculated as described above.

Mechanism of inhibition. SBI-0797750 was mechanistically characterized as described previously with slight modifications (17). Plates and *Pf*GluPho concentrations were prepared as described above using the orthogonal assay with substrate and enzyme mix. To determine the mode of inhibition, either G6P or $NADP^+$ were titrated at various constant concentrations against different compound concentrations, keeping the second substrate in saturation (200 μM). Measurement without adding substrate served as a positive control. Increasing NADPH fluorescence was monitored as described for the orthogonal assay. The relationship between initial velocity (v_0) and substrate concentrations ([S]) at various constant compound concentrations was analyzed by replotting the data in a Lineweaver-Burk plot and calculating $1/K_m$ and $1/V_{max}$ values with the GraphPad Prism 8 software (GraphPad, San Diego, CA, USA) to determine the compound mode of inhibition (competitive or mixed type).

Reversibility of the inhibition. The reversibility of the *Pf*GluPho inhibition by SBI-0797750 was tested by incubating the enzyme with high compound concentrations, followed by dilution to a compound concentration below the IC_{50} and subsequent determination of the enzyme activity. In detail, 1.65 μM *Pf*GluPho was incubated with 1.65 μM SBI-0797750 for 10 min at 22°C. Afterward, the enzyme-inhibitor mixture was diluted to a compound concentration below IC_{50} (3.3 nM) and again incubated for 10 min at 22°C to allow dissociation. Afterward, $NADP^+$ and G6P were added to start the reaction, either at substrate saturation (200 μM) or at concentrations close to the K_m (6.5 μM $NADP^+$, 19 μM G6P). For comparison, controls containing either no inhibitor (100% activity) or inhibitor at the concentration remaining after dilution were prepared. NADPH production was monitored at ex340 using the Tecan Infinite M200 plate reader (Tecan, Maennedorf, Switzerland) in 96-well plates. Specific activities were calculated from reaction rates. Inhibition was considered irreversible if the activity of the sample after dilution was significantly below the activity of the controls. Inhibition was considered reversible if the activity of the sample was equal to that of the controls.

Cloning and heterologous overexpression of the hGrx1-roGFP2, roGFP2-Orp1, and Mito-roGFP2-Orp1 constructs. The genetically encoded ratiometric sensor of the intracellular redox potential, hGrx1-roGFP2, was previously genomically integrated and stably expressed in NF54-*attB* parasites by using the pDC2-CAM-*attP* expression vector (21). Heterologous overexpression of hGrx1-roGFP2 to evaluate the *in vitro* interactions of SBI-0797750 and antimalarial drugs with the recombinant redox probe was performed according to Kasozi et al. (28). The genetically encoded ratiometric sensor of cytosolic H_2O_2 metabolism roGFP2-Orp1 and the mitochondrion-targeted sensor Mito-roGFP2-Orp1 were recently stably expressed in NF54-*attB* parasites by using the pDC2-CAM-*attP* expression vector (22). Heterologous overexpression of roGFP2-Orp1 to evaluate the *in vitro* interactions of SBI-0797750 and antimalarial drugs with the recombinant redox probe was performed according to Rahbari et al. (29).

Cultivation and transfection of *P. falciparum*. The CQ-sensitive *P. falciparum* 3D7 and NF54-*attB* strains were cultivated and transfected according to Kasozi et al. (28) and Rahbari et al. (22), respectively. Briefly, the strains were propagated in A+ RBCs in RPMI 1640 medium supplemented with 0.5% (wt/vol) Albumax, 9 mM glucose, 0.2 mM hypoxanthine, 2.1 mM L-glutamine, 25 mM HEPES, and 22 μg mL^{-1} gentamicin at 3.3% hematocrit and 37°C in a gaseous mixture consisting of 3% O_2, 3% CO_2, and 94% N_2. Deviating from that, NF54 parasites for the gametocyte assays were cultured in O+ RBCs at 10% hematocrit with 10% human serum instead of Albumax. *Plasmodium falciparum* parasites were synchronized with sorbitol and Percoll treatment (30, 31). To generate pure gametocyte cultures, prior to induction of sexual commitment, highly synchronous asexual parasites were seeded into multiple T75 flasks at a starting parasitemia of 0.06%, followed by daily medium changes of half the culture volume. Sexual commitment was induced on day 5 postsetup by doubling the medium volume (32, 33). Subsequently, medium was changed daily, with fresh medium containing 50 mM *N*-acetyl-D-glucosamine (GluNAc) to prevent asexual parasite development (34). The cultures were maintained for 8 to 10 days until pure gametocyte cultures were observed and were again enriched with Percoll for follow-up experiments. *P. falciparum* trophozoites were enriched via magnetic separation (35). Cell lysates were obtained via saponin lysis (36). Parasitemia was counted on Giemsa-stained blood smears.

***In vitro* activity of SBI-0797750 against *P. falciparum* 3D7 and NF54-*attB* asexual parasites.** Parasite growth inhibition was studied, and the half maximal effective concentration (EC_{50}) of antimalarial drugs or compounds against *P. falciparum* was calculated using either the [^{3}H]hypoxanthine incorporation assay according to Kasozi et al. (28) or the SYBR green I-based fluorescence assay for parasite nucleic acids according to Ekland et al. (37) in 96-well format with modifications. For the [^{3}H]hypoxanthine assay, the DMSO-diluted compounds were serially double diluted in hypoxanthine-free medium in

96-well microtiter plates. Synchronized ring-stage parasites in hypoxanthine-free complete medium were added to each well (0.15% parasitemia, 1.25% final hematocrit) and incubated for 48 h under cell culture conditions. Negative-control wells contained only RBCs, and positive-control wells contained only infected RBCs (iRBCs). Afterward, [^{3}H]hypoxanthine was added at a final concentration of 0.5 μCi/well, and the plate further incubated for 24 h. Plates were then frozen at −80°C for at least 1 h and thawed, and cells were harvested on glass fiber filters. After drying, the radioactivity in counts per minute from each well was measured and calculated proportional to the growth of *P. falciparum* in comparison to RBCs and iRBCs.

For SYBR green I assays, the DMSO-diluted compounds were serially double diluted in complete medium in 96-well microtiter plates. Synchronized ring-stage parasites in complete medium were added to each well (0.15% parasitemia, 1.25% final hematocrit) and incubated for 48 h (NF54-attB) or 44 h (3D7) at 37°C. Then, 20 μL of 5× SYBR green (10,000× stock solution) in lysis buffer (20 mM Tris-HCl, 5 mM EDTA, 0.16% [wt/vol] saponin, and 1.6% [vol/vol] Triton X-100) were added to each well and incubated in the dark for 24 h at room temperature (RT). Fluorescence was measured in the Clariostar plate reader at ex494/em530. For EC_{50} calculation, the percent growth inhibition was plotted against the log drug concentration using GraphPad Prism 8 software (GraphPad, San Diego, CA, USA).

***In vitro* activity of SBI-0797750 against *P. falciparum* NF54 gametocytes.** To test SBI-0797750 on *P. falciparum* NF54 gametocytes, sexual commitment was first induced as described above. At 9 to 11 days after induction of sexual commitment, when pure gametocyte cultures were observed, similar numbers of the mature stage V gametocytes were plated in 96-well plates. DMSO-diluted SBI-0797750 stock was serially double diluted in medium and added to each well. Each 96-well plate per experiment contained at least four wells that were cultured without drugs (positive control), three wells of DMSO-only controls, and a varying number of duplicate wells with decreasing concentrations of the inhibitor. Upon addition of the inhibitor, the 96-well plate was left for 3 days without medium change. Subsequently, smears of each well were prepared, Giemsa stained, and counted. The gametocyte numbers of the drug-cultured wells were related to the number of gametocytes observed in the positive control. GraphPad Prism 8 software was used to prepare graphs and calculate EC_{50}s.

***In vitro* characterization of SBI-0797750 using recombinant hGrx1-roGFP2 and roGFP2-Orp1.** SBI-0797750 was used at 10 nM to 1 mM in degassed standard reaction buffer (100 mM potassium phosphate, 1 mM EDTA; pH 7.0). The *in vitro* interaction of the pharmacologically used antimalarial drugs ATS and CQ with the purified hGrx1-roGFP2 protein was previously determined and did not have an effect at the concentrations used in this study (28). For roGFP2-Orp1, ATS and CQ did not affect the fluorescence ratio of the probe either (29). ML304 was measured as described by Haeussler et al. (26). The *in vitro* interactions of hGrx1-roGFP2 and roGFP2-Orp1 with SBI-0797750 were characterized as described by Schuh et al. (21) and Rahbari et al. (22), respectively.

Confocal imaging and image processing. A Leica confocal system TCS SP5 inverted microscope equipped with the objective HCX PL APO 63.0× 1.30 GLYC 37°C UV connected to a 37°C temperature chamber was used. The argon laser power was set to 20%; scanning was performed at a frequency of 400 Hz and a resolution of 512 by 512 pixels. The smart gain and smart offset were 950 V and −0.9%, respectively. With a sequential scan, we excited the hGrx1-roGFP2 and roGFP2-Orp1/Mito-roGFP2-Orp1 probes at 405 nm and 488 nm and detected emission at 500 to 550 nm. Laser intensity was adjusted to match the full dynamic range of the probe to the dynamic range of the detector (hGrx1-roGFP2: 405 nm, 10%; 488 nm, 4%; roGFP2-Orp1: 405 nm, 10%; 488 nm, 4%; Mito-roGFP2-Orp1: 405 nm, 10%; 488 nm, 5%). Autofluorescence images were simultaneously taken at ex405/em430 to 450 and were individually defined together with the background for every image, but no fluorescence signal could be detected. Leica LAS AF Lite software for fluorescence analysis was used. The 405/488-nm ratio was calculated. The graphs were plotted using GraphPad Prism 8 software (GraphPad, San Diego, CA, USA). For imaging, only parasites showing fluorescent signals at both 405 and 488 nm excitation and an intact host cell were chosen.

Effect of SBI-0797750 and other antimalarials on glutathione and H_2O_2 redox homeostasis. The effect of ML304, its derivative SBI-0797750, and the antimalarial drugs ATS and CQ as reference drugs on *P. falciparum* were investigated in 4 h and 24 h of incubation experiments. The EC_{50} of ATS (4.2 nM), CQ (6.9 nM), and ML304 (1.7 μM) on NF54-*attB* parasites were determined previously (22). Trophozoite stage parasites (26 to 30 h post invasion) of NF54-*attB*$^{[hGrx1\text{-}roGFP2]}$, NF54-*attB*$^{[roGFP2\text{-}Orp1]}$, and NF54-*attB*$^{[Mito\text{-}roGFP2\text{-}Orp1]}$ (6 to 8% parasitemia) were treated with different SBI-0797750, ML304, ATS, and CQ concentrations (1× to 100× EC_{50}) for 4 h. Subsequently, free thiol groups were blocked with 2 mM *N*-ethylmaleimide (NEM) for 15 min at 37°C. The parasites were magnetically enriched (Miltenyi Biotec, Germany) and returned to cell culture for at least 1 h to recover. For 24 h experiments, a 5-mL culture (5% hematocrit, 6 to 8% parasitemia) of ring-stage parasites (6 to 10 h postinvasion) was treated with different concentrations of SBI-0797750, ML304, ATS, and CQ (1× to 100× EC_{50}). Prior to enrichment, cysteines were blocked with 2 mM NEM for 15 min at 37°C. Enriched parasites were returned to cell culture to recover for at least 1 h. Thereafter, cells were washed and resuspended in Ringer's solution (122.5 mM NaCl, 5.4 mM KCl, 1.2 mM $CaCl_2$, 0.8 mM $MgCl_2$, 11 mM D-glucose, 25 mM HEPES, 1 mM NaH_2PO_4; pH 7.4). Fifty microliters of cells were seeded onto poly-L-lysine-coated μ-slides with 18 wells (flat) (Ibidi, Martinsried, Germany) and measured using CLSM (confocal laser scanning microscopy) with excitation wavelengths of 405 nm and 488 nm. All experiments included nontreated parasites as controls and both fully reduced and fully oxidized parasites with 10 mM dithiothreitol (DTT) and 1 mM diamide (DIA), respectively (2 min incubation), prior to blocking with NEM. Each experiment was carried out three times. Between 10 and 20 microscopy images were taken each time, resulting in at least 30 experimental values per concentration and incubation time. Means and errors (indicated as standard deviations [SD]) are shown. A one-way analysis of variance (ANOVA) with 95% confidence

intervals with Dunnett's multiple-comparison test (GraphPad Prism 8 software; GraphPad, San Diego, CA, USA) was applied for statistical analysis of significance. OxD of the glutathione redox sensor was calculated as follows:

$$\mathrm{OxD} = \frac{R - R_{\mathrm{red}}}{\frac{I485_{\mathrm{ox}}}{I485_{\mathrm{red}}}(R_{\mathrm{ox}} - R) + (R - R_{\mathrm{red}})}$$

R represents the 405/488 nm fluorescence ratio, R_{red} and R_{ox} are the 405/488-nm fluorescence ratios of fully reduced or fully oxidized parasites, $I485_{ox}$ represents the fluorescence intensity (FI) at 488 nm for fully oxidized parasites, and $I485_{red}$ is the FI at 488 nm for fully reduced parasites.

Treatment of RBCs with *Pf*GluPho inhibitor SBI-0797750 and *Hs*G6PD inhibitor CB83. This study was carried out in accordance with the Declaration of Helsinki and authorized by the local ethical committee. Blood samples were collected in heparin-containing vacutainers from G6PD-normal and -deficient adult donors after confirmed consent. RBCs were washed three times with phosphate-buffered saline containing 10 mM glucose (PBS-G) to deplete white blood cells and platelets. Cells were sedimented at 1,200 $\times$ *g* for 5 min after each washing step. A final washing step was performed in incubation buffer (50 mM HEPES, pH 7.4, supplemented with 110 mM NaCl, 5 mM KCl, 1 mM $MgCl_2$, 1 mM NaH_2PO_4, 20 mM glucose). RBCs were sedimented at 2,700 $\times$ *g* for 5 min. The cell pellet was resuspended in incubation buffer at a hematocrit of 40% and incubated in a humidified CO_2-air incubator at 37°C for recovery. After 1 h, an aliquot of RBC suspension was further diluted with incubation buffer to 2% hematocrit. Cell suspensions of 2 and 40% hematocrit were aliquoted and incubated with increasing concentrations of SBI-0797750 (between 5 nM and 20 μM; 1$\times$ to 4,000$\times$ IC_{50} against *Pf*GluPho) and CB83 (between 400 nM and 50 μM; 1$\times$ to 125$\times$ IC_{50} against *Hs*G6PD) (23). Inhibitor substances were first dissolved in DMSO to obtain 10 mM stock solutions. Before addition to the RBC suspension, the inhibitors were further diluted in PBS to obtain suitable working concentrations. Nontreated controls without inhibitor (0 nM) were instead supplemented with equivalent amounts of DMSO. The incubation of RBC suspension was performed under gentle movement in a CO_2-air cell incubator at 37°C for 24 h. Aliquots of incubated suspensions were taken at 1 and 24 h for analysis of GSH, hemolysis, and phagocytosis and at 2 h for diamide challenge.

Effect of SBI-0797750 and the *Hs*G6PD inhibitor CB83 on reduced GSH and recovery from oxidative stress with diamide in RBCs. Aliquots were taken from RBCs suspended at a hematocrit of 40% and incubated with different inhibitor concentrations for 1 and 24 h to determine the effect of the G6PD inhibitors on GSH oxidation. A colorimetric assay of GSH in RBCs was run with Ellman's reagent after precipitation of high-molecular-weight thiols with metaphosphoric acid as described by Beutler (38). Optical density (OD) was determined at 412 nm. GSH was measured in duplicate, and values were calculated as μmol/mL packed RBCs. These values were normalized to the GSH concentration in RBCs of the respective donor incubated in parallel without inhibitor supplementation (0 nM). Additionally, the effect of SBI-0797750 on GSH recovery was tested in RBCs, which were oxidatively challenged with diamide. For this, RBCs were preincubated with or without 2 μM SBI-0797750 (400$\times$ IC_{50} against *Pf*GluPho) at 40% hematocrit in a CO_2-air cell incubator at 37°C for 2 h. Thereafter, cells were placed on ice and supplemented with 0.5 and 1 mM diamide (final concentrations in G6PD-deficient and G6PD-normal RBC suspensions, respectively) at time zero (0 min). RBC suspensions were kept for 3 min on ice and then transferred to 37°C for another 2 h to monitor the recovery of reduced glutathione. Aliquots of the suspension were taken at 0, 3, 30, 60, and 120 min for GSH quantification. The values from RBCs of 5 G6PD-normal and 8 G6PD-deficient donors are presented as means and standard errors (SE). Statistical significance was calculated with a nonparametric Mann-Whitney test.

Effect of SBI-0797750 and the *Hs*G6PD inhibitor CB83 on the hemolysis of nonparasitized G6PD-deficient and G6PD-normal RBCs. Hemolysis was determined by measuring hemoglobin release from incubated RBCs into the supernatant. For this, aliquots from RBC suspensions were taken at 1 and 24 h of incubation and centrifuged at 1,200 $\times$ *g* for 5 min. The collected supernatant was further centrifuged at 16,000 $\times$ *g* for 15 s to sediment cell debris. Aliquots of the clear RBC-free supernatants and of the entire RBC suspension were solubilized in duplicate with 0.1 M NaOH containing 3 mM EDTA and 0.05% (vol/vol). Triton X-100, and hemoglobin content was quantified with heme-dependent luminol-enhanced luminescence (39). The hemolysis rate was calculated by referring the heme content of the RBC-free supernatant to that of respective RBC suspension. Statistical values and analysis were carried out as described above.

Effect of SBI-0797750 and *Hs*G6PD inhibitor CB83 on the phagocytosis of nonparasitized G6PD-deficient and G6PD-normal RBCs by human phagocytes. Treated or nontreated RBCs with increasing concentrations of G6PD inhibitors were used in an *in vitro* phagocytosis assay with human monocytes of the immortalized cell line THP-1 to verify potential damage to RBCs that leads to phagocytosis. Fluorescence-labeled and opsonized RBCs were added to suspend and preactivate THP-1 cells as described by Gallo et al. (40). The occurrence of phagocytosis was assessed via flow cytometry (FACSCalibur; BD Biosciences, Franklin Lakes, NJ, USA), quantifying fluorescence-positive THP-1 cells and the intensity of fluorescence per phagocyte. Both parameters mirror the vulnerability of RBCs for phagocytosis. To standardize the phagocyte activity between different experiments, IgG-anti-D-opsonized RBCs were included as a positive phagocytosis control, and phagocytosis values can be referred to this internal cellular standard (40). Statistical values and analysis were carried out as described above.

SUPPLEMENTAL MATERIAL

Supplemental material is available online only.

SUPPLEMENTAL FILE 1, PDF file, 0.2 MB.

ACKNOWLEDGMENTS

This work was supported by NIH grant R01AI104916 to L.B. and A.B.P. and in part by an NIH Molecular Libraries grant (U54HG005033) to the Conrad Prebys Center for Chemical Genomics at the Sanford Burnham Medical Research Institute, one of the comprehensive centers of the NIH Molecular Libraries Probe Production Centers Network (MLPCN) during the 2008 to 2014 term of the NIH Molecular Libraries Program production phase. The Hessian LOEWE Center DRUID (project B3) and the German Research Foundation (grant BE1540/23-2 within the DFG Priority Program 1710 on Thiol Switches) also supported this work.

We thank Siegrid Franke for her excellent technical assistance. We thank David A. Fidock for sharing the NF54-*attB* strain with us.

REFERENCES

1. WHO. 2020. World Malaria Report 2020. https://www.who.int/publications/i/item/9789240015791.
2. Cowman AF, Healer J, Marapana D, Marsh K. 2016. Malaria: biology and disease. Cell 167:610–624. https://doi.org/10.1016/j.cell.2016.07.055.
3. Naing C, Whittaker MA, Nyunt Wai V, Mak JW. 2014. Is Plasmodium vivax malaria a severe malaria?: a systematic review and meta-analysis. PLoS Negl Trop Dis 8:e3071. https://doi.org/10.1371/journal.pntd.0003071.
4. WHO. 2017. World malaria report 2017. http://apps.who.int/iris/bitstream/handle/10665/259492/9789241565523-eng.pdf;jsessionid=5AC595247B17EBAC2AA1EE5F4BD070CB?sequence=1.
5. Mbengue A, Bhattacharjee S, Pandharkar T, Liu H, Estiu G, Stahelin RV, Rizk SS, Njimoh DL, Ryan Y, Chotivanich K, Nguon C, Ghorbal M, Lopez-Rubio J-J, Pfrender M, Emrich S, Mohandas N, Dondorp AM, Wiest O, Haldar K. 2015. A molecular mechanism of artemisinin resistance in Plasmodium falciparum malaria. Nature 520:683–687. https://doi.org/10.1038/nature14412.
6. Mok S, Ashley EA, Ferreira PE, Zhu L, Lin Z, Yeo T, Chotivanich K, Imwong M, Pukrittayakamee S, Dhorda M, Nguon C, Lim P, Amaratunga C, Suon S, Hien TT, Htut Y, Faiz MA, Onyamboko MA, Mayxay M, Newton PN, Tripura R, Woodrow CJ, Miotto O, Kwiatkowski DP, Nosten F, Day NPJ, Preiser PR, White NJ, Dondorp AM, Fairhurst RM, Bozdech Z. 2015. Drug resistance. Population transcriptomics of human malaria parasites reveals the mechanism of artemisinin resistance. Science 347:431–435. https://doi.org/10.1126/science.1260403.
7. Cappellini MD, Fiorelli G. 2008. Glucose-6-phosphate dehydrogenase deficiency. Lancet 371:64–74. https://doi.org/10.1016/S0140-6736(08)60073-2.
8. Gómez-Manzo S, Marcial-Quino J, Vanoye-Carlo A, Serrano-Posada H, Ortega-Cuellar D, González-Valdez A, Castillo-Rodríguez RA, Hernández-Ochoa B, Sierra-Palacios E, Rodríguez-Bustamante E, Arreguin-Espinosa R. 2016. Glucose-6-phosphate dehydrogenase: update and analysis of new mutations around the world. Int J Mol Sci 17:2069. https://doi.org/10.3390/ijms17122069.
9. Arese P, Turrini F, Schwarzer E. 2005. Band 3/complement-mediated recognition and removal of normally senescent and pathological human erythrocytes. Cell Physiol Biochem 16:133–146. https://doi.org/10.1159/000089839.
10. Cappadoro M, Giribaldi G, O'Brien E, Turrini F, Mannu F, Ulliers D, Simula G, Luzzatto L, Arese P. 1998. Early phagocytosis of glucose-6-phosphate dehydrogenase (G6PD)-deficient erythrocytes parasitized by Plasmodium falciparum may explain malaria protection in G6PD deficiency. Blood 92:2527–2534. https://doi.org/10.1182/blood.V92.7.2527.2527_2527_2534.
11. Howes RE, Battle KE, Satyagraha AW, Baird JK, Hay SI. 2013. G6PD deficiency: global distribution, genetic variants and primaquine therapy. Adv Parasitol 81:133–201. https://doi.org/10.1016/B978-0-12-407826-0.00004-7.
12. Ashley EA, Pyae Phyo A, Woodrow CJ. 2018. Malaria. Lancet 391:1608–1621. https://doi.org/10.1016/S0140-6736(18)30324-6.
13. Jortzik E, Becker K. 2012. Thioredoxin and glutathione systems in Plasmodium falciparum. Int J Med Microbiol 302:187–194. https://doi.org/10.1016/j.ijmm.2012.07.007.
14. Preuss J, Jortzik E, Becker K. 2012. Glucose-6-phosphate metabolism in Plasmodium falciparum. IUBMB Life 64:603–611. https://doi.org/10.1002/iub.1047.
15. Jortzik E, Mailu BM, Preuss J, Fischer M, Bode L, Rahlfs S, Becker K. 2011. Glucose-6-phosphate dehydrogenase-6-phosphogluconolactonase: a unique bifunctional enzyme from Plasmodium falciparum. Biochem J 436:641–650. https://doi.org/10.1042/BJ20110170.
16. Allen SM, Lim EE, Jortzik E, Preuss J, Chua HH, MacRae JI, Rahlfs S, Haeussler K, Downton MT, McConville MJ, Becker K, Ralph SA. 2015. Plasmodium falciparum glucose-6-phosphate dehydrogenase 6-phosphogluconolactonase is a potential drug target. FEBS J 282:3808–3823. https://doi.org/10.1111/febs.13380.
17. Preuss J, Hedrick M, Sergienko E, Pinkerton A, Mangravita-Novo A, Smith L, Marx C, Fischer E, Jortzik E, Rahlfs S, Becker K, Bode L. 2012. High-throughput screening for small-molecule inhibitors of Plasmodium falciparum glucose-6-phosphate dehydrogenase 6-phosphogluconolactonase. J Biomol Screen 17:738–751. https://doi.org/10.1177/1087057112442382.
18. Preuss J, Maloney P, Peddibhotla S, Hedrick MP, Hershberger P, Gosalia P, Milewski M, Li YL, Sugarman E, Hood B, Suyama E, Nguyen K, Vasile S, Sergienko E, Mangravita-Novo A, Vicchiarelli M, McAnally D, Smith LH, Roth GP, Diwan J, Chung TDY, Jortzik E, Rahlfs S, Becker K, Pinkerton AB, Bode L. 2012. Discovery of a Plasmodium falciparum glucose-6-phosphate dehydrogenase 6-phosphogluconolactonase inhibitor (R,Z)-N-((1-ethylpyrrolidin-2-yl)methyl)-2-(2-fluorobenzylidene)-3-oxo-3,4-dihydro-2H-benzob1,4thiazine-6-carboxamide (ML276) that reduces parasite growth in vitro. J Med Chem 55:7262–7272. https://doi.org/10.1021/jm300833h.
19. Maloney P, Hedrick M, Peddibhotla S, Hershberger P, Milewski M, Gosalia P, Li L, Preuss J, Sugarman E, Hood B, Suyama E, Nguyen K, Vasile S, Sergienko E, Salanawil S, Stonich D, Su Y, Dahl R, Mangravita-Novo A, Vicchiarelli M, McAnally D, Smith LH, Roth G, Diwan J, Chung TD, Pinkerton Ab Bode L, Becker K. 2010. Probe Reports from the NIH Molecular Libraries Program. A 2nd selective inhibitor of Plasmodium falciparum glucose-6-phosphate dehydrogenase (PfG6PDH)—probe 2. NIH, Bethesda, MD.
20. Haeussler K. 2019. Characterization and inhibition of NADPH-producing enzymes from the pentose phosphate pathway of Plasmodium parasites. Doctoral thesis. Justus-Liebig-Universität Gießen, Giessen, Germany.
21. Schuh AK, Rahbari M, Heimsch KC, Mohring F, Gabryszewski SJ, Weder S, Buchholz K, Rahlfs S, Fidock DA, Becker K. 2018. Stable integration and comparison of hGrx1-roGFP2 and sfroGFP2 redox probes in the malaria parasite Plasmodium falciparum. ACS Infect Dis 4:1601–1612. https://doi.org/10.1021/acsinfecdis.8b00140.
22. Rahbari M, Rahlfs S, Przyborski JM, Schuh AK, Hunt NH, Fidock DA, Grau GE, Becker K. 2017. Hydrogen peroxide dynamics in subcellular compartments of malaria parasites using genetically encoded redox probes. Sci Rep 7:10449. https://doi.org/10.1038/s41598-017-10093-8.
23. Preuss J, Richardson AD, Pinkerton A, Hedrick M, Sergienko E, Rahlfs S, Becker K, Bode L. 2013. Identification and characterization of novel human glucose-6-phosphate dehydrogenase inhibitors. J Biomol Screen 18:286–297. https://doi.org/10.1177/1087057112462131.

24. Becker K, Tilley L, Vennerstrom JL, Roberts D, Rogerson S, Ginsburg H. 2004. Oxidative stress in malaria parasite-infected erythrocytes: host-parasite interactions. Int J Parasitol 34:163–189. https://doi.org/10.1016/j.ijpara.2003.09.011.
25. Uyoga S, Skorokhod OA, Opiyo M, Orori EN, Williams TN, Arese P, Schwarzer E. 2012. Transfer of 4-hydroxynonenal from parasitized to non-parasitized erythrocytes in rosettes. Proposed role in severe malaria anemia. Br J Haematol 157:116–124. https://doi.org/10.1111/j.1365-2141.2011.09015.x.
26. Haeussler K, Berneburg I, Jortzik E, Hahn J, Rahbari M, Schulz N, Preuss J, Zapol'skii VA, Bode L, Pinkerton AB, Kaufmann DE, Rahlfs S, Becker K. 2019. Glucose 6-phosphate dehydrogenase 6-phosphogluconolactonase: characterization of the Plasmodium vivax enzyme and inhibitor studies. Malar J 18:22. https://doi.org/10.1186/s12936-019-2651-z.
27. Siciliano G, Santha Kumar TR, Bona R, Camarda G, Calabretta MM, Cevenini L, Davioud-Charvet E, Becker K, Cara A, Fidock DA, Alano P. 2017. A high susceptibility to redox imbalance of the transmissible stages of Plasmodium falciparum revealed with a luciferase-based mature gametocyte assay. Mol Microbiol 104:306–318. https://doi.org/10.1111/mmi.13626.
28. Kasozi D, Mohring F, Rahlfs S, Meyer AJ, Becker K. 2013. Real-time imaging of the intracellular glutathione redox potential in the malaria parasite Plasmodium falciparum. PLoS Pathog 9:e1003782. https://doi.org/10.1371/journal.ppat.1003782.
29. Rahbari M, Rahlfs S, Jortzik E, Bogeski I, Becker K. 2017. H2O2 dynamics in the malaria parasite Plasmodium falciparum. PLoS One 12:e0174837. https://doi.org/10.1371/journal.pone.0174837.
30. Lambros C, Vanderberg JP. 1979. Synchronization of Plasmodium falciparum erythrocytic stages in culture. J Parasitol 65:418–420. https://doi.org/10.2307/3280287.
31. Wahlgren M, Berzins K, Perlmann P, Björkman A. 1983. Characterization of the humoral immune response in Plasmodium falciparum malaria. I. Estimation of antibodies to P falciparum or human erythrocytes by means of microELISA. Clin Exp Immunol 54:127–134.
32. Buchholz K, Burke TA, Williamson KC, Wiegand RC, Wirth DF, Marti M. 2011. A high-throughput screen targeting malaria transmission stages opens new avenues for drug development. J Infect Dis 203:1445–1453. https://doi.org/10.1093/infdis/jir037.
33. Fivelman QL, McRobert L, Sharp S, Taylor CJ, Saeed M, Swales CA, Sutherland CJ, Baker DA. 2007. Improved synchronous production of Plasmodium falciparum gametocytes in vitro. Mol Biochem Parasitol 154:119–123. https://doi.org/10.1016/j.molbiopara.2007.04.008.
34. Gupta SK, Schulman S, Vanderberg JP. 1985. Stage-dependent toxicity of N-acetyl-glucosamine to Plasmodium falciparum. J Protozool 32:91–95. https://doi.org/10.1111/j.1550-7408.1985.tb03020.x.
35. Paul F, Roath S, Melville D, Warhurst DC, Osisanya JO. 1981. Separation of malaria-infected erythrocytes from whole blood: use of a selective high-gradient magnetic separation technique. Lancet ii:70–71. https://doi.org/10.1016/s0140-6736(81)90414-1.
36. Orjih AU. 1994. Saponin haemolysis for increasing concentration of Plasmodium falciparum infected erythrocytes. Lancet 343:295. https://doi.org/10.1016/s0140-6736(94)91142-8.
37. Ekland EH, Schneider J, Fidock DA. 2011. Identifying apicoplast-targeting antimalarials using high-throughput compatible approaches. FASEB J 25:3583–3593. https://doi.org/10.1096/fj.11-187401.
38. Beutler E. 1975. Red cell metabolism. A manual of biochemical methods, 2nd ed. Grune & Stratton, New York, NY.
39. Schwarzer E, Turrini F, Arese P. 1994. A luminescence method for the quantitative determination of phagocytosis of erythrocytes, of malaria-parasitized erythrocytes and of malarial pigment. Br J Haematol 88:740–745. https://doi.org/10.1111/j.1365-2141.1994.tb05112.x.
40. Gallo V, Skorokhod OA, Schwarzer E, Arese P. 2012. Simultaneous determination of phagocytosis of Plasmodium falciparum-parasitized and non-parasitized red blood cells by flow cytometry. Malar J 11:428. https://doi.org/10.1186/1475-2875-11-428.

3.2. Publication II

Crystal structure of *Leishmania donovani* glucose 6-phosphate dehydrogenase reveals a unique N-terminal domain

Berneburg I, Rahlfs S, Becker K & Fritz-Wolf K

Communic Biol 5, 1353

2023

https://doi.org/10.1038/s42003-022-04307-7

communications biology

ARTICLE

https://doi.org/10.1038/s42003-022-04307-7 OPEN

Crystal structure of *Leishmania donovani* glucose 6-phosphate dehydrogenase reveals a unique N-terminal domain

Isabell Berneburg [1], Stefan Rahlfs[1], Katja Becker[1] & Karin Fritz-Wolf [1,2]✉

Since unicellular parasites highly depend on NADPH as a source for reducing equivalents, the pentose phosphate pathway, especially the first and rate-limiting NADPH-producing enzyme glucose 6-phosphate dehydrogenase (G6PD), is considered an excellent antitrypanosomatid drug target. Here we present the crystal structure of *Leishmania donovani* G6PD (*Ld*G6PD) elucidating the unique N-terminal domain of *Kinetoplastida* G6PDs. Our investigations on the function of the N-domain suggest its involvement in the formation of a tetramer that is completely different from related *Trypanosoma* G6PDs. Structural and functional investigations further provide interesting insights into the binding mode of *Ld*G6PD, following an ordered mechanism, which is confirmed by a G6P-induced domain shift and rotation of the helical N-domain. Taken together, these insights into *Ld*G6PD contribute to the understanding of G6PDs' molecular mechanisms and provide an excellent basis for further drug discovery approaches.

[1] Biochemistry and Molecular Biology, Interdisciplinary Research Center, Justus Liebig University, Giessen, Germany. [2] Max Planck Institute for Medical Research, Heidelberg, Germany. ✉email: Karin.Fritz-Wolf@ernaehrung.uni-giessen.de

The vector-borne infectious disease leishmaniasis is one of 20 poverty-related, neglected tropical diseases. It is caused by the protozoan parasite of the genus *Leishmania*, belonging to the *Trypanosomatidae* family, and infects 0.7 to one million people with 20,000 to 30,000 deaths annually in tropical, subtropical, and southern European regions. The species *Leishmania donovani* causes the most severe form, often fatal if untreated[1,2]. Currently, there are only a few drugs available for leishmaniasis treatment and after decades of use, resistant strains have emerged[3–5]. Therefore, new drug targets and anti-infective agents with new mechanisms of action are urgently required.

The enzymes of the pentose phosphate pathway (PPP) are considered promising drug targets for controlling trypanosomatids[5–7]. Throughout their life cycle, parasites must withstand the action of reactive oxygen and nitrogen species (ROS/RNS) produced by the host's immune system[8]. To counteract antioxidant defense mechanisms such as the trypanothione-dependent thiol system, which is crucial for redox balance in trypanosomatids, the parasites highly depend on NADPH as the primary electron source[9,10]. The PPP, which is divided into a unidirectional oxidative branch where NADPH is produced, and a non-oxidative branch that ends with ribose 5-phosphate, a crucial product for nucleotide biosynthesis, greatly contributes to the total NADPH pool. The housekeeping enzyme glucose 6-phosphate dehydrogenase (G6PD) (EC 1.1.1.49) is the first and rate-limiting enzyme of the PPP. It catalyzes the oxidation of glucose 6-phosphate (G6P) originating from glycolysis to 6-phospho-D-glucono-1,5-lactone (6PL), whereby the cofactor $NADP^+$ is reduced to NADPH. 6-phosphogluconate dehydrogenase (EC 1.1.1.44), the third enzyme of this oxidative branch generates a second NADPH molecule[10]. In trypanosomatids, the malic enzyme, which uses malate to produce pyruvate and NADPH, provides a second relevant source of NADPH[11,12]. However, RNAi downregulation of G6PD or 6-phosphogluconate dehydrogenase highly reduces the growth of *Trypanosoma brucei* bloodstream parasites, confirming the central role of these enzymes[7,13]. Additionally, some human steroids (e.g., dehydroepiandrosterone, epiandrosterone), have been shown to specifically inhibit *Trypanosoma* G6PDs, resulting in reduced parasite growth and a destroyed redox balance[7,13–15]. Since *Leishmania* promastigotes entering mammalian macrophages are exposed to enormous oxidative stress induced by enzymes such as NADPH oxidase or NO-synthase[16–18], an adequate NADPH pool is even more important for these parasites. Moreover, the mode of action of commonly used antileishmanial drugs such as amphotericin B[19], sodium antimony gluconate[20], and miltefosine[21] is thought to be related to increased ROS production, and resistance to these drugs to an upregulation of the PPP[18]. These results clearly indicate a crucial role of the pentose phosphate pathway enzyme G6PD for *Leishmania* parasite survival and therefore its excellent suitability as a drug target, as previously shown for other unicellular parasites such as *Trypanosoma*[7,13–15] and *Plasmodium*[22–25].

In the present study, we describe the crystal structures of *Leishmania donovani* G6PD (*Ld*G6PD), both native and complexed with one or both substrates. The N-terminal domain, unique to *Kinetoplastida* G6PDs, is fully visible in our *Ld*G6PD wild-type (wt) crystal structures. Two *Ld*G6PD mutants provide interesting insights into the role of the additional N-terminal domain, which seems to be essential for tetramerization. Structural and kinetic investigations further elucidated the substrate binding mode of the enzyme, which seems to follow an ordered mechanism and is also evident through a domain shift due to G6P binding. The reported structural and functional characteristics of *Ld*G6PD provide an excellent basis for further structure-based inhibitor studies and drug optimization.

Results

Oligomerization and kinetic characterization of *Ld*G6PD wt, *Lm*G6PD wt, and mutants. G6PD of *L. donovani* (*Ld*G6PD wt) and *L. major* (*Lm*G6PD), as well as two *Ld*G6PD mutants (*Ld*G6PD^{C138S}, *Ld*G6PD$^{60–562}$), were recombinantly produced (Fig. S1). To investigate the oligomerization behavior of *Leishmania* G6PDs, we performed size exclusion chromatography (SEC) under different conditions (see methods). The SEC profiles of native *Ld*G6PD wt revealed two stable peaks with elution patterns equivalent to tetrameric and dimeric forms of the enzyme, with the dimer peak dominating approximately twofold over the tetramer peak, independently of enzyme concentration (12–300 µM) (Fig. 1). The same elution profile could be observed for native *Lm*G6PD wt. Dimer and tetramer fractions remained in their original conformation when separately collected and reapplied to the SEC column (Fig. S2d). Steady-state kinetics revealed a specific activity of the *Ld*G6PD wt dimer of 200.0 ± 14.1 U mg^{-1}, with apparent K_M values of 54.4 ± 2.8 µM for the substrate G6P and 15.9 ± 1.1 µM for the cosubstrate $NADP^+$. Compared to other

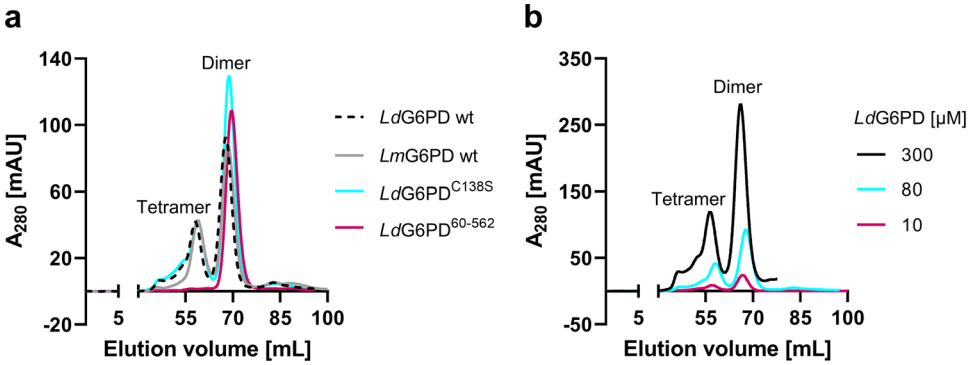

Fig. 1 SEC analysis of recombinant *Ld*G6PD and *Lm*G6PD wt and of *Ld*G6PD mutants under native conditions. Full-length G6PD was gel-filtrated on a HiLoad 16/60 Superdex 200 column pre-equilibrated in buffer A (500 mM NaCl, 50 mM Tris, pH 7.8). **a** The SEC profiles of *Ld*G6PD wt (66.7 kDa) (black dotted, retention volume (rv) 1. peak = 58 mL = 300 kDa, rv 2. peak = 68 mL = 133 kDa) and *Lm*G6PD wt (66.8 kDa) (gray, rv 1. peak = 59 mL = 276 kDa, rv 2. peak = 68 mL = 133 kDa) display two peaks with elution patterns equivalent to a dimer and a tetramer and remained stable in the *Ld*G6PD^{C138S} mutant (66.7 kDa) (blue, rv 1. peak = 59 mL = 276 kDa, rv 2. peak = 68 mL = 133 kDa). The SEC profile of the *Ld*G6PD$^{60-562}$ mutant (60.3 kDa) displays one peak with elution patterns equivalent to a dimer (red, rv = 69 mL = 112 kDa). **b** SEC profiles of *Ld*G6PD wt under different enzyme concentrations, 300 µM (black, rv 1. peak = 56 mL = 341 kDa, 2. Peak = 66 mL = 156 kDa), 80 µM (blue, rv 1. peak = 58 mL = 300 kDa, rv 2. peak = 68 mL = 133 kDa), and 10 µM (red, rv 1. peak = 57 mL = 325 kDa, rv 2. peak = 67 mL = 144 kDa) display two peaks with stable elution patterns equivalent to a dimer and a tetramer. Representative chromatograms ($n \geq 2$) are shown for each condition.

Table 1 Comparative kinetic parameters of recombinant *Ld*G6PD wt and mutants, *Lm*G6PD, *Tc*G6PD, *Pf*GluPho, and *Hs*G6PD.

	G6P				$NADP^+$			
	V_{max} (U · mg^{-1})	K_M (μM)	k_{cat} (s^{-1})	k_{cat}/K_M (μM^{-1} · s^{-1})	V_{max} (U · mg^{-1})	K_M (μM)	k_{cat} (s^{-1})	k_{cat}/K_M (μM^{-1} · s^{-1})
***Ld*G6PD^{Dimer}**	200.0 ± 14.1	54.4 ± 2.8	222.5 ± 15.7	4.1 ± 0.2	204.7 ± 13.3	15.9 ± 1.1	227.7 ± 14.8	14.5 ± 1.6
***Ld*G6PD^{Tetramer}**	189.2 ± 7.7	75.4 ± 5.5	208.1 ± 5.1	2.8 ± 0.2	185.1 ± 12.9	14.2 ± 0.9	203.6 ± 13.6	14.9 ± 3.0
***Ld*G6PD^{C138S}**	228.1 ± 12.5	63.3 ± 2.3	253.6 ± 13.9	4.0 ± 0.1	224.7 ± 13.8	14.6 ± 1.6	249.8 ± 15.3	17.3 ± 0.8
***Ld*G6PD$^{60-562}$**	239.8 ± 10.6	65.4 ± 3.5	240.8 ± 10.6	3.7 ± 0.1	232.7 ± 18.7	14.3 ± 2.2	233.7 ± 18.8	17.0 ± 2.5
***Lm*G6PD**	187.0 ± 2.8	57.9 ± 4.6	208.1 ± 3.1	3.6 ± 0.3	187.7 ± 1.6	11.4 ± 1.5	208.8 ± 1.8	17.9 ± 3.5
***Tc*G6PD**[29,39]	99.4 ± 9.1	77 ± 20	62 ± 3	0.81	99.4 ± 9.1	16 ± 3	52 ± 2	3.3
***Pf*GluPho**[24]	5.9 ± 1.0	20.3 ± 5.6	10.7 ± 1.8	0.53	5.9 ± 0.6	6.1 ± 1.3	10.1 ± 0.9	1.66
***Hs*G6PD**	113.8 ± 6.7	70.1 ± 15.5	118.9 ± 7.0	1.7 ± 0.3	105.8 ± 7.2	22.9 ± 2.8	110.5 ± 7.6	5.0 ± 0.7

Values are expressed as mean ± SD from at least three independent determinations with different enzyme batches; each including at least three measurements.

G6PDs characterized so far, the specific activity is remarkably high, as is the overall catalytic efficiency (Table 1). In contrast, catalytic efficiency of the *Ld*G6PD tetramer was significantly lower as specific activity remained equal, but the apparent K_M for G6P was about 40% higher (75.4 ± 5.5 μM) compared to the dimer fraction. Furthermore, the oligomerization pattern of *Ld*G6PD was neither affected by the presence of substrates nor by varying ionic strength (0.1–1 M NaCl) or pH values (4.8–7.8) (Fig. S2a, b). Nevertheless, very low pHs (4.5) reduced the specific activity by about 40% (114.5 + 8.2 U mg^{-1}). Moreover, neither reductive (5 mM DTT) nor oxidative conditions (2 mM H_2O_2) affected the elution patterns of *Ld*G6PD compared to native conditions (Fig. S2c), suggesting the formation of dimers and tetramers independent from redox status and intermolecular disulfide bonds. In line with that, the kinetic properties of the enzyme were not affected under the same conditions.

Crystallization and structure determination of *Ld*G6PD. We obtained monoclinic and orthorhombic crystals of *Ld*G6PD wt, *Ld*G6PD^{C138S}, and *Ld*G6PD$^{60–562}$ (Table 2). The crystals of the apoenzyme obeyed P121 symmetry with four monomers in the asymmetric unit (AU) and diffracted to 2.8 Å. The *Ld*G6PD wt and *Ld*G6PD^{C138S} crystals in complex with and without its substrate G6P and/or its cofactor NADP(H) crystallized in space group C121 with two monomers in the AU. Crystals containing only NADP(H) diffracted to a resolution up to 1.7 Å, and crystals containing G6P or G6P and NADP(H) to 3.3 Å and 2.5 Å, respectively. The crystal of the truncated mutant *Ld*G6PD$^{60–562}$ obeyed C222 symmetry with one monomer in the AU and diffracted to 1.9 Å.

The structure of the apoenzyme was solved at 2.8 Å resolution via the molecular replacement method, using *Hs*G6PD (PDBID: 5UKW) as a search model. Diffraction data of all other crystals were phased via molecular replacement methods using the structure of the apoenzyme. All data collection and refinement statistics are summarized in Table 2. The electron density of the *Ld*G6PD core, comprising residues 5-470 and 483-552, is well defined in all our structures except two loops comprising residues D50-K64 and T471-D482. These loops have an increased B-factor; in some structures, they are not defined by the electron density (Table S1).

Overall structure of *Ld*G6PD reveals a unique N-domain. Similar to other G6PDs of this family, the *Ld*G6PD dimer (Fig. 2a) adopts the canonical G6PD fold with RMSD values for the dimer core domain of 2.6 Å and 2.1 Å to human (*Hs*G6PD; PDBID: 2BH9) and *Trypanosoma cruzi* G6PD (*Tc*G6PD; PDBID: 5AQ1)[26–29], respectively (Fig. S3). The *Ld*G6PD monomer contains three domains: an N-domain (Q5-K49), the $NADP^+$ binding "Rossmann-like" domain (residues D50-I248), and a β + α domain (residues D249-K552). Each subunit has a discrete active site with an $NADP^+$ and G6P binding domain. The latter is located between the "Rossmann-like" and the β + α domain. The N-domain consists of two α-helices comprising residues Q5-K49 and is linked to the "Rossmann-like" domain via a connecting loop (D50-K64).

The apo form crystallizes in space group P121 with two dimers (AB and CD) in the AU. Via P121 symmetry operation, a tetramer can be formed from each dimer (ABA'B' or CDC'D') (Figs. 2b, c, 3a). In contrast, the *Ld*G6PD wt and the *Ld*G6PD^{C138S} mutant, complexed with NADP(H), G6P, or both substrates, adopt C121 space group symmetry with one dimer in the AU (AB). However, via crystallographic symmetry operation, the same kind of tetramer can be formed as with the apo form (Fig. 3b). Analysis of this tetramer, comprising two AUs, revealed two positions P1 and P2 of the N-domain of subunit B (N^B), which are related by a crystallographic symmetry operation and both located near the main domain of subunit B and B', respectively. In addition, the electron density of the loop D50-K64 (varies depending on the structure, Table S1), connecting the main domain of subunit B to N^B, is very low. Finally, we chose to associate P1 with subunit B and deposited the AU with this content in the PDB (Fig. 2a). The position of N-domain A (N^A) is unambiguous and described below.

As mentioned above, each N-domain comprises two α-helices α1 (~D11-R31) and α2 (~I36-K49) connected with a short loop (Figs. 2, 4). Tetramer contacts between the four subunits (A, B, A', B') exist mainly between the α-helices of the N-domains (Fig. 3). Substrate binding influences the contacts between the subunits and are described in more detail in the following section.

Substrate binding leads to conformational changes and influences tetramer contacts. Superimposing the dimeric apo *Ld*G6PD structure (PDBID: 7ZHT) with the NADP(H)-complexed *Ld*G6PD structures (PDBIDs: 7ZHU, 7ZHY) revealed RMSD values of 1 Å with 982 and 978 residues, respectively. Comparing the apo structure (Figs. 3a, 4a, b) with the structures complexed with G6P, NADP(H) or both substrates (Figs. 3b, 4c, d) reveals a rotation of the N-domain by about 45° upon ligand binding. In contrast to this striking realignment of the N-domains, only marginal differences in the position of the N-domains are evident between the ligand-bound structures.

In the apo structure, the N-domain of subunit A (N^A) interacts with the flexible loop (T471-D482) of both subunits (Fig. 3a). Within subunit A, the helical residues A26^A-E30^A (α1) interact with loop residues Y472^A-Y476^A (Fig. 4a). Residues E30^A-K32^A are bound to the β-strand S442^A-A444^A (β13). Furthermore, the R31^A side chain interacts with E467^A and D469^A (β14). Upon

Table 2 Data collection and refinement statistics.

	*Ld*G6PD wt				*Ld*G6PD$^{60-562}$	*Ld*G6PD^{C138S}	
PDB code	7ZHT	7ZHU	7ZHV	7ZHW	7ZHX	7ZHY	7ZHZ
Ligand	Apo	NADP(H)	G6P	G6P, NADP(H)	NADP(H)	NADP(H)	G6P, NADP(H)
Data collection							
Space group	P 1 2 1	C 1 2 1	C 1 2 1	C 1 2 1	C 2 2 2	C 1 2 1	C 1 2 1
Cell dimensions							
a, *b*, *c* (Å)	117.7, 65.8, 189.2	223.2, 65.7, 119.3	218.7, 67.8, 120.8	215.8, 66.8, 121.0	75.8, 229.7, 83.6	223.2, 65.7, 119.9	218.2, 66.0, 120.0
α, *β*, *γ* (°)	90, 92.4, 90	90, 120.5, 90	90, 121.7, 90	90, 120.7, 90	90, 90, 90	90, 120.8, 90	90, 120.7, 90
Resolution (Å)	39.2–2.8 (2.9–2.8)	48.1–1.7 (1.76–1.7)	44.1–3.1 (3.2–3.1)	49.3–3.3 (3.4–3.3)	47.3–1.9 (2.0–1.9)	47.95–2.0 (2.1–2.0)	48.8–2.5 (2.6–2.5)
R-merge (%)	11.4 (234.7)	4.7 (132.0)	11.5 (424.5)	9.3 (158.3)	5.6 (101.5)	5.7 (96.1)	5.8 (133.4)
$I/\sigma I$	8.6 (0.7)	11.9 (0.6)	6.9 (0.3)	9.8 (1.3)	18.9 (1.7)	12.3 (1.2)	12.0 (1.0)
Completeness (%)	98.1 (97.6)	97.8 (97.2)	96.7 (95.6)	99.1 (98.7)	99.6 (99.2)	99.6 (99.2)	99.4 (98.8)
Redundancy	2.8 (2.9)	2.7 (2.7)	2.9 (3.0)	5.1 (5.2)	5.6 (5.5)	3.5 (3.2)	3.5 (3.3)
Molecules per AU	4	2	2	2	1	2	2
Wilson B-factor	73.9	34.0	133.9	124.8	33.4	40.3	75.6
$CC_{1/2}$ (%)	99.9 (44.6)	99.9 (40.6)	99.8 (25.7)	99.9 (69.7)	99.9 (81.2)	99.9 (54.3)	99.9 (52.2)
Refinement							
Resolution (Å)	2.8	1.7	3.3	3.3	1.9	2.0	2.5
No. reflections	70481	159688	22260	22435	58616	102071	50909
R_{work}/R_{free} (%)	24.4 (42.2)/ 30.4 (46.2)	19.7 (39.4)/ 22.8 (41.6)	25.8 (50.7)/ 31.4 (53.5)	23.6 (44.5)/ 25.8 (44.5)	18.2 (31.3)/ 21.0 (36.1)	18.4 (37.6)/ 21.9 (40.2)	24.9 (50.4)/ 29.8 (50.1)
No. atoms							
Proteins	16027	8591	8342	8457	3826	8481	8344
Ligands	51	283	21	145	99	288	163
Water	26	890	4	1	381	753	25
Protein residues	2023	1077	1055	1069	481	1062	1055
B-factors							
Proteins	91.2	48.8	138.8	144.5	41.3	45.7	92.9
Ligands	98.1	52.9	161.4	169.2	43.5	51.2	111.0
Water	68.6	51.8	84.3	143.6	45.5	47.4	71.0
Ramachandran plot (%)							
Favored (%)	94.2	97.4	97.1	94.7	97.9	97.2	96.3
R. m. s. deviations							
Bonds lengths	0.009	0.007	0.01	0.003	0.009	0.019	0.003
Bond angles	1.71	0.90	1.18	0.62	0.98	1.08	0.67

Values in parentheses are for highest-resolution shell.

substrate binding the contacts to β13 are lost due to the rotation of N^A and the resulting displacement of residues $E30^A$-$K32^A$ (Fig. 4c). However, the flexible loop ($T471^A$-$D482^A$) of subunit A also rearranges, thereby retaining $T474^A$ and $Q27^A$ binding (α1). Due to weak electron density, this interaction is not seen in structures with bound G6P (Table S1). As in a turnstile, the bonds between $R31^A$ and $E467^A$ and $D469^A$ remain intact because the side chains also rearrange.

Additionally, N^A (apo structure) interacts with not only subunit A but also B; the N-terminus of helix $\alpha2^A$ ($Q38^A$) is bonded to the flexible loop residues $T471^B$ and $H473^B$ (Figs. 4a, S4a). The N-domain rotation (N^A) due to substrate binding replaces this contact via hydrophobic interactions between $D34^A$-$D35^A$ and $T474^B$-$R475^B$ (Figs. 4c, S4b). The latter interaction is well defined by the electron density in almost all our structures with bound substrates except those with low resolution (3.3 Å) (Table S1).

As mentioned before, there are two positions P1 and P2 of N-domain N^B, which can be linked to the main domain of subunit B or B', respectively. Linking P1 to subunit B (Fig. 2b), results in no dimeric interactions between N^B and subunit A, but in all our structures there are multiple contacts with the "Rossmann-like" domain of subunit B. In the apo form, $\alpha1^B$ ($A12^B$-$Q27^B$) interacts via van der Waals forces with the helical residues $D117^B$-$W121^B$ ($\alpha4^B$) and $E135^B$-$E141^B$ ($\alpha5^B$) (Fig. 4b). Upon substrate binding and the resulting rotation of N^B, the interactions are visible between the helical residues $G19^B$-$A26^B$ ($\alpha1^B$), $H123^B$-$K128^B$ ($\alpha4^B$) and $E141^B$ ($\alpha5^B$) (Fig. 4d). Furthermore, $Q27^B$ is hydrogen-bonded to $S134^B$. Tetramer contacts between the four subunits (A, B, A', B') exist mainly between the α-helices of the N-domains (Figs. 2b and 3). Remarkably, there is one additional tetrameric contact, formed between N^B ($Q48^B$–$K49^B$) and the flexible loop ($Y476^{B'}$-$D477^{B'}$) of subunit B' and vice versa.

If we connect position P2 of N-domain N^B to subunit B, the above-described dimeric interactions with the "Rossmann-like" domain would take place between N^B and subunit B' and would therefore be tetrameric interactions (Fig. 2c). However, the interactions between residues $Q48^B$-$K49^B$ and loop residues $Y476^B$-$D477^B$ would occur only within subunit B, rather than between two dimers as in the association of P1 to subunit B (Fig. 3b). Moreover, linking P2 to subunit B results in very fragile connections between the N- and the main domain. The connection would be via loop residues $Q48^B$-$K64^B$ and $Y476^B$-$D477^B$ (Fig. 3b), which show increased B-factors or are disordered in some structures (Table S1). For these reasons, we consider it more likely that P1 and not P2 of N-domain N^B is associated with subunit B.

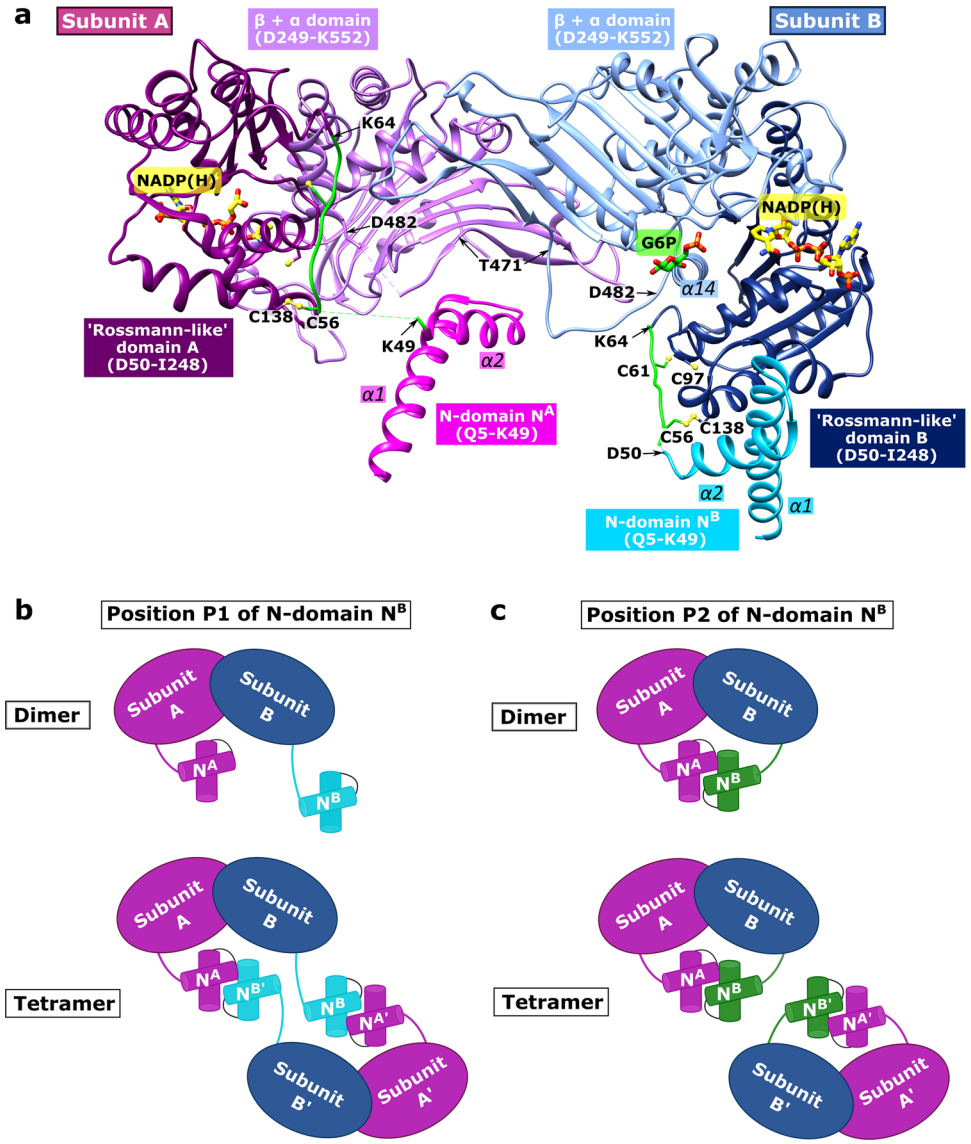

Fig. 2 Overview of the *Ld*G6PD *wt* dimer and schematic model of the *Ld*G6PD oligomerization. a *Ld*G6PD wt dimer in complex with NADP(H) (PDBID: 7ZHU) with position P1 of N-domain B (N^B) is shown in ribbon presentation. The β-α domain (D249-K552) of subunits A and B is colored light purple and light blue, respectively. The "Rossmann-like" domain (D50-I248) of subunits A and B is colored dark magenta and navy blue, respectively. The helical N-domain with helices α1 (~D11-R31) and α2 (~I36-K49) is colored magenta in subunit A (N^A) and cyan in subunit B (N^B). The connecting loop (residues D50-K64 in subunit A and B) between the N- and the "Rossmann-like" domain, is colored green. Regions with bad or missing electron density are shown in dotted lines (subunit A: D50-S55, Y476-R479; subunit B: R51-E54). Helix α14 as part of the G6P binding site, the flexible loop (T471-D482), and important cysteines (C56, C61, C97, C138, yellow) are labeled. NADP(H) (yellow) and G6P (green), and residues are shown as stick models. To mark the G6P binding pocket, G6P is taken from the superimposed structure with bound G6P (ribbons not shown, PDBID: 7ZHZ). **b** Schematic *Ld*G6PD dimer and tetramer involving position P1 of N-domain B (N^B). Subunit B is colored blue and N^B of subunit B in position P1 is colored cyan. Subunit A and A′ with N-domain A (N^A) and A′ ($N^{A'}$) are colored magenta. **c** Schematic *Ld*G6PD dimer and tetramer involving position P2 of N-domain B (N^B). Subunit B is colored blue and N^B of subunit B in position P2 is colored green. Subunit A and A′ with N^A and $N^{A'}$ are colored magenta (created with BioRender.com).

However, the described conformational changes upon NADP(H) binding did not extend to the $NADP^+$ binding pocket. Therefore, only minor differences occurred between the apo structure and structures complexed with NADP(H) or G6P with regard to the $NADP^+$ binding pocket. Residues forming the $NADP^+$ binding pocket are shown in Fig. 5a.

Significantly larger conformational changes than in the structures complexed with NADP(H) are observed after binding substrate G6P. Superimposition of the dimeric structures complexed with G6P (PDBID: 7ZHV) or with G6P and NADP(H) (PDBIDs: 7ZHW, 7ZHZ) with either the apo form (PDBID: 7ZHT; 965 residues) or the NADP(H)-bound form (PDBID: 7ZHU; 1055 residues) revealed RMSD values of 1.6 and 1.8 Å, respectively. Moreover, the angle between the "Rossmann-like" domain and the β + α domain is reduced when G6P is bound (Fig. 6a). There are significant conformational differences in the vicinity of the G6P binding pocket in the structures with (PDBID: 7ZHZ) and without bound G6P (PDBIDs: 7ZHU, 7ZHY). Structural comparison of the monomers shows that regions I248–I260 (α9) and P481–F499 (α14) rearrange, with the main chain atoms shifting by about 1.5 Å and the Y251 side chain by about 3 Å (Fig. 6a, b). Furthermore, residues H250, K254, M256 (α9), H312 (α12), and Y484 (α14) adopt different side-chain conformations (Fig. 6b). Moreover, in the structures

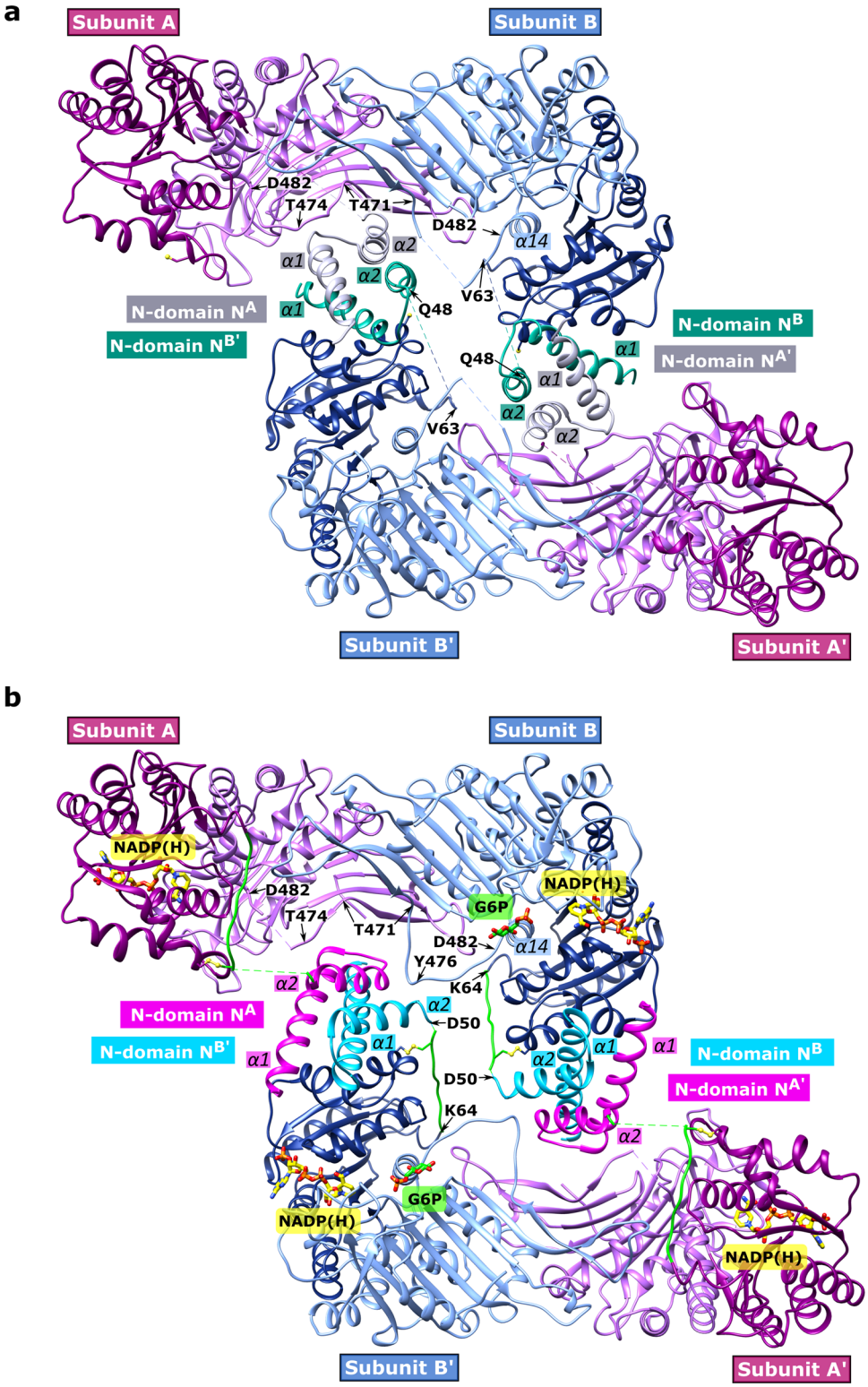

Fig. 3 Overview of the *Ld*G6PD *wt* tetramer. The tetramers of the apo **a** and the NADP(H)-complexed structures **b** are shown in the same orientation. The β-α domain (D249-K552) of subunits A/A′ and B/B′ is colored light purple and light blue, respectively. The "Rossmann-like" domain (D50-I248) of subunits A/A′ and B/B′ is colored dark magenta and navy blue, respectively. **a** apo structure. The helical N-terminal domain with α1 (~D11-R31) and α2 (~I36-K49) is colored gray in subunit A and A′ (N-domains N^A and $N^{A'}$) and colored dark cyan in subunit B and B′ (N-domains N^B and $N^{B'}$ with position P1). Dotted lines indicate regions with bad or missing electron density (subunit A/A′: G52-V63; subunit B/B′: K49-K62, T474-D477). **b** NADP(H)-complexed structure. N-domains N^A and $N^{A'}$ are colored magenta and N-domains N^B and $N^{B'}$ (position P1) are colored cyan. The connecting loop (D56-K64) is colored green, and dotted lines indicate regions with bad or missing electron density (subunit A/A′: D50-S55, Y476-R479; subunit B/B′: R51-E54). NADP(H) (yellow) and G6P (green) and residues are shown as sticks models. Important residues of the flexible loop (T471-D482) and the connected helix α14 (P481-L492) are directly or indirectly affected by the N-domains and marked with labels or arrows. The apo structure and the NADP(H)-complexed structure were used (PDBIDs: 7ZHT, 7ZHU), and G6P is taken from a superimposed structure with bound G6P (ribbon not shown, PDBID: 7ZHZ).

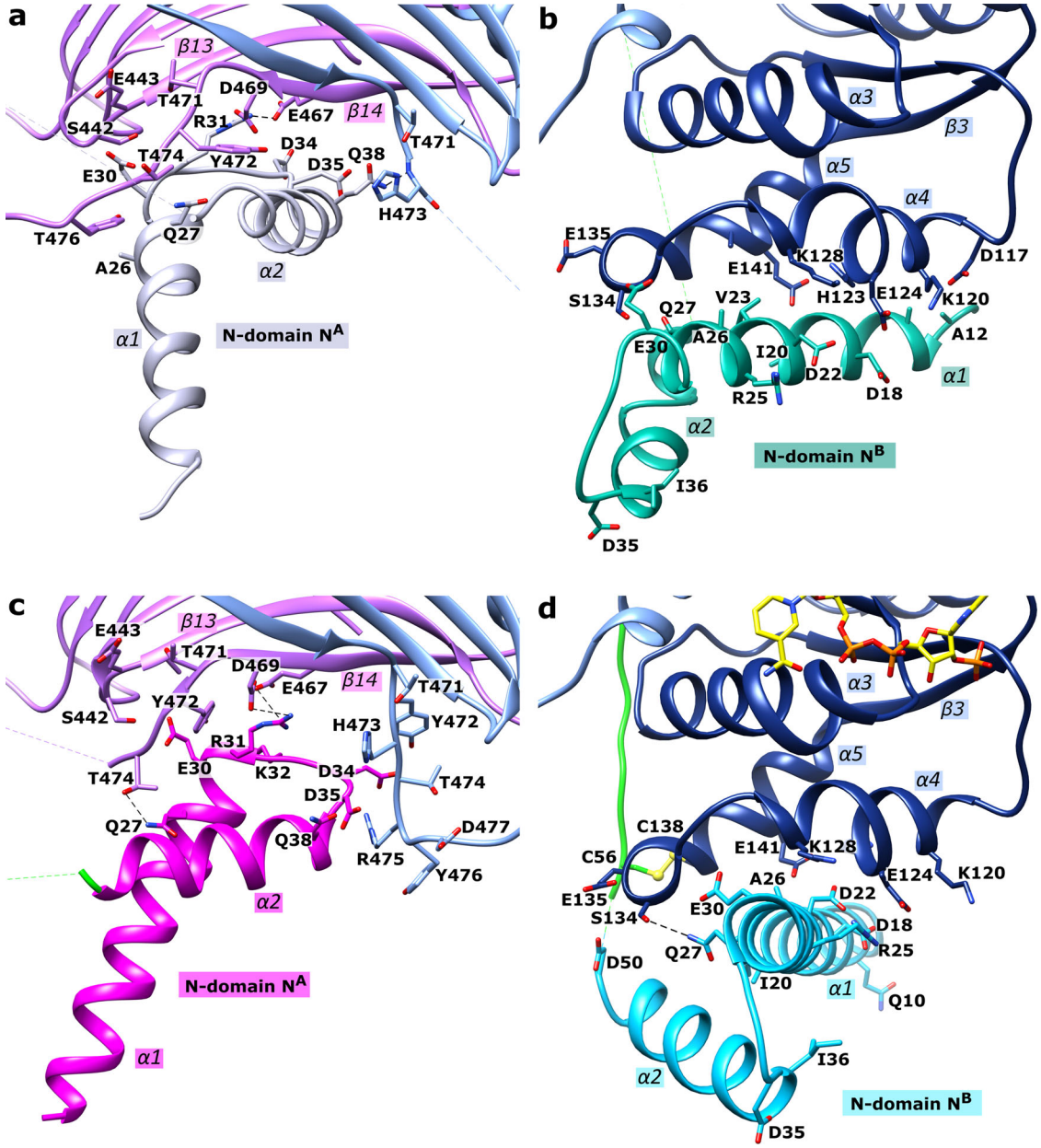

Fig. 4 Close-up of the *Ld*G6PD wt N-domains. The dimers of the apo and the NADP(H)-complexed structures are shown in the same orientation (PDBIDs: 7ZHT, 7ZHU). The β-α domain of subunits A or B are colored light purple and light blue, respectively. The "Rossmann-like" domain of subunit B is colored navy blue. The connecting loop (D50-K64) is colored green. **a** apo structure: N-domain A (N^A) is colored gray. **b** apo structure: N-domain B (N^B, position P1) is colored dark cyan. **c** NADP(H)-complexed structure: N-domain A (N^A) is colored magenta. **d** NADP(H)-complexed structure: N-domain B (N^B, position P1) is colored cyan; NADP(H) is colored yellow. Important residues are shown in stick models and hydrogen bonds are indicated with black dotted lines. Respective α-helices and β-sheets are numbered.

without bound G6P, the backbone atoms D482-A483 are located at the same position as the pyranose ring of G6P in G6P-complexed structures. Remarkably in all structures, G6P is bound only in subunit B of the G6PD dimer, although subunits A and B are essentially similar (RMSD ~ 0.7 Å). Minor shifts (~0.7 Å) occur for regions D117-E135 (α4) and cofactor NADP(H), and slightly higher shifts are observed for Y251 (1.5 Å) and residues P481-L492 (α14; 1.3 Å).

Comparison with homologous structures, in which the pyranose ring of G6P points towards $NADP^+$, revealed a corresponding G6P binding pocket in *Ld*G6PD, which is formed by residues K220, D249-Y251, F286-E288, K406, and K411-V413 (Fig. 5b). According to homologous structures, the pyranose ring of G6P would be coordinated by residues K220, E288, I304, D307, H312, and K406, and the phosphate moiety would be bound by residues H250, Y251, K254, K411, and Q440.

However, in G6P-bound *Ld*G6PD structures, the position of G6P that best explains the electron density is different from that of homologous G6PD structures[26–29]. Compared to these structures, the G6P conformation is rotated by 180° and located in a cleft, formed by amino acids D482-A483, Q440, H250-Y251, and K254 (Fig. 5b). The pyranose ring is hydrogen-bonded to K254, A483, and Q440, which also interacts with the phosphate. Interestingly, in homologous structures residue K254 is used for phosphate binding. In our structures, the phosphate is bound by residues H250, Y251, and K411. Overall, the phosphate moiety

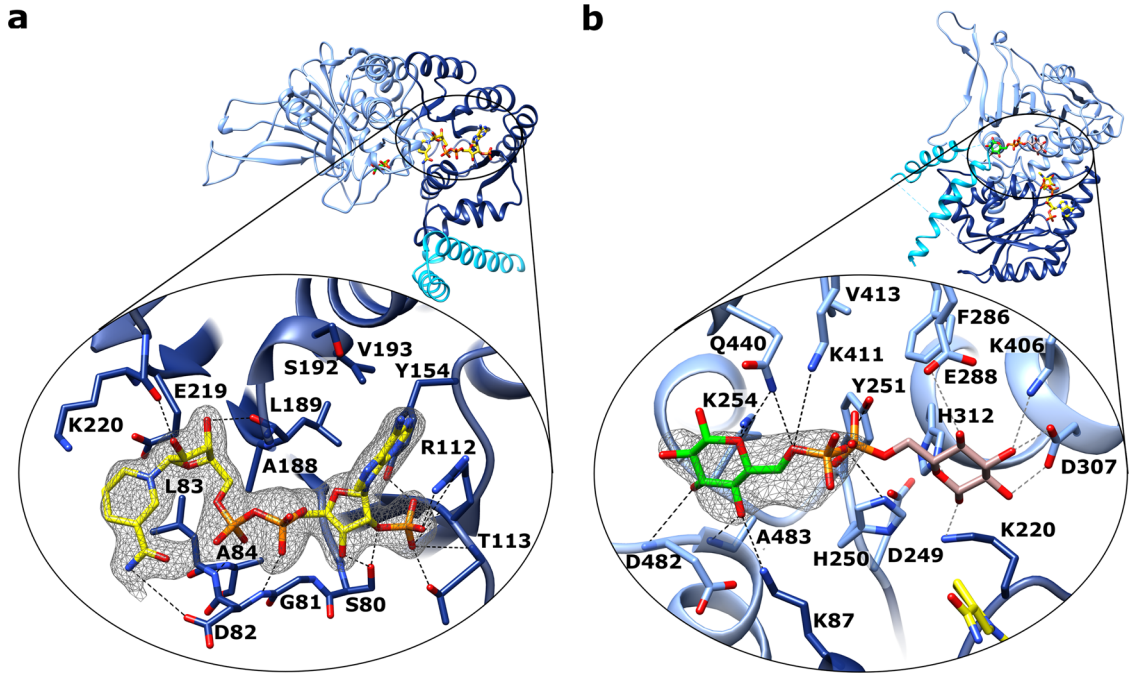

Fig. 5 Active site close-up of *Ld*G6PD. Ribbons and residues of the "Rossmann-like" domain are colored navy blue and of the β-α domain light blue. **a** Close-up of the $NADP^+$ binding pocket of the *Ld*G6PD structures (PDBID: 7ZHU) within the "Rossmann-like" domain. The NADP(H) moiety is colored yellow. Electron density map (F_O-F_C polder omit map) contoured at 4.0 σ for NADP(H), is shown in black. **b** Closeup of the G6P binding pocket. G6P is shown in two conformations. In brown, the G6P conformation from the superimposed *Tc*G6PD structure (PDBID: 5AQ1) with the pyranose ring pointing towards the NADP(H) moiety (yellow). In green, the G6P conformation of the *Ld*G6PD structures (PDBID: 7ZHZ). Electron density map (F_O-F_C polder omit map) contoured at 4.0 σ for G6P, is shown in black. Residues of the $NADP^+$ and the G6P binding pocket, are shown in stick models, and hydrogen bonds are indicated with black dotted lines or with gray dotted lines for the G6P moiety from the *Tc*G6PD structure.

shifts by only 1.7 Å compared to homologous G6PD structures (PDBIDs: 5AQ1, 6D24).

Taken together, binding NADP(H), G6P, or both results in a rotational shift of the two N-domains. This affects the interfaces between the N-domains and the core domain, particularly the contact region to the flexible loop T471-D482 so that residues of α14 (P481-L492) that participate in G6P binding are also affected. The $NADP^+$ binding site is less affected with only minor shifts. Furthermore, binding G6P induces a structural rearrangement of residues I248-I260 (α9) and P481-F499 (α14). Without bound G6P, the H250 and K254 side chains face away from the binding pocket, making the usual interaction with G6P impossible (Fig. 6a, b). Moreover, Y251 points into the G6P binding pocket, which would lead to clashes with the phosphate moiety of G6P in *Ld*G6PD and homologous structures (Fig. 6b, d).

Truncation of residues 1–59 indicates the N-terminal extension is involved in *Ld*G6PD tetramerization. To investigate a potential function of the helical N-domain conserved in *Kinetoplastida* G6PDs, we generated a truncation mutant lacking the N-domain that includes residues 1–59 (*Ld*G6PD$^{60\text{-}562}$). Moreover, the *Ld*G6PD wt structure, complexed with NADP(H), revealed a disulfide bond between C138 and C56; however, with minor conformational changes, an alternative disulfide bond between C138 and C61 or C56 and C97 is also possible (Fig. 2a). Therefore, we generated a second mutant by replacing C138 with a serine (*Ld*G6PD^{C138S}). We hypothesized that both mutations will impair enzyme activity due to truncation or altered orientation of the N-domain.

Comparing the *Ld*G6PD^{C138S} structures to the wt structures revealed no major conformational changes (RMSD = 0.4 Å with 1056 residues). Accordingly, the mutation revealed no alternative disulfide bridge and the oligomerization profile did not significantly differ from the wt (Fig. 1a). Although the K_M of G6P increased by about 20%, indicating a lower affinity, the activity V_{max} increased to the same extent so that catalytic efficiency remained stable (Table 1). For $NADP^+$, catalytic efficiency slightly increased from $14.5 \pm 1.6\ \mu M^{-1}\ s^{-1}$ to $17.3 \pm 0.8\ \mu M^{-1}\ s^{-1}$ due to the increased V_{max} but stable K_M.

In contrast to the wt and *Ld*G6PD^{C138S} crystals, which contain the physiological dimer in the AU, the truncation mutant *Ld*G6PD$^{60–562}$ crystallized in an orthorhombic space group (C222) with one molecule in the AU (Table 2). Consequently, the physiological dimer is formed by a crystallographic two-fold rotation axis. However, our usual tetramer (Fig. 3) cannot be constructed via crystallographic symmetry operations. Instead, a different tetramer is formed via C222 symmetry operations (Fig. 6c), which interestingly resembles the G6PD tetramer of related *Trypanosoma* species. Here, the *Ld*G6PD dimer–dimer interface is mainly formed by salt bridges (R268, K324, R326, D335, E336, and D393), keeping the dimers in a back-to-back orientation. Similar to our truncation mutant, *Trypanosoma* G6PDs have always been crystallized as truncated forms and therefore lack the first N-terminal 57 or 37 residues[28,29].

Superimposing the respective NADP(H)-bound *Ld*G6PD$^{60–562}$ (PDBID: 7ZHX) and *Ld*G6PD wt dimer (PDBID: 7ZHU) revealed an overall shift of 0.8 Å (475 residues) and small shifts (up to 1.4 Å) of the β + α and "Rossmann-like" domains, resulting in a slightly more open conformation of the truncation mutant. In accordance with these structural results and in contrast to the stable dimer-to-tetramer equilibrium of *Ld*G6PD wt, the tetramer was no longer visible in the SEC profiles of *Ld*G6PD$^{60–562}$ but only a single peak corresponding to the dimer form of the mutant (Fig. 1a). However, the crystallographic and SEC observations were not reflected by impaired catalytic efficiency of the enzyme (Table 1).

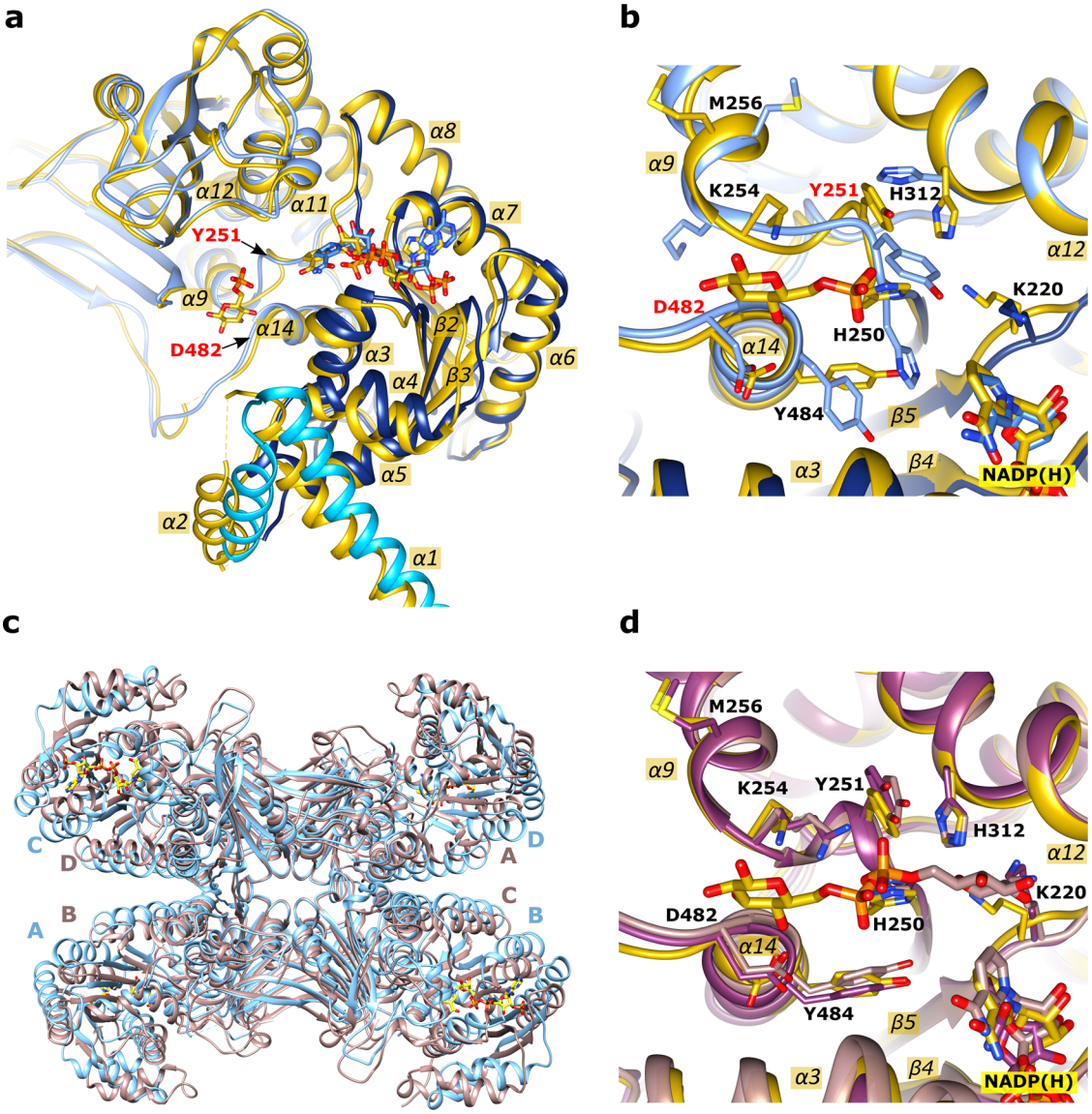

Fig. 6 G6P-induced rearrangements of *Ld*G6PD wt and structural comparison with orthologues. Superimposition of the NADP(H)-complexed structure (PDBID: 7ZHU; blue) with the structure complexed with G6P and NADP(H) (PDBID: 7ZHZ; yellow). Residue Y251 (red) marks the G6P-induced active site shift of the loop comprising residues H250-K254. **a** The superimposed dimers (only monomer B is shown) show the G6P-induced shift of the N- and the "Rossman-like" domain. Residue D482 (red) marks the end of the flexible loop (T471-D482), connected to α14 **b** Active site close-up. Here, monomers B of both structures are superimposed. The superimposition shows the different sidechain conformations of residues lining the G6P binding site and the rearrangement of region H250-K254. **c, d** Comparison with orthologues. **c** Superimposition of the *T. cruzi* G6PD tetramer with the *Ld*G6PD$^{60\text{-}562}$ mutant. Both enzymes were crystallized lacking the helical N-domains. The apo-structure of the *Tc*G6PD tetramer (PDBID: 6D23) with subunits A-D is colored brown and that of the NADP(H)-complexed *Ld*G6PD$^{60\text{-}562}$ tetramer (PDBID: 7ZHX) light blue. **d** Superimposed active sites of the *Ld*G6PD structure (with bound G6P and NADP(H); PDBID: 7ZHZ; yellow) with the *Tc*G6PD (with bound G6P; PDBID: 5AQ1; brown) and *Hs*G6PD structure (with bound $NADP^+$; PDBID: 2BH9; purple). Figure **d** is shown in the same orientation as **b**. Respective α-helices and β-sheets are numbered.

Mechanistic considerations of *Leishmania* G6PD. In order to determine the catalytic binding mechanism of the substrates, G6P and $NADP^+$ were titrated at various constant concentrations of the second substrate, and the relationship between substrate concentration and initial enzyme velocity was analyzed. For both substrates, the intersection of the Lineweaver–Burk plots left of the ordinate points towards a sequential order mechanism of substrate binding, in which both substrates must bind to the enzyme before product formation can occur[30] (Fig. 7a, b). Furthermore, the lines intercept below the abscissa, indicating that binding the first substrate promotes binding of the second substrate.

To differentiate between ordered and random sequential mechanisms of *Ld*G6PD, we conducted inhibition studies with the product inhibitor NADPH and the dead-end inhibitor glucosamine 6-phosphate (GlcN 6-P), an analog of G6P[31–33]. NADPH was found to be a competitive inhibitor with respect to $NADP^+$ in *Ld*G6PD as indicated by the intersection on the x-axis (Fig. 7c) and increasing K_M values with increasing inhibitor concentrations (Fig. S5a). Likewise, GlcN 6-P shows a competitive inhibition pattern towards G6P (Figs. 7e, S5c). Towards $NADP^+$, GlcN 6-P had no inhibitory effect (Figs. 7d, S5b). In contrast, NADPH was also found to be a competitive inhibitor with respect to G6P (Figs. 7f, S5d).

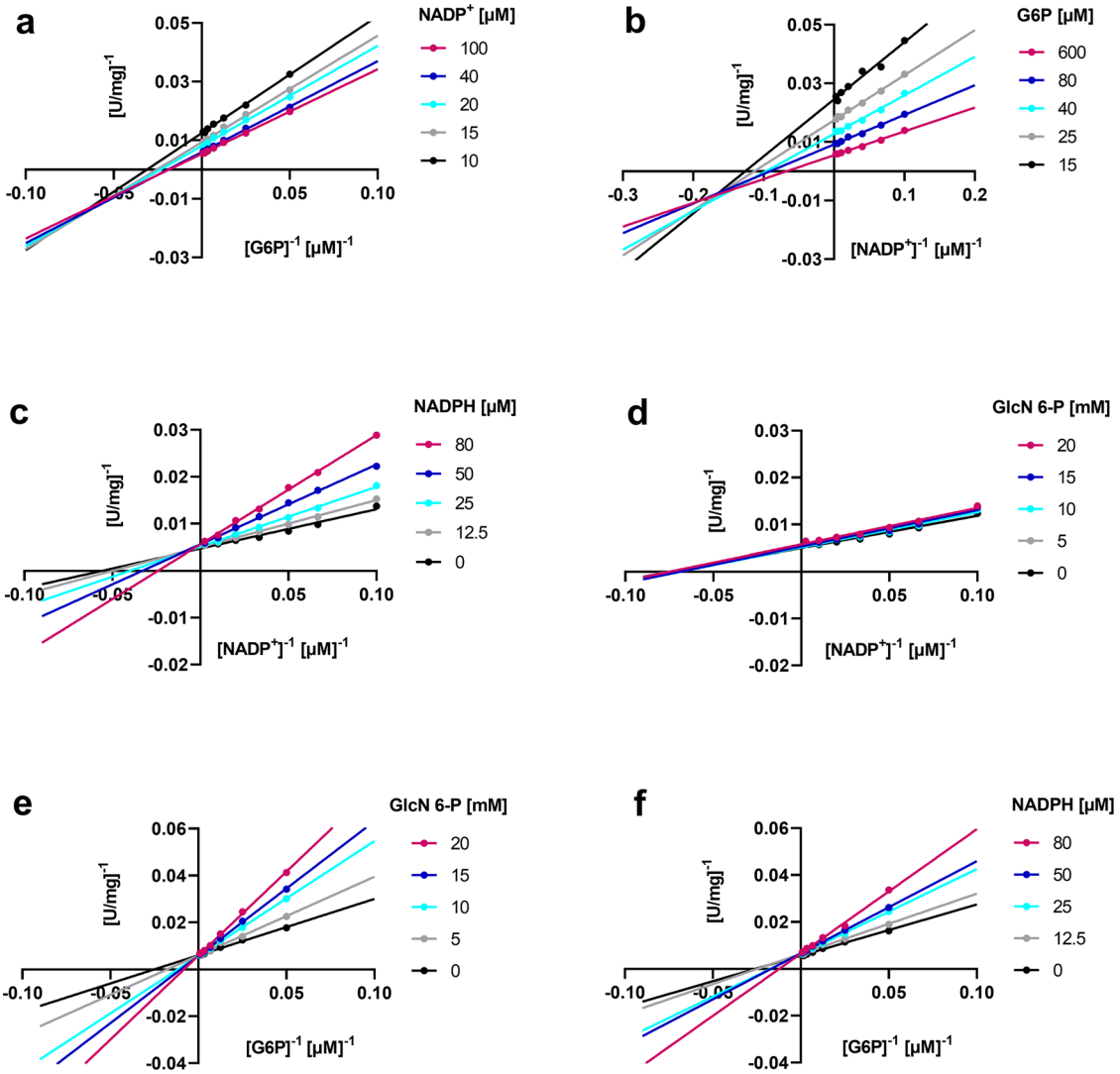

Fig. 7 *Ld*G6PD's sequential binding mechanism for the substrates $NADP^+$ and G6P and inhibition by the product inhibitor NADPH and the dead-end inhibitor glucosamine 6-phosphate. a $NADP^+$ and **b** G6P, as well as **c, f** NADPH and **d, e** glucosamine 6-phosphate (GlcN 6-P) were titrated at various constant concentrations of the substrate G6P or cosubstrate $NADP^+$. The primary double reciprocal plots of $[U/100\ mg]^{-1}$ against $[G6P]^{-1}$ and $[NADP^+]^{-1}$, respectively, are shown. Plots **a** and **b** intercept left of the ordinate, indicating a sequential binding mode of the substrates. Plots **c**, **e**, and **f** intercept on the ordinate, indicating a competitive inhibition of NADPH against $NADP^+$ and G6P and of GlcN 6-P against G6P, but not against $NADP^+$. **d** Representative graphs from three independent replications are shown.

Discussion

In this work, we present the crystal structure and biochemical characterization of *Leishmania donovani* G6PD. We were able to visualize the N-domain, which is unique in *Trypanosomatida*, providing interesting insights into its function and suggesting a central role in oligomerization. Additionally, we detected substrate-induced domain shifts extending to the active site of the enzyme. These conformational changes have never been observed in other G6PDs described so far. The crystallographic data also perfectly fit the kinetically determined binding mechanism of *Ld*G6PD. Finally, a much higher catalytic activity than homologous G6PDs supported these unique features, highlighting the central role of this enzyme in helping *Leishmania* parasites cope with oxidative stress.

Our kinetic investigations revealed a specific activity of about 200 U mg^{-1} (Table 1) of recombinant *Ld*G6PD and *Lm*G6PD, with a 3–4-fold higher catalytic efficiency than G6PDs from other species. Moreover, SEC profiles of wt *Ld*G6PD and *Lm*G6PD revealed two peaks under native conditions, equivalent to a dimer and a tetramer (Fig. 1a), whereas the tetramer fraction showed reduced catalytic efficiency compared to the dimer. Consequently, *Leishmania* G6PDs potentially exist in dynamic dimer–tetramer equilibrium, as with other G6PDs[26,29,33,34]. However, in contrast to homologous G6PDs[35–37], varying ionic strength, pH, enzyme concentration, or the presence of substrates did not affect this equilibrium (Fig. 1b, S2). The catalytic efficiency of *Ld*G6PD also remained unaffected under these conditions, except at very low pH (4.5), resulting in a 40% decrease in activity. However, *Leishmania* amastigotes in particular manage to keep the cytosolic pH largely neutral within the acidic parasitophorous vacuole[38], and enzyme activity could be restored when measured under neutral pH (7.5). Furthermore, reducing or oxidizing agents affected neither oligomerization nor the catalytic efficiency of *Ld*G6PD, whereas enzyme activity of the related *Tc*G6PD was almost abolished under such conditions[29,39]. The resistance of *Ld*G6PD to changing environmental conditions is probably an adaptation of *Leishmania* parasites, which are exposed to an extremely redox-active environment within the parasitophorous

vacuole in host macrophages and therefore rely on an adequate G6PD-derived NADPH pool.

Other trypanosomatid G6PDs such as from *Trypanosoma cruzi* or *Crithidia fasciculate* have been previously shown to form tetramers with a back-to-back orientation of the two dimers and a dimer–dimer interface predominantly formed by salt bridges[28,29]. Since the respective amino acids are conserved in *Kinetoplastida*, therefore also present in *Leishmania* G6PDs, all *Kinetoplastida* G6PDs have been postulated to likely form this kind of tetramers[28,29]. However, although the *Ld*G6PD SEC profiles showed an additional tetramer peak, varying ionic strength did not affect the dimer-tetramer equilibrium of *Ld*G6PD wt, suggesting a minor contribution of salt bridges in *Ld*G6PD tetramer formation.

T. cruzi G6PDs were always crystallized as truncated variants without the N-terminal domain[28,29]. If we also truncate the entire N-domain in *Ld*G6PD (*Ld*G6PD$^{60-562}$), we are able to construct via crystallographic symmetry operations the same tetramer arrangement as seen for *Tc*G6PD (Fig. 6c). However, the SEC profile of the truncation mutant exhibited a pure dimer, without the additional tetramer fraction (Fig. 1a). Our crystallization studies with full-length *Ld*G6PD always reveal a tetramer in which the N-domains form the dimer–dimer interface leading to a face-to-face orientation of the two dimers (Fig. 3). Therefore, we suggest that the N-domains are essential for forming the *Ld*G6PD tetramer.

In accordance with previous findings on *Tc*G6PD[28,29,39], truncation of the N-domain did not change the catalytic efficiency of the *Ld*G6PD dimer (Table 1). Only minor conformational changes of the core domains in the crystal structure of *Ld*G6PD$^{60-562}$ confirmed this when compared to the wt.

As mentioned earlier, we observed reduced catalytic efficiency of the tetramer with an increased K_M for G6P but similar activity compared to the dimer. Since there are two possible positions of N-domain of subunit B (N^B), the choice of P1 or P2 determines dimeric and tetrameric contacts (Figs. 2b, c, 3). If position P1 belongs to monomer B (Fig. 2b) a tetramer is formed with a dimer–dimer interface between the N-domains. Another tetramer contact in this scenario exists between N^B and the flexible loop (T471-D482) of subunit B' and vice versa between N-domain of subunit B' ($N^{B'}$) and subunit B (Fig. 3b). Conversely, if we would associate position P2 with monomer B (Fig. 2c), these contacts would be dimeric, and the dimer–dimer interface of the tetramer would reduce to the interaction between helix α1 of N^B or $N^{B'}$ and the "Rossmann-like" domain (α4) of subunit B' or B, respectively. We assume that P1 of N-domain N^B is connected to subunit B. Therefore, the N-domain of subunit B' ($N^{B'}$) influences the flexible loop (T471-D482) of subunit B and consequently affects the G6P binding site (α14; P481-L492) (Figs. 3, 6a, b). This tetrameric interaction perfectly explains the increased K_M for G6P of the tetramer, whereas K_M of $NADP^+$ and the overall activity remained unaffected compared to the dimer.

Finally, which function the tetramer has in vivo must still be clarified. Although the conditions we tested had no effect on oligomerization, there are many other factors that could influence the dimer–tetramer equilibrium, such as the product-to-substrate ratio, various other ROS, or protein interactions. For example, p53 is known to regulate human G6PD activity[40], and in trypanomatids, trypanothione reductase, a direct NADPH consumer, is thought to interact with G6PD[41]. Maybe the unique N-domain is also involved in such protein interactions, but this needs to be investigated in further studies.

The kinetic mechanism of various G6PDs has been intensively investigated and controversially discussed. While kinetic studies support an ordered sequential binding mechanism for many G6PDs[31,42–44] a rapid equilibrium random sequential mechanism has been demonstrated for others such as *Hs*G6PD and *P. falciparum* G6PD[32,33]. To investigate the sequential binding mechanisms of *Ld*G6PD in more detail, we used product inhibition studies (Fig. 7). Under saturating conditions, NADPH acts as a competitive inhibitor against $NADP^+$, as does the dead-end inhibitor glucosamine 6-phosphate (GlcN 6-P) against G6P. Surprisingly, NADPH also acts as a competitive inhibitor against G6P when $NADP^+$ is in saturation, while GlcN 6-P does not compete with $NADP^+$ when G6P is in saturation. These observations suggest that $NADP^+$ can bind equally well to the free enzyme and the enzyme binary complex with already bound G6P, whereas G6P prefers binding to the free enzyme. This indicates that *Ld*G6PD follows an ordered sequential mechanism, where substrate binding and product release occur in a specifically ordered fashion. Our data even suggest that *Ld*G6PD follows a special ordered mechanism, the Theorell–Chance mechanism (Fig. 8). In this special case, substrate binding and product release occur so rapidly that the ternary complex EAB (*Ld*G6PD-G6P-$NADP^+$) exists for only a very short time and is therefore not kinetically significant[30,45]. For *Ld*G6PD this means that the substrate G6P (A) binds first to build EA (*Ld*G6PD-G6P) followed by binding of the cosubstrate $NADP^+$ (B) to form the product 6-phospho-D-glucono-1,5-lactone (6PL) (P), followed by formation of NADPH (Q). However, product formation (P, Q) occurs immediately after binding $NADP^+$ (B) so that the ternary complexes EAB and EPQ exist transiently but at such a low concentration that they cannot be detected via initial rate studies.

This fits well with our crystallographic observations of *Ld*G6PD. We observed conformational changes compared to the apo structure due to G6P binding alone (Fig. 6a, b). Within the G6P binding pocket, this conformational change was mainly visible through Y251 and surrounding residues (H250-Y254) (Fig. 6b). In structures without bound G6P, these residues (H250-Y254) always point to the G6P binding pocket, making catalysis impossible.

Interestingly, NADP(H) is always visible in both monomers of the dimer, while G6P is visible in monomer B only. Therefore, it seems that both monomers do not convert their substrates synchronously but rather delayed from each other, in which the occupancy of one binding site suppresses the catalysis of the other. The substrate-induced 45° rotation of the N-domains compared to the apo structure could be involved in this phenomenon (Figs. 3, 6). Therefore, the N-domain rotation changes the N-domain contacts to the main chain and the interaction between all subunits. Consequently, the contacts of N-domain A to the flexible loop B are reduced in the apo structure, influencing the G6P binding site (Figs. 3, 6, S4).

Our hypothesis that G6P binds first is further strengthened by the fact that we obtained crystals only by adding G6P (PDBID: 7ZHV) but not when crystallizing with $NADP^+$ alone. Therefore, structures complexed only with $NADP^+$, were always crystallized under catalysis. Accordingly, the bound $NADP^+$ could also be the product NADPH. Finally, we interpret the G6P-induced shift,

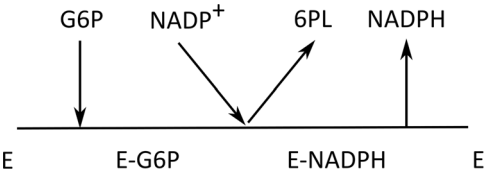

Fig. 8 Proposed Theorell–Chance mechanism *Ld*G6PD. G6P binds first to *Ld*G6PD followed by $NADP^+$ to generate the products 6-phospho-D-glucono-1,5-lactone (6PL) and NADPH without forming a significant ternary complex; E = enzyme *Ld*G6PD.

leading to a 45° rotation of the N-domain and a decreased angle between the β-α domain and the "Rossmann-like" domain, as a conformational change towards the catalytic form.

Interestingly, we observed a rearrangement of the G6P binding site upon G6P binding. In structures from other species, with or without bound G6P, the G6P binding site is similar to our structures with bound G6P, but not to the *Ld*G6PD structures without G6P (Fig. 6b, d).

However, the G6P conformation in the *Ld*G6PD structures is different from homologous G6PDs. Although the phosphate is similarly bound, the pyranose ring is rotated by 180° around the phosphate and therefore points in the opposite direction (Fig. 5b). In this conformation, the ring is located in a channel that extends to the center of the tetramer (Fig. 3). Consequently, electron transfer with $NADP^+$ and hence catalysis are impossible. We hypothesize that this conformation is a waiting position of G6P, whose position either results from the absence of $NADP^+$ (PDBID: 7ZHV) or is inhibited from catalysis by NADPH as a product inhibitor (PDBIDs: 7ZHW, 7ZHZ). However, as a feature of the postulated Theorell–Chance mechanism, the ternary complex exists only for a very short time, which could also explain why the true catalytic form is not visible in any of our structures.

The crystallographic and biochemical characterization of *Ld*G6PD presented in this study, revealed a trypanosomatid G6PD structure that contains the complete N-domain, unique to G6PDs of the *Kinetoplastida* family. Interestingly, our investigations on the function of the helical N-domain, indicated essentiality for *Ld*G6PD tetramerization and showed that the N-domain changes its position upon substrate binding. In contrast to homologous species, we observed G6P-dependent domain motions that kinetic studies supported, revealing an ordered mechanism with G6P binding first, followed by $NADP^+$. We believe that these insights from *Ld*G6PD will significantly contribute to the understanding of G6PDs' molecular mechanisms and will provide an excellent basis for further drug discovery approaches.

Methods

PCR amplification, cloning, and site-directed mutagenesis of G6PDs. For heterologous overexpression in *E. coli*, the genes encoding wt *Ld*G6PD (UniProt acc. no. A2CIL3) and *Lm*G6PD (UniProt acc. no. Q4Q3K1) were ordered codon-optimized from BioCat GmbH (Heidelberg, Germany) and subcloned into the pET28a(+) vector using BamHI and HindIII restriction sites, thereby enabling N-terminally His-tagged proteins (Table S2).

To characterize the potential function of the N-terminal domain (covering the first 49 amino acids) two mutants were generated. C138 was replaced with serine (*Ld*G6PD^{C138S}) using the Q5® site-directed mutagenesis kit (New England Biolabs GmbH) with the construct pET28a(+)-*Ld*G6PD wt as a template. Furthermore, we generated a truncated construct lacking the first 59 N-terminal amino acids (*Ld*G6PD$^{60–562}$). PCR was performed using Q5 polymerase and the construct pET28a(+)-*Ld*G6PD wt used as a template. The PCR product was gel purified, digested with BamHI and HindIII and subsequently cloned into the BamHI-HindIII site of a pET28a(+) vector. All primers used in the present study are described in Table S3. The constructs were verified via sequencing from LGC genomics (Berlin, Germany) using standard primers within the T7 promotor and the T7 terminator sequence of the pET28a(+) vector.

Expression and purification of His-tagged *Ld*G6PD wt, *Ld*G6PD^{C138S}, *Ld*G6PD$^{60–562}$, *Lm*G6PD wt. Expression plasmids encoding for *Ld*G6PD and *Lm*G6PD wt and the corresponding mutants were transformed in *E. coli* C43 (DE3) cells using a pET28a(+) vector. Cells with the respective plasmid were grown at 37 °C in lysogeny broth medium containing 50 μg mL^{-1} kanamycin. When the optical density at 600 nm reached ~0.5, heterologous overexpression was subsequently induced for 4 h by adding 0.5 mM IPTG. Cells were harvested via centrifugation (15 min, 12,000 × *g*, 4 °C), suspended in buffer A (500 mM NaCl, 50 mM Tris, pH 7.8), mixed with protease inhibitors (4 nM cystatin, 150 nM pepstatin, 100 μM PMSF) and stored at −20 °C until lysis. For cell lysis, lysozyme and DNaseI were added to the cell suspension and incubated for ~12 h at 4 °C, followed by three cycles of sonication and centrifugation (30 min, 25,000 × *g*, 4 °C). The supernatant was applied to a Ni-NTA column for IMAC purification, pre-equilibrated with buffer A. Recombinant N-terminally His-tagged proteins were eluted with buffer A containing increasing (100–500 mM) imidazole concentrations. The fractions containing the recombinant protein were pooled and concentrated using an ultrafiltration unit (Vivaspin 20, 30-kDa filter cut-off; Sartorius, Göttingen, Germany). As an additional purification step and to determine the oligomerization state of the respective enzymes, size exclusion chromatography (SEC) was performed with an ÄKTA FPLC system, using a HiLoad 16/60 Superdex 200 column (GE Healthcare, Freiburg, Germany) pre-equilibrated with buffer A. To investigate the oligomerization behavior, SEC was performed under native, reductive (5 mM DTT), and oxidative (2 mM H_2O_2) conditions, as well as in the presence of substrates (100 μM G6P, $NADP^+$, G6P + $NADP^+$). Protein elution was detected at 280 nm and evaluated using the UNICORN software 7.2. The peaks of interest containing the recombinant protein were collected and concentrated and enzyme purity was assessed with Coomassie blue-stained SDS-PAGE gels (12% polyacrylamide). Enzyme concentration was determined by measuring the absorbance of the protein solution at 260 and 280 nm using the Eppendorf BioSpectrometer (Hamburg, Germany) followed by calculating the final concentration with the molecular weight and extinction coefficient of the respective enzymes (*Ld*G6PD wt/*Ld*G6PD^{C138S}: 66.7 kDa, 63,113 M^{-1} cm^{-1}; *Ld*G6PD$^{60–562}$: 60.3 kDa, 61,623 M^{-1} cm^{-1}; *Lm*G6PD wt: 66.8 kDa, 63,175 M^{-1} cm^{-1}). After SEC, a final yield of 0.5–2 mg soluble, pure, and active G6PD per litre *E. coli* culture was achieved for all proteins tested in this study. The enzymes remained stable for at least 10 days when stored at 4 °C and 3 months when stored at −80 °C with the addition of 250 mM $AmSO_4$, as verified via enzyme activity measurements.

Enzymatic characterization of *Ld*G6PD wt, *Ld*G6PD^{C138S}, *Ld*G6PD$^{60–562}$, *Lm*G6PD. Using the spectrophotometer Evolution 300 (Thermo Scientific, Dreieich, Germany), G6PD activity was determined at 25 °C by following NADPH [$\varepsilon_{340} = 6{,}220$ M^{-1} cm^{-1}] production at 340 nm according to Beutler[46]. All reactions were performed in buffer B (50 mM Tris, 3.3 mM $MgCl_2$, 0.005% Tween, 1 mg mL^{-1} BSA, pH 7.5), whereas the enzymes were pre-diluted in buffer C (50 mM Tris, 0.005% Tween, 1 mg mL^{-1} BSA, pH 7.5). The reaction mixture with a final volume of 500 μL contained 200 μM $NADP^+$, varying concentrations of the respective G6PDs (0.95–1.3 nM), and 800 μM G6P. To determine the apparent K_M values and V_{max}, the substrate (1400–10 μM G6P) and the cosubstrate (500–2 μM $NADP^+$) were varied reciprocally. To determine the reaction mechanism, G6P was titrated at various concentrations of $NADP^+$ and vice versa. All measurements were performed at least in triplicate, and the apparent kinetic constants were calculated via nonlinear regression using the GraphPad Prism 9.0 software.

Inhibition studies. For product inhibition studies, the initial rates were measured for a series of NADPH concentrations (0–80 μM) with G6P in saturation (800 μM) and varying $NADP^+$ concentrations from 10 to 400 μM. Likewise, the experiment was carried out by varying the G6P concentration from 20 to 1200 μM with $NADP^+$ in saturation (200 μM) and again a series of NADPH concentrations (0–80 μM). In analogous fashion, 0–20 μM GlcN 6-P was used as an inhibitor covering the same combinations and ranges of substrate concentrations as used in the experiments with NADPH.

Protein crystallization. For crystallization of *Ld*G6PD wt and the respective mutants, *Ld*G6PD^{C138S} and *Ld*G6PD$^{60–562}$, the enzymes were concentrated to ~10 mg mL^{-1} in buffer A. Crystallization plates were prepared using a Digilab Honeybee 961 crystallization robot generating drops by mixing 0.2 μL reservoir solution with 0.2 μL protein solution. G6PD crystals were grown in a 96-well format with the sitting drop vapor diffusion technique. Initial crystallization conditions were identified within the screening of the JCSG Core I suite (Quiagen) and further optimized by screening around the initially identified conditions. Immediately after preparation, the plates were kept at 10 °C because crystal growth proceeded very fast, resulting in unstable, low-resolution crystals. Suitable crystals could only be obtained in complex with substrate and cosubstrate (1 mM each). *Ld*G6PD wt and *Ld*G6PD^{C138S} crystallized best in a reservoir containing 10% PEG 3000 and 100–150 mM $AmSO_4$. The mutant *Ld*G6PD$^{60–562}$ crystallized in a reservoir containing 6% PEG 3000 and 200 mM $AmCl_2$ instead of $AmSO_4$.

We crystallized the *Ld*G6PD wt dimer and tetramer fraction separately. From the dimer fraction, we obtained crystals complexed with and without NADP(H), with G6P, and with both G6P and NADP(H). From the tetramer fraction, we used a crystal complexed with NADP(H) and G6P. From the dimer fraction of the *Ld*G6PD^{C138S} mutant we got crystals complexed with NADP(H) and with both G6P and NADP(H). For the truncation mutant *Ld*G6PD$^{60–562}$ we obtained crystals in complex with NADP(H) only. A prerequisite for well-diffracting crystals (<2 Å) was the presence of both ligands, G6P, and $NADP^+$ in the crystallization buffer (Table 2, Table S1).

Data collection and processing. Diffraction data for all crystals were collected at beamline X10SA (Pilatus 6 M for the crystals of *Ld*G6PD wt and Eiger2 16 M for the crystals of *Ld*G6PD mutants) of the Swiss Light Source in Villigen, Switzerland at 100 K and processed with XDS[47]. Before data collection, crystals were soaked in mother liquor with a final concentration of 35% ethylene glycol.

The apoenzyme (PDBID: 7ZHT) crystallized in space group P121 with four monomers in the AU unit (Table 2). The wt enzyme in complex with G6P (PDBID: 7ZHV), the wt enzyme and the mutant *Ld*G6PD^{C138S} in complex with NADP(H) (PDBIDs: 7ZHU, 7ZHY), as well as in complex with G6P and NADP(H) (PDBIDs: 7ZHW, 7ZHZ), crystallized in space group C121 with two monomers in the AU. All structures complexed with G6P or NADP(H) show C121 space group symmetry, but the structures with G6P have an a-axis shortened by about 5 Å. In addition to the two monoclinic crystal forms (P121, C121), we obtained orthorhombic crystals (C222) for the N-terminal truncation mutant *Ld*G6PD$^{60–562}$ (PDBID: 7ZHX) with one monomer in the AU.

Structure determination and refinement. A search model of *Ld*G6PD was generated via homology modeling with SWISS-MODEL[48] by using *Hs*G6PD (PDBID: 5UKW) as at template. The modeled *Ld*G6PD monomer comprises residues 70–549. In spite of the high sequence identity of 53% (Fig. S3), attempts to solve the structure of the apoenzyme using the canonical G6PD dimer were unsuccessful. Instead, a truncated version of the modeled *Ld*G6PD monomer was used, where loops on the surface, comprising residues 170–179, 359–376, 471–480, and 546–549, were deleted. The initial R_{free} value after the first refinement was 37%. The AU of the final solution contained four monomers, which form two canonical G6PD dimers. In contrast to other G6PDs, *Ld*G6PD contains an additional N-terminal domain, which was only visible in one dimer of the apo structure. Diffraction data of all other crystals were phased via molecular replacement methods using the structure of the apoenzyme. During refinement, 8% of all reflections for the wt crystals complexed with NADP(H) were omitted and used for calculation of an R_{free} value; for the other crystals, 10% of all reflections were used. The final statistics are shown in Table 2.

Interestingly, the apo structure and all structures complexed with G6P have much lower resolution (≥2.8 Å), than the structures in which only NADP(H) is bound (≤1.9 Å) (Table S2). The electron density of the *Ld*G6PD core comprising residues 5–470 and 483–552 is well defined in all our structures. In some structures, the electron density of the N-terminal domain (N-domain), covering the first 49 residues, is also well defined, although the temperature factors of the atoms are about 1.5 times higher than the average value of the core atoms. Two loops comprising residues D50-K64 and T471-D482 are defined by the electron density in some structures (Table S1), but the B-factor of these residues is at least twice the average B-factor.

The PHENIX program suite[49,50] served for reflection phasing and structure refinement. The interactive graphics program and Coot[51] were used for model building. Molecular graphics images were produced using the UCSF Chimera package[52].

Statistics and reproducibility. Data analysis was performed using GraphPad Prism Version 9.0 software. Data are presented as means ± SD. Reproducibility was confirmed by performing at least two independent determinations from different enzyme batches (for Fig. 1, Fig. S2) or three independent determinations with different enzyme batches, each including at least three (for Table 1) or two measurements (for Fig. 7 and Fig. S5) as described in the figure legend.

Reporting summary. Further information on research design is available in the Nature Portfolio Reporting Summary linked to this article.

Data availability

Coordinates and measured reflection amplitudes have been deposited in the Worldwide Protein Data Bank RCSB PDB (http://pdb.org): code 7ZHT for *Ld*G6PD wt in its apo form; code 7ZHU for *Ld*G6PD wt in complex with NADP(H); code 7ZHV for *Ld*G6PD wt in complex with G6P; code 7ZHW for *Ld*G6PD wt in complex with NADP(H) and G6P; code 7ZHX for the truncation mutant *Ld*G6PD$^{60–562}$ in complex with NADP(H); code 7ZHY for mutant *Ld*G6PD^{C138S} in complex with NADP(H) and 7ZHZ for the *Ld*G6PD^{C138S} mutant in complex with NADP(H) and G6P. All source data behind the graphs and charts and unprocessed scans presented in the figures are presented in Supplementary Data 1.

Received: 10 May 2022; Accepted: 28 November 2022;
Published online: 09 December 2022

References

1. WHO. Leishmaniasis. https://www.who.int/news-room/fact-sheets/detail/leishmaniasis (2021).
2. Burza, S., Croft, S. L. & Boelaert, M. Leishmaniasis. *Lancet* **392**, 951–970 (2018).
3. Chakravarty, J. & Sundar, S. Current and emerging medications for the treatment of leishmaniasis. *Expert Opin. Pharmacother.* **20**, 1251–1265 (2019).
4. Roatt, B. M. et al. Recent advances and new strategies on leishmaniasis treatment. *Appl. Microbiol. Biotechnol.* **104**, 8965–8977 (2020).
5. Loureiro, I. et al. Potential drug targets in the pentose phosphate pathway of trypanosomatids. *Curr. Med. Chem.* **25**, 5239–5265 (2018).
6. Comini, M. A., Ortíz, C. & Cazzulo, J. J. Drug targets in trypanosomal and leishmanial pentose phosphate pathway. In *Trypanosomatid Diseases* (edited by Jäger, T., Koch O. & Flohé L.) 297–313 (Wiley-VCH Verlag GmbH & Co. KGaA, Weinheim, Germany, 2013).
7. Gupta, S., Igoillo-Esteve, M., Michels, P. A. M. & Cordeiro, A. T. Glucose-6-phosphate dehydrogenase of trypanosomatids: characterization, target validation, and drug discovery. *Mol. Biol. Int.* **2011**, 135701 (2011).
8. Vonlaufen, N., Kanzok, S. M., Wek, R. C. & Sullivan, W. J. Stress response pathways in protozoan parasites. *Cell. Microbiol.* **10**, 2387–2399 (2008).
9. Krauth-Siegel, R. L. & Comini, M. A. Redox control in trypanosomatids, parasitic protozoa with trypanothione-based thiol metabolism. *Biochim. Biophys. Acta* **1780**, 1236–1248 (2008).
10. Kovářová, J. & Barrett, M. P. The pentose phosphate pathway in parasitic trypanosomatids. *Trends Parasitol.* **32**, 622–634 (2016).
11. Leroux, A. E., Maugeri, D. A., Opperdoes, F. R., Cazzulo, J. J. & Nowicki, C. Comparative studies on the biochemical properties of the malic enzymes from Trypanosoma cruzi and Trypanosoma brucei. *FEMS Microbiol. Lett.* **314**, 25–33 (2011).
12. Giordana, L. et al. Molecular and functional characterization of two malic enzymes from Leishmania parasites. *Mol. Biochem. Parasitol.* **219**, 67–76 (2018).
13. Cordeiro, A. T., Thiemann, O. H. & Michels, P. A. M. Inhibition of Trypanosoma brucei glucose-6-phosphate dehydrogenase by human steroids and their effects on the viability of cultured parasites. *Bioorg. Med. Chem.* **17**, 2483–2489 (2009).
14. Cordeiro, A. T. & Thiemann, O. H. 16-bromoepiandrosterone, an activator of the mammalian immune system, inhibits glucose 6-phosphate dehydrogenase from Trypanosoma cruzi and is toxic to these parasites grown in culture. *Bioorg. Med. Chem.* **18**, 4762–4768 (2010).
15. Ortíz, C. et al. Glucose 6-phosphate dehydrogenase from trypanosomes: selectivity for steroids and chemical validation in bloodstream Trypanosoma brucei. *Molecules* **26**, 358 (2021).
16. Solbach, W. & Laskay, T. The host response to leishmania infection. In *Advances in Immunology*, 1st ed. Vol. 74 (edited by Dixon F.J.) 275–317 (Elsevier textbooks, s.l., 1999).
17. Moradin, N. & Descoteaux, A. Leishmania promastigotes: building a safe niche within macrophages. *Front. Cell. Infect. Microbiol.* **2**, 121 (2012).
18. Ghosh, A. K. et al. Metabolic reconfiguration of the central glucose metabolism: a crucial strategy of Leishmania donovani for its survival during oxidative stress. *FASEB J.* **29**, 2081–2098 (2015).
19. Purkait, B. et al. Mechanism of amphotericin B resistance in clinical isolates of Leishmania donovani. *Antimicrob. Agents Chemother.* **56**, 1031–1041 (2012).
20. Sudhandiran, G. & Shaha, C. Antimonial-induced increase in intracellular Ca^{2+} through non-selective cation channels in the host and the parasite is responsible for apoptosis of intracellular Leishmania donovani amastigotes. *J. Biol. Chem.* **278**, 25120–25132 (2003).
21. Mishra, J. & Singh, S. Miltefosine resistance in Leishmania donovani involves suppression of oxidative stress-induced programmed cell death. *Exp. Parasitol.* **135**, 397–406 (2013).
22. Allen, S. M. et al. Plasmodium falciparum glucose-6-phosphate dehydrogenase 6-phosphogluconolactonase is a potential drug target. *FEBS J.* **282**, 3808–3823 (2015).
23. Maloney, P. *et al.* A selective inhibitor of plasmodium falciparum glucose-6-phosphate dehydrogenase (PfG6PDH). In *Probe Reports from the NIH Molecular Libraries Program.* (Bethesda (MD), 2010).
24. Haeussler, K. et al. Glucose 6-phosphate dehydrogenase 6-phosphogluconolactonase: characterization of the Plasmodium vivax enzyme and inhibitor studies. *Malar. J.* **18**, 22 (2019).
25. Berneburg, I. et al. An optimized dihydrodibenzothiazepine lead compound (SBI-0797750) as a potent and selective inhibitor of Plasmodium falciparum and P. vivax glucose 6-phosphate dehydrogenase 6-phosphogluconolactonase. *Antimicrob. Agents Chemother.* **66**, e0210921 (2022).
26. Au, S. W. N., Gover, S., Lam, V. M. S. & Adams, M. J. Human glucose-6-phosphate dehydrogenase: the crystal structure reveals a structural NADP + molecule and provides insights into enzyme deficiency. *Structure* **8**, 293–303 (2000).
27. Kotaka, M. et al. Structural studies of glucose-6-phosphate and NADP+ binding to human glucose-6-phosphate dehydrogenase. *Acta Crystallogr. Sect. D: Biol. Crystallogr.* **61**, 495–504 (2005).
28. Mercaldi, G. F., Dawson, A., Hunter, W. N. & Cordeiro, A. T. The structure of a Trypanosoma cruzi glucose-6-phosphate dehydrogenase reveals differences from the mammalian enzyme. *FEBS Lett.* **590**, 2776–2786 (2016).
29. Ortíz, C., Botti, H., Buschiazzo, A. & Comini, M. A. Glucose-6-phosphate dehydrogenase from the human pathogen Trypanosoma cruzi evolved unique structural features to support efficient product formation. *J. Mol. Biol.* **431**, 2143–2162 (2019).

30. Cleland, W. The kinetics of enzyme-catalyzed reactions with two or more substrates or products. *Biochim. Biophys. Acta* **67**, 104–137 (1963).
31. Levy, H., Christoff, M., Ingulli, J. & Ho, E. M. Glucose-6-phosphate dehydrogenase from Leuconostoc mesenteroides: revised kinetic mechanism and kinetics of ATP inhibition. *Arch. Biochem. Biophys.* **222**, 473–488 (1983).
32. Wang, X.-T., Au, S. W. N., Lam, V. M. S. & Engel, P. C. Recombinant human glucose-6-phosphate dehydrogenase. Evidence for a rapid-equilibrium random-order mechanism. *Eur. J. Biochem.* **269**, 3417–3424 (2002).
33. Jortzik, E. et al. Glucose-6-phosphate dehydrogenase-6-phosphogluconolactonase: a unique bifunctional enzyme from Plasmodium falciparum. *Biochem. J.* **436**, 641–650 (2011).
34. Rowland, P., Basak, A. K., Gover, S., Levy, H. & Adams, M. J. The three–dimensional structure of glucose 6–phosphate dehydrogenase from Leuconostoc mesenteroides refined at 2.0 Å resolution. *Structure* **2**, 1073–1087 (1994).
35. Cohen, P. & Rosemeyer, M. A. Subunit interactions of glucose-6-phosphate dehydrogenase from human erythrocytes. *Eur. J. Biochem.* **8**, 8–15 (1969).
36. Wrigley, N. G., Heather, J. V., Bonsignore, A. & Flora, A. Human erythrocyte glucose 6-phosphate dehydrogenase: electron microscope studies on structure and interconversion of tetramers, dimers and monomers. *J. Mol. Biol.* **68**, 483–499 (1972).
37. Ranzani, A. T. & Cordeiro, A. T. Mutations in the tetramer interface of human glucose-6-phosphate dehydrogenase reveals kinetic differences between oligomeric states. *FEBS Lett.* **591**, 1278–1284 (2017).
38. Glaser, T. A., Baatz, J. E., Kreishman, G. P. & Mukkada, A. J. pH homeostasis in Leishmania donovani amastigotes and promastigotes. *PNAS* **85**, 7602–7606 (1988).
39. Igoillo-Esteve, M. & Cazzulo, J. J. The glucose-6-phosphate dehydrogenase from Trypanosoma cruzi: its role in the defense of the parasite against oxidative stress. *Mol. Biochem. Parasitol.* **149**, 170–181 (2006).
40. Jiang, P. et al. p53 regulates biosynthesis through direct inactivation of glucose-6-phosphate dehydrogenase. *Nat. Cell Biol.* **13**, 310–316 (2011).
41. Ghosh, A. K. et al. Glucose-6-phosphate dehydrogenase and Trypanothione reductase interaction protects Leishmania donovani from metalloid mediated oxidative stress. *Free Radic. Biol. Med.* **106**, 10–23 (2017).
42. Ulusu, N. N., Tandogan, B. & Tezcan, F. E. Kinetic properties of glucose-6-phosphate dehydrogenase from lamb kidney cortex. *Biochimie* **87**, 187–190 (2005).
43. Guo, H., Han, J., Wu, J. & Chen, H. Heteroexpression and functional characterization of glucose 6-phosphate dehydrogenase from industrial Aspergillus oryzae. *J. Microbiol. Biotechnol.* **29**, 577–586 (2019).
44. Tsai, C. S. & Chen, Q. Purification and kinetic characterization of hexokinase and glucose-6-phosphate dehydrogenase from Schizosaccharomyces pombe. *Biochem. Cell. Biol.* **76**, 107–113 (1998).
45. Purich, D. L. *Enzyme Kinetics. Catalysis & Control; a Reference of Theory and Best-Pratice Methods*. 1st ed. (Elsevier/AP, Amsterdam, 2010).
46. Beutler, E. *Red Cell Metabolism. A Manual of Biochemical Methods*. 3rd ed. (Grune & Stratton, Orlando, 1984).
47. Kabsch, W. Integration, scaling, space-group assignment and post-refinement. *Acta Crystallogr. Sect. D: Biol. Crystallogr.* **66**, 133–144 (2010).
48. Waterhouse, A. et al. SWISS-MODEL: homology modelling of protein structures and complexes. *Nucleic Acids Res.* **46**, W296–W303 (2018).
49. Adams, P. D. et al. PHENIX: a comprehensive Python-based system for macromolecular structure solution. *Acta Crystallogr. Sect. D: Biol. Crystallogr.* **66**, 213–221 (2010).
50. Moriarty, N. W., Tronrud, D. E., Adams, P. D. & Karplus, P. A. A new default restraint library for the protein backbone in Phenix: a conformation-dependent geometry goes mainstream. *Acta Crystallogr. Sect. D: Biol. Crystallogr.* **72**, 176–179 (2016).
51. Emsley, P. & Cowtan, K. Coot: model-building tools for molecular graphics. *Acta Crystallogr. Sect. D: Biol. Crystallogr.* **60**, 2126–2132 (2004).
52. Pettersen, E. F. et al. UCSF Chimera–a visualization system for exploratory research and analysis. *J. Comput. Chem.* **25**, 1605–1612 (2004).

Acknowledgements

The authors wish to thank Michaela Stumpf for her excellent technical assistance. Furthermore, we would like to thank Ilme Schlichting and Miroslaw Tarnawski for the thoughtfully arranged data collection. Diffraction data were collected at beamline X10SA, Swiss Light Source, Paul Scherrer Institute, Villigen, Switzerland, and the authors thank the beamline staff for the excellent setup. The LOEWE Center DRUID (Projects B3 and E3) of the Hessian Excellence Program supported this work.

Author contributions

Conceptualization (K.B., K.F.W., I.B.); Data curation (I.B., K.F.W.); Formal analysis (I.B., K.F.W.); Funding acquisition (K.B.); Investigation (I.B.); Methodology (I.B., K.F.W., S.R.); Resources (K.B., K.F.W.); Software (K.F.W.); Supervision (K.B., K.F.W.); Validation (K.F.W., I.B.); Visualization (I.B.); Roles/Writing—original draft (I.B.); Writing—review & editing (K.F.W., I.B., K.B., S.R.).

Funding

Open Access funding enabled and organized by Projekt DEAL.

Competing interests

The authors declare no competing interests.

Additional information

Supplementary information The online version contains supplementary material available at https://doi.org/10.1038/s42003-022-04307-7.

Correspondence and requests for materials should be addressed to Karin Fritz-Wolf.

Peer review information *Communications Biology* thanks the anonymous reviewers for their contribution to the peer review of this work. Primary Handling Editor: Gene Chong. Peer reviewer reports are available.

Reprints and permission information is available at http://www.nature.com/reprints

Publisher's note Springer Nature remains neutral with regard to jurisdictional claims in published maps and institutional affiliations.

3.3. Publication III

Structure of *Leishmania donovani* 6-phosphogluconate dehydrogenase and inhibition by phosphine gold(I) complexes: A potential approach to leishmaniasis treatment

Berneburg I, Stumpf M, Velten A-S, Rahlfs S, Przyborski J, Becker K, Fritz-Wolf K

Int J Mol Sci 24

2023

https://doi.org/10.3390/ijms24108615

International Journal of
Molecular Sciences

MDPI

Article

Structure of *Leishmania donovani* 6-Phosphogluconate Dehydrogenase and Inhibition by Phosphine Gold(I) Complexes: A Potential Approach to Leishmaniasis Treatment

Isabell Berneburg [1], Michaela Stumpf [1], Ann-Sophie Velten [1], Stefan Rahlfs [1], Jude Przyborski [1], Katja Becker [1] and Karin Fritz-Wolf [1,2,*]

[1] Biochemistry and Molecular Biology, Interdisciplinary Research Center, Justus Liebig University, 35392 Giessen, Germany; isabell.berneburg@ernaehrung.uni-giessen.de (I.B.)
[2] Max Planck Institute for Medical Research, 69120 Heidelberg, Germany
* Correspondence: karin.fritz@mr.mpg.de; Tel.: +49-6221486275

Abstract: As unicellular parasites are highly dependent on NADPH as a source for reducing equivalents, the main NADPH-producing enzymes glucose 6-phosphate dehydrogenase (G6PD) and 6-phosphogluconate dehydrogenase (6PGD) of the pentose phosphate pathway are considered promising antitrypanosomatid drug targets. Here we present the biochemical characterization and crystal structure of *Leishmania donovani* 6PGD (*Ld*6PGD) in complex with NADP(H). Most interestingly, a previously unknown conformation of NADPH is visible in this structure. In addition, we identified auranofin and other gold(I)-containing compounds as efficient *Ld*6PGD inhibitors, although it has so far been assumed that trypanothione reductase is the sole target of auranofin in *Kinetoplastida*. Interestingly, 6PGD from *Plasmodium falciparum* is also inhibited at lower micromolar concentrations, whereas human 6PGD is not. Mode-of-inhibition studies indicate that auranofin competes with 6PG for its binding site followed by a rapid irreversible inhibition. By analogy with other enzymes, this suggests that the gold moiety is responsible for the observed inhibition. Taken together, we identified gold(I)-containing compounds as an interesting class of inhibitors against 6PGDs from *Leishmania* and possibly from other protozoan parasites. Together with the three-dimensional crystal structure, this provides a valid basis for further drug discovery approaches.

Keywords: leishmaniasis; 6-phosphogluconate dehydrogenase; pentose phosphate pathway; auranofin; phosphine gold(I)-complexes

Citation: Berneburg, I.; Stumpf, M.; Velten, A.-S.; Rahlfs, S.; Przyborski, J.; Becker, K.; Fritz-Wolf, K. Structure of *Leishmania donovani* 6-Phosphogluconate Dehydrogenase and Inhibition by Phosphine Gold(I) Complexes: A Potential Approach to Leishmaniasis Treatment. *Int. J. Mol. Sci.* **2023**, *24*, 8615. https://doi.org/10.3390/ijms24108615

Academic Editor: Manlio Tolomeo

Received: 28 March 2023
Revised: 8 May 2023
Accepted: 9 May 2023
Published: 11 May 2023

1. Introduction

Leishmaniasis is a vector-borne infectious disease that is classified by the World Health Organization as one of 20 poverty-related and neglected tropical diseases. It is caused by the protozoan parasite of the genus *Leishmania*, which belongs to the *Trypanosomatidae* family. Every year, 0.7 to one million people become infected, and 20,000 to 30,000 people die from leishmaniasis in tropical, subtropical and southern European regions. The species *Leishmania donovani* causes the most severe form, also known as kala-azar or "black fever" and is often fatal if untreated [1,2]. Currently, there are only a few drugs available for leishmaniasis treatment. Most of them have severe side effects and show highly divergent activities across subspecies. After decades of use, resistant parasites have emerged [3–5], which is why ambitious efforts to develop new drug targets and antileishmanial agents are urgently required.

Throughout their life cycle, many parasites, and *Leishmania* parasites in particular, are exposed to high levels of oxidative stress. For example, the tissue stages of *Leishmania*—amastigotes—reside in mammalian macrophages and must withstand the action of reactive oxygen and nitrogen species (ROS/RNS) produced by enzymes such as NADPH oxidase or nitric oxide (NO) synthase [6–9]. The antioxidant defense and redox balance of the

parasites rely on the trypanothione-dependent thiol system, including trypanothione and trypanothione reductase, and depend on NADPH as the primary electron source [10,11]. As the pentose phosphate pathway (PPP) is the main NADPH supplier in most parasites, the enzymes of this key metabolic pathway are considered promising drug targets for the control of unicellular parasites such as *Leishmania*, *Trypanosoma* [3,12,13] and *Plasmodium* [14,15]. NADPH is produced in the first, unidirectional oxidative branch of the PPP. The second, non-oxidative branch of the PPP ends with ribose 5-phosphate, a crucial product for nucleotide biosynthesis. In total, two molecules NADPH are produced by the oxidative PPP. Glucose 6-phosphate dehydrogenase (G6PD) (EC 1.1.1.49) is the first enzyme of this pathway and catalyzes the oxidation of glucose 6-phosphate (G6P) from glycolysis to 6-phospho-D-glucono-1,5-lactone, whereby the cofactor $NADP^+$ is reduced to one molecule, NADPH. 6-phosphocluconate dehydrogenase (6PGD) (EC 1.1.1.44) is the third enzyme of the oxidative branch and generates a second NADPH molecule by decarboxylating 6-phosphogluconate (6PG) to ribulose 5-phosphate (R5P) and CO_2 [11]. In trypanosomatids, enzymes of the PPP as well as other glycolytic enzymes are localized in the cytosol as well as in peroxisome-related glycosomes, probably allowing a fast adaption to environmental changes and preventing accumulation of toxic metabolites [16–18]. G6PD, the first enzyme of the PPP, is considered to be the rate-limiting enzyme of this pathway. However, 6PGD activity also influences the PPP and glycolytic enzymes. 6PGD inhibition leads to an accumulation of toxic 6PG, which in turn inhibits the glycolytic enzyme glucose 6-phosphate isomerase [19]. This triggers a positive feedback loop leading to more glucose 6-phosphate flux via the PPP and consequently inhibition of glycolysis [3,20,21] and has been shown to be lethal to some eukaryotes, such as *Trypanosoma brucei* [20], which belong to the same family as *Leishmania*. However, RNAi knockdown of 6PGD in bloodstream *Trypanosoma brucei* (*Tb*6PGD^{RNAi}), which leads to reduced 6PGD activity and subsequent cell death, suggests that loss of the oxidative branch of the PPP is lethal, rather than inhibition of glycolysis or lack of ribose 5-phosphate for nucleotide biosynthesis, as neither the addition of fructose nor ribose prevented cell death of the *Tb*6PGD^{RNAi} cell line [22]. The suitability of *Tb*6PGD as drug target is further supported by *Tb*6PGD inhibitors that enable selective inhibition compared to the mammalian counterpart [23]. Since *Leishmania* 6PGD shares high sequence similarity to other trypanosomatid 6PGDs and at the same time differs significantly from its human counterpart, 6PGD has also been proposed as a drug target in *Leishmania* [24]. Moreover, strains resistant to commonly used antileishmanial drugs such as miltefosine [25], amphotericin-B [26] and sodium antimony gluconate [27], whose mode of action is thought to be associated with increased ROS production, showed an upregulation of the PPP [9].

Recently, the FDA-approved drug auranofin, which has been used for decades against rheumatoid arthritis [28,29], received increasing attention because of its potential to be repurposed as an antiparasitic drug [30–34]. Its antiparasitic activity has also been demonstrated for *Trypanosoma* [35,36] and *Leishmania* spp. [37–39]. Although the mechanism of action (MOA) of auranofin and other gold(I)-containing drugs is still a matter of debate as they appear to have multiple targets, the suggested MOA in *Kinetoplastida* is the inhibition of the redox enzyme trypanothione reductase (TR) [36,37,39], and thus comparable to the target thioredoxin reductase (TrxR) in mammals [40–42] and several other parasites [31,43]. Inhibition of these redox enzymes is associated with a disruption of redox homeostasis, leading to severe oxidative stress and cytotoxic effects in vitro [38,39,44]. However, recent studies on auranofin resistance in several protozoan parasites, such as *Toxoplasma gondii*, *Entamoeba histolytica* and *Giardia lamblia*, suggest that TrxR may not be the sole target of auranofin, as auranofin-resistant parasite strains accumulate less ROS, without any mutations in the TrxR gene or changes in TrxR expression levels [34,45,46]. These studies prompted us to test auranofin against other redox enzymes, such as the NADPH-producing enzymes of the PPP. Indeed, auranofin and other gold(I)-containing compounds inhibit *Ld*6PGD in the low micromolar range, whereas the human enzyme is hardly affected at these concentrations. This gives reason to reinterpret previous in vivo studies with auranofin in *Kinetoplastida*, as

its MOA can no longer be attributed solely to TR inhibition. Mode-of-inhibition studies of auranofin indicated an initial competition with the 6PG binding site followed by a rapid irreversible inhibition. In addition, we solved the three-dimensional crystal structure of *Ld*6PGD in complex with NADP(H), revealing a previously unknown conformation of NADPH. Finally, these structural and biochemical insights into *Ld*6PGD provide an excellent basis for further structure-based studies on gold(I)-containing compounds as an interesting class of protozoan 6PGD inhibitors.

2. Results and Discussion

2.1. Production, Oligomerization Behavior and Kinetic Characterization of Ld6PGD wt

Leishmania donovani 6PGD was recombinantly produced using a pET28a vector in *E. coli* (DE3) cells and resulted in a final yield of 1–4 mg soluble, pure and active *Ld*6PGD per liter of *E. coli* culture (Figure S1).

To investigate the oligomerization behavior of *Ld*6PGD, we performed size exclusion chromatography (SEC) under different conditions. Under native conditions, the SEC profiles of *Ld*6PGD wt revealed one stable peak representing a molecular mass of 94–111 kDa (Figure 1a), which is equivalent to the dimeric form of the *Ld*6PGD wt and in accordance with previously published SEC profiles from *Leishmania* 6PGDs [24,47]. Varying *Ld*6PGD concentrations did not affect the elution profile (Figure S2). Moreover, the elution pattern of *Ld*6PGD was neither affected by reductive (5 mM DTT) nor by oxidative conditions (2 mM H_2O_2) (Figure 1a), suggesting the formation of the dimer is independent from intermolecular disulfide bonds. Most other 6PGDs are active as homodimers and also exhibited a dimer in the crystal structure, such as human 6PGD (*Hs*6PGD) [48–50] (PDBIDs: 5UQ9 [50]; 2JKV, to be published) or 6PGDs from *Ovis aries* (PDBID: 1PGO [51]), *Saccharomyces cerevisiae* (PDBID: 2P4Q [52]), *Plasmodium falciparum* (*Pf*6PGD) (PDBID: 6FQX [49]), *Lactococcus lactis* (PDBID: 2IYO [53]), *Geobacillus stearothermophilus* (PDBID: 2W8Z [54]) or from the related *Trypanosoma brucei* 6PGD (*Tb*6PGD) (PDBID: 1PGJ [55]). Hanau et al. [21,56] found that *Tb*6PGD exists in a dynamic dimer–tetramer equilibrium, which is shifted towards the tetramer in presence of the product NADPH. Therefore, we tested whether the oligomerization of *Ld*6PGD is similarly affected and performed SEC in the presence of substrates and products. In contrast to the *Tb*6PGD [56], our studies do not support a dimer–tetramer equilibrium for *Leishmania* 6PGDs, since the dimer remained unaffected under the conditions tested (Figure 1b).

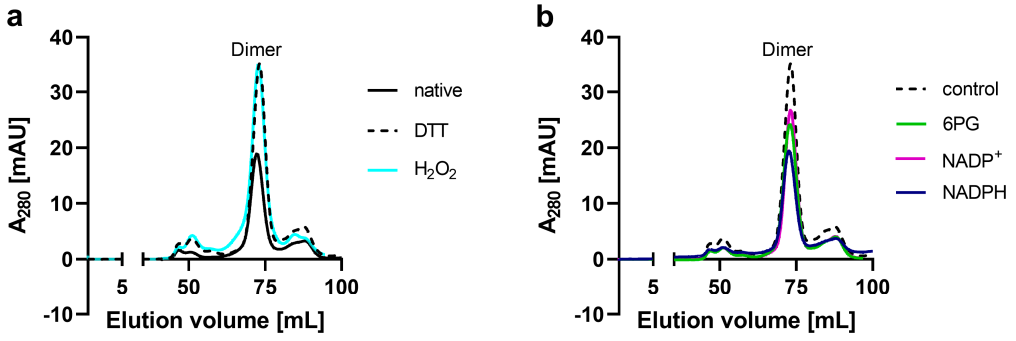

Figure 1. SEC analysis of recombinant *Ld*6PGD. Full-length *Ld*6PGD wt was gel filtrated on a HiLoad 16/60 Superdex 200 column pre-equilibrated in buffer A (500 mM NaCl, 50 mM Tris, pH 7.8). (**a**) SEC profiles of *Ld*6PGD wt under native, reductive and oxidative conditions. SEC of *Ld*6PGD wt under native conditions (black, rv = 72.3 mL ≙ 93.9 kDa), in the presence of 5 mM DTT (black-dotted, rv = 73.2 mL ≙ 87.3 kDa) and 2 mM H_2O_2 (cyan, rv = 72.8 mL ≙ 89.9 kDa) revealed identical elution patterns with one peak equivalent to a dimer. (**b**) SEC profiles of *Ld*6PGD wt in the presence or absence of ligands. SEC in the presence of 0.2 mM 6PG (green, rv = 72.95 mL ≙ 88.8 kDa), in the presence of 0.2 mM $NADP^+$ (magenta, rv = 73.2 mL ≙ 87.2 kDa) and 0.2 mM NADPH (purple, rv = 72.6 mL ≙ 91.5 kDa). For comparative reasons, a control without ligands is shown (black-dotted, rv = 73.2 mL ≙ 87.3 kDa). Representative chromatograms ($n \geq 2$) are shown for each condition.

Steady-state kinetics revealed a specific activity of the *Ld*6PGD wt dimer of 33.3 ± 5.1 U·mg^{-1} with apparent K_M values of 20.2 ± 2.9 µM for the substrate 6PG and 13.7 ± 1.2 µM for the cosubstrate NADP$^+$. Based on these values, we calculated a catalytic efficiency of 1.5 ± 0.02 µM^{-1}·s^{-1} for 6PG and of 2.2 ± 0.2 µM^{-1}·s^{-1} for NADP$^+$ (Table 1). These values are very similar to other 6PGDs characterized so far [47,49,57,58] and nearly identical to 6PGDs of the related *Trypanosoma* species *T. cruzi* and *T. brucei* [59,60], with which *Leishmania* 6PGD shares a high sequence identity of approximately 70%.

Table 1. Comparative kinetic parameters of recombinant 6PGD from *Leishmania donovani* and different homologous species.

	6PG				NADP$^+$			
	V_{max} (U·mg^{-1})	K_M (µM)	k_{cat} (s^{-1})	k_{cat}/K_M (µM^{-1}·s^{-1})	V_{max} (U·mg^{-1})	K_M (µM)	k_{cat} (s^{-1})	k_{cat}/K_M (µM^{-1}·s^{-1})
Leishmania donovani	33.3 ± 5.1	20.2 ± 2.9	30.8 ± 4.7	1.5 ± 0.02	33.1 ± 5.2	13.7 ± 1.2	30.5 ± 4.8	2.2 ± 0.2
Leishmania donovani [47]	n/a	80.2 ± 7.4	1.0 ± 0.02	0.01	n/a	22.4 ± 2.7	0.9 ± 0.02	0.04
Trypanosoma cruzi [60]	32	22.2	n/a	n/a	32	5.9	n/a	n/a
Trypanosoma brucei [59,60]	31.3	3.5	27	7.7	31.2	1.5	27	18
Plasmodium falciparum [49]	8.0 ± 1.8	11.3 ± 2.7	7.1 ± 2.5	0.6	8.0 ± 1.8	9.0 ± 4.2	7.6 ± 2.2	0.84
Giardia lamblia [58]	26.2	49.2	n/a	n/a	26.2	139.9	n/a	n/a
Human [49]	22.1 ± 1.2	33.7 ± 7.1	22.2 ± 0.3	0.6	22.1 ± 1.2	6.9 ± 2.0	21.4 ± 0.8	3.1
Sheep liver [57]	18.8 ± 0.9	16.1 ± 1.3	n/a	n/a	18.8 ± 0.9	6.76 ± 1.6	n/a	n/a

n/a—not available. Values are expressed as mean ± SD from at least three independent determinations with different enzyme batches, each including at least three measurements.

2.2. Crystallization and Structure Determination of Ld6PGD

We obtained orthorhombic ($P2_12_12_1$) crystals of the *Ld*6PGD wt in complex with NADP(H) (PDBID: 8C79). The structure was solved at 3.1 Å by the molecular replacement method, using *T. brucei* 6PGD (PDBID: 1PGJ) as a template, which shares 72% sequence identity with *Ld*6PGD (Figure 2). The crystal contained two monomers in the asymmetric unit (AU), which were essentially similar to an RMSD of 0.4 Å (478 residues). The omit maps displayed clear density for one phosphate ion in each subunit and one NADP(H) molecule in subunit A. In subunit B, most of the NADP(H) molecule is well defined by electron density, except for the nicotinamide and the adenine moieties, which are not visible. The structure contains a complete model of *Ld*6PGD, comprising residues 1–478, two NADP(H) molecules, two phosphate ions and one water molecule. Despite the relatively high Wilson B-factor of 129 Å^2, the structure is well defined by the electron density and displays good stereochemistry. All data collection and refinement statistics are summarized in Table 2.

2.3. Overall Structure of Ld6PGD

The primary sequences as well as the three-dimensional structures within the 6PGD family are highly conserved. This is also true for *Ld*6PGD, which shares high sequence similarity and identity with other 6PGDs of this family (Figure 2). Similar to other members of the 6PGD family, *Ld*6PGD is a functional homodimer and adopts the canonical 6PGD fold (Figure 3) with RMSD values for the dimer of 1.4 Å (956 residues), 1.0 Å (954 residues) and 1.8 Å (878 residues) to human (37% sequence identity; PDBID: 2JKV; NADP$^+$-complexed structure), *T. brucei* (72% sequence identity; PDBID: 1PGJ; apo structure) and *P. falciparum* 6PGD (34% sequence identity; PDBIDs: 6FQZ; 6PG-complexed structure), respectively.

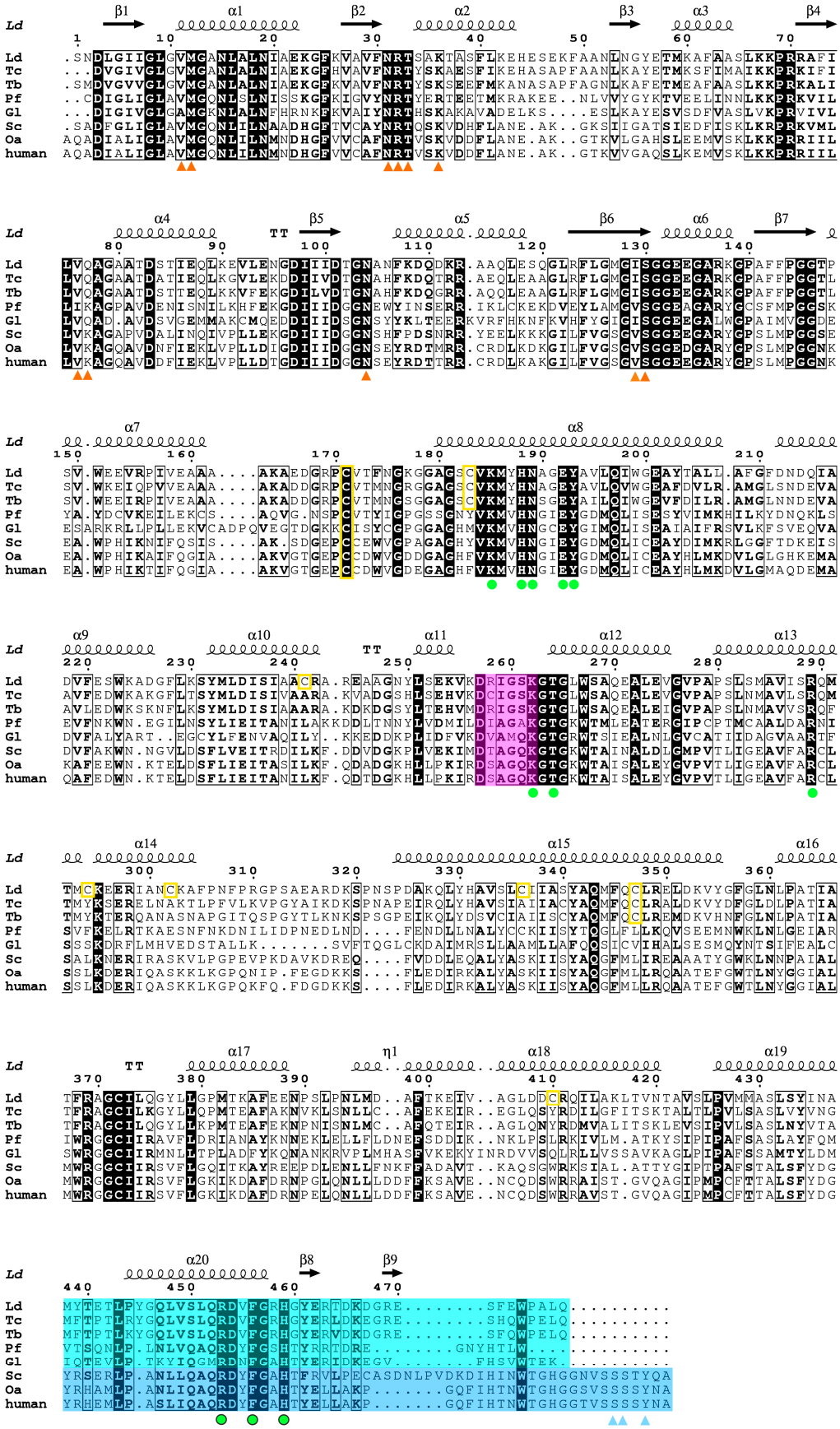

Figure 2. Structure-based multiple sequence alignment of 6PGDs from various species. Shown 6PGD sequences correspond to *Leishmania donovani* (Ld; acc. no. Q18L02), *Trypanosoma cruzi* (Tc; acc. no.

Q6WAT5), *Trypanosoma brucei brucei* (Tb; acc. no. P31072), *Plasmodium falciparum* (Pf; acc. no. Q8IKT2), *Giardia lamblia* (Gl; acc. no. A8BWM8), *Saccharomyces cerevisiae* (Sc; acc. no. P38720), *Ovis aries* (Oa; acc. no. P00349) and *Homo sapiens* (human; acc. no. P52209). Strictly conserved residues are highlighted with black background, while highly similar residues, with similar physicochemical properties in at least six out of the eight sequences, are shown in bold letters. The secondary structure elements of *Ld*6PGD (PDBID: 8C79) are displayed above the sequence alignment. Residues of the $NADP^+$ binding site are displayed as orange triangles. Blue triangles correspond to the *Hs*6PGD sequence and indicate additional residues, which are involved in $NADP^+$ binding. The 6PG binding site comprises residues from both subunits and is therefore displayed as green dots for one subunit and green dots with black outlines for the adjacent subunit. Yellow-colored boxes indicate cysteines of the *Ld*6PGD structure. Residues of the active site loop (D257-T262) are highlighted in magenta. Residues of the C-terminal domain of protozoan species and multicellular species with elongated C-terminus are highlighted in cyan and blue, respectively. The structure-based multiple sequence alignment was performed using the program ESPript 3.0.

Table 2. Data collection and refinement statistics.

PDB Code	8C79
Data collection	
Space group	P 21 21 21
Cell dimensions	
a, b, c (Å)	65.87, 117.35, 128.91
α, β, γ (°)	90, 90, 90
Resolution (Å)	46.1–3.1 (3.2–3.1)
R-merge (%)	8.7 (184.6)
$I/\sigma I$	9.9 (0.9)
Completeness (%)	99.57 (99.95)
Redundancy	5.1 (5.2)
Molecules per AU	2
Wilson B-factor	129.0
$CC_{1/2}$ (%)	99.8 (34.8)
Refinement	
Resolution (Å)	3.1
No. reflections	18,687
R_{work}/R_{free} (%)	26.2 (41.3)/31.7 (45.0)
No. atoms	
Proteins	7278
Ligands	87
Water	1
Protein residues	956
B-factors	
Proteins	126.6
Ligands	121.0
Water	93.8
Ramachandran plot (%)	
Favored (%)	97.5
R. m. s. deviations	
Bonds lengths	0.011
Bond angles	0.94

Values in parentheses are for the highest-resolution shell.

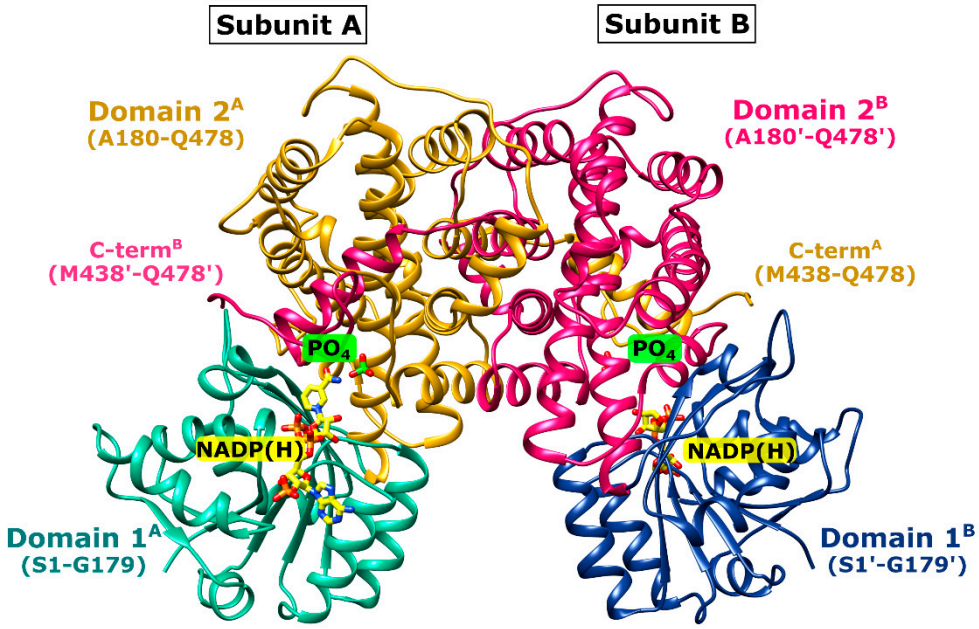

Figure 3. Overview of the *Ld*6PGD wt dimer. *Ld*6PGD wt dimer in complex with NADP(H) and phosphate (PO_4) is shown in ribbon presentation. The "Rossmann-like" domain 1 (S1-K179) of subunits A (domain 1^A) and B (domain 1^B) is colored light green and navy blue, respectively. Domain 2 (A180-Q478) of subunits A (domain 2^A) and B (domain 2^B) is colored gold and magenta, respectively. The C-terminal domain of domain 2 comprises residues M348-Q478. Within the 6PG binding site, a PO_4 ion (green) is visible instead of the substrate 6PG. The cosubstrate NADP(H) (yellow) and the PO_4 (green) of subunit A and B are shown as stick models.

The *Ld*6PGD monomer contains the typical 6PGD domains: the smaller N-terminal "Rossmann-like" domain 1 (S1-K177), which is composed of a mixed parallel and anti-parallel seven-stranded β-sheet, and the larger, mainly α-helical domain 2 (A180-Q478). The C-terminal tail of domain 2 (M438-Q478) invades the neighboring subunit so that each active site is built by residues of both subunits (Figure 3). Each subunit of the homodimer comprises a $NADP^+$ and a 6PG binding site (Figures 4 and S3). The 6PG binding site is located in a cleft of domain 2 and includes the following residues: S130-G132, K185, N189, E192, Y193, K262, T264, and R289 from one subunit and R453′ and H459′ from the adjacent monomer. NADP(H) is bound by conserved residues of domain 1. Upon catalysis, the binding site of the nicotinamide ring and 6PG overlaps and is formed by M12, E192, N104, I129-G132, K185, N189 and F456′ and H459′ from the other subunit.

2.4. Active Site in the Ld6PGD Structure

In our *Ld*6PGD structure, NADP(H) is located at the conserved $NADP^+$ binding site (Figure 4a). The amino acids N31, R32 and T33 interact with one of the phosphates, N31 and N104 with the ribose moieties and the diphosphates are bound by main chain atoms of residues V11 and M12. Via van der Waals forces, I129 and S130 interact with the nicotinamide ring, which is also hydrogen bonded to a phosphate ion. This phosphate ion is located at the same position as the phosphate moiety of homologous 6PG-complexed structures (PDBIDs: 2IYO, 6FQZ) (Figure 4b) and also interacts with homologous strictly conserved residues (Y193, K262, T264, R289 and R453′, H459′ from the adjacent subunit) in a similar manner to other 6PGDs. Moreover, a hydrogen bond (2.6 Å) is visible between the phosphate ion and the nicotinamide ring (N7N atom) of NADP(H). It is known for many 6PGDs that a flexible active site loop adopts an open and a closed conformation depending on substrate binding [49]. The active site loop adopts the closed conformation when the 6PG binding site is occupied by ligands or at least by anions such as phosphate, sulfate or citrate, all of which are capable of interacting with residues of the C-terminal

tail. According to this, the active site loop residues (D257-T262) of the *Ld*6PGD structure, complexed with a phosphate at the 6PG binding site, adopt the closed conformation.

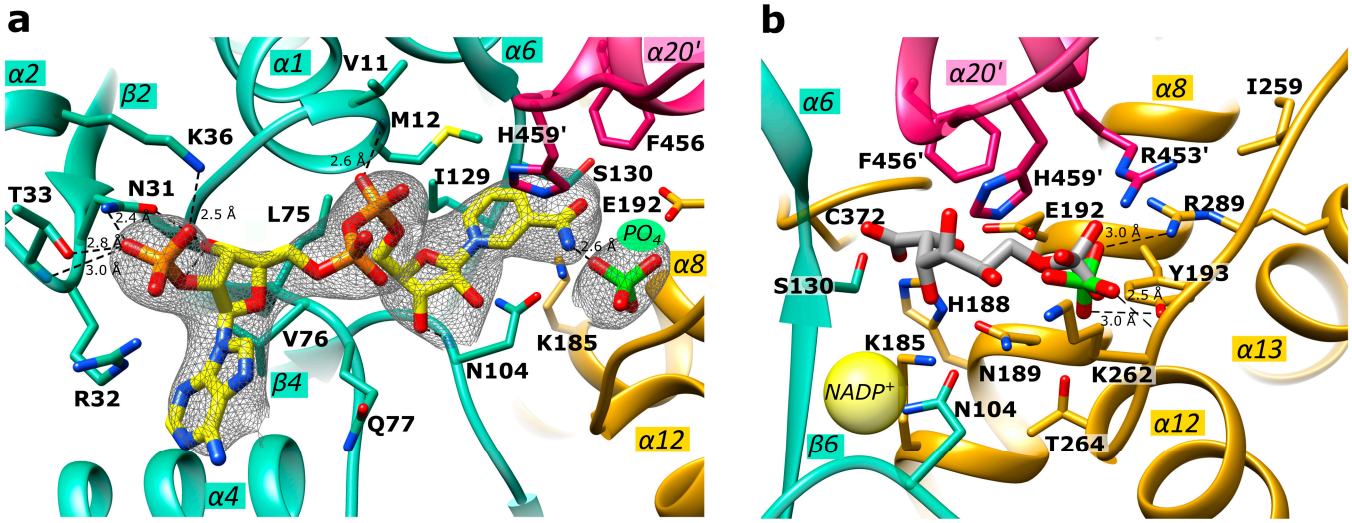

Figure 4. Active site close-up of *Ld*6PGD. The active site of monomer A is shown. Ribbons and residues of domain 1 are colored light green and of domain 2, gold. The C-terminal part of domain 2 of monomer B is colored magenta. (**a**) Close-up of the NADP(H) binding pocket within the "Rossmann-like" domain. The NADP(H) moiety is colored yellow. Within the 6PG binding pocket, a phosphate ion (PO_4) is visible (green). Electron density map (F_O-F_C polder map) contoured at 3.0 σ for NADP(H) and PO_4 is shown in black. (**b**) Close-up of the 6PG binding pocket. 6PG (gray) is shown from the superimposed *Pf*6PGD structure (PDBID: 6FQZ) with the PO_4 moiety at the same position as the PO_4 visible in our structure (green). The approximate position of $NADP^+$ is marked with a yellow ball. Residues of the $NADP^+$ and the 6PG binding pocket are shown in stick models, and hydrogen bonds are indicated with black dotted lines.

2.5. Mechanistic Considerations

There is clear electron density for an NADP(H)-molecule and a phosphate ion in the active site, which are connected by a hydrogen bond (Figures 4 and S3). Since *Ld*6PGD was crystallized under catalysis, in the presence of both substrates, 6PG and $NADP^+$, it could be also the products (R5P, NADPH) or an intermediate state of substrate and product that are visible in the active site. A structural comparison of the *Ld*6PGD structure with homologous $NADP^+$-complexed structures (*Ovis aries*, PDBID: 1PGN; *Lactococcus lactis*, PDBID: 2IYP; *Hs*6PGD, PDBID: 2JKV) revealed that the NADP(H) molecule is bound very similarly in these structures, except for the nicotinamide ring (Figure 5a), which adopts the same conformation as in the NADPH-complexed 6PGD structure from *Ovis aries* (PDBID: 1PGO) (Figure 5b).

It has been shown earlier that the orientation of the nicotinamide ring indicates whether $NADP^+$ or NADPH is bound [51]. When the cosubstrate is reduced to NADPH, the nicotinamide ring rotates from syn to anti and points therefore towards the 6PG binding site, which also involves a rotation of the ribose and phosphate moieties so that the ribose oxygen atoms then point towards the solvent (Figure 5b). Considering only the position of the nicotinamide ring, which is similarly oriented as in the NADPH-complexed structure from *Ovis aries* (PDBID: 1PGO), we conclude that NADPH is bound in the *Ld*6PGD structure. On the other hand, the position of the ribose unit and phosphates in the *Ld*6PGD structure corresponds to the $NADP^+$-complexed structures, thus $NADP^+$ would be bound in the *Ld*6PGD structure (Figure 5a).

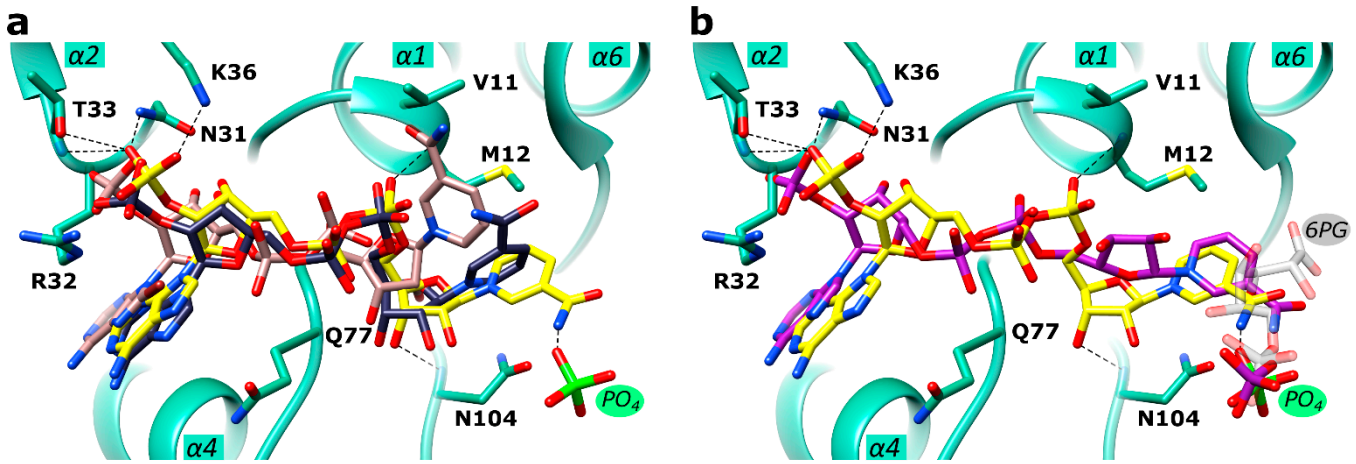

Figure 5. Comparison of $NADP^+$ and NADPH conformations in *Ld*6PGD and orthologues. The structures from *Ld*6PGD, human (*Hs*), *Ovis aries (Oa)* and *Plasmodium falciparum* (*Pf*) are superimposed, but for clarity, only the ribbon and residues of domain 1 of the *Ld*6PGD structure are shown and colored light green. (**a**) NADP(H) from the *Ld*6PGD structure is colored yellow. The $NADP^+$ molecule from the $NADP^+$-complexed structures of *Hs*6PGD (PDBID: 2JKV) and of *Oa*6PGD (PDBID: 1PGN) is colored navy blue and nude, respectively. (**b**) NADP(H) from the *Ld*6PGD structure is shown in yellow and NADPH from the NADPH-complexed *Oa*6PGD structure (PDBID: 1PGO) in purple. 6PG (transparent) is taken from the *Pf*6PGD structure (PDBID: 6FQZ) with the phosphate moiety at the same position as the PO_4 (green) visible in our structure. In this conformation, 6PG would clash with bound NADP(H) of the *Ld*6PGD and the NADPH-complexed *Oa*6PGD structure. Residues of the $NADP^+$ and the 6PG binding pocket are shown in stick models, and hydrogen bonds are indicated with black dotted lines.

It is known that the product NADPH acts as a competitive inhibitor against $NADP^+$ and as a non-competitive inhibitor against 6PG [61–63]. Since crystallization with an excess of 6PG and $NADP^+$ in the crystallization buffer, and thus under catalysis, could have resulted in a feedback inhibition by high concentrations of the product NADPH, we suggest that *Ld*6PGD is complexed with NADPH in its inhibitory conformation, in which the nicotinamide ring occupies part of the 6PG binding site. Consequently, we suggest that the bound phosphate moiety is from 6PG and not from the product R5P. As the nicotinamide ring occupies part of the 6PG binding pocket, we hypothesize that only the phosphate component of 6PG can bind at the usual site, while the rest of the 6PG molecule must be flexible and therefore not visible in the electron density (Figures 4a and 5b). Theoretically, the postulated NADPH conformation in the *Ld*6PGD structure could also be an artefact due to the phosphate ion forcing the positively charged nicotinamide ring of $NADP^+$ into this position, and thereby forming a hydrogen bond between these two entities. In this case, this interaction should also be seen in the human 6PGD structure (PDBID: 2JKV) complexed with $NADP^+$ and a sulfate ion. However, this is not the case, the cofactor adopts the $NADP^+$ typical conformation, supporting our hypothesis that in our structure, NADPH is bound in its inhibitory conformation.

2.6. Ld6PGD Is a Target of the Gold Inhibitor Auranofin

In this study, we tested auranofin (Figure 6), a gold(I)-containing drug that has been used for decades to treat rheumatoid arthritis [28,29], against *Ld*6PGD. We determined IC_{50} values of 8.6 ± 1.0 µM (K_i = 3.8 ± 0.4 µM) against recombinant *Ld*6PGD (Table 3). Interestingly, the plasmodial *Pf*6PGD was inhibited at similar concentrations with IC_{50} values of 20.1 ± 1.5 µM, but the human *Hs*6PGD was not inhibited up to a concentration of 100 µM auranofin (Table 3). Although several studies have shown that auranofin is also active against *Kinetoplastida* parasites [36,37,39], to our knowledge, no study has yet identified 6PGD as a potential target of auranofin in these parasites. This raises the

question of whether the inhibition of *Ld*6PGD is relevant or negligible for the MOA of auranofin in *Leishmania* parasites. Depending on the *Leishmania* species and parasite stage in vitro, EC_{50} values of auranofin and other gold(I)-containing derivatives reported in the literature range from low micromolar (10^{-5} to 10^{-6}) [37,64] to nanomolar (10^{-7} to 10^{8}) [38,44] concentrations, making gold(I)-containing drugs similarly effective to common antileishmanial drugs such as antimony in vitro [65,66]. Based on co-crystallization and inhibition studies, it was previously suggested that this high in vitro efficacy is solely due to the inhibition of trypanosomatid TR [37,64]. The authors reported K_i values of 155 ± 35 nM against recombinant TR from *Leishmania infantum* (*Li*TR) [37]. However, although these studies suggest that auranofin inhibits TR more efficiently than *Ld*6PGD, the inhibition of *Ld*6PGD in the lower micromolar range cannot be ignored, especially when interpreting the MOA of auranofin in vitro and in vivo. The cytotoxic effect of auranofin on trypanosomatid parasites has previously been explained by an increase in ROS and induced apoptotic-like cell death and is consistent with the hypothesized MOA of TR inhibition [38,39,44]. However, these effects were only observed at concentrations of 10–50 µM, which is surprising, given the nanomolar activity against *Li*TR. Since, in our studies, *Ld*6PGD was completely inhibited at 50 µM auranofin, the MOA could also be explained by the inhibition of the *Ld*6PGD. Some in vitro studies reported EC_{50} values significantly lower than the K_i of auranofin against *Li*TR [38,44]. This could be explained by the fact that inhibition of TR as a central redox enzyme could also affect the activity of other downstream redox enzymes and consequently the overall redox balance. However, our observations also suggest a synergistic effect based on dual TR and 6PGD inhibition, as the activity of TR as a NADPH consumer is directly dependent on the activity of 6PGD and G6PD as NADPH producers, which would accelerate the generation of ROS and consequently the cytotoxic effect of auranofin on trypanosomatid parasites. Finally, our data suggest that the MOA of auranofin should be reconsidered and the contribution of 6PGD inhibition to the overall MOA of auranofin in *Kinetoplastida* further investigated.

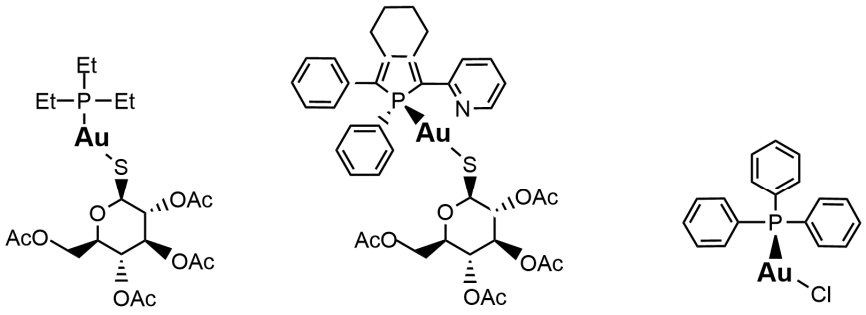

Auranofin **GoPi-sugar** **Ph_3PAuCl**

Figure 6. Chemical structures of the gold(I)-based compounds auranofin, GoPi-sugar and Ph_3PAuCl (chloro(triphenylphosphine)gold(I)).

Table 3. Biochemical activities of auranofin, GoPi-sugar and Ph_3PAuCl.

	IC_{50} [µM] for Recombinant Protein		
Compound	***Ld6PGD***	***Pf6PGD***	***Hs6PGD***
Auranofin	8.6 ± 1.0	20.1 ± 1.5	>100
GoPi-sugar	9.4 ± 2.1	n.d.	n.d.
Ph_3PAuCl	2.1 ± 0.3	n.d.	n.d.

n.d.—not determined. Values are expressed as mean ± SD from three independent determinations with different enzyme batches, each including three measurements.

2.7. Auranofin Competes with the 6PG Binding Site and Binds Irreversibly to Ld6PGD

To investigate the mode of inhibition (MOI) of auranofin against *Ld*6PGD, various compound concentrations were titrated against the substrates $NADP^+$ and 6PG, and the relationship between initial velocity and substrate concentrations was analyzed. Michaelis–Menten kinetics indicate a non-competitive inhibition against $NADP^+$, as the K_M remained stable and V_{max} decreased with increasing auranofin concentrations (Figure 7a). In contrast, the MOI against 6PG cannot be clearly classified. Both V_{max} and K_M increased with increasing concentrations of auranofin, corresponding to a mixed type of inhibition. However, the strong increase in K_M of 6PG suggests competitive inhibition (Figure 7b). This was confirmed by determination of IC_{50} values at saturation. Incubation of the enzyme with auranofin and 6PG at saturation resulted in IC_{50} values of 40.5 ± 1.9 µM. When instead auranofin and the enzyme were incubated with $NADP^+$ at saturation, the IC_{50} was unaffected, again supporting the non-competitive inhibition against $NADP^+$.

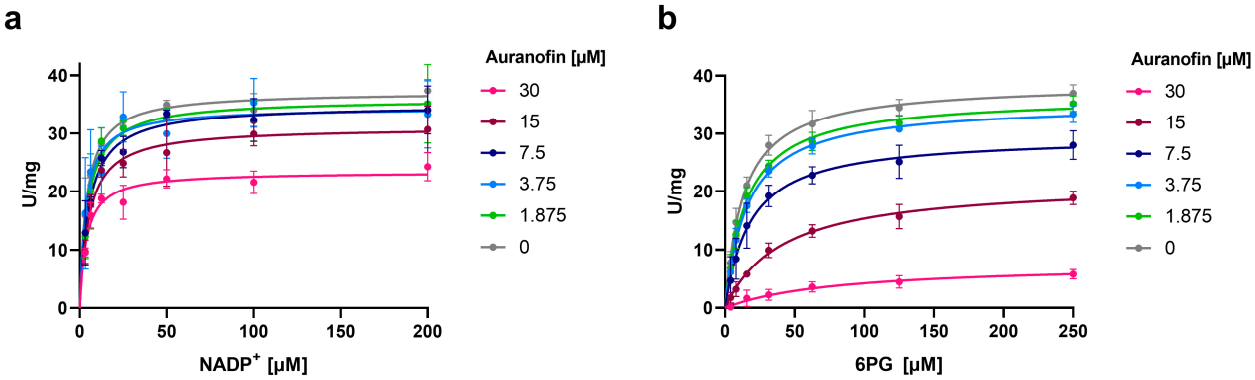

Auranofin [µM]	30	15	7.5	3.75	1.875	0
V_{max} [U/mg]	23.34	31.07	34.92	34.45	35.9	37.16
K_M [µM]	3.79	5.32	5.39	3.59	4.74	4.02

Auranofin [µM]	30	15	7.5	3.75	1.875	0
V_{max} [U/mg]	7.71	21.59	29.59	35.23	36.43	38.71
K_M [µM]	81.71	40.63	18.21	16.15	15.21	13.23

Figure 7. Mechanism of inhibition of auranofin against *Ld*6PGD. Various compound concentrations were titrated against (**a**) $NADP^+$ or (**b**) 6PG. Michaelis–Menten graphs of [U/mg] against $NADP^+$ [µM] and 6PG [µM], respectively, are shown. (**a**) The K_M value for $NADP^+$ stays constant with a minor reduction in V_{max}, indicating a non-competitive inhibition of auranofin against $NADP^+$. (**b**) The K_M value for 6PG increases and V_{max} decreases with increasing compound concentrations, indicating a mixed type of inhibition. Representative graphs from two independent replications are shown, each including at least two measurements.

In addition, we investigated whether the inhibition of *Ld*6PGD by auranofin is reversible or irreversible. For this purpose, the enzyme was first incubated with a high concentration of auranofin (pre-dilution, 30 µM), followed by a dilution below the IC_{50} (3 µM, post-dilution) and incubated again to allow compound dissociation (Figure 8). Compared to controls containing either no auranofin (CTL, 0 µM) or an auranofin concentration equal to the post-dilution concentration (CTL, 3 µM), *Ld*6PGD activity could not be restored after dilution, indicating an irreversible type of inhibition. This is consistent with previous studies of auranofin and other gold(I)-containing compounds, which also observed irreversible binding of this class of compounds to their targets [41,67–69]. The irreversible inhibition of *Ld*6PGD also explains the ambiguous competitive inhibition mode against 6PG described above. We therefore suggest that the competition of auranofin with 6PG is followed by a rapid irreversible reaction in which a covalent product is formed, explaining why high concentrations of 6PG increase the IC_{50} but do not abolish the inhibition. Several studies indicated that the true pharmacophore of auranofin is triethylphosphanuidylgold(1+) $[Au(PEt)_3]^+$ or simply the gold ion Au(I) alone, rather than the whole auranofin molecule which binds to target proteins, such as TrxR and TR [31,37,41,42,70] or metalloenzymes such as ureases and metallo-β-lactamases [69,71]. In vivo, the thiosugar of auranofin

acts more as a carrier ligand and is already displaced by protein thiols or free thiols in the blood. In vitro, selenocysteine or cysteine residues, typically activated by histidines or metal-ions, are necessary to release $[Au(PEt)_3]^+$ or Au(I) from the thiosugar or other ligands and enable covalent and thus irreversible binding to the target proteins [37,67–72]. Since the active site of *Ld*6PGD lacks a typical cysteine pair, we investigated whether only the gold moiety is responsible for *Ld*6PGD inhibition or whether the thiosugar or even the whole auranofin molecule is involved in the MOI. For that purpose, we tested two gold(I)-containing compounds—GoPi-sugar, sharing the thiosugar group with auranofin, and Ph_3PAuCl (chloro(triphenylphosphine)gold(I)), an auranofin variant which in contrast lacks the thiosugar group (Figure 6). With 9.4 ± 2.1 µM, the IC_{50} of GoPi-sugar against *Ld*6PGD is almost identical to that of auranofin. Interestingly, Ph_3PAuCl showed even better activity against *Ld*6PGD, with an IC_{50} of 2.1 ± 0.3 µM (Table 3). We suggest that it is again the gold moiety ($[Au(PEt)_3]^+$ or Au(I)) that is mainly responsible for the MOI, as it is the only common feature of the three compounds tested. The higher IC_{50} of auranofin and GoPi-sugar compared to Ph_3PAuCl may be due to the large thiosugar, hindering the access to the target site.

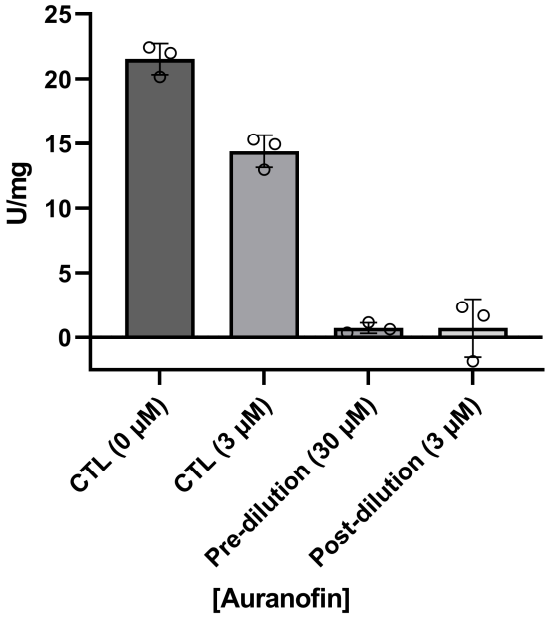

Figure 8. Reversibility of *Ld*6PGD inhibition by auranofin. Reversibility of *Ld*6PGD inhibition by auranofin was determined by incubating the enzyme with a high compound concentration of 30 µM (pre-dilution), followed by dilution to 3 µM (post-dilution). The undiluted sample was completely inhibited, and dilution did not restore activity compared to the control containing the same final compound concentration (CTL, 3 µM). Therefore, the inhibition of *Ld*6PGD by auranofin is irreversible. Treatment without auranofin was used as 100% activity control (CTL, 0 µM). The measurements were performed using the substrates 6PG and $NADP^+$ at K_M concentrations. Values are expressed as mean ± SD from three independent measurements with different enzyme batches, each including three measurements.

It remains to be determined to which site of the enzyme the gold moiety binds. As described above, Au(I) or $[Au(PEt)_3]^+$ of various gold(I)-compounds bind preferentially to cysteines or selenocysteines within the active site of their targets. Therefore, we analyzed the nine cysteines of *Ld*6PGD, three of which are *Leishmania*-specific (C241, C294 and C410) (Figure 2). Potential cysteine pairs not found in the human 6PGD are C183-C347, C294-C347′ and C336-C410. However, in the *Ld*6PGD structure, no disulfide bond is visible between the respective cysteines, and there are no neighboring residues such as histidine and aspartic acid, or alternatively glutamic acid, which could activate the cysteines to covalently bind the gold moiety. In addition, the corresponding cysteines are not in close

proximity to the active site, which is why the competitive binding mechanism towards 6PG could only be explained by long chain forces, but this is not evident from the structure. Therefore, based on our kinetic studies, we suggest that the gold moiety binds directly to the 6PG binding site, but by a different mechanism than that previously described. The gold moiety could also be coordinated between M12 and H459 within the 6PG binding site. Asp454 and Glu133 could accept a proton from M12 and H459, providing the necessary negative partial charge to allow the covalent binding to the gold moiety (Figure 9). However, these residues are conserved among 6PGDs, which raises the question of why *Ld*6PGD and *Pf*6PGD are efficiently inhibited (Table 3), but the human 6PGD is not inhibited by the gold(I)-compounds we tested. In contrast to protozoan and prokaryotic 6PGDs, 6PGDs from multicellular species, such as from *Homo sapiens*, *Ovis aries*, *Saccharomyces cerevisiae* or from *Schistosoma* parasites, have an elongated C-terminal domain of about 10–15 residues that could cover the active site and thus sterically prevent auranofin from binding to the 6PG active site. However, while residues S478, S479 and Y481 of *Hs*6PGD (PDBID: 2JKV) are involved in $NADP^+$ binding (Figure 9), the exact function of this C-terminal elongation or whether it alters its conformation in a substrate-dependent manner is not fully understood. For example, it is fully visible in the $NADP^+$-complexed *Hs*6PGD structure and covering the active site (PDBID: 2JKV), but it is not visible in all other solved 6PGD structures from multicellular species, whether the substrate and cosubstrate are bound or not (PDBIDs: 4GWG, 4GWK, 1PGJ, 1PGO, 1PGN, 1PGQ, 2P4Q). In addition, there are conflicting studies as to whether the substrates bind by an ordered or random sequential binding mechanism [49,52,59,61,73,74], which could influence the position of the elongated C-terminus and therefore the binding of auranofin.

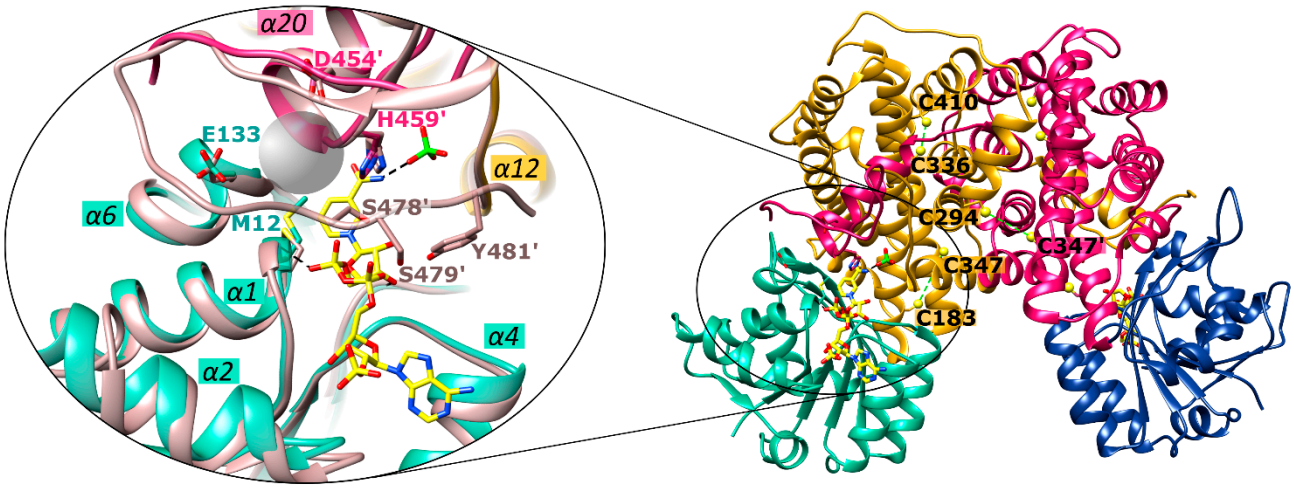

Figure 9. Potential binding site of gold(I) complexes in *Ld*6PGD. The structures from *Ld*6PGD and *Hs*6PGD (PDBID: 2JKV) are superimposed and residues from the *Ld*6PGD structure that are potentially involved in binding of the gold moiety from auranofin and other gold-containing compounds are shown. Ribbons and residues of domain 1^A and 1^B from the *Ld*6PGD structure are colored light green and navy blue, and of domain 2^A and domain 2^B, gold and magenta, respectively. NADP(H) and the phosphate moiety from the *Ld*6PGD structure are colored yellow and green, respectively. Ribbons and residues from the superimposed *Hs*6PGD structure are colored nude, and additional residues from the elongated C-terminus of the *Hs*6PGD structure which are involved in $NADP^+$ binding are shown. In addition, cysteines that are absent in the human structure are shown in the overall view and potential cysteine pairs linked by a green dotted line.

3. Materials and Methods

3.1. Reagents

All reagents used were of the highest available purity. $NADP^+$ and NADPH were purchased from Biomol (Hamburg, Germany) and Ni-NTA agarose from Cube Biotech

(Monheim am Rhein, Germany). All other reagents were obtained from Merck (Darmstadt, Germany), Roth (Karlsruhe, Germany) or Sigma-Aldrich (Steinheim, Germany).

3.2. Expression and Purification of His-Tagged Ld6PGD wt

For heterologous overexpression in *E. coli*, the gene encoding wt *Ld*6PGD (UniProtKB acc. no. Q18L02) was ordered codon-optimized from Eurofins genomics (Ebersberg, Germany) and subcloned into the pET28a(+) vector, using BamHI and HindIII restriction sites, encoding a N-terminally His-tagged protein.

*Ld*6PGD wt was heterologously overexpressed in *E. coli* C43 (DE3) cells. pET28a(+) expression plasmid encoding for *Ld*6PGD wt was transformed in *E. coli* C43 (DE3) cells. Cells containing the respective plasmid were grown at 37 °C in lysogeny broth medium (LB) containing 50 $\mu g \cdot mL^{-1}$ kanamycin. Expression was subsequently induced for 5 h with 0.5 mM IPTG at OD_{600} ~ 0.6. Cells were harvested via centrifugation (15 min, 12,000× *g*, 4 °C), suspended in buffer A (500 mM NaCl, 50 mM Tris, pH 7.8), mixed with protease inhibitors (4 nM cystatin, 150 nM pepstatin, 100 µM PMSF) and stored at −20 °C until cell lysis. For cell lysis and solubilization of the enzyme, lysozyme, DNaseI and 10% glycerol were added to the cell suspension and incubated for ~15 h at 4 °C, followed by three cycles of sonication and centrifugation (30 min, 25,000× *g*, 4 °C). For IMAC purification, the supernatant was applied to a Ni-NTA column, pre-equilibrated with buffer A. Recombinant N-terminally His-tagged proteins were eluted with buffer A containing 50–500 mM imidazole. The fractions containing the recombinant protein were pooled and concentrated using an ultrafiltration unit (Vivaspin 20, 30-kDa filter cut-off; Satorius, Göttingen, Germany). As an additional purification step, and to determine oligomerization state of the respective enzymes, SEC was performed with an ÄKTA FPLC system, using a HiLoad 16/60 Superdex 200 column (GE Healthcare, Freiburg, Germany) pre-equilibrated with buffer A. SEC was performed under native, reductive (5 mM DTT) and oxidative (2 mM H_2O_2) conditions as well as in the presence of the substrate (0.2 mM $NADP^+$, 0.2 mM 6PG) and product (0.2 mM NADPH). Protein elution was detected at 280 nm and evaluated using the UNICORN software 7.2. The peaks of interest containing the recombinant protein were collected, and concentrated and enzyme purity was assessed with Coomassie-blue-stained SDS-PAGE gels (12% polyacrylamide). The enzyme concentration was determined by measuring the absorbance of the protein solution at 260 and 280 nm using an Eppendorf BioSpectrometer (Hamburg, Germany) and finally calculated using the molecular weight and extinction coefficient of the respective enzymes (*Ld*6PGD wt: 55.4 kDa, 48,610 $M^{-1} \cdot cm^{-1}$). After SEC, a final yield of 1–4 mg soluble, pure and active 6PGD per liter *E. coli* culture was achieved for recombinant *Ld*6PGD. The enzyme remained stable for at least ten days when stored at 4 °C and three months when stored at −80 °C with the addition of 250 mM $AmSO_4$, as verified via enzyme activity measurements.

3.3. Enzymatic Characterization of Ld6PGD wt

6PGD activity was determined at 25 °C by following NADPH [ε_{340} = 6220 $M^{-1} \cdot cm^{-1}$] production at 340 nm according to Beutler [75] using the spectrophotometer Evolution 300 (Thermo Scientific, Dreieich, Germany). All measurements were performed in buffer B (50 mM Tris, 3.3 mM $MgCl_2$, 0.005% Tween, 1 mg/mL BSA, pH 7.5), whereas the enzyme was pre-diluted in buffer C (50 mM Tris, 0.005% Tween, 1 mg/mL BSA, pH 7.5). The reaction mixture with a final volume of 500 µL contained 200 µM $NADP^+$, varying concentrations of the 6PGDs (5–9 nM) and 300 µM 6PG. To determine the apparent K_M values and V_{max}, the substrate (8–500 µM 6PG) and the cosubstrate (8–400 µM $NADP^+$) were varied reciprocally. All measurements were performed with three biological independent replicates, each containing at least three measurements, and the apparent kinetic constants were calculated via nonlinear regression using the GraphPad Prism 9.0 software (GraphPad, San Diego, CA, USA).

3.4. Enzymatic Characterization of Gold(I)-Based Compounds

Dose–response curves of gold(I)-based compounds against *Ld*6PGD were determined in 96-well plates using a Tecan Infinite M200 plate reader (Tecan, Maennedorf, Switzerland). An amount of 10 mM of each compound was dissolved in 100% DMSO and afterwards diluted in assay buffer to the required concentrations (highest final compound concentration of 100 µM). The DMSO tolerance of the enzymes was determined in advance by incubating the enzymes with up to 6% DMSO and determining their activity. Up to this concentration, no impairment of the enzymes' catalytic activity was observed. In addition, a DMSO control was included in each measurement.

Different compound concentrations were added to one volume of enzyme mix (final concentrations: 50 mM Tris (pH 7.5), 0.005% Tween 20, 1 mg·mL^{-1} BSA, 0.7 nM *Ld*6PGD/0.7 nM *Pf*6PGD/0.9 nM *Hs*6PGD) and incubated for ten minutes. To start the reaction, one volume substrate mix (final concentrations: 50 mM Tris (pH 7.5), 0.005% Tween 20, 1 mg·mL^{-1} BSA, 3.3 mM $MgCl_2$, 25/20/25 µM 6PG, 20 µM $NADP^+$ for *Ld*6PGD, *Pf*6PGD and *Hs*6PGD) was added to the wells. To increase the sensitivity of the assay, the increase of NADPH was monitored by measuring the fluorescence of NADPH at excitation 340 nm/emission 460 nm (ex340/em460). The substrate mix without 6PG served as a positive control (100% inhibition) and without the compound, but with DMSO as a negative control (100% activity). The assay contained both substrates either in saturation or at concentrations close to K_M to facilitate the identification of competitive inhibitors. The reaction rate was calculated by dividing the relative fluorescence units (RFU) by time, and only a linear increase in absorbance/fluorescence was considered. IC_{50} values were calculated using GraphPad Prism 9.0 software and Microsoft Excel.

For the mechanistic characterization of auranofin, either $NADP^+$ (0–200 µM) or 6PG (0–250 µM) was titrated at different constant compound concentrations around the IC_{50} (0–30 µM), while keeping the second substrate in saturation (6PG: 300 µM, $NADP^+$: 200 µM). To determine the compound mode of inhibition, the relationship between initial velocity (v_0) and substrate concentrations ([S]) at various constant compound concentrations was analyzed by plotting the data as Michaelis–Menten curves using GraphPad Prism; K_M values and V_{max} were calculated with GraphPad Prism as well.

The reversibility of *Ld*6PGD inhibition by auranofin was tested by incubating the enzyme with high compound concentrations, followed by dilution to a compound concentration below IC_{50} and subsequent determination of the enzyme activity. In detail, 14 nM *Ld*6PGD was incubated with 30 µM auranofin for 10 min at room temperature. Afterwards, the enzyme/inhibitor mixture was diluted to a compound concentration below IC_{50} (3 µM) and again incubated for 10 min at room temperature to allow dissociation. Afterwards, $NADP^+$ and 6PG were added to start the reaction, either at substrate saturation (300 µM 6PG, 200 µM $NADP^+$) or at concentrations close to K_M (25 µM 6PG, 20 µM $NADP^+$). For comparison, controls containing either no inhibitor (100% activity) or inhibitor in the concentration remaining after dilution were prepared. NADPH production was monitored at ex340 nm using the Tecan Infinite M200 plate reader in 96-well plates. Specific activities were calculated from reaction rates. Inhibition was considered irreversible if the activity of the sample after dilution was significantly below the activity of the controls. Inhibition was considered reversible if the activity of the sample was equal to the controls.

3.5. Protein Crystallization

For crystallization of *Ld*6PGD wt, the enzyme was concentrated to approximately 8 mg·mL^{-1} in buffer A. A Honeybee 961 crystallization robot (Digilab) was used to prepare the crystallization plates. Drops were generated by mixing 0.2 µL of reservoir solution with 0.2 µL of protein solution. 6PGD crystals were grown in a 96-well format with the sitting-trop vapor diffusion technique at room temperature. Suitable crystals could only be obtained in the presence of the substrate (6PG, 1 mM) and cosubstrate ($NADP^+$, 1 mM) in the crystallization buffer (buffer A). The best *Ld*6PGD crystals were obtained in a reservoir

containing 24% PEG 3000 and 40 mM of magnesium formate. We produced *Ld*6PGD crystals in complex with NADP(H) diffracting to a resolution up to 3.1 Å.

3.6. Data Collections and Processing

Diffraction data for all crystals were collected at X10SA (detector: DECTRIS EIGER2 XE 16M) of the Swiss Light Source in Villigen, Switzerland, at 100 K and processed with XDS [76]. Before data collection, crystals were soaked in mother liquor with a final concentration of 25% ethylene glycol.

The *Ld*6PGD crystals obey $P2_12_12$ space group symmetry and contain two monomers in the asymmetric unit.

3.7. Structure Determination and Refinement

The structure was solved by the molecular replacement method. We have generated a search model of *Ld*6PGD by homology modeling with SWISS-MODEL [77] by using the 6PGD dimer from *T. brucei* (PDBID: 1PGJ) as a template, which shares 72% sequence identity with *Ld*6PGD. The first refinement revealed an initial R_{free} of 40%, comprising residues 15–478 of both monomers. After several rounds of model correction and completion of the model with the interactive graphics program Coot, the final R_{free} value dropped to 31.7%. The structure was refined to a resolution of 3.1 Å. The asymmetric unit contains two PGD monomers (A, B), two NADP(H), two phosphate ions and one water molecule. The two ions and one NADP(H) molecule could be clearly determined in the first difference map, the second NADPH was only partially visible. The overall temperature factor of the structure is relatively high at 125 $Å^2$ but fits well with the measured Wilson B factor of 129 $Å^2$. Despite the moderate resolution, the electron density of the structure is well defined for the entire model (1–478), indicating good phases due to a matching model. During refinement, 10% of all reflections were omitted and used for calculation of an R_{free} value, the final statistics are shown in Table 2.

The PHENIX program suite [78,79] served for reflection phasing and structure refinement. The interactive graphics program Coot [80] was used for model building. The structures were superimposed using the SSM algorithm tool [81], implemented in the Coot graphics package. The SSM tool is a structural alignment based on secondary structure matching. Molecular graphics images were produced using the UCSF Chimera package [82].

4. Conclusions

Since resistance against commonly used antileishmanial drugs such as miltefosine [25], amphotericin-B [26] and sodium antimony gluconate [27] has already emerged [3–5], new drug targets and antileishmanial agents are urgently required. The crystal structure and biochemical characterization of *Ld*6PGD presented in this study provides a first step to validate 6PGDs from *Leishmania* parasites as a promising antitrypanosomatid drug target. In addition, we suggest gold(I)-containing compounds as a promising class of selective *Ld*6PGD inhibitors. As the human 6PGD was not inhibited at micromolar concentrations, we postulate that the elongated C-terminal domain of the human enzyme sterically prevents auranofin from binding to the 6PG active site, demonstrating that selective inhibition of this conserved enzyme is possible. Co-crystallization studies are underway to investigate the exact *Ld*6PGD binding site of auranofin, or rather of the gold moiety, and will provide the basis for further structure-based activity relationship studies.

Supplementary Materials: The supporting information can be downloaded at: https://www.mdpi.com/article/10.3390/ijms24108615/s1.

Author Contributions: Conceptualization, K.B., K.F.-W. and I.B.; methodology, I.B. and K.F.-W.; software, K.F.-W.; validation, K.F.-W. and I.B.; formal analysis, I.B. and K.F.-W.; investigation, I.B., K.F.-W., A.-S.V. and M.S.; resources, K.B. and J.P.; data curation, K.F.-W. and I.B.; writing—original draft preparation, I.B.; writing—review and editing, K.F.-W., I.B., S.R., K.B. and J.P.; visualization, I.B.;

supervision, K.B. and K.F.-W.; project administration, K.B.; funding acquisition, K.B., J.P. and S.R. All authors have read and agreed to the published version of the manuscript.

Funding: This research was funded by LOEWE Center DRUID (Novel Drug Targets against Poverty-Related and Neglected Tropical Infectious Diseases) (Project B3/E3) within the Hessian Excellence Program.

Data Availability Statement: Coordinates and measured reflection amplitudes have been deposited in the Worldwide Protein Data Bank RCSB PDB (http://pdb.org): code 8C79 for *Ld*6PD wild type in complex with NADP(H).

Acknowledgments: The authors wish to thank Ilme Schlichting for the continued support over many years. Diffraction data were collected at beamline X10SA, Swiss Light Source, Paul Scherrer Institute, Villigen, Switzerland, and the authors thank the beamline staff for the excellent setup.

Conflicts of Interest: The authors declare no conflict of interest.

References

1. WHO. Leishmaniasis. Available online: https://www.who.int/news-room/fact-sheets/detail/leishmaniasis (accessed on 27 May 2022).
2. Burza, S.; Croft, S.L.; Boelaert, M. Leishmaniasis. *Lancet* **2018**, *392*, 951–970. [CrossRef] [PubMed]
3. Loureiro, I.; Faria, J.; Santarem, N.; Smith, T.K.; Tavares, J.; Cordeiro-da-Silva, A. Potential Drug Targets in the Pentose Phosphate Pathway of Trypanosomatids. *Curr. Med. Chem.* **2018**, *25*, 5239–5265. [CrossRef] [PubMed]
4. Chakravarty, J.; Sundar, S. Current and emerging medications for the treatment of leishmaniasis. *Expert Opin. Pharmacother.* **2019**, *20*, 1251–1265. [CrossRef] [PubMed]
5. Roatt, B.M.; de Oliveira Cardoso, J.M.; De Brito, R.C.F.; Coura-Vital, W.; de Oliveira Aguiar-Soares, R.D.; Reis, A.B. Recent advances and new strategies on leishmaniasis treatment. *Appl. Microbiol. Biotechnol.* **2020**, *104*, 8965–8977. [CrossRef] [PubMed]
6. Solbach, W.; Laskay, T. The Host Response to Leishmania Infection. In *Advances in Immunology, 1st, ed.*; Dixon, F.J., Ed.; Elsevier: Amsterdam, The Netherlands, 1999; pp. 275–317, ISBN 9780120224746.
7. Vonlaufen, N.; Kanzok, S.M.; Wek, R.C.; Sullivan, W.J. Stress response pathways in protozoan parasites. *Cell. Microbiol.* **2008**, *10*, 2387–2399. [CrossRef]
8. Moradin, N.; Descoteaux, A. Leishmania promastigotes: Building a safe niche within macrophages. *Front. Cell. Infect. Microbiol.* **2012**, *2*, 121. [CrossRef]
9. Ghosh, A.K.; Sardar, A.H.; Mandal, A.; Saini, S.; Abhishek, K.; Kumar, A.; Purkait, B.; Singh, R.; Das, S.; Mukhopadhyay, R.; et al. Metabolic reconfiguration of the central glucose metabolism: A crucial strategy of Leishmania donovani for its survival during oxidative stress. *FASEB J.* **2015**, *29*, 2081–2098. [CrossRef]
10. Krauth-Siegel, R.L.; Comini, M.A. Redox control in trypanosomatids, parasitic protozoa with trypanothione-based thiol metabolism. *Biochim. Biophys. Acta* **2008**, *1780*, 1236–1248. [CrossRef]
11. Kovářová, J.; Barrett, M.P. The Pentose Phosphate Pathway in Parasitic Trypanosomatids. *Trends Parasitol.* **2016**, *32*, 622–634. [CrossRef]
12. Comini, M.A.; Ortíz, C.; Cazzulo, J.J. Drug Targets in Trypanosomal and Leishmanial Pentose Phosphate Pathway. In *Trypanosomatid Diseases*; Jäger, T., Koch, O., Flohé, L., Eds.; Wiley-VCH Verlag GmbH & Co. KGaA: Weinheim, Germany, 2013; pp. 297–313, ISBN 9783527670383.
13. Gupta, S.; Igoillo-Esteve, M.; Michels, P.A.M.; Cordeiro, A.T. Glucose-6-phosphate dehydrogenase of trypanosomatids: Characterization, target validation, and drug discovery. *Mol. Biol. Int.* **2011**, *2011*, 135701. [CrossRef]
14. Allen, S.M.; Lim, E.E.; Jortzik, E.; Preuss, J.; Chua, H.H.; MacRae, J.I.; Rahlfs, S.; Haeussler, K.; Downton, M.T.; McConville, M.J.; et al. Plasmodium falciparum glucose-6-phosphate dehydrogenase 6-phosphogluconolactonase is a potential drug target. *FEBS J.* **2015**, *282*, 3808–3823. [CrossRef]
15. Berneburg, I.; Peddibhotla, S.; Heimsch, K.C.; Haeussler, K.; Maloney, P.; Gosalia, P.; Preuss, J.; Rahbari, M.; Skorokhod, O.; Valente, E.; et al. An Optimized Dihydrodibenzothiazepine Lead Compound (SBI-0797750) as a Potent and Selective Inhibitor of Plasmodium falciparum and P. vivax Glucose 6-Phosphate Dehydrogenase 6-Phosphogluconolactonase. *Antimicrob. Agents. Chemother.* **2022**, *66*, e0210921. [CrossRef]
16. Hannaert, V.; Bringaud, F.; Opperdoes, F.R.; Michels, P.A. Evolution of energy metabolism and its compartmentation in Kinetoplastida. *Kinetoplastid. Biol. Dis.* **2003**, *2*, 11. [CrossRef]
17. Michels, P.A.M.; Bringaud, F.; Herman, M.; Hannaert, V. Metabolic functions of glycosomes in trypanosomatids. *Biochim. Biophys. Acta* **2006**, *1763*, 1463–1477. [CrossRef]
18. Haanstra, J.R.; van Tuijl, A.; Kessler, P.; Reijnders, W.; Michels, P.A.M.; Westerhoff, H.V.; Parsons, M.; Bakker, B.M. Compartmentation prevents a lethal turbo-explosion of glycolysis in trypanosomes. *Proc. Natl. Acad. Sci. USA* **2008**, *105*, 17718–17723. [CrossRef]

19. Marchand, M.; Kooystra, U.; Wierenga, R.K.; Lambeir, A.M.; van Beeumen, J.; Opperdoes, F.R.; Michels, P.A. Glucosephosphate isomerase from Trypanosoma brucei. Cloning and characterization of the gene and analysis of the enzyme. *Eur. J. Biochem.* **1989**, *184*, 455–464. [CrossRef]
20. Hanau, S.; Rinaldi, E.; Dallocchio, F.; Gilbert, I.H.; Dardonville, C.; Adams, M.J.; Gover, S.; Barrett, M.P. 6-phosphogluconate dehydrogenase: A target for drugs in African trypanosomes. *Curr. Med. Chem.* **2004**, *11*, 2639–2650. [CrossRef]
21. Hanau, S.; Helliwell, J.R. 6-Phosphogluconate dehydrogenase and its crystal structures. *Acta Crystallogr. F Struct. Biol. Commun.* **2022**, *78*, 96–112. [CrossRef]
22. Kerkhoven, E.J.; Achcar, F.; Alibu, V.P.; Burchmore, R.J.; Gilbert, I.H.; Trybiło, M.; Driessen, N.N.; Gilbert, D.; Breitling, R.; Bakker, B.M.; et al. Handling uncertainty in dynamic models: The pentose phosphate pathway in Trypanosoma brucei. *PLoS Comput. Biol.* **2013**, *9*, e1003371. [CrossRef]
23. Ruda, G.F.; Campbell, G.; Alibu, V.P.; Barrett, M.P.; Brenk, R.; Gilbert, I.H. Virtual fragment screening for novel inhibitors of 6-phosphogluconate dehydrogenase. *Bioorg. Med. Chem.* **2010**, *18*, 5056–5062. [CrossRef]
24. González, D.; Pérez, J.L.; Serrano, M.L.; Igoillo-Esteve, M.; Cazzulo, J.J.; Barrett, M.P.; Bubis, J.; Mendoza-León, A. The 6-phosphogluconate dehydrogenase of Leishmania (Leishmania) mexicana: Gene characterization and protein structure prediction. *J. Mol. Microbiol. Biotechnol.* **2010**, *19*, 213–223. [CrossRef] [PubMed]
25. Mishra, J.; Singh, S. Miltefosine resistance in Leishmania donovani involves suppression of oxidative stress-induced programmed cell death. *Exp. Parasitol.* **2013**, *135*, 397–406. [CrossRef] [PubMed]
26. Purkait, B.; Kumar, A.; Nandi, N.; Sardar, A.H.; Das, S.; Kumar, S.; Pandey, K.; Ravidas, V.; Kumar, M.; De, T.; et al. Mechanism of amphotericin B resistance in clinical isolates of Leishmania donovani. *Antimicrob. Agents. Chemother.* **2012**, *56*, 1031–1041. [CrossRef] [PubMed]
27. Sudhandiran, G.; Shaha, C. Antimonial-induced increase in intracellular Ca^{2+} through non-selective cation channels in the host and the parasite is responsible for apoptosis of intracellular Leishmania donovani amastigotes. *J. Biol. Chem.* **2003**, *278*, 25120–25132. [CrossRef]
28. Finkelstein, A.E.; Walz, D.T.; Batista, V.; Mizraji, M.; Roisman, F.; Misher, A. Auranofin. New oral gold compound for treatment of rheumatoid arthritis. *Ann. Rheum. Dis.* **1976**, *35*, 251–257. [CrossRef]
29. Katz, W.A.; Alexander, S.; Bland, J.H.; Blechman, W.; Bluhm, G.B.; Bonebrake, R.A.; Falbo, A.; Greenwald, R.A.; Hartman, S.; Hobbs, T.; et al. The efficacy and safety of auranofin compared to placebo in rheumatoid arthritis. *J. Rheumatol. Suppl.* **1982**, *8*, 173–178.
30. Kuntz, A.N.; Davioud-Charvet, E.; Sayed, A.A.; Califf, L.L.; Dessolin, J.; Arnér, E.S.J.; Williams, D.L. Thioredoxin glutathione reductase from *Schistosoma mansoni*: An essential parasite enzyme and a key drug target. *PLoS Med.* **2007**, *4*, e206. [CrossRef]
31. Caroli, A.; Simeoni, S.; Lepore, R.; Tramontano, A.; Via, A. Investigation of a potential mechanism for the inhibition of SmTGR by Auranofin and its implications for Plasmodium falciparum inhibition. *Biochem. Biophys. Res. Commun.* **2012**, *417*, 576–581. [CrossRef]
32. Bonilla, M.; Denicola, A.; Novoselov, S.V.; Turanov, A.A.; Protasio, A.; Izmendi, D.; Gladyshev, V.N.; Salinas, G. Platyhelminth mitochondrial and cytosolic redox homeostasis is controlled by a single thioredoxin glutathione reductase and dependent on selenium and glutathione. *J. Biol. Chem.* **2008**, *283*, 17898–17907. [CrossRef]
33. Tejman-Yarden, N.; Miyamoto, Y.; Leitsch, D.; Santini, J.; Debnath, A.; Gut, J.; McKerrow, J.H.; Reed, S.L.; Eckmann, L. A reprofiled drug, auranofin, is effective against metronidazole-resistant Giardia lamblia. *Antimicrob. Agents Chemother.* **2013**, *57*, 2029–2035. [CrossRef]
34. Ma, C.I.; Tirtorahardjo, J.A.; Jan, S.; Schweizer, S.S.; Rosario, S.A.C.; Du, Y.; Zhang, J.J.; Morrissette, N.S.; Andrade, R.M. Auranofin Resistance in Toxoplasma gondii Decreases the Accumulation of Reactive Oxygen Species but Does Not Target Parasite Thioredoxin Reductase. *Front. Cell. Infect. Microbiol.* **2021**, *11*, 618994. [CrossRef]
35. Lobanov, A.V.; Gromer, S.; Salinas, G.; Gladyshev, V.N. Selenium metabolism in Trypanosoma: Characterization of selenoproteomes and identification of a Kinetoplastida-specific selenoprotein. *Nucleic Acids Res.* **2006**, *34*, 4012–4024. [CrossRef]
36. Da Silva, M.T.A.; Silva-Jardim, I.; Portapilla, G.B.; de Lima, G.M.A.; Costa, F.C.; Anibal, F.d.F.; Thiemann, O.H. In vivo and in vitro auranofin activity against Trypanosoma cruzi: Possible new uses for an old drug. *Exp. Parasitol.* **2016**, *166*, 189–193. [CrossRef]
37. Ilari, A.; Baiocco, P.; Messori, L.; Fiorillo, A.; Boffi, A.; Gramiccia, M.; Di Muccio, T.; Colotti, G. A gold-containing drug against parasitic polyamine metabolism: The X-ray structure of trypanothione reductase from Leishmania infantum in complex with auranofin reveals a dual mechanism of enzyme inhibition. *Amino Acids* **2012**, *42*, 803–811. [CrossRef]
38. Sharlow, E.R.; Leimgruber, S.; Murray, S.; Lira, A.; Sciotti, R.J.; Hickman, M.; Hudson, T.; Leed, S.; Caridha, D.; Barrios, A.M.; et al. Auranofin is an apoptosis-simulating agent with in vitro and in vivo anti-leishmanial activity. *ACS Chem. Biol.* **2014**, *9*, 663–672. [CrossRef]
39. Abou-El-Naga, I.F.; Mady, R.F.; Fawzy Hussien Mogahed, N.M. Efectividad in vitro de tres fármacos aprobados y su interacción sinérgica contra Leishmania infantum. *Biomedica* **2020**, *40*, 89–101. [CrossRef]
40. Gromer, S.; Arscott, L.D.; Williams, C.H.; Schirmer, R.H.; Becker, K. Human placenta thioredoxin reductase. Isolation of the selenoenzyme, steady state kinetics, and inhibition by therapeutic gold compounds. *J. Biol. Chem.* **1998**, *273*, 20096–20101. [CrossRef]
41. Urig, S.; Fritz-Wolf, K.; Réau, R.; Herold-Mende, C.; Tóth, K.; Davioud-Charvet, E.; Becker, K. Undressing of phosphine gold(I) complexes as irreversible inhibitors of human disulfide reductases. *Angew. Chem. Int. Ed Engl.* **2006**, *45*, 1881–1886. [CrossRef]

42. Shoeib, T.; Atkinson, D.W.; Sharp, B.L. Structural analysis of the anti-arthritic drug Auranofin: Its complexes with cysteine, selenocysteine and their fragmentation products. *Inorganica Chimica Acta* **2010**, *363*, 184–192. [CrossRef]
43. Debnath, A.; Parsonage, D.; Andrade, R.M.; He, C.; Cobo, E.R.; Hirata, K.; Chen, S.; García-Rivera, G.; Orozco, E.; Martínez, M.B.; et al. A high-throughput drug screen for Entamoeba histolytica identifies a new lead and target. *Nat. Med.* **2012**, *18*, 956–960. [CrossRef]
44. Feng, L.; Pomel, S.; Latre de Late, P.; Taravaud, A.; Loiseau, P.M.; Maes, L.; Cho-Ngwa, F.; Bulman, C.A.; Fischer, C.; Sakanari, J.A.; et al. Repurposing Auranofin and Evaluation of a New Gold(I) Compound for the Search of Treatment of Human and Cattle Parasitic Diseases: From Protozoa to Helminth Infections. *Molecules* **2020**, *25*, 5075. [CrossRef] [PubMed]
45. Shaulov, Y.; Sarid, L.; Trebicz-Geffen, M.; Ankri, S. Entamoeba histolytica Adaption to Auranofin: A Phenotypic and Multi-Omics Characterization. *Antioxidants* **2021**, *10*, 1240. [CrossRef] [PubMed]
46. Leitsch, D.; Müller, J.; Müller, N. Evaluation of Giardia lamblia thioredoxin reductase as drug activating enzyme and as drug target. *Int. J. Parasitol. Drugs Drug Resist.* **2016**, *6*, 148–153. [CrossRef] [PubMed]
47. Jakkula, P.; Narsimulu, B.; Qureshi, I.A. Biochemical and structural insights into 6-phosphogluconate dehydrogenase from Leishmania donovani. *Appl. Microbiol. Biotechnol.* **2021**, *105*, 5471–5489. [CrossRef]
48. Pearse, B.M.; Rosemeyer, M.A. Human 6-phosphogluconate dehydrogenase. Purification of the erythrocyte enzyme and the influence of ions and NADPH on its activity. *Eur. J. Biochem.* **1974**, *42*, 213–223. [CrossRef]
49. Haeussler, K.; Fritz-Wolf, K.; Reichmann, M.; Rahlfs, S.; Becker, K. Characterization of Plasmodium falciparum 6-Phosphogluconate Dehydrogenase as an Antimalarial Drug Target. *J. Mol. Biol.* **2018**, *430*, 4049–4067. [CrossRef]
50. Sun, Y.; Bandi, M.; Lofton, T.; Smith, M.; Bristow, C.A.; Carugo, A.; Rogers, N.; Leonard, P.; Chang, Q.; Mullinax, R.; et al. Functional Genomics Reveals Synthetic Lethality between Phosphogluconate Dehydrogenase and Oxidative Phosphorylation. *Cell Rep.* **2019**, *26*, 469–482.e5. [CrossRef]
51. Adams, M.J.; Ellis, G.H.; Gover, S.; Naylor, C.E.; Phillips, C. Crystallographic study of coenzyme, coenzyme analogue and substrate binding in 6-phosphogluconate dehydrogenase: Implications for NADP specificity and the enzyme mechanism. *Structure* **1994**, *2*, 651–668. [CrossRef]
52. He, W.; Wang, Y.; Liu, W.; Zhou, C.-Z. Crystal structure of Saccharomyces cerevisiae 6-phosphogluconate dehydrogenase Gnd1. *BMC Struct. Biol.* **2007**, *7*, 38. [CrossRef]
53. Sundaramoorthy, R.; Iulek, J.; Barrett, M.P.; Bidet, O.; Ruda, G.F.; Gilbert, I.H.; Hunter, W.N. Crystal structures of a bacterial 6-phosphogluconate dehydrogenase reveal aspects of specificity, mechanism and mode of inhibition by analogues of high-energy reaction intermediates. *FEBS J.* **2007**, *274*, 275–286. [CrossRef]
54. Cameron, S.; Martini, V.P.; Iulek, J.; Hunter, W.N. Geobacillus stearothermophilus 6-phosphogluconate dehydrogenase complexed with 6-phosphogluconate. *Acta Crystallogr. Sect. F Struct. Biol. Cryst. Commun.* **2009**, *65*, 450–454. [CrossRef]
55. Phillips, C.; Dohnalek, J.; Gover, S.; Barrett, M.P.; Adams, M.J. A 2.8 A resolution structure of 6-phosphogluconate dehydrogenase from the protozoan parasite Trypanosoma brucei: Comparison with the sheep enzyme accounts for differences in activity with coenzyme and substrate analogues. *J. Mol. Biol.* **1998**, *282*, 667–681. [CrossRef]
56. Hanau, S.; d'Empaire, L.P.; Capone, I.; Alberighi, S.; Montioli, R.; Dallocchio, F. Evidence for dimer/tetramer equilibrium in Trypanosoma brucei 6-phosphogluconate dehydrogenase. *Biochim. Biophys. Acta* **2013**, *1834*, 2647–2652. [CrossRef]
57. Dyson, J.E.; D'Orazio, R.E.; Hanson, W.H. Sheep liver 6-phosphogluconate dehydrogenase: Isolation procedure and effect of pH, ionic strength, and metal ions on the kinetic parameters. *Arch. Biochem. Biophys.* **1973**, *154*, 623–635. [CrossRef]
58. Morales-Luna, L.; Hernández-Ochoa, B.; Martínez-Rosas, V.; González-Valdez, A.; Cárdenas-Rodríguez, N.; Enríquez-Flores, S.; Marcial-Quino, J.; Gómez-Manzo, S. Cloning, purification, and characterization of the 6-phosphogluconate dehydrogenase (6 PGDH) from Giardia lamblia. *Mol. Biochem. Parasitol.* **2021**, *244*, 111383. [CrossRef]
59. Hanau, S.; Rippa, M.; Bertelli, M.; Dallocchio, F.; Barrett, M.P. 6-Phosphogluconate dehydrogenase from Trypanosoma brucei. Kinetic analysis and inhibition by trypanocidal drugs. *Eur. J. Biochem.* **1996**, *240*, 592–599. [CrossRef]
60. Esteve, M.I.; Cazzulo, J.J. The 6-phosphogluconate dehydrogenase from Trypanosoma cruzi: The absence of two inter-subunit salt bridges as a reason for enzyme instability. *Mol. Biochem. Parasitol.* **2004**, *133*, 197–207. [CrossRef]
61. Price, N.E.; Cook, P.F. Kinetic and chemical mechanisms of the sheep liver 6-phosphogluconate dehydrogenase. *Arch. Biochem. Biophys.* **1996**, *336*, 215–223. [CrossRef]
62. Rippa, M.; Giovannini, P.P.; Barrett, M.P.; Dallocchio, F.; Hanau, S. 6-Phosphogluconate dehydrogenase: The mechanism of action investigated by a comparison of the enzyme from different species. *Biochim. Biophys. Acta* **1998**, *1429*, 83–92. [CrossRef]
63. Weisz, K.S.; Schofield, P.J.; Edwards, M.R. Human brain 6-phosphogluconate dehydrogenase: Purification and kinetic properties. *J. Neurochem.* **1985**, *44*, 510–517. [CrossRef]
64. Colotti, G.; Ilari, A.; Fiorillo, A.; Baiocco, P.; Cinellu, M.A.; Maiore, L.; Scaletti, F.; Gabbiani, C.; Messori, L. Metal-based compounds as prospective antileishmanial agents: Inhibition of trypanothione reductase by selected gold complexes. *ChemMedChem* **2013**, *8*, 1634–1637. [CrossRef] [PubMed]
65. Baiocco, P.; Colotti, G.; Franceschini, S.; Ilari, A. Molecular basis of antimony treatment in leishmaniasis. *J. Med. Chem.* **2009**, *52*, 2603–2612. [CrossRef] [PubMed]
66. Ashutosh; Sundar, S.; Goyal, N. Molecular mechanisms of antimony resistance in Leishmania. *J. Med. Microbiol.* **2007**, *56*, 143–153. [CrossRef] [PubMed]

67. Angelucci, F.; Sayed, A.A.; Williams, D.L.; Boumis, G.; Brunori, M.; Dimastrogiovanni, D.; Miele, A.E.; Pauly, F.; Bellelli, A. Inhibition of Schistosoma mansoni thioredoxin-glutathione reductase by auranofin: Structural and kinetic aspects. *J. Biol. Chem.* **2009**, *284*, 28977–28985. [CrossRef] [PubMed]
68. Jortzik, E.; Farhadi, M.; Ahmadi, R.; Tóth, K.; Lohr, J.; Helmke, B.M.; Kehr, S.; Unterberg, A.; Ott, I.; Gust, R.; et al. Antiglioma activity of GoPI-sugar, a novel gold(I)-phosphole inhibitor: Chemical synthesis, mechanistic studies, and effectiveness in vivo. *Biochim. Biophys. Acta* **2014**, *1844*, 1415–1426. [CrossRef]
69. Sun, H.; Zhang, Q.; Wang, R.; Wang, H.; Wong, Y.-T.; Wang, M.; Hao, Q.; Yan, A.; Kao, R.Y.-T.; Ho, P.-L.; et al. Resensitizing carbapenem- and colistin-resistant bacteria to antibiotics using auranofin. *Nat. Commun.* **2020**, *11*, 5263. [CrossRef]
70. Salinas, G.; Gao, W.; Wang, Y.; Bonilla, M.; Yu, L.; Novikov, A.; Virginio, V.G.; Ferreira, H.B.; Vieites, M.; Gladyshev, V.N.; et al. The Enzymatic and Structural Basis for Inhibition of Echinococcus granulosus Thioredoxin Glutathione Reductase by Gold(I). *Antioxid. Redox Signal.* **2017**, *27*, 1491–1504. [CrossRef]
71. Mazzei, L.; Massai, L.; Cianci, M.; Messori, L.; Ciurli, S. Medicinal Au(I) compounds targeting urease as prospective antimicrobial agents: Unveiling the structural basis for enzyme inhibition. *Dalton Trans.* **2021**, *50*, 14444–14452. [CrossRef]
72. Marzo, T.; Cirri, D.; Gabbiani, C.; Gamberi, T.; Magherini, F.; Pratesi, A.; Guerri, A.; Biver, T.; Binacchi, F.; Stefanini, M.; et al. Auranofin, Et3PAuCl, and Et3PAuI Are Highly Cytotoxic on Colorectal Cancer Cells: A Chemical and Biological Study. *ACS Med. Chem. Lett.* **2017**, *8*, 997–1001. [CrossRef]
73. Topham, C.M.; Matthews, B.; Dalziel, K. Kinetic studies of 6-phosphogluconate dehydrogenase from sheep liver. *Eur. J. Biochem.* **1986**, *156*, 555–567. [CrossRef]
74. Moritz, B.; Striegel, K.; de Graaf, A.A.; Sahm, H. Kinetic properties of the glucose-6-phosphate and 6-phosphogluconate dehydrogenases from Corynebacterium glutamicum and their application for predicting pentose phosphate pathway flux in vivo. *Eur. J. Biochem.* **2000**, *267*, 3442–3452. [CrossRef]
75. Beutler, E. *Red Cell Metabolism: A Manual of Biochemical Methods*, 3rd ed.; Grune & Stratton: Orlando, FL, USA, 1984; ISBN 0808916726.
76. Kabsch, W. Integration, scaling, space-group assignment and post-refinement. *Acta Crystallogr. Sect. D Biol. Crystallogr.* **2010**, *66*, 133–144. [CrossRef]
77. Waterhouse, A.; Bertoni, M.; Bienert, S.; Studer, G.; Tauriello, G.; Gumienny, R.; Heer, F.T.; de Beer, T.A.P.; Rempfer, C.; Bordoli, L.; et al. SWISS-MODEL: Homology modelling of protein structures and complexes. *Nucleic Acids Res.* **2018**, *46*, W296–W303. [CrossRef]
78. Adams, P.D.; Afonine, P.V.; Bunkóczi, G.; Chen, V.B.; Davis, I.W.; Echols, N.; Headd, J.J.; Hung, L.-W.; Kapral, G.J.; Grosse-Kunstleve, R.W.; et al. PHENIX: A comprehensive Python-based system for macromolecular structure solution. *Acta Crystallogr. Sect. D Biol. Crystallogr.* **2010**, *66*, 213–221. [CrossRef]
79. Moriarty, N.W.; Tronrud, D.E.; Adams, P.D.; Karplus, P.A. A new default restraint library for the protein backbone in Phenix: A conformation-dependent geometry goes mainstream. *Acta Crystallogr. Sect. D Biol. Crystallogr.* **2016**, *72*, 176–179. [CrossRef]
80. Emsley, P.; Cowtan, K. Coot: Model-building tools for molecular graphics. *Acta Crystallogr. Sect. D Biol. Crystallogr.* **2004**, *60*, 2126–2132. [CrossRef]
81. Krissinel, E.; Henrick, K. Secondary-structure matching (SSM), a new tool for fast protein structure alignment in three dimensions. *Acta Crystallogr. Sect. D Biol. Crystallogr.* **2004**, *60*, 2256–2268. [CrossRef]
82. Pettersen, E.F.; Goddard, T.D.; Huang, C.C.; Couch, G.S.; Greenblatt, D.M.; Meng, E.C.; Ferrin, T.E. UCSF Chimera—A visualization system for exploratory research and analysis. *J. Comput. Chem.* **2004**, *25*, 1605–1612. [CrossRef]

Acknowledgements / Danksagung

Zu allererst möchte ich **Prof. Dr. Katja Becker** meinen herzlichsten Dank aussprechen. Danke für die Möglichkeit meine Dissertation zu einem so spannenden Thema anfertigen zu dürfen. Danke für das stets offene Ohr, die Inspiration, Motivation und vor allem für das entgegengebrachte Vertrauen, wodurch ich nicht nur viele Labormethoden lernen, sondern auch außerhalb meiner Komfortzone Verantwortung übernehmen durfte. Sei es durch das Vortragen von Ergebnissen auf (inter)nationalen Konferenzen, das Schreiben von Publikationen, das Anwerben von Kooperationspartnern oder die Einblicke in das Schreiben von Anträgen und Gutachten.

Prof. Dr. Peter Friedhoff danke ich herzlich für die Übernahme der Zweitbetreuung und auch den weiteren Mitgliedern der Prüfungskommission, **Prof. Dr. Eveline Baumgart-Vogt** und **Prof. Dr. Ritva Tikkanen** möchte ich für ihr Interesse an meiner Arbeit danken.

Ebenfalls danken möchte ich Prof. **Dr. Jude Przyborski** für die Vertretung von Prof. Dr. Katja Becker, für das entgegengebrachte Vertrauen, Engagement und die freundliche Aufnahme.

Darüber hinaus bin ich sehr dankbar, dass ich mit meinem Projekt Teil des LOEWE Center DRUID Konsortiums sein durfte. Mein besonderer Dank gilt an dieser Stelle **Prof. Dr. Peter Kolb** (Philipps-Universität Marburg), **Prof. Dr. Ger van Zandbergen** (Paul-Ehrlich-Institut, Langen) und **Dr. Stefan Rahlfs**, die die Projektleitung von Prof. Dr. Katja Becker übernommen haben und mich bei der Umsetzung meiner Ziele tatkräftigt unterstützt haben. Vielen Dank für die intensive Kooperation und den hilfreichen Input. Außerdem danke ich für die lehrreichen Einblicke, die ich als Gastwissenschaftlerin am Paul-Ehrlich-Institut erlangen durfte. I would also like to thank **Dr. Jonathan Spector** and **Dr**. **Douglas Auld** from the Novartis Institutes for BioMedical Research (NIBR, Cambridge, USA) for the valuable opportunity to work in their group. I am thankful to **Chun-Hao Chiu** for assisting me with the high-throughput screening and would also like to thank **Zachary Nguyen** and **Kirk Wright** for their introduction and support with the SPR experiments.

I would also like to thank **Dr. Anthony Pinkerton** and colleagues (Sanford Burnham Prebys Medical Discovery Institute, La Jolla, USA), **Prof. Dr. Lars Bode** (University of California, La Jolla, USA) as well as **Prof. Dr. Evelin Schwarzer** and colleagues (University of Torino, Turin, Italy) for the successful collaboration on the SBI-0797750 project.

Des Weiteren möchte ich **Prof. Dr. Grevelding** und **PD. Dr. Simone Häberlein** für die gelungene Kooperation im Schistosomen Projekt danken.

Der gesamten **AG Becker / Przyborski** danke ich für das familiäre Umfeld und die gute Zusammenarbeit. Ein besonderer Dank geht an **Dr. Karin Fritz-Wolf**. Danke für die Einführung in die Labor- und Software-Skills und das Lösen der in dieser Arbeit dargestellten Kristallstrukturen. Vor allem bin ich dankbar für die vielen lehrreichen Gespräche und Ratschläge. Die intensiven Diskussionen über so manch hart zu knackende Proteinstruktur und darüber hinaus waren so wertvoll und werde ich sehr vermissen. Weiterhin möchte ich

Michaela Stumpf für ihre tatkräftige Unterstützung im Labor, die vielen Labortricks, Ratschläge und die Einführung in die Bedienung von FPLC und „Honeybee“ danken. **Dr. Kristina Häußler** und **Marina Fischer** danke ich für ihre geduldige und ausführliche Einführung in die Enzymkinetik. **Dr. Katrin Buchholz** danke ich für die Einführung in die Malaria Zellkultur und die lehrreichen Stunden zur reversen Genetik. Auch **Siegrid Franke** war in Zellkulturfragen eine große Hilfe. Weiterhin danke ich meinen Masterstudierenden **Selina Ohl**, **Massimo Pez**, **Clarissa Gödde** und **Leonie Schmieder** für ihr Engagement im Labor. Ein großer Dank gilt außerdem „meinen“ Auszubildenden **Melanie Moos** und **Ann-Sophie Velten**. Euch etwas beibringen zu dürfen war mir immer eine große Freude, und ich habe selbst so viel zurückbekommen. Danke für eure tatkräftige und vor allem unkomplizierte Unterstützung im Labor. Ein weiterer großer Dank geht an **Dr. Christina Brandstädter** und **Dr. Julia Hahn**. Danke für euren biochemischen und kinetischen Input, euer offenes Ohr und die vielen wertvollen Ratschläge. Nicht zuletzt danke ich besonders meiner Büro-Crew, **Dr. Melissa Dillenberger** und **Dr. Susanne Schipper**. Durch euch war das Doktorandenleben gleich viel leichter. Danke für die vielen hilfreiche Brainstorming Momente, euer offenes Ohr, die beruhigenden Worte und auch für die vielen Erlebnisse außerhalb von Labor und Büro.

Ganz besonders danken möchte ich meinem **Partner**, meiner **Familie** und meinen **Freunden** für ihre Unterstützung, ihre Geduld, ihr Verständnis und die schönen Ablenkungen während der letzten Jahre.